

Mathematical and Numerical Modeling of Healthy and Unhealthy Cerebral Arterial Tissues

THÈSE N° 6232 (2014)

PRÉSENTÉE LE 16 SEPTEMBRE 2014

ÉCOLE POLYTECHNIQUE FÉDÉRALE DE LAUSANNE
À LA FACULTÉ DES SCIENCES DE BASE
CHAIRE DE MODÉLISATION ET CALCUL SCIENTIFIQUE

ET

À L'INSTITUTO SUPERIOR TÉCNICO (IST) DA UNIVERSIDADE DE LISBOA
CENTRO DE MATEMÁTICA E APLICAÇÕES

PROGRAMME DOCTORAL EN MATHÉMATIQUES

ET

DOUTORAMENTO EM MATEMÁTICA

POUR L'OBTENTION DU GRADE DE DOCTEUR ÈS SCIENCES (PhD)

PAR

Paolo TRICERRI

acceptée sur proposition du jury:

Prof. K. Hess Bellwald, présidente du jury
Prof. A. Quarteroni, Prof. A. Sequeira, directeurs de thèse
Prof. D. Ambrosi, rapporteur
Prof. M. Picasso, rapporteur
Prof. A. M. Robertson, rapporteuse



ÉCOLE POLYTECHNIQUE
FÉDÉRALE DE LAUSANNE

Suisse
2014

To my grandparents

Acknowledgements

My PhD represents definitively a unique and precious experience in my life which has surely changed me for the better, especially from a personal point of view. When I will think back to the last four years I have spent in Portugal and Switzerland, I will not remember just the tough and discouraging times but, above all, the people who have helped me on my way and those with whom I have shared unforgettable moments.

Among them, I want to express my deepest gratitude to my two advisors, Adélia Sequeira and Alfio Quarteroni for the great opportunity they gave me welcoming me into their groups at IST and EPFL. They have always been supportive and, asking me to give my best, motivated me to acquire new competences and tackle new problems with enthusiasm. You also gave the chance to discover two beautiful, but also completely different, countries and this has incredibly opened my mind. I wish to thank Simone DeParis for having been an important reference when facing administrative issues in the IST-EPFL project and for the help he gave me at the beginning of the path. Furthermore I must thank Luca Dède; although we have had our strong disagreements, his loyal guidance has been of enormous relevance for my work and our discussions have represented moments of great professional growth.

During these years I have been lucky to be part of two international teams composed of friendly and competent people, past and present. I wish to thank all of them for the humorous moments as well as for the nice times spent in conferences. Particularly, I would like to remember Simone Rossi, my IST-EPFL companion, with whom I have gone through many difficulties but, eventually, we have always succeeded.

I consider my PhD experience unforgettable also for the all friends I have been able to make both in Portugal and Switzerland. I thank Shab, Andrea, François, Giorgia, Soumya, Ana for our beautiful dinners, funny chats, and parties in Bairro Alto. I also wish to thank Alberto, who has become a very close friend over the years, for having always found time to talk with me. I cannot forget our dinners at Sr. Manuel, in Lisbon. On the Swiss side, let me sincerely thank Claudia, Elena, Ale, Cristina, Eleonora, Pol, Hélène, and Radu. The nice times spent together and your smiles are among the brightest memories I have from the PhD. I also want to thank the people from the Lausanne Folks group for having animated my last two years of PhD as well as my friends from Ticino with whom I have had really nice and long parties. I also want to thank my Italian friends with whom I managed to stay in close contact during these years and who have always welcomed me like I have never left from Italy.

Desidero ringraziare tutta la mia famiglia per il sostegno e la forza che, da sempre, ha saputo darmi. In particolare, i miei genitori per avermi educato ai valori del lavoro, dell'onestà, e del rispetto verso gli altri che ogni giorno guidano i miei comportamenti. Voglio anche ringraziare enormemente mia sorella Chiara e mio fratello Carlo che so, e sento, essere sempre al mio fianco.

Lausanne, August 26, 2014

P. T.

Abstract

Over the last two decades, we have witnessed an increasing application of mathematical models and numerical simulations for the study of the cardiovascular system. Indeed, both tools provide an important contribution to the analysis of the functioning of the different components of the cardiovascular system (i.e. heart, vessels and blood) and of their interactions either in physiological and pathological conditions. For this reason, reliable constitutive models for the cardiac, arterial and venous tissues as well as for the blood are an essential prerequisite for a number of different objectives that range from the improved diagnostic to the study of the onset and development of cardiovascular diseases (e.g. atherosclerosis or aneurysms). This work focuses on the mathematical and numerical modeling of healthy and unhealthy cerebral arterial tissue. In particular, it presents a detailed analysis of different constitutive models for the arterial tissue by means of finite element numerical simulations of arterial wall mechanics and fluid-structure interaction problems occurring in hemodynamics. Hyperelastic isotropic and anisotropic constitutive laws are considered for the description of the passive mechanical behavior of the vessels. An anisotropic multi-mechanism model, specifically proposed for the cerebral arterial tissue, for which the activation of the collagen fibers occurs at finite strains is employed. Firstly, the constitutive laws are numerically validated by considering numerical simulations of static inflation tests on a cylindrical geometry representing a specimen of anterior cerebral artery. With this regard, the material parameters for the constitutive law are obtained from the data fitting of experimental measurements obtained on the same vessel. The constitutive models are critically discussed according to their capability of describing the physiological highly nonlinear behavior of arteries and on other numerical aspects related to the computational simulation of arterial wall mechanics. Afterwards, simulations of the blood flow and vessel wall interactions are carried out on idealized blood vessels in order to analyze the influence of the modeling choice for the arterial wall on hemodynamic and mechanical quantities that are commonly considered as indicators of physiological or pathological conditions of arteries. We also consider the numerical simulations of unhealthy cerebral arterial tissues by taking into account the mechanical weakening of the vessel wall that occurs during early development stages of cerebral aneurysms by means of static inflation and FSI simulations. We employ both isotropic and anisotropic models study the effects of the mechanical degradation on hemodynamic and mechanical quantities of interest. The FSI simulations are carried out both on idealized geometries of blood vessels and on domains representing idealized and anatomically realistic cerebral aneurysms.

Keywords: Arterial wall mechanics, hyperelastic isotropic and anisotropic models, multi-mechanism model, fluid-structure interaction, healthy and unhealthy cerebral arterial tissue.

Résumé

Depuis deux décennies maintenant, nous assistons à une demande croissante en matière de modèles mathématiques et simulations numériques pour l'étude du système cardiovasculaire. De fait, ces deux outils apportent une contribution importante à l'analyse des différents composants du système cardiovasculaire (cœur, vaisseaux, et sang) et à celle de leurs interactions, que ce soit dans des conditions physiologiques ou pathologiques. Pour cette raison, développer des modèles de comportement fiables pour le sang et les tissus cardiaques, artériels et veineux est une condition essentielle pour atteindre un certain nombre d'objectifs relatifs à l'amélioration du diagnostic et de l'étude de maladies cardiovasculaires l'athérosclérose ou les anévrismes, par exemple. Ce travail est axé sur la modélisation mathématique et numérique du tissu artériel cérébral sain et malade . En particulier, il présente une analyse détaillée de différents modèles de comportement pour le tissu artériel au moyen d'éléments finis pour les simulations numériques de la mécanique de la paroi artérielle et les problèmes d'interaction fluide-structure se produisant en hémodynamique. On recourt à des lois de comportement isotrope et anisotrope hyperélastique pour la description de la mécanique' passive des vaisseaux ; en particulier, nous considérons un modèle anisotrope multi-mécanismes est en particulier proposé pour le tissu artériel cérébral, pour lequel l'activation des fibres de collagène a lieu à des déformations finis. Les lois de comportement sont d'abord numériquement validées par l'examen des simulations numériques de tests d'inflation statiques sur une géométrie cylindrique représentant un échantillon de l'artère cérébrale antérieure. Acet égard, les paramètres de matériau pour la loi de comportement sont calculés à partir de l'ajustement de mesures expérimentales obtenues sur le même vaisseau. Les modèles de comportement sont discutés en fonction de leur capacité à décrire le comportement physiologique fortement non linéaire des artères. D'autres aspects numériques liés à la simulation numérique de la mécanique de la paroi artérielle sont également examinés. Des simulations de l'écoulement du sang et des interactions de paroi du récipient sont ensuite réalisées sur les vaisseaux sanguins idéalisés. Ceci permet d'analyser l'influence du type de modélisation de la paroi artérielle sur les quantités hémodynamiques et mécaniques. Ces dernières sont en effet généralement considérées comme de bons indicateurs des conditions physiologiques ou pathologiques des artères. Nous considérons également les simulations numériques des tissus artériels cérébraux atteints en tenant compte de l'affaiblissement mécanique de la paroi du vaisseau se produisant pendant les phases précoces de développement de l'anévrisme cérébral. Celles-ci sont réalisées au moyen d'inflation statique et de simulations FSI. Nous employons deux modèles isotropes et anisotropes pour étudier les effets de la dégradation mécanique sur les quantités d'intérêt hémodynamiques et mécaniques. Les simulations FSI sont effectuées tant sur les géométries idéalisées des vaisseaux sanguins que sur les domaines représentant des anévrismes cérébraux idéalisés et anatomiquement réalistes.

Mots-clés : Mécanique des artères, modèles isotropes et anisotropes hyperélastique, modèle multi-mécanismes, interaction fluide-structure, tissu artériel cérébral sain et malade.

Extrato

Ao longo das duas últimas décadas, temo-nos deparado com uma crescente aplicação de modelos matemáticos e simulações numéricas no estudo do sistema cardiovascular. Para o efeito, estas ferramentas proporcionam uma contribuição importante para a análise do funcionamento dos diferentes componentes do sistema cardiovascular (coração, vasos e no sangue) e de suas interações, quer em condições fisiológicas quer em condições patológicas. Por esta razão, os modelos constitutivos fiáveis para análise dos tecidos cardíaco, arteriais e venosos, assim como para o sangue, são um pré-requisito essencial para uma série de objectivos variados, que vão desde um diagnóstico melhorado ao estudo do aparecimento e desenvolvimento de doenças cardiovasculares (por exemplo, aterosclerose ou aneurismas). Este trabalho concentra-se na modelagem matemática e numérica de tecido arterial cerebral saudável e patológico. Em particular, apresenta-se uma análise detalhada dos diferentes modelos constitutivos para o tecido arterial usando simulações numéricas pelo método dos elementos finitos da mecânica da parede arterial e problemas de interação fluido-estrutura que ocorrem em hemodinâmica. Leis constitutivas hiperelásticas isotrópicas e anisotrópicas são consideradas para a descrição do comportamento mecânico passivo dos vasos. Um modelo anisotrópico multi-mecanismo, especificamente proposto para o tecido arterial cerebral, é utilizado para que a ativação das fibras de colágeno ocorram em dadas deformações. Em primeiro lugar, as leis constitutivas são numericamente validadas considerando simulações numéricas de testes estáticos de inflação numa geometria cilíndrica idealizadas que representa uma amostra da artéria cerebral anterior. Para este efeito, os parâmetros relevantes para estas leis constitutivas são obtidos a partir da obtenção de medições experimentais obtidos no mesmo tipo de vaso. Os modelos constitutivos são discutidos de acordo com a sua capacidade de descrever o comportamento fisiológico não-linear das artérias e noutros aspectos numéricos relacionados com a simulação computacional da mecânica da parede arterial. Depois, simulações do fluxo sanguíneo e interações com a parede do vaso são realizadas em vasos sanguíneos idealizados, a fim de analisar a influência da escolha de modelos para a parede arterial com valores mecânicos e hemodinâmicos que são comumente considerados como indicadores de condições patológicas das artérias. Consideramos também as simulações numéricas de tecidos arteriais cerebrais saudáveis, tendo em conta o enfraquecimento da parede do vaso que ocorre durante as fases iniciais de desenvolvimento de aneurismas cerebrais por meio de inflação estática e simulações FSI. Modelos isotrópicos e anisotrópicos foram utilizados para estudar os efeitos da degradação mecânica para valores mecânicos e hemodinâmicos de interesse. As simulações FSI são realizadas tanto em geometrias de vasos sanguíneos idealizadas, bem como em domínios que representam aneurismas cerebrais idealizados e anatomicamente realistas.

Palavras-chave: Mecânica da parede arterial, modelos isotrópicos e anisotrópicos hiperelásticos, modelo multi-mecanismo, interação fluido-estrutura, tecido arterial cerebral saudável e insalubre.

Contents

Acknowledgements	iii
Abstract (English)	v
Résumé (French)	vii
Extrato (Portuguese)	ix
1 Introduction	1
I Biomechanics of the arterial tissue	7
2 Histology and mechanical properties of healthy arterial tissue	9
2.1 Histology of healthy arterial tissue	9
2.2 Mechanical behavior of the healthy arterial tissue	11
3 Continuum Mechanics: preliminaries	15
3.1 Introduction to Continuum Mechanics	15
3.1.1 Kinematics of a continuous body	15
3.1.2 The concept of mechanical stress	18
3.2 Fundamental principles in continuum mechanics	19
3.2.1 The mass balance	20
3.2.2 The balance of the momentum of forces	21
3.2.3 The second law of thermodynamics	22
3.3 Modeling principles for continuous elastic bodies	23
3.4 General form of constitutive models	24
4 Constitutive modeling of the arterial tissue	27
4.1 The polyconvexity condition	28
4.2 Constitutive models for the healthy cerebral arterial tissue	29
4.2.1 Isotropic constitutive laws	30
4.2.2 Anisotropic constitutive laws	37
4.3 Modeling the nearly-incompressible behavior of arteries	47
4.3.1 Volumetric-Isochoric split of the deformation gradient tensor	50
4.3.2 Volumetric strain energy functions	52
4.3.3 Isochoric strain energy functions	53
4.3.4 Remarks on the volumetric-isochoric split	57

5	Numerical validation of constitutive models for the arterial tissue	63
5.1	Numerical approximation: the Finite Element Method	64
5.1.1	Strong and weak formulations of the structural mechanics problem	64
5.1.2	Numerical discretization	65
5.1.3	Linearization of the nonlinear discrete structural problem	66
5.2	Implementation and numerical aspects of simulations of arterial wall mechanics	67
5.2.1	Efficient implementation of highly nonlinear constitutive models in <code>LifeV</code>	68
5.2.2	Mathematical description of the collagen fibers activation	70
5.2.3	Finite element approximation of a multi-mechanism model	70
5.2.4	Remarks on the numerical solution of the nonlinear discrete problem	74
5.3	Representative problems	76
5.4	Numerical simulations of static inflation tests	84
5.4.1	The set of experimental measurements and the least squares data fitting	84
5.4.2	Numerical simulations of inflation tests	90
5.4.3	Conclusions	100
II	Fluid-Structure Interaction Problems for the Cardiovascular System	103
6	Mathematical Modeling of Fluid-Structure Interaction problems	105
6.1	Mathematical formulation of the Fluid-Structure Interaction Problem	108
6.2	Space-Time discretization and solution of the FSI problem	113
7	Applications to hemodynamics: healthy cerebral vessels	117
7.1	Problem setting	117
7.2	Numerical simulations on idealized blood vessels	119
7.2.1	FSI simulations on a straight cylinder	119
7.2.2	On the collagen fibers activation in FSI numerical simulations	132
7.2.3	FSI simulations on a toroidal vessel geometry	135
7.2.4	Conclusions	138
III	Biomechanics of unhealthy arterial tissue	141
8	Mathematical modeling and numerical simulations of unhealthy arterial tissue	143
8.1	Cerebral aneurysms and their histopathology	145
8.2	Mathematical modeling of arterial tissue weakening	149
8.3	Numerical simulations of unhealthy arterial tissue mechanics: static inflation tests	151
8.3.1	Calibration of the weakening parameter D for unhealthy cerebral arterial tissue	152
8.3.2	Numerical simulations of inflation tests on unhealthy cerebral arterial tissue	155
9	Fluid-Structure Interaction numerical simulations of unhealthy cerebral arteries	161
9.1	Setup of the fluid-structure interaction simulations	163
9.2	Numerical simulations on idealized geometries of vessels	164
9.3	Numerical simulations on cerebral aneurysms	175
9.3.1	Idealized saccular aneurysm	175
9.3.2	Anatomically realistic geometry of saccular aneurysm	186
9.3.3	Conclusions	194

10 Conclusions and future perspectives	197
Bibliography	201
Curriculum Vitae	217

1 Introduction

In the past two decades, thanks to the increasing availability of computational resources and the progresses in imaging and geometry reconstruction techniques, the interest in numerical simulations for the study of the cardiovascular system, both in physiological and pathological conditions, has significantly increased. Indeed, medical decisions critically depend on the understanding of the physiological interactions (biological, chemical, and mechanical) between the blood and the wall of the arteries that govern the correct functioning of the cardiovascular system, as well as of pathological conditions associated to cardiovascular diseases. In this regard, numerical simulations have become an effective tool to study the physiology of the cardiovascular system, as well as to predict the natural course of its diseases and, possibly, the occurrence of cardiovascular accidents [Formaggia et al., 2009; Sforza et al., 2009; Cebal et al., 2005; Jeong and Rhee, 2012]. Cardiovascular diseases, such as hypertension, atherosclerosis, or aneurysms, may fundamentally harm the cardiovascular system, especially the heart, arteries, and veins, and represent the leading causes of patients' mortality and morbidity in industrialized countries [Murray and Lopez, 1996]. The significant biological complexity of the cardiovascular system poses numerous challenges for its mathematical modeling and numerical simulation. For instance, the mathematical description of the constituents of the cardiovascular system, namely the heart, blood vessels, and blood, should correctly describe their most important features by representing the phenomena at hand and by taking into account the main biological interactions among their components. At the same time, the numerical simulations of these complex phenomena should provide reliable results, based on their validation with respect to experimental measurements, in reasonable computational times.

This work addresses the study of the cardiovascular system both in physiological and pathological conditions by means of mathematical models and numerical simulations [Formaggia et al., 2009]. In particular, we focus on the cerebral vasculature and blood circulation, as done e.g. in [McGloughlin, 2011; Torii et al., 2008, 2009, 2006; Chen et al., 2009; Valencia et al., 2013; Valencia and Solis, 2006; Bazilev et al., 2010; Bazilevs et al., 2010; Sforza et al., 2009; Oubel et al., 2010; Cebal et al., 2011, 2003, 2005; Marzo et al., 2010; Reymond et al., 2010]. More specifically, we address the mathematical and numerical modeling of healthy and unhealthy cerebral arterial tissues. In this respect, we remark that mathematical models for the arterial tissue must capture the main features of the mechanical response of arteries to applied external loads [Holzapfel and Gasser, 2000; Schriefl, 2012; Monson, 2001; Monson et al.; Kenneth et al., 2008]; at the same time, reliable results, for which quantities of interest that cannot be measured in *in vivo* condition, should be obtained from the numerical simulations of both arterial wall mechanics and blood flows in compliant arteries, that is arteries that deform under the action of the blood flow [Nichols and O'Rourke, 1998]. In the biomedical community, the

research on cerebral aneurysms by means of numerical simulations has focused so far mostly on the simulation of the blood flow either in rigid [Zakaria et al., 2008; Oshima et al., 2005; Lou et al., 2008; Mantha et al., 2006; Castro et al., 2006; Baek et al., 2010; Gambaruto and João, 2012; Hoi et al., 2006; Ford et al., 2008; Augsburger, 2008] and in compliant arteries [Torii et al., 2009; Valencia and Solis, 2006; Bazilev et al., 2010; Bazilevs et al., 2010; Torii et al., 2010, 2007; Isaksen et al., 2008]. These works have investigated many aspects related to the blood flow in aneurysms; for instance, the flow structures inside developed aneurysms [Mantha et al., 2006; Baek et al., 2010; Gambaruto and João, 2012; Hoi et al., 2006; Ford et al., 2008], the influence of the geometrical configuration [Torii et al., 2009; Zakaria et al., 2008; Castro et al., 2006; Lou et al., 2008; Mantha et al., 2006; Augsburger, 2008], the role of the boundary conditions of the mathematical problem describing the blood flow [Oshima et al., 2005; Torii et al., 2007], or the distribution of mechanical stresses inside the aneurysm dome during the cardiac cycle [Bazilev et al., 2010; Bazilevs et al., 2010; Torii et al., 2010; Isaksen et al., 2008]. However, few works, namely [Torii et al., 2008; Chen et al., 2009; Valencia et al., 2013; Valencia and Solis, 2006], have addressed the influence of the constitutive model for the vessel wall on the numerical results, and associated hemodynamical indicators. In these works the arterial tissue is typically described as an isotropic material with both linear and nonlinear models. Conversely, in this thesis we consider both the nonlinear isotropic and anisotropic constitutive laws for the vessel wall that represent the state of the art of the arterial tissue modeling [Valencia et al., 2013; Holzapfel and Gasser, 2000; Li and Robertson, 2009b; Dalong et al., 2012; Delfino et al., 1997; Calvo et al., 2007; Balzani et al., 2013; Weisbecker et al., 2011; Gasser and Holzapfel, 2006; Gasser et al., 2002]. Our analysis is carried out by means of numerical simulations of biomechanical and biomedical applications of interest including idealized and patient-specific cerebral arteries. Indeed, this work aims at providing a contribution within the context of finite element ([Quarteroni and Valli, 1999b]) realistic numerical simulations of cerebral arteries and the cardiovascular system at large. In particular, the numerical simulations of the interactions between blood flow and vessels that occur in cerebral arteries and aneurysms are addressed. For this reason, we discuss the mathematical modeling of healthy arterial tissue and that of unhealthy arteries. In particular, for the healthy arterial tissue, we consider both isotropic ([Delfino et al., 1997; Balzani, 2006; Treloar, 1975; Holzapfel, 2000]) and anisotropic ([Calvo et al., 2007; Holzapfel and Gasser, 2000; Gasser and Holzapfel, 2006; Gasser et al., 2002]) laws, and a multi-mechanism model ([Wulandana and Robertson, 2005; Li and Robertson, 2009a,b; Dalong et al., 2012]) specifically proposed for cerebral arteries, that can capture the stiffening effect in the mechanical response of healthy arteries at finite strains [Holzapfel and Gasser, 2000; Scott et al., 1972]. The unhealthy conditions of arteries that occur during the onset of aneurysms [Humphrey and Canham, 2000], are described by means of the approach firstly proposed in [Kachanov, 1958] based on the concept of internal state variable. According to [Kachanov, 1958], the degradation of the mechanical properties of a material (i.e. the arterial wall) can be modeled at the macroscopic scale by means of a dimensionless internal state variable $D \in [0, 1]$ which represents the degradation of the material, being intact for $D = 0$ and fully degraded for $D = 1$. This approach has been adopted in [Calvo et al., 2007; Li and Robertson, 2009a; Dalong et al., 2012; Weisbecker et al., 2011; Famaey et al., 2012] to describe different types of damaged biological tissues, e.g. arteries or ligaments. Different damage models have been proposed in literature to describe the degradation of the mechanical properties of the arterial tissue as a result of mechanical and chemical external factors [Li and Robertson, 2009a; Dalong et al., 2012; Balzani et al., 2013; Calvo et al., 2007; Weisbecker et al., 2011; Balzani et al., 2012; De Souza Neto et al., 1998; Simo and Ju, 1987]. However, so far, such models have only been considered in the numerical simulations of angiography [Dalong et al., 2012; Balzani et al., 2013, 2006b] and arterial clamping [Famaey et al., 2012] rather than for fluid-structure interaction (FSI) simulations of the blood-flow in compliant arteries. This can be explained by considering that the damage caused by medical interventions can be assumed to be related only to the deformations of the vessel registered during the surgery and on the fact that the time scales

characterizing the operation and the creation of damage are comparable. Conversely, we consider a simplified weakening model for which the progressive degradation of the mechanical properties of the healthy tissue is described by a set of prescribed levels of mechanical weakening through the parameter D . Our choice is motivated by the fact that we aim at evaluating how the constitutive model for the arterial tissue influences the spatial and temporal distributions of relevant quantities in the clinical context, namely blood pressure, blood flow pattern, vessel wall displacement, and Wall Shear Stress (WSS), rather than describing the growth and enlargement of a cerebral aneurysm by numerical simulations, as done e.g. in [Baek et al., 2006; Kroon and Holzapfel, 2007; Chatziprodromou et al., 2007; Watton et al., 2009b]. We focus on the numerical simulation of few cardiac cycles as done e.g. in [Torii et al., 2008; Chen et al., 2009; Valencia et al., 2013; Valencia and Solis, 2006; Bazilev et al., 2010; Bazilevs et al., 2010; Torii et al., 2010; Isaksen et al., 2008; Malossi, 2012; Crosetto et al., 2013; Malossi and Bonemann, 2013] rather than simulating the complex, and not fully understood, biological processes of the onset, growth, and rupture of aneurysms ([Humphrey and Canham, 2000; Campbell and Roach, 1981; Sekhar and Heros, 1981; Ferguson, 1972b; Scott et al., 1972; Kroon and Holzapfel, 2007; Sherif et al., 2014]); indeed, the latter processes occur at different time scales, spanning months or years, and cannot be practically studied by means of FSI simulations. Therefore, in order to study the influence of the constitutive model for the tissue on the numerical results, we present finite element numerical simulations of static inflation tests and FSI problems both in idealized geometries of the Anterior Cerebral Artery (ACA) and patient-specific blood vessels in healthy and unhealthy conditions.

This work is divided into three parts, which we summarize in the following.

- *Part I* deals with the numerical validation of the isotropic and anisotropic constitutive models for the healthy arterial tissues. With this aim, **Chapter 2** introduces their histology together with the main features of their passive mechanical behavior [Nichols and O'Rourke, 1998; Humphrey, 2002]. With this aim, the different layers of the arterial wall, their composition and their mechanical contribution to the overall passive mechanical behavior are described; in particular, the nonlinearity and anisotropy of the arterial mechanical behavior are discussed. In this work, we describe the cerebral arteries and blood flow at the macroscopic scale, as commonly done in both biomechanical and biomedical communities [Formaggia et al., 2009; Fung, 1993; Humphrey, 2002]. As a consequence, the artery is viewed as a continuous media for which mass, displacement, and energy are described by means of the scalar, vectorial, and tensorial fields, according to the continuum mechanics theory [Holzapfel, 2000; Odgen, 1997]. **Chapter 3** recalls the basic concepts of the continuum mechanics theory; in particular, the concept of mechanical stress as a consequence of the deformations of the body is discussed [Holzapfel, 2000]. Then, the Partial Differential Equations (PDEs) governing the mechanical response of a body are detailed together with the second law of thermodynamics. In particular, we introduce the concept of strain energy function (or constitutive law) [Holzapfel, 2000; Odgen, 1997] that is generally used to model the mechanical response of a body. **Chapter 4** deals with the mathematical modeling of the arterial tissue. Firstly, we discuss the modeling principles and mathematical conditions (such as the polyconvexity condition [Balzani, 2006; Ball, 1977b,a, 1997; Dacorogna, 2000; Ciarlet, 1988; Marsden and Hughes, 1983]) that a strain energy function must satisfy to be deemed physically admissible and to ensure the existence of solutions of the arterial wall mechanics problem. Afterward, we present a review of both the standard nonlinear isotropic and anisotropic constitutive models for arteries proposed in literature [Treloar, 1975; Vanishav and Vossoughi, 1983; Takamizawa and Hayashi, 1987; Delfino et al., 1997; Balzani, 2006; Holzapfel, 2000; Holzapfel and Gasser, 2000; Li and Robertson, 2009b]. Indeed, the former are still largely used in the biomechanics community [Delfino et al., 1997; Gundiah et al., 2008; Crosetto et al., 2013] due to their capability

of describing the nonlinear mechanical response of the tissue without requiring information on its fibrous constituent, while the latter are receiving increasing attention ([Dalong et al., 2012; Calvo et al., 2007; Balzani et al., 2006a, 2012]) in numerical simulations due to the advancements in microscopy techniques making available information about the orientation and distribution of the collagen fibers [Schriefl, 2012; Hill et al., 2012]. The isotropic constitutive laws employed in this work are the St. Venant-Kirchhoff [Holzapfel, 2000] and first and second order exponential laws [Delfino et al., 1997; Balzani, 2006]. Such choices are motivated by the fact that the St. Venant-Kirchhoff is still largely used in the study of blood flow in compliant arteries as e.g. in [Formaggia et al., 2009; Valencia et al., 2013; Malossi, 2012; Crosetto, 2011], while the two exponential type laws are suitable to capture the nonlinear behavior of arteries over finite strains [Delfino et al., 1997; Torii et al., 2007; Williamson et al., 2003]. Regarding the anisotropic laws, we consider two types of them: one for which the recruitment of the collagen fibers occurs as soon as their deformed length is greater than their length at zero strains [Holzapfel and Gasser, 2000; Gasser and Holzapfel, 2006; Gasser et al., 2002] (i.e. when no external loads act on the artery) and the second, referred to as the multi-mechanism model and specifically proposed for cerebral arteries in [Li and Robertson, 2009b; Wulandana and Robertson, 2005], that captures the recruitment of the collagen fibers at finite strains. Indeed, the activation of the collagen fibers once they are stretched beyond a certain threshold, therefore once a certain level of deformation of the tissue is reached, is considered the underlying mechanism of the stiffening effect reported in the mechanical response of arteries at finite strains [Holzapfel and Gasser, 2000; Scott et al., 1972; Hill et al., 2012]. Finally, the chapter deals with the mathematical modeling and numerical simulation of the nearly-incompressible behavior of arteries. Indeed, the arterial tissue shows a quasi incompressible behavior in physiological conditions [Carew et al., 1968] and its numerical simulation poses different numerical challenges due, for instance, to the occurrence either of locking phenomena or ill-conditioned linear systems [Hughes, 2000; Bonet and Wood, 1997; Brinkhues et al., 2013]. In this work, we model the nearly incompressible behavior of arteries by means of the multiplicative decomposition of the deformation gradient in a volumetric and an isochoric part [Flory, 1961] as alternative to other approaches [Glowinski and Le Tallec, 1982, 1984; Elguedj et al., 2008; Weiss et al., 1996; Simo et al., 1985; Masud and Truster, 2013]. **Chapter 5** addresses the numerical validation of the constitutive models under consideration. With this aim, the finite element numerical approximation of the structural mechanics problem, the consequent linearization of the nonlinear discrete system of equations, and the contributions to the development of the C++ finite element `LifeV` [Éco, 2010], which we use to obtain the numerical results, are detailed. Then, the numerical validation of the isotropic and anisotropic laws by means of finite element simulations of static inflation tests on a cylindrical idealized specimen of ACA is presented. In order to describe the mechanical behavior of healthy ACAs the material parameters for the different constitutive laws must be correctly determined. With this aim, the mathematical models are adequately fitted to a set of experimental data measuring the mechanical response of ACAs [Scott et al., 1972]. To conclude, the good agreement between the constitutive laws obtained from the numerical results and the data fitting is highlighted and critically discussed by analyzing different important aspects related to the numerical simulations in biomechanical applications. The discussion focuses on the capability of reproducing the data fitting by the different models and commenting the effectiveness of the adopted approach for the numerical simulations of the nearly-incompressible behavior of arteries in biomechanical applications.

- *Part II* addresses numerical simulations of FSI problems in hemodynamics on idealized geometries of healthy blood vessels with different constitutive models. **Chapter 6** presents a literature

review of FSI simulations for blood flows in compliant arteries ([Torii et al., 2008, 2009; Valencia et al., 2013; Bazilevs et al., 2010; Malossi, 2012; Crosetto et al., 2013; Malossi and Bonemann, 2013; Crosetto, 2011; Moireau et al., 2012; Janela et al., 2010c]). In addition, it recalls the Arbitrary Lagrangian-Eulerian (ALE) formulation ([Formaggia et al., 2009]) for the coupled FSI problem and the numerical methods used for its solutions [Crosetto, 2011; Nobile, 2001; Pozzoli, 2011; Küttler et al., 2010]. **Chapter 7** presents the FSI numerical simulations for two geometries of blood vessels, namely a cylindrical and a toroidal geometry. The numerical results obtained with the different models are critically analyzed by comparing the flow field, the vessel wall displacement, and the deformations of the collagen fibers for the anisotropic laws. More precisely, the numerical simulations on the straight cylinder point out the fact that, for such configuration of the FSI system, the choice of the constitutive model does not significantly affect the numerical results, namely the blood flow and vessel wall dynamics. At the same time, we highlight that when the multi-mechanism model is employed, it is possible to capture the progressive activation and deactivation of the collagen fibers throughout the vessel wall during the cardiac cycle. Indeed, we will show that the collagen fibers located on the internal surface of the vessel wall are mechanically active for the largest part of the cardiac cycle, while the ones located on the external parts of the tissue reach the active state only during the peak of the systolic phase. With these simulations, we aim at understanding the influence of the material law and, for the anisotropic models, the role and importance of including the collagen fibers in the model.

- *Part III* deals with the mathematical and numerical modeling of unhealthy arterial tissues; in particular, we focus on the mechanical weakening that occurs during the onset of cerebral aneurysms [Humphrey and Canham, 2000; Campbell and Roach, 1981; Sekhar and Heros, 1981; Ferguson, 1972b; Scott et al., 1972; Kroon and Holzapfel, 2007; Sherif et al., 2014]. We consider a mechanical weakening model for which the mechanical integrity of the healthy arterial tissue is reduced by a prescribed factor measured by means of the dimensionless degradation parameter $D \in [0, 1]$, as initially proposed in [Kachanov, 1958]. We focus on the influence on the deformations and mechanical stresses inside the arterial wall of the constitutive model for different levels of weakening, i.e. for different values of D . **Chapter 8** introduces the etiology, histopathology, and medical treatments to aneurysms [McGloughlin, 2011; Stehbens, 1989; Caranci et al., 2013]. Then, the mathematical modeling of damaged arterial tissue is presented. In particular, we discuss some of the models proposed in literature ([Li and Robertson, 2009a; Dalong et al., 2012; Balzani et al., 2013; Calvo et al., 2007; Weisbecker et al., 2011; Balzani et al., 2012; De Souza Neto et al., 1998; Simo and Ju, 1987]) and we introduce the simplified weakening model considered in this work. Afterward, Chapter 8 presents numerical simulations of static inflation tests on a specimen of ACA in which the mechanical weakening occurs only in a limited region of the computational domain. The arterial tissue is described by the second order exponential type law [Balzani, 2006] and the two anisotropic models introduced in Chapter 4 ([Holzapfel and Gasser, 2000; Li and Robertson, 2009b]). Once again, the numerical results are critically analyzed and the importance of the choice of the constitutive equations when modeling unhealthy arterial tissues is highlighted. **Chapter 9** considers FSI numerical simulations on idealized weakened blood vessels and patient-specific cerebral aneurysms. The first set of simulations that is presented involves the idealized geometries of blood vessel already considered in Chapter 6. In this case, the influence on the WSS and other mechanical indicators of the level of the mechanical weakening and of the constitutive models is evaluated. Finally, numerical simulations on geometries of aneurysms are discussed. On the idealized geometry of an aneurysm, the second order isotropic model [Balzani, 2006] and the anisotropic law for which the collagen fibers recruitment is measured with respect to their length in the reference configuration [Holzapfel and Gasser, 2000] are

taken into account, due to the possibility of exactly prescribing the characteristic direction of the collagen fibers inside the vessel wall. On the other hand, in the case of the patient-specific geometry of an aneurysm, the first and second order exponential isotropic models [Delfino et al., 1997; Balzani, 2006] are used to describe the mechanical behavior of the arterial tissue. The numerical simulations on the idealized vessels and aneurysm will point out that the choice of an anisotropic constitutive model for the vessel wall rather than an isotropic one strongly affects the numerical results.

Finally, we draw some conclusions and summarize the innovative contributions of this work in the field of computational hemodynamics for cerebral arteries and aneurysms. Furthermore, we discuss possible future developments, mainly consisting in addressing the most critical numerical aspects related to the use of the multi-mechanism model in finite element arterial wall mechanics and FSI simulations and the further validation of the numerical results with respect to experimental measurements.

Biomechanics of the arterial tissue **Part I**

2 Histology and mechanical properties of healthy arterial tissue

In the human body, systemic arteries, i.e. vessels that are part of the systemic circulation Nichols and O'Rourke [1998], carry the oxygenated blood from the heart to the periphery of the circulatory system. Arteries are classified as *elastic*, *muscular*, based on their biological function and size. Large vessels located close to the heart such as, for instance, the thoracic and abdominal aorta belong to the first group. They are characterized by distinct elastic properties which make them suitable for smoothing the pulsating blood pressure waves originating from the heart; therefore, they are exposed to high circumferential deformations Nichols and O'Rourke [1998]; Schriefl [2012]. Muscular arteries are located at the periphery of the circulatory system such as, for instance, the femoral or cerebral arteries. Such vessels are smaller in diameter than the elastic vessels and undergo small deformations compared to the ones occurring for elastic arteries. Muscular arteries are responsible for the regulation of the blood flow via vasoconstriction and vasodilatation. This chapter describes the histology and the mechanical behavior of the healthy arterial tissue from a general point of view. More precisely, Sec. 2.1 describes the layered structure of the healthy arterial tissue highlighting the mechanical role of each layer. Afterwards, in Sec. 2.2, the mechanical response of healthy arteries to physiological deformations is presented. In particular, the aspects of the mechanical behavior of healthy arterial tissue which are important within the context of constitutive modeling that will be considered in Ch. 4 are discussed.

2.1 Histology of healthy arterial tissue

Although different biological functions, the tissue composing elastic and muscular arteries and arterioles presents a common layered structure. The walls of healthy arteries consist mainly of three concentric layers. From the innermost to the outermost, these are: the *tunica intima*, the *tunica media*, and the *tunica adventitia*. In addition, the intima and media layers and the media and adventitia layers are separated by the *internal elastic lamina* and *external elastic lamina*, respectively. The general structure of the healthy arterial tissue is represented in Fig. 2.1.

The tunica intima consists of the vascular endothelium, which is a single layer of cells, and a thin layer of elastin and collagen fibers that anchors it to the internal elastic lamina Nichols and O'Rourke [1998]. In healthy young individuals the intima is very thin and its contribution to the overall mechanical properties of the arterial tissue is negligible. However, since the tunica intima thickens and stiffens with age, its contribution might become mechanically significant with aging or when atherosclerosis occurs Schriefl [2012]; Holzapfel and Gasser [2000].

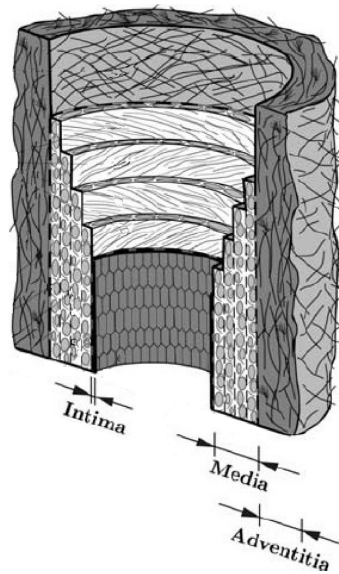


Figure 2.1: Representation of the three main layers composing healthy arterial tissue. Picture from Holzapfel and Gasser [2000]

The tunica media forms the large part of the vessel wall; it is composed of a complex network of smooth muscle cells, elastin and collagen fibers organized in a varying number of medial lamellar units Rhodin [1980]; Holzapfel [2009]. As reported in Schriefl [2012], the collagen fibers are mostly circumferentially oriented; in addition, the close interconnection between the elastin, collagen fibers and smooth muscle cells gives the media of high strength, resilience and the ability to resist to loads in both the longitudinal and circumferential directions. For this reason, from the mechanical point of view, it is the principal determinant of mechanical properties of the arterial tissue. It is worth pointing out that the structure of the media layer changes according to the type of artery that is being considered. Indeed, for instance, the arrangement of the smooth muscle cells in muscular arteries and arterioles is different from the one observed in elastic arteries due to their important role in governing vasoconstriction or vasodilatation of peripheral vessels.

The tunica adventitia consists mainly of fibroblasts and fibrocytes (cells that produce collagen and elastin) and thick bundles of collagen fibrils forming a fibrous tissue whose most important function is the protection of the vessel wall from overstretch and rupture Nichols and O'Rourke [1998]. The collagen fibers are arranged to form helical structures around the vessel wall and are in a wavy state which makes them unable to load bear until they are completely straighten. It is worth pointing out that, the thickness of the adventitia changes with the artery location; in particular, it decreases when moving to the periphery of the circulatory system. The interested reader may refer to Schriefl [2012]; Sommer [2008] for a more detailed description of the composition of all the three layers.

This work focuses on the mathematical modeling and numerical simulations of the cerebral arterial tissue mechanics. The human brain accounts for just three percent of the body weight but its activity requires one-fourth of the total cardiac output. The normal function of the brain's control centers is dependent upon adequate supply of oxygen and nutrients through a dense network of arteries establishing the cerebral blood circulation, represented in Fig. 2.2(a). Arterial blood is supplied to the brain through four main arteries, the left and right internal carotid arteries and the left and right vertebral arteries. Branches of these four vessels eventually join together at the base of the brain to

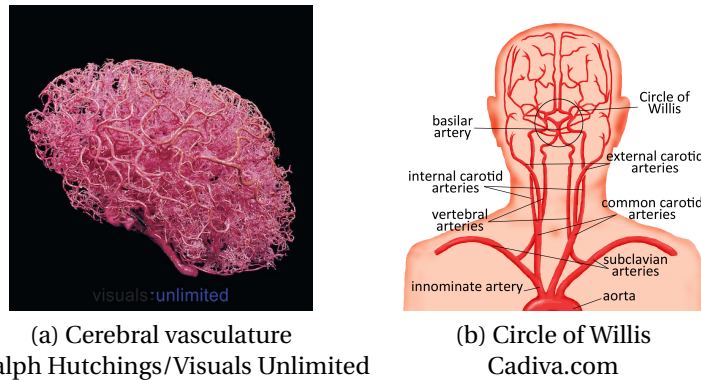


Figure 2.2: Cerebral vasculature and Circle of Willis

form the Circle of Willis as in Fig. 2.2(b). Due to the physiological relevance of the cerebral vasculature, the study of cerebral arteries by means of mathematical models and numerical simulations aims at providing the physicians a reliable tool toward a better understanding of the physiological, and possibly pathological, cerebral hemodynamics. For this reason, a preliminary characterization of the mechanical behavior of healthy cerebral arterial tissue is extremely important before investigating the changes in the mechanical properties of the tissue that occur in pathological states of arteries, such those resulting from cerebrovascular accidents. In the next section, the main features of the mechanical behavior of healthy arteries, that will be modeled in Ch. 4 and Ch. 5, are described.

2.2 Mechanical behavior of the healthy arterial tissue

The description of the mechanical behavior of arteries by means of mathematical models relies on the availability and quality of experimental measurements that aim at characterizing the response of the tissue under different loading conditions. Such experimental data might be obtained from *in vivo* tests or from *in vitro* experiments that mimic real load conditions in a physiological environment. *In vivo* tests are obviously preferable because the vessel is observed under real life conditions. However, such experiments have major limitations because of the influence of different factors (such as, for instance, hormones and nerve control) whose effects on the mechanical behavior of the tissue cannot be controlled. An important advantage of the *in vitro* mechanical tests is that the mechanical properties of each layer composing the vessel wall can be studied separately as, for instance, in Sommer [2008]; Sommer et al. [2010]. Moreover, if the passive mechanical response of arteries, provided by the elastin and collagen fibers in the media and adventitia layers, is studied, the active contribution of the smooth muscle cells can be appropriately inhibited by means of chemical agents. For this reason, since the pioneer works in Cox [1974]; Dobrin and Rovick [1969], *in vitro* tests are carried out in order to measure the mechanical properties of the arterial tissue. In order to fully characterize the mechanical behavior of an anisotropic material such as the arterial tissue, inflation-extension and twist tests which can only be carried out *in vitro* are necessary Holzapfel and Gasser [2000]. When experimental tests are carried out, the tissue is assumed to be composed of an incompressible material, i.e. its volume does not change under deformation processes; for this reason, under certain hypothesis on the anisotropy of the material, the mechanical properties of a three-dimensional specimen of artery can be determined from two-dimensional tests. However, either uniaxial and biaxial mechanical tests on different types of arteries that aim to describe their passive response are available, see e.g. Scott et al. [1972]; Monson [2001]; Monson et al.; Kenneth et al. [2008]; McLaughlin [2011]; Carew et al. [1968]. Such mechanical

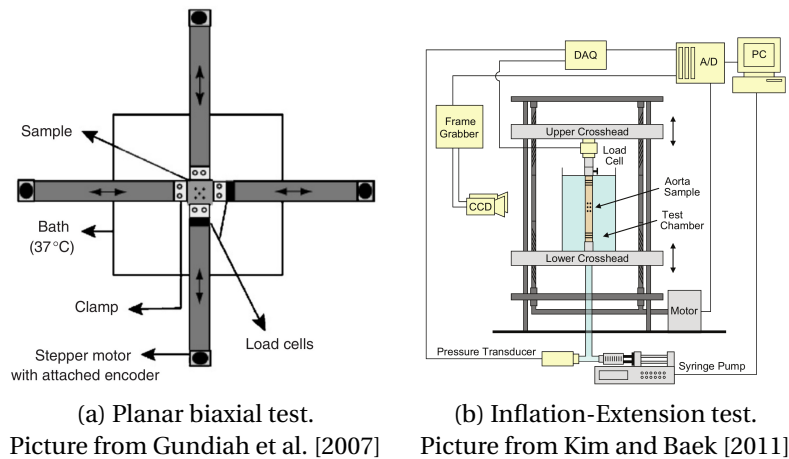


Figure 2.3: Experimental settings for biaxial mechanical tests

tests provide important information that are used to describe, by means of mathematical models, the response of the tissue Humphrey [2002]; Holzapfel and Gasser [2000]; Fung [1993]. In Fig. 2.3, the experimental settings for planar biaxial and inflation-extension tests are presented. As it will be discussed in Ch. 5, the data extracted from the experimental studies are then employed, under certain modeling assumptions, to estimate the material parameters for the constitutive law that will model the tissue. More precisely, from the experimental measurements of deformations and the applied traction/inflation forces applied in the experimental setting, the mechanical stresses occurring inside the specimen of artery are computed; afterwards, the material parameters of constitutive laws are computed from least-squares data fitting of the experimental observations.

As described in Fung [1993]; Humphrey [1995a], when mechanical tests on specimens of arteries are carried out, the arterial tissue must undergo few initial loading and unloading cycles. Afterwards, it shows an almost repeatable cyclic behavior from which the experimental data can be extracted. The interested reader may refer to e.g. Sommer [2008]; Monson [2001] for a detailed description of the mechanical testing protocols commonly followed in experimental studies. Fig. 2.4 presents the passive stress-strain relations, i.e. when the effect of smooth muscle cells is inhibited, characterizing either the initial cycles composing the so-called pre-conditioning phase of the tissue and the response of a generic specimen of vessel wall. From the red curve in Fig. 2.4, it can be observed that the mechanical behavior of the arterial tissue is highly nonlinear over finite strains with a typical exponential-type behavior. Arteries can be described as fiber-reinforced and nearly-incompressible materials where different families of collagen fibers can be identified Hill et al. [2012] that are embedded in an extracellular matrix, mainly composed of elastin, also referred to as the background material. It is worth pointing out that the background material can be described as isotropic; in addition, it is responsible for the mechanical response of the tissue to small deformations and it shows a nearly linear mechanical response, as in Fig. 2.4 Fung [1993]. On the other hand, the collagen fibers, that are seen as the fiber-reinforcing component of the tissue, do not contribute to the mechanical overall mechanical response of the vessel wall until they are completely straightened. Indeed, as reported in e.g. Scott et al. [1972]; Burton [1954]; Roach and Burton [1957]; Hill et al. [2012], in the small deformations regime, the collagen fibers are in a wavelike state that makes them not able to contribute to the overall mechanical response of the vessel wall. With increasing deformations, the wavelike fibers are straightened and they contribute to the overall mechanical response of the tissue leading to an increase in the mechanical stiffness of the material, being the collagen fibers much stiffer than the background material Humphrey [2002]; Fung

2.2. Mechanical behavior of the healthy arterial tissue

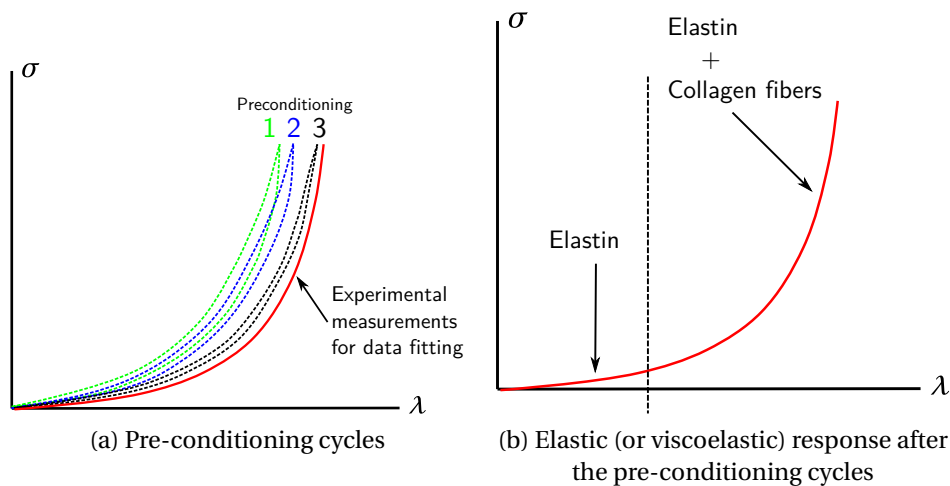


Figure 2.4: Schematic diagram of the typical stress(σ)-strain(λ) relation for a specimen of arterial tissue in passive conditions

[1993]. Since the structure of an artery can be interpreted as a thick-walled tube, increasing internal pressure induces a higher gain of circumferential deformations outside than inside the arterial wall. The effects of this feature is the capability of the arterial wall of leveling, in physiological conditions, the circumferential stresses: inside the media is stiffer and undergoes lower deformations, while outside the adventitia is less stiff and undergoes higher deformations. As discussed in Balzani [2006]; Vanishav and Vossoughi [1983]; Greenwald et al. [1997], this property of the arterial tissue plays an important role in the definition of the pre-stretch and pre-stress states of human arteries. Pre-stretch and pre-stress states of arteries are not considered in this work; therefore, the interested reader may refer to Balzani [2006] and references therein for a detailed insight on this topic.

For the mathematical description of the mechanical behavior of arterial tissue, either elastic or viscoelastic models can be employed for the different types of arteries along the arterial tree Fung [1993]; Holzapfel and Gasser [2000]. For instance, elastic arteries are commonly described by means of elastic models, while muscular arteries, due to the important role played by the smooth muscle cells in the regulation of the blood pressure along the arterial tree, can be modeled by means of viscoelastic laws. As mentioned before, this work focuses on the mathematical modeling and numerical simulations of the cerebral arterial tissue mechanics. In Scott et al. [1972]; Monson [2001]; Monson et al.; Kenneth et al. [2008]; McGloughlin [2011] viscoelastic effects on the mechanical response of the vessel wall are not reported; for this reason only elastic laws are considered in this work. However, as it will be presented in Ch. 4, the constitutive laws are able to capture the two main features of the mechanical behavior of arteries: nonlinearity and anisotropy.

3 Continuum Mechanics: preliminaries

Bodies can be described at different modeling scales, e.g. macroscopic or microscopic. The choice of the adequate representing scale is driven by the level of knowledge of the complexity of the internal microstructures of the body and the engineering application of interest. In Biomechanics, a macroscopic approach, which models a biological body as a continuous body (also called continuous medium) by means of certain fields quantities such as mass, displacement, and energy, is adopted. Indeed, a microscopic approach taking into account the interactions among all the particles composing the body is not adequate, being extremely expensive. In this work, the biological bodies under consideration are modeled at the macroscopic scale and their response to external forces is described by means of the vectorial and tensorial fields defined in the continuum mechanics theory.

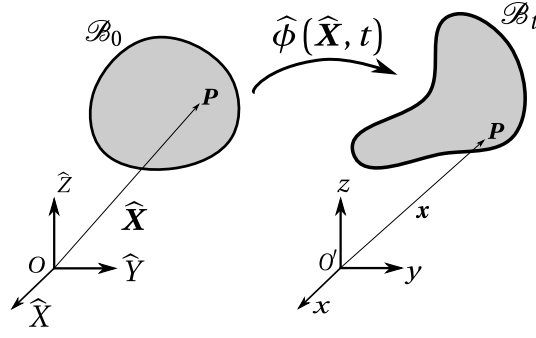
This chapter recalls the basic concepts of the continuum mechanics theory. Sec. 3.1 introduces the vectorial and tensorial fields necessary to represent the motion of a continuous medium. In addition, it deals with the description of the mechanical stresses occurring inside the body during its motion. Sec. 3.2 deals with the partial differential equations governing the deformations of a body under the action of external loads. In particular, the conservation equations of mass and linear momentum are presented together with the second law of thermodynamics. Sec. 3.3 discusses the fundamental principles for the mathematical modeling of continuous bodies, while the general form of the constitutive models considered in this work is introduced in Sec. 3.4.

3.1 Introduction to Continuum Mechanics

In this section the basic concepts of continuum mechanics are introduced. For the sake of brevity, only the kinematic and mechanical quantities necessary to formulate the governing equations in Sec. 3.2 are presented. For an extensive insight into the mechanics of continuous bodies and their mathematical modeling, the interested reader may refer, for instance, to Holzapfel [2000]; Odgen [1997] and references therein.

3.1.1 Kinematics of a continuous body

A continuous body \mathcal{B} is viewed as the composition of a continuous set of particles and it is assumed to have a continuous distribution of matter in space and time. The continuous medium is immersed in a three-dimensional Euclidean space, namely \mathbb{R}^3 , where a reference frame of right-handed, Cartesian


 Figure 3.1: Reference \mathcal{B}_0 and current \mathcal{B}_t configurations of a continuous body

coordinate axes at a fixed origin $(O, \hat{X}, \hat{Y}, \hat{Z})$ is introduced, see Fig. 3.1. As the body \mathcal{B} moves in the space from one instant t_0 to another instant t , it occupies a continuum sequence of regions denoted by $\mathcal{B}_0, \dots, \mathcal{B}_t$. The region occupied by \mathcal{B} at the time t_0 is referred to as the reference configuration and it is indicated with \mathcal{B}_0 while, at any given time t , it is called the current configuration, indicated by \mathcal{B}_t (see Fig. 3.1). In the following, it is assumed that $t_0 = 0$. The position of a particle P in the reference and current configuration is identified by the set of material and spatial coordinates, respectively; the former are the components of the position vector \hat{X} in \mathcal{B}_0 while the latter are the components of the position vector \mathbf{x} in \mathcal{B}_t , as in Fig. 3.1. Although from a general point of view the coordinates of $\hat{X} \in \mathcal{B}_0$ and $\mathbf{x} \in \mathcal{B}_t$ might be referred to two different coordinates systems, as for instance $(O, \hat{X}, \hat{Y}, \hat{Z})$ and (O', x, y, z) in Fig. 3.1, in this work, it is assumed that the reference frames for the two configurations coincide, that is $(O, \hat{X}, \hat{Y}, \hat{Z}) \equiv (O', x, y, z)$. The motion from the reference configuration \mathcal{B}_0 to the current configuration \mathcal{B}_t is represented by a nonlinear, continuous and invertible transformation

$$\hat{\phi}(\hat{X}, t) : \mathcal{B}_0 \times \mathbb{R}_+ \rightarrow \mathcal{B}_t \quad \text{s.t.} \quad \mathbf{x} = \hat{\phi}(\hat{X}, t), \quad (3.1)$$

that, at the time $t > 0$, maps each material point $\hat{X} \in \mathcal{B}_0$ into the corresponding spatial point $\mathbf{x} \in \mathcal{B}_t$. It is assumed that the nonlinear map $\hat{\phi}(\hat{X}, t)$ and its inverse have the necessary regularity properties in order to define the vectorial and tensorial fields describing the motion and the deformations of the body; namely the map $\hat{\phi}$ is supposed to be a diffeomorphism defined on \mathcal{B}_0 . In the following, for convenience, the arguments of the functions representing the kinematic and mechanical quantities under consideration will be omitted; the independent variables for a material field are (\hat{X}, t) while for a spatial field they are (\mathbf{x}, t) .

During motion and deformation, the displacement experienced by each point $\hat{X} \in \mathcal{B}_0$ is measured by the material displacement field $\hat{\mathbf{d}}$ which is defined as $\hat{\mathbf{d}} = \mathbf{x} - \hat{X} \in \mathbb{R}^3$. Consequently, the material velocity field is defined as $\hat{\mathbf{v}} = \frac{\partial \hat{\mathbf{d}}}{\partial t}$. Locally, the deformations (i.e. the changes of size and shape) of \mathcal{B} experienced during its motion are measured by the deformation gradient tensor \mathbf{F} , usually defined in terms of the material coordinates as:

$$\mathbf{F} := \frac{\partial \mathbf{x}}{\partial \hat{X}} = \frac{\partial \hat{\phi}}{\partial \hat{X}} = \frac{\partial \hat{\mathbf{d}}}{\partial \hat{X}} + \mathbf{I}, \quad (3.2)$$

where $\frac{\partial \hat{\mathbf{d}}}{\partial \hat{X}}$ is the material gradient of $\hat{\mathbf{d}}$, and \mathbf{I} is the second order identity tensor in \mathbb{R}^3 . When the deformation gradient tensor \mathbf{F} does not depend on \hat{X} , namely $\mathbf{F} = \mathbf{F}(t)$, the deformation is said to be homogeneous; on the other hand, when $\mathbf{F} = \mathbf{F}(\hat{X}, t)$ the deformation is said to be inhomogeneous. The

deformation gradient tensor \mathbf{F} is a primary measure of the deformations of the continuous medium \mathcal{B} since it describes how infinitesimal material elements (e.g. volumes) in \mathcal{B}_0 transform into their spatial counterparts in \mathcal{B}_t , Holzapfel [2000]. In particular,

$$J = \det(\mathbf{F}), \quad (3.3)$$

that is called the volume ratio, is of particular relevance in the continuum mechanics theory; indeed it models the deformations of infinitesimal material volume elements $d\hat{V}$ into infinitesimal spatial volumes dv by means of the relation:

$$dv = Jd\hat{V}. \quad (3.4)$$

It is worth pointing out that, in the continuum mechanics theory, the physically admissible deformations are the ones for which $J > 0$; indeed, $J \neq 0$ due to the regularity assumptions on the nonlinear map $\hat{\phi}$ and its inverse, and the case $J < 0$ is not considered physically admissible due to the impenetrability of matter Holzapfel [2000]; Odgen [1997]. The deformations of material line and surfaces elements are also described by means of the deformation gradient \mathbf{F} . Indeed, an infinitesimal material line segment, represented by the vector $d\hat{\mathbf{X}}$, is mapped into the infinitesimal spatial line segment $d\mathbf{x}$ by means of the relation

$$d\mathbf{x} = \mathbf{F}d\hat{\mathbf{X}}. \quad (3.5)$$

Infinitesimal oriented material and spatial surface elements, which can be defined as $d\hat{\mathbf{A}} = d\hat{A}\hat{\mathbf{n}}$ and $d\mathbf{a} = da\mathbf{n}$, with $\hat{\mathbf{n}}$ and \mathbf{n} the normal unit vectors to the infinitesimal areas $d\hat{A}$ and da in \mathcal{B}_0 and \mathcal{B}_t , respectively, are related through the Nanson's formula Holzapfel [2000], as follows:

$$d\mathbf{a} = J\mathbf{F}^{-T}d\hat{\mathbf{A}}. \quad (3.6)$$

As shown in Holzapfel [2000]; Odgen [1997], the deformation gradient tensor \mathbf{F} can be split multiplicatively into a unique rotation second order tensor \mathbf{R} and a unique, positive definite, and symmetric stretch tensor \mathbf{U} , or \mathbf{V} , as follows:

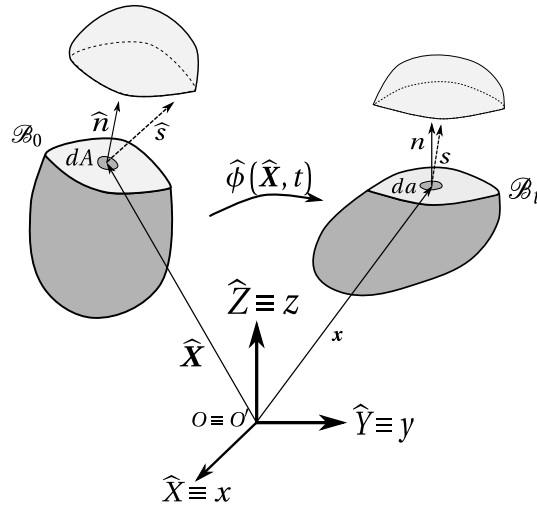
$$\mathbf{F} = \mathbf{R}\mathbf{U} = \mathbf{V}\mathbf{R}. \quad (3.7)$$

The rotation tensor \mathbf{R} is orthogonal and it represents local changes in orientation while the tensor \mathbf{U} (or equivalently \mathbf{V}) takes into account local changes in shape of the body. The two equivalent decompositions of \mathbf{F} in Eq. (3.7) are called the left ($\mathbf{R}\mathbf{U}$) and right ($\mathbf{V}\mathbf{R}$) polar decomposition of \mathbf{F} , respectively. In Eq. (3.7), the right tensor \mathbf{U} is defined with respect to the reference configuration while \mathbf{V} acts in the current configuration.

Other two important second order tensors measuring the strains of a continuous body (i.e. the changes in length between two neighboring point $\hat{\mathbf{X}}_1$ and $\hat{\mathbf{X}}_2$ in \mathcal{B}_0) in the material coordinates are the right Cauchy-Green tensor \mathbf{C} and the Green-Lagrange strain tensor \mathbf{E} , defined as:

$$\mathbf{C} := \mathbf{F}^T\mathbf{F} \quad \text{and} \quad \mathbf{E} := \frac{1}{2}(\mathbf{C} - \mathbf{I}), \quad (3.8)$$

respectively. It has to be remarked that, the tensors \mathbf{C} and \mathbf{E} describe only local changes of shape and they are not affected by local changes of orientation. Indeed, given the polar decomposition of Eq. (3.7),


 Figure 3.2: Stress vectors in the reference configuration ($\hat{\mathbf{s}}$) and in the current configuration (\mathbf{s})

the two strain tensors can be formulated in terms only of the stretch tensor \mathbf{U} as follows:

$$\mathbf{C} = \mathbf{F}^T \mathbf{F} = (\mathbf{R}\mathbf{U})^T \mathbf{R}\mathbf{U} = \mathbf{U}^T \mathbf{R}^T \mathbf{R}\mathbf{U} = \mathbf{U}^T \mathbf{U} \quad \text{and} \quad (3.9)$$

$$\mathbf{E} = \frac{1}{2}(\mathbf{U}^T \mathbf{U} - \mathbf{I}), \quad (3.10)$$

where the orthogonality property of rotation tensors (see Lang [1968]) has been used in the last equality of Eq. (3.9). The spatial counterpart of \mathbf{C} and \mathbf{E} can be obtained by considering the left polar decomposition of \mathbf{F} in Eq. (3.8) Holzapfel [2000]. As it will be discussed in Sec. 3.4, the right Cauchy-Green and Green-Lagrange strain tensors are of particular relevance in the mathematical formulation of constitutive models for continuous bodies due to the fact that they depend only on local deformations of the body.

3.1.2 The concept of mechanical stress

When external forces are applied on a physical body an internal loading state is generated in the current configuration, as a consequence of deformations. The internal loading state is described by the notion of stress, which in turn is postulated from the concept of surface traction forces. These forces are defined per unit of area and they act either on the boundary surface of \mathcal{B} or on an (imaginary) internal surface of the body, as represented in Fig. 3.2. From the physical point of view, traction forces acting on the boundary surface of \mathcal{B} are generated by the application of external loads and mechanical constraints of the displacement of the body; on the other hand, the traction forces acting on internal surfaces within the body represent the forces that are transmitted between the two deformed portions of the body across the cutting surface; see Fig. 3.2. In the current configuration, the internal surface traction force per unit of area is indicated by the vector \mathbf{s} and the resultant traction force $d\mathbf{f}$, acting on the infinitesimal spatial surface element da , is defined as $d\mathbf{f} = \mathbf{s}da$. The material representation of \mathbf{s} is indicated by the force field per unit of area $\hat{\mathbf{s}}$, for which it has to be verified that

$$d\mathbf{f} = \mathbf{s}da = \hat{\mathbf{s}}d\hat{A}. \quad (3.11)$$

The vector \mathbf{s} is referred to as the Cauchy (or true) traction vector while $\hat{\mathbf{s}}$ is called the first Piola-Kirchhoff (or nominal) traction vector Holzapfel [2000]; Odgen [1997]. As represented in Fig. 3.2, the traction forces are defined with respect to the cutting surface which is uniquely identified by its normal vector, indicated as $\hat{\mathbf{n}}$ or \mathbf{n} if in \mathcal{B}_0 or in \mathcal{B}_t , respectively. In the continuum mechanics theory, the existence of a second order tensor $\boldsymbol{\sigma}$, called the Cauchy stress tensor, defined on the current configuration, is postulated in order to define the traction force \mathbf{s} at the spatial point \mathbf{x} and at the time t for all the possible infinite cutting surfaces; thus, the vector \mathbf{s} is defined as:

$$\mathbf{s} = \boldsymbol{\sigma} \mathbf{n}, \quad (3.12)$$

and, similarly, the material vector field $\hat{\mathbf{s}}$ can be written as

$$\hat{\mathbf{s}} = \mathbf{P} \hat{\mathbf{n}}, \quad (3.13)$$

where \mathbf{P} is called the first Piola-Kirchhoff tensor and it represents a tensorial field defined on the reference configuration. When $\mathbf{n}^T \boldsymbol{\sigma} \mathbf{n} > 0$ the traction force $\boldsymbol{\sigma} \mathbf{n}$ in Eq. (3.12) is referred to as tensile stress; in the other case, if $\mathbf{n}^T \boldsymbol{\sigma} \mathbf{n} < 0$, the traction force is called compressive stress. By inserting Eq. (3.6) into Eq. (3.11), the force field described by \mathbf{s} can be formulated in the reference configuration as:

$$\hat{\mathbf{s}} = J \boldsymbol{\sigma} \mathbf{F}^{-T} \hat{\mathbf{n}} = \mathbf{P} \hat{\mathbf{n}}, \quad (3.14)$$

from which the definition of the first Piola-Kirchhoff tensor is deduced,

$$\mathbf{P} = J \boldsymbol{\sigma} \mathbf{F}^{-T}. \quad (3.15)$$

From the physical point of view, the Cauchy stress tensor $\boldsymbol{\sigma}$ measures the physical (true) stresses that occur inside and on the boundary surface of the body \mathcal{B} as a consequence of the deformations; on the other hand the first Piola-Kirchhoff tensor \mathbf{P} is the mathematical representation of $\boldsymbol{\sigma}$ in the reference configuration \mathcal{B}_0 . An alternative material stress tensor, that is of particular interest in the formulation of constitutive relations for the mathematical modeling of continuous bodies (see Sec. 3.2.3), is the second Piola-Kirchhoff tensor, defined as:

$$\mathbf{S} = \mathbf{F}^{-1} \mathbf{P}. \quad (3.16)$$

The interested reader may refer to Holzapfel [2000]; Odgen [1997] for a detailed description of the mathematical properties of the tensors $\boldsymbol{\sigma}$, \mathbf{P} , \mathbf{S} and the definition of additional stress tensors describing the internal loading state in continuous bodies.

3.2 Fundamental principles in continuum mechanics

This section deals with the fundamental principles of continuum mechanics governing physical systems modeled at the macroscopic scale. From a general point of view, a physical system is a collection of matter or a quantity of mass in space such as, for instance, continuous bodies Holzapfel [2000]. The fundamental principles of continuum mechanics involve the balance of physical quantities such as the mass, linear and angular momentum of forces, mechanical energy, and the second law of thermodynamics; however, only the balance of mass, linear momentum and the second law of thermodynamics are considered. This choice is motivated by the fact that the balance of angular momentum and mechanical energy are automatically satisfied by the constitutive models that are presented in Ch. 4

and by the fact that only isothermal processes are considered in this work. The principles described in Secs. 3.2.1 and 3.2.2 are presented both in the material and spatial forms since they will be employed for the description of the vessel wall mechanics and of the blood flow in arteries.

3.2.1 The mass balance

The balance of mass postulates that the total amount of mass of a physical system is not affected by deformation processes. In this work, only closed systems that do not exchange mass with the surroundings are considered; therefore, the total mass must be conserved during motion. The mass of \mathcal{B} in the reference and current configuration is defined by means of two continuous functions $\rho_0(\hat{\mathbf{X}}) > 0$ and $\rho(\mathbf{x}, t) > 0$, called the material and spatial mass density, respectively; the material mass density is time independent, being defined on the reference configuration \mathcal{B}_0 which is fixed in time. Let us consider an arbitrary material control volume $\hat{\omega} \subset \mathcal{B}_0$, the conservation of mass states that

$$\frac{D}{Dt} \int_{\hat{\omega}} \rho_0 dV = \frac{D}{Dt} \int_{\omega} \rho dV = 0, \quad (3.17)$$

where the operator $\frac{D}{Dt}$ indicates the material time derivative Holzapfel [2000] and ω indicates the arbitrary spatial control volume in \mathcal{B}_t corresponding to $\hat{\omega}$ in \mathcal{B}_0 . By inserting Eq. (3.4) in the integral over ω , and by the arbitrariness of the control volumes $\hat{\omega}$ and ω , the relation between the material and spatial density functions is deduced:

$$\rho_0 = \rho J. \quad (3.18)$$

The material formulation of the local form of the conservation of mass reads as follows:

$$\frac{D}{Dt} \rho_0 = 0 \quad \text{in } \mathcal{B}_0, \quad (3.19)$$

and its spatial counterpart is

$$\frac{\partial}{\partial t} \rho + \nabla \cdot (\rho \mathbf{v}) = 0 \quad \text{in } \mathcal{B}_t, \quad (3.20)$$

where $\frac{\partial}{\partial t}$ is the spatial time derivative, $\nabla \cdot (\bullet)$ indicates the divergence operator in the spatial coordinates and \mathbf{v} is the spatial velocity field Holzapfel [2000]. In the following, only continuous bodies for which the density functions are constant, are considered. Therefore, the spatial form of the conservation of mass reduces to the homogeneous equation

$$\nabla \cdot \mathbf{v} = 0 \quad \text{in } \mathcal{B}_t. \quad (3.21)$$

A continuous body for which Eq. (3.21) is satisfied for any type of motion is called incompressible, and Eq. (3.21) is usually referred to as the incompressibility constraint. An alternative form of the incompressibility constraint reads as follows Holzapfel [2000]:

$$J = 1 \quad \text{in } \mathcal{B}_0, \quad (3.22)$$

and the satisfaction of the incompressibility constraint is of particular interest when modeling biological materials Fung [1993]; Robertson et al. [2008].

3.2.2 The balance of the momentum of forces

The balance principles of the linear and angular momentum of forces describe the balance between the variation in time of the linear and angular momentum of a continuous body and the resultant force and momentum of external loads applied on \mathcal{B} . In this section only the balance of the linear momentum is presented; for the formulation of the angular momentum equation, the interested reader may refer to Holzapfel [2000]; Odgen [1997].

Let us consider an arbitrary spatial control volume $\omega \subset \mathcal{B}_t$ on which either surface traction and body forces act. The former are defined on the boundary $\partial\omega$ of ω and they are described by the spatial vector-valued function $\mathbf{t}(\mathbf{x}, t, \mathbf{n})$ while the latter are represented by the spatial vectorial field $\mathbf{b}(\mathbf{x}, t)$. The total force acting on ω in the current configuration has the additive form:

$$\mathbf{f}(t) = \int_{\partial\omega} \mathbf{t} \, d\mathbf{a} + \int_{\omega} \mathbf{b} \, dv. \quad (3.23)$$

The balance principle of linear momentum in spatial coordinates reads

$$\frac{D}{Dt} \int_{\omega} \rho \mathbf{v} \, dv = \int_{\partial\omega} \mathbf{t} \, d\mathbf{a} + \int_{\omega} \mathbf{b} \, dv, \quad (3.24)$$

for any arbitrary control volume ω in \mathcal{B}_t . By means of the Reynold's transport theorem and other standard results of the continuum mechanics theory Holzapfel [2000], the local spatial formulation of the balance of Eq. (3.24) reads as follows:

$$\rho \frac{D}{Dt} \mathbf{v} - \nabla \cdot \boldsymbol{\sigma} - \mathbf{b} = \mathbf{0} \quad \text{in } \mathcal{B}_t. \quad (3.25)$$

In the material coordinates, Eq. (3.25) transforms into the following equation:

$$\rho_0 \frac{D}{Dt} \hat{\mathbf{v}} - \hat{\nabla} \cdot \hat{\mathbf{P}} - \hat{\mathbf{B}} = \mathbf{0} \quad \text{in } \mathcal{B}_0, \quad (3.26)$$

where $\hat{\nabla} \cdot$ is the divergence operator in the material coordinates $\hat{\mathbf{X}}$, and $\hat{\mathbf{B}}$ is the function \mathbf{b} referred to the reference configuration \mathcal{B}_0 . In the context of solid mechanics, Eq. (3.26) is usually formulated in terms of the material displacement field $\hat{\mathbf{d}}$; therefore, the time derivative of the material velocity field $\hat{\mathbf{v}}$ is replaced by the second order time derivative of $\hat{\mathbf{d}}$. In Holzapfel [2000]; Odgen [1997] it is shown that the balance principle of the angular momentum is automatically satisfied if the symmetry condition $\boldsymbol{\sigma} = \boldsymbol{\sigma}^T$ on the Cauchy stress tensor describing the continuous body is verified. For biological materials such as the arterial tissue or the blood, the symmetry condition on the Cauchy stress tensor is considered to be a constitutive condition; therefore, it is satisfied by the models that are presented later and, for this reason, the balance of angular momentum is not addressed here. In addition, since our work focuses only on isothermal deformation processes, the energy of the physical system is only of mechanical type and only dependent on the action of external forces Holzapfel [2000]. As explained in Holzapfel [2000]; Odgen [1997], for isothermal processes, the balance of linear momentum implies the balance of the mechanical energy of the system; therefore, the mathematical formulation of this balance principle is not presented here.

3.2.3 The second law of thermodynamics

The experimental observations for which heat always “flows” from the warmer to the colder region of a body \mathcal{B} are represented by the second law of thermodynamics, also known as the entropy inequality or the Clausius - Duhem inequality. This fundamental physical principle is formulated in terms of the entropy variable, indicated by \mathcal{S} , of the continuous body Callen [1985] defined as

$$\mathcal{S} = \int_{\mathcal{B}_0} \eta dV, \quad (3.27)$$

where η is the scalar-valued field representing the local entropy in \mathcal{B} Holzapfel [2000]; Odgen [1997]. For closed systems, energy can be exchanged between the system and its surroundings in the form of work or heat. The entropy inequality postulates that the changes in time of the entropy \mathcal{S} is greater or equal than the total entropy supply \mathcal{Q} , that is:

$$\frac{D}{Dt} \mathcal{S} \geq \mathcal{Q}, \quad (3.28)$$

defined a:

$$\mathcal{Q} = \int_{\mathcal{B}_t} \frac{\rho r}{\theta} dv - \int_{\partial \mathcal{B}_t} \frac{\mathbf{q} \cdot \mathbf{n}}{\theta} d\mathbf{a}, \quad (3.29)$$

being r the entropy volumetric source term defined per unit of volume caused by internal heat production, \mathbf{q} is the entropy flux per unit of area, described in terms of heat flux, through the boundary $\partial \mathcal{B}_t$ in the current configuration, and $\theta = \theta(\mathbf{x}, t)$ denotes the absolute temperature. In Eq. (3.29), the entropy fluxes are assumed to be proportional to heat fluxes r and \mathbf{q} through the factor $\frac{1}{\theta}$ Holzapfel [2000]; Callen [1985]. As shown in Holzapfel [2000], the local spatial form of Eq. (3.29) reads:

$$\rho \frac{D}{Dt} \eta - \frac{\rho r}{\theta} + \nabla \cdot \left(\frac{\mathbf{q}}{\theta} \right) \geq 0 \quad \text{in } \mathcal{B}_t, \quad (3.30)$$

which can be transformed into the following equivalent form

$$\rho \left(\theta \frac{D}{Dt} \eta - \frac{D}{Dt} e \right) + \boldsymbol{\sigma} : \mathbf{D} - \frac{1}{\theta} \mathbf{q} \cdot \nabla \theta \geq 0 \quad \text{in } \mathcal{B}_0, \quad (3.31)$$

where e is the mechanical energy in the current configuration, and $\mathbf{D} = \frac{\nabla \mathbf{v} + \nabla \mathbf{v}^T}{2}$ is the symmetric part of the spatial gradient of \mathbf{v} Holzapfel [2000]. When describing the deformations of pure elastic materials, such as those presented in Ch. 4, the existence of a scalar-valued Helmholtz free energy function per unit of mass $\mathcal{W} = e - \theta \eta$ is postulated. The introduction of \mathcal{W} into Eq. (3.31) and the restriction to isothermal processes for which $\frac{D}{Dt} \theta = 0$ and $\mathbf{q} = \mathbf{0}$ reduce Eq. (3.31) to the following inequality:

$$\boldsymbol{\sigma} : \mathbf{D} - \rho \frac{D}{Dt} \mathcal{W} \geq 0 \quad (3.32)$$

which describes the internal dissipation of energy occurring inside the body \mathcal{B} as a consequence of a deformation process. As presented in Holzapfel [2000]; Balzani [2006], the entropy inequality in the reference configuration is:

$$\mathbf{S} : \frac{D}{Dt} \mathbf{E} - \frac{D}{Dt} \widehat{\mathcal{W}} \geq 0 \quad \text{in } \mathcal{B}_0, \quad (3.33)$$

where $\widehat{\mathcal{W}}$ is the free energy function per unit of volume and it is defined on the reference configuration \mathcal{B}_0 as $\widehat{\mathcal{W}} = \rho_0 \mathcal{W}$. For pure elastic materials the free energy $\widehat{\mathcal{W}}$ depends only on the deformations, $\widehat{\mathcal{W}} = \widehat{\mathcal{W}}(\mathbf{E})$, and the internal dissipation related to a closed deformation process vanishes. Therefore, Eq. (3.33) becomes

$$\mathbf{S} : \frac{D}{Dt} \mathbf{E} - \frac{\partial}{\partial \mathbf{E}} \widehat{\mathcal{W}} : \frac{D}{Dt} \mathbf{E} = 0 \quad \text{in } \mathcal{B}_0, \quad (3.34)$$

from which the constitutive equation:

$$\mathbf{S} = \frac{\partial \widehat{\mathcal{W}}}{\partial \mathbf{E}} \quad \text{in } \mathcal{B}_0, \quad (3.35)$$

is deduced. From Eq. (3.35), all the tensorial fields introduced in Sec. 3.1.2 can be defined in order to characterize the mechanical stresses of a continuous body \mathcal{B} as a function of its deformations. As reported in Humphrey [2003]; Lawton [1954]; Flory [1956]; Treloar [1975], the absolute temperature θ , at which the deformation process occurs, influences the mechanical behavior of a continuous body. However, the effects of the absolute temperature on the deformations and stresses inside a continuous body \mathcal{B} are not considered and the mathematical models presented in the next sections are formulated independently of θ .

3.3 Modeling principles for continuous elastic bodies

The behavior of a continuous body under the action of external loads is governed by the balance principles of Sec. 3.2. In detail, four equations are available: one scalar equation coming from the balance of mass and three equations derived from the balance of linear momentum. On the other hand, in Eqs. (3.20) and (3.25), ten unknowns appear: the spatial density ρ , the three components of the spatial velocity field \mathbf{v} which depends on the deformation map $\widehat{\phi}(\widehat{\mathbf{X}}, t)$, and the six independent components of the symmetric Cauchy stress tensor $\boldsymbol{\sigma}$. In order to close the system of equations, the components of $\boldsymbol{\sigma}$ need to be defined as constitutive quantities depending on $\widehat{\phi}(\widehat{\mathbf{X}}, t)$. Since in this work pure elastic bodies are considered, once a Helmholtz free energy function $\widehat{\mathcal{W}} = \widehat{\mathcal{W}}(\mathbf{E})$ is provided, the independent components of $\boldsymbol{\sigma}$ can be determined by means of Eqs. (3.35), (3.16) and (3.15). In the context of continuum mechanics, the Helmholtz free energy function is usually referred to as the strain (stored) energy function Taber [2004]. A mathematical model (also called constitutive model or law) for a continuous body is determined by the choice of the scalar-valued function $\widehat{\mathcal{W}}$; in Humphrey [2003] a set of guidelines for the construction of constitutive models for biological materials is presented. As discussed in Holzapfel [2000]; Balzani [2006]; Truesdell and Toupin [1960]; Truesdell [1969]; Gummert [1999]; De Souza Neto et al. [1998], a strain energy function has to obey several principles in order to be deemed physically admissible. Among them, the most important are:

- *principle of consistency*: any constitutive model must satisfy the balance principles on Sec. 3.2;
- *principle of determinism for the stress*: the mechanical stresses in a body \mathcal{B} at a given time t are determined by the history of motion of \mathcal{B} and they are independent of its future behavior;
- *principle of local action*: the determination of the stresses at a given particle \mathbf{P} in \mathcal{B} is independent

of the motion outside an arbitrary neighborhood of \mathbf{P} ;

- *principle of equipresence*: for a body \mathcal{B} , a quantity which appears as an independent variable in one constitutive equation must be present in all others characterizing the mechanical behavior of \mathcal{B} ;
- *principle of frame indifference*: any constitutive model must be invariant under changes of location and orientation of the reference frame and under any arbitrary change of observer. This means that the constitutive equations of a body \mathcal{B} are required to be unchanged under rigid rototraslation of the reference frame. In addition, the invariance under any arbitrary change of observer (also referred to as principle of material symmetry in Balzani [2006]) is the requirement that the constitutive laws must be invariant when rigid transformations such as rotations and/or reflections are applied on the reference configuration Naghdi [1984]; Green and Nagdi [1979]. As it will be shown in Sec. 3.4, the principle of frame indifference plays an important role in continuum mechanics in determining the form of the constitutive equations.

3.4 General form of constitutive models

In this work, the arterial tissue and the blood are both assumed to be Cauchy materials, for which the principle of determinism for the stresses reduces to the dependency of the mechanical stresses inside the body on the current state of deformation Holzapfel [2000]; Odgen [1997]. In addition, in order to satisfy the principle of frame indifference, the functional dependence of the strain energy function \mathcal{W} on the deformations of the body is restricted to the dependency on the right Cauchy-Green tensor \mathbf{C} , or equivalently on \mathbf{E} , rather than on the deformation gradient tensor \mathbf{F} . Let us consider the superimposition of a rigid body motion on the current configuration \mathcal{B}_t described by means of the relation

$$\tilde{\mathbf{x}} = \mathbf{Q}\mathbf{x} + \mathbf{w}, \quad (3.36)$$

where \mathbf{Q} and \mathbf{w} are a second order tensor representing a rotation Lang [1968] and a constant translation vector in \mathbb{R}^3 , respectively (see Fig. 3.3(a)). The matrix $\mathbf{Q} \in \text{SO}(3)$ with $\det(\mathbf{Q}) = 1$, being $\text{SO}(3)$ the special orthogonal group of the second order tensors in \mathbb{R}^3 Lang [1968]. The deformation gradient and the right Cauchy-Green tensors defined in the new deformed configuration $\tilde{\mathcal{B}}_t$ (see Fig. 3.3(a)) are defined as $\tilde{\mathbf{F}} = \mathbf{Q}\mathbf{F}$ and $\tilde{\mathbf{C}} = \mathbf{C}$ Holzapfel [2000]. The strain energy function \mathcal{W} is invariant under the superimposition of rigid motions if it satisfies the relation

$$\widehat{\mathcal{W}}(\mathbf{F}) = \widehat{\mathcal{W}}(\tilde{\mathbf{F}}) \quad \forall \mathbf{Q} \in \text{SO}(3), \forall \mathbf{F}. \quad (3.37)$$

Eq. (3.37) must be verified for any arbitrary rigid body motion; therefore, by choosing $\mathbf{Q} = \mathbf{R}^T$, where \mathbf{R} is the rotation tensor of the polar decomposition of \mathbf{F} (see Eq. (3.7)), and by considering the polar decomposition of \mathbf{F} described in Sec. 3.1, it can be shown that

$$\widehat{\mathcal{W}}(\mathbf{F}) = \widehat{\mathcal{W}}(\mathbf{Q}\mathbf{F}) = \widehat{\mathcal{W}}(\mathbf{R}^T \mathbf{R}\mathbf{U}) = \widehat{\mathcal{W}}(\mathbf{U}) = \widehat{\mathcal{W}}(\sqrt{\mathbf{C}}) = \widehat{\mathcal{W}}(\mathbf{C}). \quad (3.38)$$

Eq. (3.38) indicates that, if the strain energy function depends on the deformation gradient \mathbf{F} only through \mathbf{C} , then condition in Eq. (3.37) is automatically satisfied.

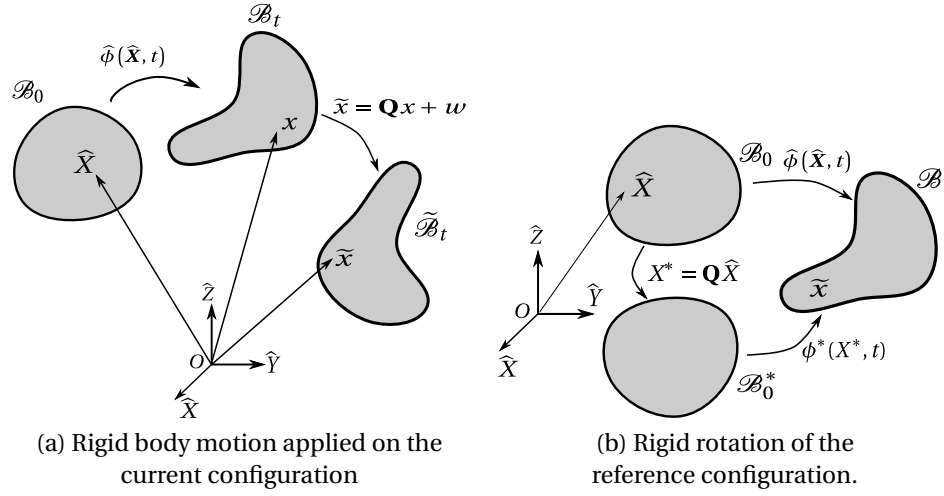


Figure 3.3: Rigid body motions on the current (a) and reference (b) configuration of a continuous body \mathcal{B}_0 with respect to which a constitutive model has to be invariant.

The principle of material symmetry Balzani [2006] demands that no rigid rotations \mathbf{Q} , either proper or improper, applied to the reference configuration \mathcal{B}_0 can modify the constitutive quantities; see Fig. 3.3(b). Let us consider the symmetry group $\mathcal{G}_{\mathcal{B}} = \{\mathbf{Q} \in \mathbb{R}^{3 \times 3} : \mathbf{Q}^T \mathbf{Q} = \mathbf{I} \text{ and } \det(\mathbf{Q}) = \pm 1\}$ associated to the continuous body \mathcal{B} . If a rigid rotation $\mathbf{Q}^T \in \mathcal{G}_{\mathcal{B}}$ is applied on the reference configuration, namely $\mathbf{X}^* = \mathbf{Q}^T \hat{\mathbf{X}}$, the principle of material symmetry states that scalar, vectorial and tensorial fields transform as follows:

$$\left\{ \begin{array}{l} \hat{\mathbf{t}} \rightarrow \hat{\mathbf{t}} \\ \hat{\mathbf{t}} \rightarrow \mathbf{Q} \hat{\mathbf{t}} \\ \hat{\mathbf{T}} \rightarrow \mathbf{Q}^T \hat{\mathbf{T}} \mathbf{Q}, \end{array} \right. \quad (3.39)$$

where $\hat{\mathbf{t}}$, $\hat{\mathbf{t}}$, and $\hat{\mathbf{T}}$ represent a scalar, vectorial and tensorial field in the reference configuration, respectively. The symmetry properties of a body \mathcal{B} (e.g. isotropy) can be stated in terms of the set of second order tensors $\mathbf{Q} \in \mathcal{G}_{\mathcal{B}}$ such that:

$$\widehat{\mathcal{W}}(\mathbf{C}) = \widehat{\mathcal{W}}(\mathbf{Q}^T \mathbf{C} \mathbf{Q}). \quad (3.40)$$

Indeed, as explained in Raoult [2009], if $\mathcal{G}_{\mathcal{B}} = \text{SO}(3)$ the material is said to be isotropic, otherwise it is anisotropic. In particular, in Sec. 4.2.2, the symmetry group for a particular class of anisotropic bodies that is relevant in the mathematical modeling of the arterial tissue is detailed. As mentioned in Sec. 3.2.3, the stress tensors, such as the second Piola-Kirchhoff tensor \mathbf{S} , are defined as the derivative of the strain energy function $\widehat{\mathcal{W}}$ with respect to the deformations of the body. For a strain energy function $\widehat{\mathcal{W}}$ depending on the right Cauchy-Green tensor \mathbf{C} , as in Eq. (3.38), the stress tensors of Sec. 3.1.2 read as follows:

$$\mathbf{S} = \frac{\partial \widehat{\mathcal{W}}(\mathbf{C})}{\partial \mathbf{C}}, \quad \mathbf{P} = \frac{\partial \widehat{\mathcal{W}}(\mathbf{C})}{\partial \mathbf{F}} = 2\mathbf{F} \frac{\partial \widehat{\mathcal{W}}(\mathbf{C})}{\partial \mathbf{C}}, \quad \text{and} \quad \boldsymbol{\sigma} = \frac{1}{J} \frac{\partial \widehat{\mathcal{W}}(\mathbf{C})}{\partial \mathbf{F}} \mathbf{F}^T, \quad (3.41)$$

respectively Holzapfel [2000]; Odgen [1997].

4 Constitutive modeling of the arterial tissue

Constitutive models characterize the response of a material to applied loads, which depends on the internal constitution of the material. The mathematical modeling of biological materials relies primarily on phenomenological descriptors, i.e. physical quantities related to experimental observations Fung [1993]; Robertson et al. [2008]. As pointed out in Humphrey [2003]; Fung [1993], a constitutive relation models the behavior of a material only under mechanical conditions of interest. Constitutive laws have been formulated in different theoretical frameworks; the most complex models consider either the interactions among the constituents of the vessel wall Mow et al. [1980]; Lai et al. [1993] or the natural biological evolution of the tissue by means of the growth and remodeling theory Taber [1998]; Rachev et al. [1998]; Humphrey and Rajagopal [2002b]. It is worth pointing out that, even for the most common models proposed in Mow et al. [1980]; Lai et al. [1993]; Taber [1998]; Rachev et al. [1998]; Humphrey and Rajagopal [2002b], there is controversy both on the modeling aspects (e.g. the representation of the exchanges among the constituents of the tissue) and for the determination of initial and boundary conditions for the partial (constituents) quantities. Alternatively, although most of biological materials can be classified as mixture-composite, it may be sufficient to consider, under particular conditions of interest, models proposed within the context of the finite hyperelasticity or viscoelasticity theory rather than in the full mixture theory Truesdell and Noll [1965]; Rajagopal and Tao [1995]. For instance, proximal arteries of elastic type are commonly represented by means of hyperelastic models Balzani [2006], while distal arteries of muscular type can be described either as hyperelastic materials Wulandana [2003]; Li [2009] or by taking into account their viscoelastic and pseudoelastic response Holzapfel and Gasser [2001]; Fung et al. [1979]. The mechanical conditions of interest for which the models have been proposed are represented by the physiological hemodynamical loads and vessel wall displacements occurring during one heart beat. In addition, since viscoelastic or pseudoelastic effects on the mechanical behavior of cerebral arteries are considered negligible, see Scott et al. [1972]; Monson [2001]; Monson et al.; Kenneth et al. [2008]; McGloughlin [2011], only hyperelastic models are considered in this work. The hyperelastic constitutive laws proposed in literature can be divided into two categories: phenomenological and structurally motivated laws. The former are based on bulk measurements of the mechanical response of the arterial tissue without considering information about the heterogeneous composition of the vessel wall Fung [1993]; Humphrey [2002]; Holzapfel and Ogden [2010]; the latter provide more insights into the mechanisms of the tissue components by considering, for instance, the fibrous nature of arteries Holzapfel and Gasser [2000]; Balzani [2006]; Robertson et al. [2009]. Both classes of models have been extensively used in literature to represent cerebral arteries Wulandana and Robertson [2005]; Li and Robertson [2009b]; Triccerri et al. [2014] and other types of arteries Gasser and Holzapfel [2006]; Calvo et al. [2007]; for this reason, models of both

classes are considered here. The arterial tissue behaves as a nearly incompressible material within the physiological range of deformations Carew et al. [1968]. In literature, the mathematical description of such mechanical behavior is mainly addressed by the so called \bar{F} -approach Glowinski and Le Tallec [1982, 1984]; Elguedj et al. [2008]; Weiss et al. [1996]; Simo et al. [1985] and the multiplicative decomposition of the deformation gradient \mathbf{F} into a volumetric and isochoric part Flory [1961]. However, other approaches have been proposed, such as a variational multiscale approach Masud and Truster [2013]. In this work, due to numerical motivations, which will be clarified in Ch. 5, the nearly incompressible behavior of arteries is modeled by means of the multiplicative decomposition of the deformation gradient \mathbf{F} proposed in Flory [1961].

This chapter is organized as follows. Sec. 4.1 deals with the polyconvexity condition which guarantees the existence of realistic physical solutions of the structural mechanics problem. Sec. 4.2 presents the constitutive models for the cerebral arterial tissue under consideration in this work. In Sec. 4.3, the mathematical representation of the nearly incompressible behavior of arteries, anticipated in Sec. 2.2, is addressed.

4.1 The polyconvexity condition

In the context of hyperelastic models, other restrictions on the constitutive models have to be satisfied in addition to the principles of Sec. 3.3. These conditions are introduced in order to guarantee the existence of physically admissible material responses to external loads. The conditions and the results described in this section have been obtained in the context of calculus of variations; the interested reader may refer to Balzani [2006]; Ball [1977b,a, 1997]; Dacorogna [2000]; Ciarlet [1988]; Marsden and Hughes [1983] for a detailed description. The structural mechanics problem in Eq. (3.26) can be formulated as the Euler-Lagrange equations in terms of the material displacement $\hat{\mathbf{d}}$ Balzani [2006]; Dacorogna [2000]. More specifically, it can be shown that the displacement field solving Eq. (3.26) minimizes the potential function

$$\Pi(\hat{\mathbf{d}}) = \int_{\mathcal{B}_0} \widehat{\mathcal{W}}(\widehat{\nabla} \hat{\mathbf{d}}) d\widehat{V} - \int_{\mathcal{B}_0} \rho_0 \mathbf{f} \cdot \hat{\mathbf{d}} d\widehat{V} - \oint_{\partial \mathcal{B}_0} \mathbf{t} \cdot \hat{\mathbf{d}} d\widehat{\mathbf{A}}, \quad (4.1)$$

where the terms $(-\rho_0 \mathbf{f} \cdot \hat{\mathbf{d}})$ and $(-\mathbf{t} \cdot \hat{\mathbf{d}})$ represent the volume and boundary load potentials, respectively. Two sufficient conditions that ensure the existence of minimizers for Eq. (4.1) are the coercivity of the strain energy function $\widehat{\mathcal{W}}$ and the sequential weak lower semicontinuity (s.w.l.s.) of the integral function $\mathcal{H} = \int_{\mathcal{B}_0} \widehat{\mathcal{W}} d\widehat{V}$ Ciarlet [1988]. As shown in Dacorogna [2000]; Ciarlet [1988], if the strain energy function $\widehat{\mathcal{W}}$ is a strictly convex function with respect to the deformation gradient, then the s.w.l.s. of \mathcal{H} is guaranteed. In addition, the convexity of $\widehat{\mathcal{W}}$ with respect to \mathbf{F} ensures the uniqueness of the solutions of the Euler-Lagrange equations (4.1). However, from the modeling point of view, the convexity of the strain energy function $\widehat{\mathcal{W}}$ induces significant drawbacks in materials modeling. Indeed, as shown in Ball [1997]; Hill [1957], a convex strain energy function is not able to describe instabilities in the mechanical response of materials (e.g. buckling) and the satisfaction of the principle of material frame indifference leads to physically unmotivated restrictions Coleman and Noll [1959]. In order to guarantee the s.w.l.s. of \mathcal{H} , avoiding the use of convex functions $\widehat{\mathcal{W}}$, two conditions on $\widehat{\mathcal{W}}$ are introduced: the so called quasi-convexity and the polynomial growth conditions Morrey [1952]. The quasi-convexity condition is an integral inequality Morrey [1952] and, therefore, it is only conditionally appropriate for the analysis of strain energy functions $\widehat{\mathcal{W}}$. Moreover, as discussed in Balzani [2006], the growth conditions are viewed as technical assumptions for proving that quasi-convexity implies s.w.l.s.

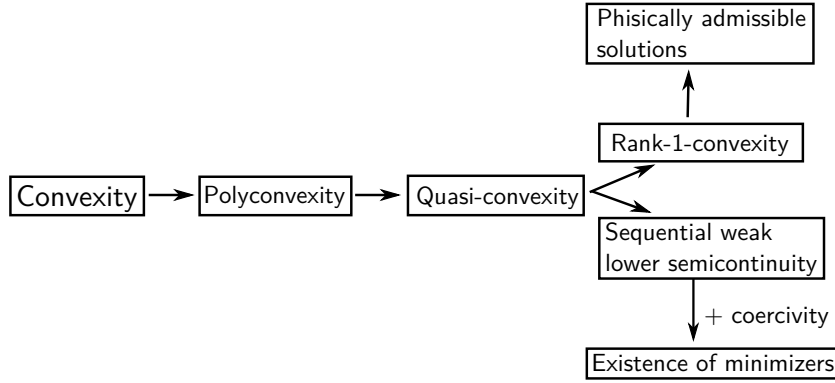


Figure 4.1: Mathematical conditions to ensure the existence of physically admissible solutions of the structural mechanics problem (the scheme is proposed in Balzani [2006])

because only the satisfaction of the quasi-convexity condition should be sufficient to achieve the s.w.l.s. of \mathcal{H} . In order to show the s.w.l.s. of \mathcal{H} , a more suitable mathematical condition has been introduced in Ball [1977a, 1997]: the polyconvexity condition.

Definition 4.1.1. A strain energy function $\widehat{\mathcal{W}}(\mathbf{F}) : \mathbb{R}^{3 \times 3} \rightarrow \mathbb{R}$ is polyconvex if and only if there exists a function $P : \mathbb{R}^{3 \times 3} \times \mathbb{R}^{3 \times 3} \times \mathbb{R} \rightarrow \mathbb{R}$, in general not unique, such that

$$\widehat{\mathcal{W}}(\mathbf{F}) = P(\mathbf{F}(\widehat{\mathbf{X}}), \text{Adj}(\mathbf{F}(\widehat{\mathbf{X}})), J(\widehat{\mathbf{X}})) \quad (4.2)$$

and the function $P(\widehat{\mathbf{X}})$ is convex for all points $\widehat{\mathbf{X}} = (\widehat{X}, \widehat{Y}, \widehat{Z}) \in \mathbb{R}^3$.

In Eq. (4.2), $\text{Adj}(\mathbf{F}) = J\mathbf{F}^{-1}$ denotes the adjugate of \mathbf{F} , defined as the transpose of the cofactor matrix of \mathbf{F} Lang [1968]. In the context of hyperelasticity, the polyconvexity condition is of particular interest because it is a pointwise condition on $\widehat{\mathcal{W}}$ (therefore it is easier to verify than the quasi-convexity) and it implies the quasi-convexity of $\widehat{\mathcal{W}}$ which in turn implies the s.w.l.s. of \mathcal{H} Dacorogna [2000].

In addition to the necessary conditions for the existence of the minimizers of Eq. (4.1), in order to guarantee physically admissible solutions, for instance related to the material stability, the so called rank-1-convexity condition is introduced. Such condition is automatically satisfied once the quasi-convexity condition is verified Dacorogna [2000]. This highlights the relevance of modeling the arterial tissue by means of polyconvex strain energy functions.

The relations among the different conditions are sketched in Fig. 4.1. The proofs of the polyconvexity and coercivity of the strain energy functions discussed in Sec. 4.2 are not presented here since they are well-established available results in literature; the interested reader may refer to e.g. Balzani [2006]; Hartmann and Neff [2003]; Schröder and Neff [2003]; Schröder et al. [2004].

4.2 Constitutive models for the healthy cerebral arterial tissue

Experimental observations Nichols and O'Rourke [1998]; Humphrey [2002] indicate that the arterial tissue shows both active and passive mechanical responses to external loads and that the mechanical behavior of arteries changes when considering *in vivo* and *in vitro* conditions. The complete mechanical characterization of the passive anisotropic behavior of blood vessels is carried out by means of

simultaneous inflation, extension, and twist tests that can only be realized in *in vitro* conditions where the active contraction of the smooth muscle cells can be inhibited Sommer [2008]; Holzapfel and Ogden [2008]; Sommer et al. [2010]. The constitutive models employed in this work describe the *in vitro* passive mechanical response of the arterial tissue; *in vivo* effects such as vasa vasorum Nichols and O'Rourke [1998], nerve control Fung [1993]; Humphrey [2002], perivascular tissue Szasz et al. [2013], and the active contraction of the smooth muscle cells Rachev and Hayashi [1999] are not considered here. The vessel wall has a layered structure (see Nichols and O'Rourke [1998]) and in Holzapfel and Gasser [2000]; Dalong et al. [2012]; Balzani et al. [2006a] a constitutive model taking into account the mechanical properties of the media and adventitia layers is proposed. However, as discussed in Dalong et al. [2012], due to the lack of experimental data on the mechanical properties of the different layers composing cerebral arteries, the constitutive models that are presented in Secs. 4.2.1 and 4.2.2 describe the tissue as a homogeneous body with constant material parameters and composed of a unique layer, as commonly done in literature either for the cerebral vessel wall Torii et al. [2008]; Valencia et al. [2013]; Bazilevs et al. [2010] or for other types of arteries Balzani et al. [2006a]; Masson et al. [2010]; Crosetto et al. [2012, 2013].

4.2.1 Isotropic constitutive laws

Isotropic constitutive models for the vessel wall are of phenomenological type for which the tissue is assumed to behave as an isotropic material regardless of its fibrous nature; the latter is taken into account by using an homogenization procedure. From the physical point of view, when arteries are modeled by means of isotropic models their mechanical response is supposed to be the same in all the spatial directions and their symmetry group $\mathcal{G}_{\mathcal{B}} = \text{SO}(3)$ (see Sec. 3.3).

One of the most known isotropic strain energy function for the arterial tissue proposed in literature is the Fung's model Fung [1993]; Fung et al. [1979]. In Fung et al. [1979], the artery is represented as a membrane and, consequently, the constitutive model depends only on the circumferential and axial deformations; this implies that the strain energy function, $\widehat{\mathcal{W}}_{Fung}^{iso}$, reads as follows:

$$\widehat{\mathcal{W}}_{Fung}^{iso} = \frac{C}{2} \left(e^{\beta_1 E_{\hat{\theta}\hat{\theta}}^2 + \beta_2 E_{\hat{z}\hat{z}}^2 + 2\beta_4 E_{\hat{\theta}\hat{\theta}} E_{\hat{z}\hat{z}}} - 1 \right), \quad (4.3)$$

where $E_{\hat{\theta}\hat{\theta}}$, $E_{\hat{z}\hat{z}}$ are the components of the Green-Lagrange tensor \mathbf{E} along the circumferential and axial direction of the artery, respectively, and $C, \beta_1, \dots, \beta_4$ are material parameters. Eq. (4.3) has been extended to the three dimensional case in cylindrical coordinates (i.e. when the blood vessel is modeled as a thick-walled structure) in Chuong and Fung [1983] under the assumption that the principal directions of the Cauchy stress tensor (i.e. the directions of the eigenvectors of $\boldsymbol{\sigma}$ in Eq. (3.12)) coincide with the radial, circumferential and axial directions of the artery and shear deformations did not occur. The most general form of the Fung's type strain energy function, $\widehat{\mathcal{W}}_{Fung,3D}^{iso}$, has been formulated in Deng et al. [1994]; Humphrey [1995b] and it reads, in cylindrical coordinates $(\hat{R}, \hat{\Theta}, \hat{Z})$, as:

$$\widehat{\mathcal{W}}_{Fung,3D}^{iso} = \frac{C}{2} (e^Q - 1), \quad (4.4)$$

where:

$$Q = \beta_1 E_{\hat{\theta}\hat{\theta}}^2 + \beta_2 E_{\hat{z}\hat{z}}^2 + \beta_3 E_{\hat{r}\hat{r}}^2 + 2\beta_4 E_{\hat{\theta}\hat{\theta}} E_{\hat{z}\hat{z}} + 2\beta_5 E_{\hat{z}\hat{z}} E_{\hat{r}\hat{r}} + 2\beta_6 E_{\hat{r}\hat{r}} E_{\hat{\theta}\hat{\theta}} + \beta_7 E_{\hat{\theta}\hat{z}}^2 + \beta_8 E_{\hat{r}\hat{z}}^2 + \beta_9 E_{\hat{r}\hat{\theta}}^2, \quad (4.5)$$

4.2. Constitutive models for the healthy cerebral arterial tissue

being $C, \beta_1, \dots, \beta_9$ material parameters. From a general point of view, in order that a strain energy function, such as for instance those in Eqs.(4.3) and (4.4), to model the mechanical behavior of arteries, the values of the material parameters must be determined. However, as discussed in Holzapfel and Gasser [2000], the material parameters in Eqs. (4.3) and (4.4) must be carefully chosen in order to guarantee the polyconvexity of the strain energy function for all states of deformations. Similar issues arise also for the following polynomial strain energy function

$$\widehat{\mathcal{W}}_{polynomial}^{iso} = c_1 E_{\widehat{\Theta}\widehat{\Theta}}^2 + c_2 E_{\widehat{Z}\widehat{Z}}^2 + c_3 E_{\widehat{\Theta}\widehat{\Theta}} E_{\widehat{Z}\widehat{Z}} + c_4 E_{\widehat{\Theta}\widehat{\Theta}}^3 + c_5 E_{\widehat{\Theta}\widehat{\Theta}}^2 E_{\widehat{Z}\widehat{Z}} + c_6 E_{\widehat{\Theta}\widehat{\Theta}} E_{\widehat{Z}\widehat{Z}}^2 + c_7 E_{\widehat{Z}\widehat{Z}}^3, \quad (4.6)$$

which has been shown to be suitable for the description of the mechanical behavior of the canine thoracic aorta Vanishav and Vossoughi [1983]. The polynomial strain energy function of Eq. (4.6) is not polyconvex for all the possible combination of the material parameters c_1, \dots, c_7 and, in Fung [1993], it has been proved that at least two different sets of material parameters are able to represent the same mechanical response of the same artery. Logarithmic strain energy functions of the form

$$\widehat{\mathcal{W}}_{log}^{iso} = -c \log \left[1 - \left(\frac{1}{2} b_1 E_{\widehat{\Theta}\widehat{\Theta}}^2 + \frac{1}{2} b_2 E_{\widehat{Z}\widehat{Z}}^2 + \frac{1}{2} b_3 E_{\widehat{\Theta}\widehat{\Theta}} E_{\widehat{Z}\widehat{Z}} \right) \right] \quad (4.7)$$

have been formulated in Takamizawa and Hayashi [1987]. It has to be remarked that the unphysical condition for which certain states of deformation are associated to infinite values of strain energy function may occur; indeed no restrictions on the argument of the logarithm function are presented in Takamizawa and Hayashi [1987] and, therefore, the argument of the logarithm function might be zero for certain states of deformation. It is worth pointing out that the strain energy function $\widehat{\mathcal{W}}$ in Eq. (4.7) is a convex function of the term

$$\zeta = \left(\frac{1}{2} b_1 E_{\widehat{\Theta}\widehat{\Theta}}^2 + \frac{1}{2} b_2 E_{\widehat{Z}\widehat{Z}}^2 + \frac{1}{2} b_3 E_{\widehat{\Theta}\widehat{\Theta}} E_{\widehat{Z}\widehat{Z}} \right). \quad (4.8)$$

Since convex functions of polyconvex scalar functions are polyconvex functions themselves Balzani [2006]; Dacorogna [2000], this implies that the strain energy function in Eq. (4.7) is polyconvex under the same requirements for which ζ of Eq. (4.8) is polyconvex. These considerations show that a logarithmic strain energy function can only be used to fit experimental data on a limited range of deformation states. It is important to remark that, as discussed in Holzapfel and Gasser [2000], the physical meaning of the material parameters in the models of Eqs.(4.3)-(4.7) is still unclear; therefore, in the parameter estimation procedure, only mathematical constraints that can ensure the polyconvexity of the strain energy function can be applied on the set of material parameters. In spite of the popularity of the Fung's model (see Holzapfel and Gasser [2000]; Fung [1993]; Humphrey [2002] and references therein), constitutive laws for which the material parameters represent measurable mechanical properties of the tissue (e.g. mechanical stiffness or shear modulus) have been preferred in this work to the ones described above.

The constitutive laws described hereafter are isotropic models for which the strain energy function is convex for all states of deformation under consideration. Thanks to the representation theorems for isotropic tensor functions (see for instance Grace and Young [1903]; Elliot [1913]; Weyl [1939]; Gurevich [1964]), they are formulated in terms of scalar-valued coordinate-independent quantities, the so called invariants. More specifically, they are defined in terms of an irreducible set of a finite number of invariants, the so called integrity basis, of the right Cauchy-Green tensor \mathbf{C} (see Eq. (3.38)) Gurevich [1964]; Spencer [1971]. The general form of an isotropic constitutive model reads as follows:

$$\widehat{\mathcal{W}} = \widehat{\mathcal{W}}(\mathbf{C}) = \widehat{\mathcal{W}}(I_1, I_2, I_3), \quad (4.9)$$

where I_i , for $i = 1, 2, 3$, are the principal invariants of \mathbf{C} defined as:

$$\begin{cases} I_1 = \text{Tr}(\mathbf{C}), \\ I_2 = \frac{1}{2} [\text{Tr}^2(\mathbf{C}) - \text{Tr}(\mathbf{C}^2)], \\ I_3 = \det(\mathbf{C}), \end{cases} \quad (4.10)$$

where the operator $\text{Tr}(\bullet)$ indicates the trace of second order tensors in \mathbb{R}^3 Holzapfel [2000]. It is straightforward to show that the principal invariants of \mathbf{C} satisfy the principle of material symmetry for any rotation matrix $\mathbf{Q} \in \text{SO}(3)$ Holzapfel [2000]. It is worth pointing out that, the general form of $\widehat{\mathcal{W}}$ in Eq. (4.9) can be split additively in the sum of two terms as follows:

$$\widehat{\mathcal{W}}(I_1, I_2, I_3) = \mathcal{U}(I_3) + \widehat{\mathcal{W}}^{iso}(I_1, I_2), \quad (4.11)$$

where $\mathcal{U}(I_3)$, for which $\mathcal{U}(I_3) = \mathcal{U}(1) = 0$, represents the mechanical response of the tissue to volumetric changes, i.e. it accounts its level of incompressibility, while $\widehat{\mathcal{W}}^{iso}(I_1, I_2)$ describes the response of the material to the deformations. The mathematical description of the response of arteries to volume-changing deformations and the possible choices for the function $\mathcal{U}(I_3)$ are addressed in Sec. 4.3; therefore, only the possible modeling choices for the strain energy function $\widehat{\mathcal{W}}^{iso}(I_1, I_2)$ are discussed in this section. One isotropic constitutive model that is largely used in literature to describe blood vessels is the linear elastic law which is based on the assumption that the stresses vary linearly with the deformations Crosetto [2011]; Malossi [2012]; Scotti et al. [2005]; Thubrikar et al. [2001]. The linear elastic model is deduced from the *St. Venant-Kirchhoff* law under the assumption of small displacements Holzapfel [2000]. The *St. Venant-Kirchhoff* strain energy function (indicated as $\widehat{\mathcal{W}}_{SVK}^{iso}$) reads as follows:

$$\widehat{\mathcal{W}}_{SVK}^{iso}(I_1, I_2) = \left(\frac{\lambda}{8} + \frac{\mu}{4}\right) I_1^2 - \left(\frac{3}{4}\lambda + \frac{\mu}{2}\right) I_1 - \frac{\mu}{2} I_2 + \frac{9}{8}\lambda + \frac{3}{4}\mu, \quad (4.12)$$

where λ and μ are the Lamé parameters, depending on the Young modulus E and Poisson's ratio ν as:

$$\lambda = \frac{E\nu}{(1+\nu)(1-2\nu)} \quad \text{and} \quad \mu = \frac{E}{2(1+\nu)}. \quad (4.13)$$

The Young modulus is a positive parameter that measures the mechanical stiffness of the material and the Poisson's ratio $\nu \in [0, 0.5)$ represents the relative change of volume of an elementary cube inside the body due to deformations of the material. It has to be remarked that the incompressible behavior of the material is yielded for $\nu \rightarrow 0.5$ Holzapfel [2000]. Despite the wide use of this model and of its linearized approximation, it has been shown that $\widehat{\mathcal{W}}_{SVK}^{iso}$ in Eq. (4.12) does not satisfy the polyconvexity condition for all states of deformations Ciarlet [1988]; Raoult [1986]; more precisely, the polyconvexity condition is violated for compression states of deformations Raoult [1986]. Other two important constitutive models employed in literature are the *Mooney-Rivlin* ($\widehat{\mathcal{W}}_{MR}^{iso}$) Treloar [1975] and *neo-Hookean* ($\widehat{\mathcal{W}}_{NH}^{iso}$) Bazilevs et al. [2010] laws whose strain energy functions read as:

$$\widehat{\mathcal{W}}_{MR}^{iso}(I_1, I_2) = C_1(I_1 - 3) + C_2(I_2 - 3) \quad (4.14)$$

and

$$\widehat{\mathcal{W}}_{NH}^{iso}(I_1) = \frac{\mu}{2}(I_1 - 3), \quad (4.15)$$

4.2. Constitutive models for the healthy cerebral arterial tissue

Material Parameters	
$E = 1.1420 \cdot 10^5$	$\nu = 0.4500$
$\alpha_1 = 7.6350 \cdot 10^4$	$\gamma_1 = 0.7410$
$\alpha_2 = 6.8220 \cdot 10^4$	$\gamma_2 = 0.0609$

Table 4.1: Material parameters for the models in Eqs.(4.12)-(4.17) from Tricerri et al. [2014]. E , α_1 , α_2 [dyn/cm²]; ν , γ_1, γ_2 [-]. In Eq. (4.14), $C_1 = C_2 = \frac{\mu}{2}$ with μ from Eq. (4.13).

respectively. In Eq. (4.14), C_1 and C_2 are two positive material parameters that satisfy the relation $\mu = C_1 + C_2$, while in Eq. (4.15) the material parameter μ coincides with the shear modulus defined in Eq. (4.13). It is worth pointing out that both models in Eqs.(4.14) and (4.15) satisfy the polyconvexity condition Hartmann and Neff [2003]; indeed, the material coefficients C_1, C_2 , and μ are positive and the two functions $\widehat{\mathcal{W}}_{MR}^{iso}$ and $\widehat{\mathcal{W}}_{NH}^{iso}$ are convex functions of the first and second invariant of \mathbf{C} , which are polyconvex functions of \mathbf{F} Hartmann and Neff [2003]; Schröder et al. [2004]. As discussed in Sec. 2.2, arteries show a stiffening effect in the high pressures regime. In order to represent such mechanical behavior, two exponential type models have been proposed: the so called *first order exponential law* ($\widehat{\mathcal{W}}_{EXP1}^{iso}$) Delfino et al. [1997] for which

$$\widehat{\mathcal{W}}_{EXP1}^{iso}(I_1) = \frac{\alpha_1}{2\gamma_1} \left(e^{\gamma_1(I_1-3)} - 1 \right), \quad (4.16)$$

and the *second order exponential model* ($\widehat{\mathcal{W}}_{EXP2}^{iso}$) Li and Robertson [2009b] whose strain energy function is

$$\widehat{\mathcal{W}}_{EXP2}^{iso}(I_1) = \frac{\alpha_2}{2\gamma_2} \left(e^{\gamma_2(I_1-3)^2} - 1 \right). \quad (4.17)$$

In Eqs.(4.16) and (4.17), α_1 , α_2 , γ_1 and γ_2 are suitable positive material parameters; α_1 and α_2 measure the mechanical stiffness of the material, while γ_1 and γ_2 are representative of the level of nonlinearity of the mechanical response of the body. Similarly to the Mooney-Rivlin and neo-Hookean models, the first and second order exponential law are convex functions of I_1 ; therefore, the two strain energy functions of Eqs.(4.16) and (4.17) satisfy the polyconvexity condition for all possible deformations \mathbf{F} (see Balzani [2006]).

Before analyzing the convexity properties of the strain energy functions of Eqs.(4.12)-(4.17), let us consider two examples that will be of particular interest for the numerical validation of the constitutive laws under consideration: the uniaxial tensile test on a cubic domain and the inflation-extension test on a cylindrical geometry. For both the cases, the physical body is assumed to be composed of incompressible material for which $J = 1$ and the strain energy function $\mathcal{U}(I_3) = 0$; therefore, the strain energy function $\widehat{\mathcal{W}} = \widehat{\mathcal{W}}^{iso}(I_1, I_2)$ and material parameters for Eqs. (4.12)-(4.17) are summarized in Tab. 4.1: they were obtained in Tricerri et al. [2014] from experimental measurements on cerebral arteries; in addition, since the Mooney-Rivlin model was not considered in Tricerri et al. [2014], in the following examples it has been assumed that $C_1 = C_2 = \frac{1}{2}\mu$ in Eq. (4.14).

For the case of a uniaxial tensile test, let us consider a cube of sides of length L_0 in the reference configuration \mathcal{B}_0 . Let us assume that a uniform tensile stress, indicated by \mathbf{s} , is applied along the outward normal to one face of the domain, as in Fig. 4.2(a); for instance $\mathbf{s} = s\mathbf{E}_1$, where $\mathbf{E}_1 = (1, 0, 0)$. The resulting homogeneous deformation of the body is represented in Fig. 4.2(b) and the associated

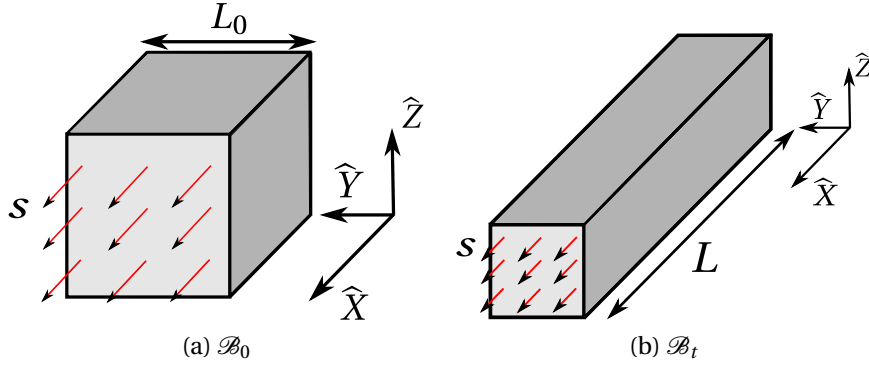


Figure 4.2: Homogeneous deformation of a cube under the action of uniform tensile stress. Reference configuration \mathcal{B}_0 (a); deformed configuration \mathcal{B}_t (b)

deformation gradient and right Cauchy-Green tensors read:

$$\mathbf{F} = \begin{pmatrix} F_{\hat{X}\hat{X}} & 0 & 0 \\ 0 & F_{\hat{Y}\hat{Y}} & 0 \\ 0 & 0 & F_{\hat{Z}\hat{Z}} \end{pmatrix} = \begin{pmatrix} \lambda_{\hat{X}} & 0 & 0 \\ 0 & \sqrt{\frac{1}{\lambda_{\hat{X}}}} & 0 \\ 0 & 0 & \sqrt{\frac{1}{\lambda_{\hat{X}}}} \end{pmatrix} \quad (4.18)$$

and

$$\mathbf{C} = \begin{pmatrix} \lambda_{\hat{X}}^2 & 0 & 0 \\ 0 & \frac{1}{\lambda_{\hat{X}}} & 0 \\ 0 & 0 & \frac{1}{\lambda_{\hat{X}}} \end{pmatrix}, \quad (4.19)$$

respectively; $\lambda_{\hat{X}} = \left(\frac{L-L_0}{L_0} + 1\right)$ measures the extension along the \mathbf{E}_1 direction and L is the deformed length along the direction of the tensile stress, as in Fig. 4.2(b). In Eq. (4.18), $F_{\hat{Y}\hat{Y}}$ and $F_{\hat{Z}\hat{Z}}$ represent the contractions of the cube along the \mathbf{E}_2 and \mathbf{E}_3 directions. In this case, the strain energy functions of Eqs.(4.12)-(4.17) depend solely on the deformation $\lambda_{\hat{X}}$ and they are represented in Fig. 4.3. For the uniaxial tensile test all the strain energy functions are convex functions in the deformation $\lambda_{\hat{X}}$. It can be noticed that all the constitutive laws satisfy the so called stress free reference configuration condition Holzapfel [2000]; Balzani [2006]. Such condition is an important requirement for material models and it postulates that, for hyperelastic materials, the strain energy is null when the body is at rest, namely in the reference configuration \mathcal{B}_0 ; this implies that, as explained in Sec. 3.1.2, for purely elastic materials only deformations can induce stresses. As shown in Fig. 4.3, for small values of deformation $\lambda_{\hat{X}}$, the Mooney-Rivlin and the neo-Hookean models have similar behaviors. The St. Venant-Kirchhoff model shows a qualitative behavior similar to the one of the exponential models for deformations $\lambda_{\hat{X}} \in [1, 2.5]$. On the other hand, for $\lambda_{\hat{X}} > 2.5$ the SVK strain energy function leads to a quite different mechanical response with respect to the exponential laws. On the contrary, the EXP1 and EXP2 models show a very similar behavior on all the range of deformations $\lambda_{\hat{X}}$. However, as represented in Fig. 4.3(b), for small and moderate vales of $\lambda_{\hat{X}}$ the values of strain energy function $\widehat{\mathcal{W}}^{iso}$ corresponding to the EXP2 function are lower compared to the ones obtained from the EXP1 model, due to the power function in the argument of the exponential term of $\widehat{\mathcal{W}}_{EXP2}^{iso}$. This, as discussed in Triccerri et al. [2014], is of

4.2. Constitutive models for the healthy cerebral arterial tissue

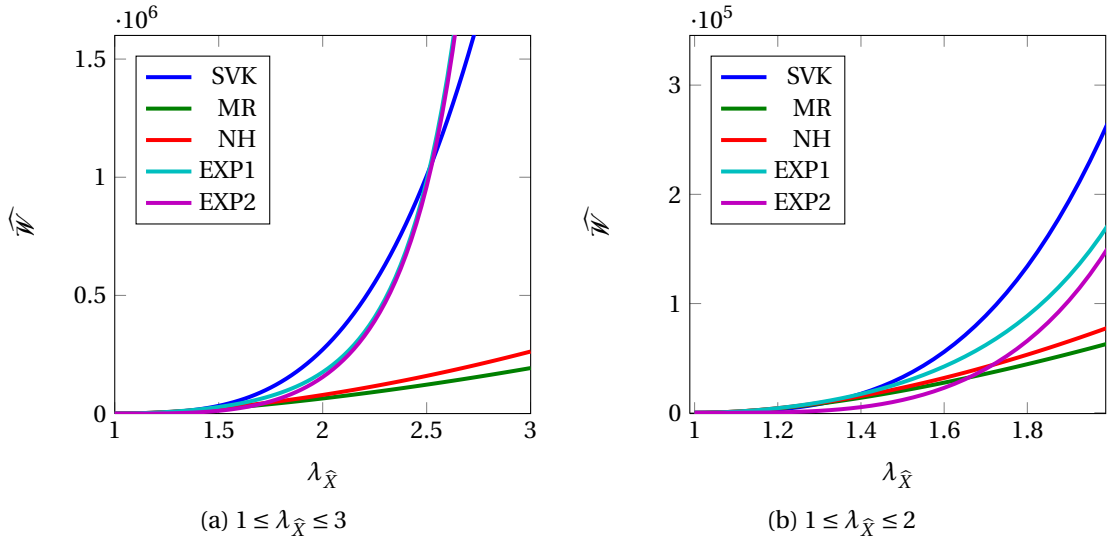


Figure 4.3: Strain energies [dyn / (s²cm²)] of Eqs.(4.12)-(4.17) for the uniaxial tensile test on a cube of Fig. 4.2(a)

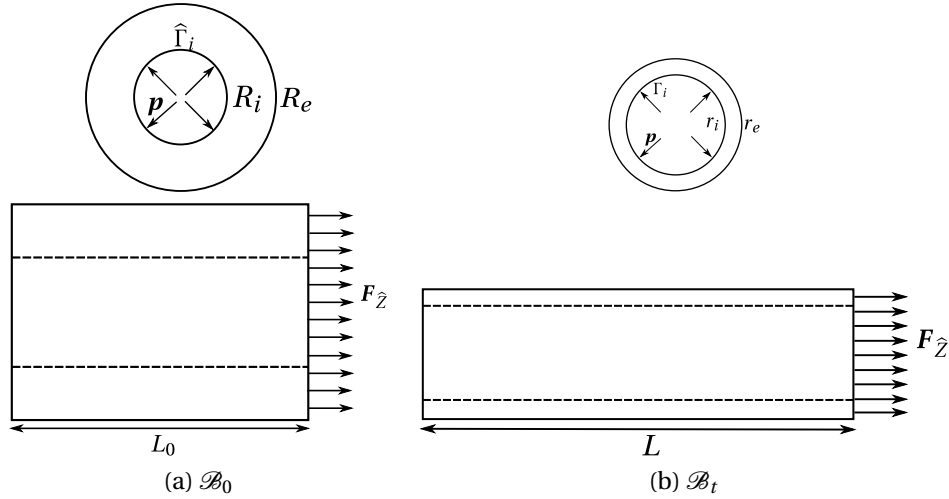


Figure 4.4: Reference \mathcal{B}_0 and current \mathcal{B}_t configurations of the cylindrical domain in inflation-extension tests

particular interest to describe the mechanical behavior of arteries in the small deformations regime. For the case of inflation-extension tests, let us consider a cylindrical domain of undeformed internal and external radii R_i and R_e , respectively, and of length L_0 (see Fig. 4.4(a)). Let us assume that a force field defined per unit of area, indicated as \mathbf{p} , acts on the internal surface $\hat{\Gamma}_i$ of the domain and that it is directed along the inward normal to $\hat{\Gamma}_i$. In addition, a tensile stress $F_{\hat{z}}$ is supposed to act on one of the two lateral extremities of the domain, as in Fig. 4.4(a). In Fig. 4.4(c), the deformed internal surface, internal and external radii and the deformed length of the cylinder are indicated as Γ_i , r_i , r_e and L , respectively. The deformation gradient tensor \mathbf{F} and the corresponding right Cauchy-Green tensor \mathbf{C}

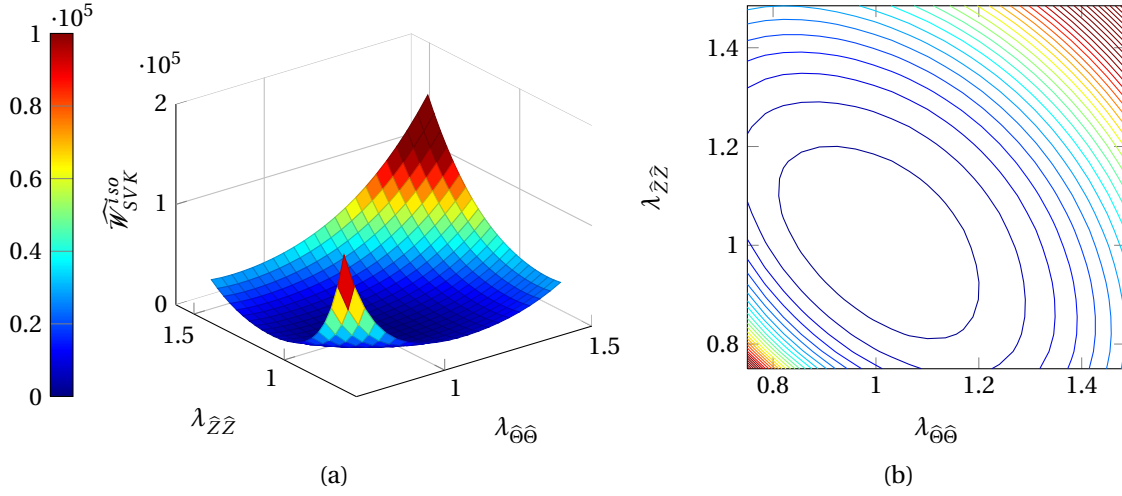


Figure 4.5: Strain energy function $\widehat{\mathcal{W}}_{SVK}^{iso}$ [dyn / (s²cm²)] of Eq. (4.12). Material parameters from Tab. 4.1

expressed in the material cylindrical coordinates $(\widehat{R}, \widehat{\Theta}, \widehat{Z}) \in \mathcal{B}_0$ read as follows:

$$\mathbf{F} = \begin{pmatrix} \frac{1}{\lambda_{\widehat{\Theta}\widehat{\Theta}}\lambda_{\widehat{Z}\widehat{Z}}} & 0 & 0 \\ 0 & \lambda_{\widehat{\Theta}\widehat{\Theta}} & 0 \\ 0 & 0 & \lambda_{\widehat{Z}\widehat{Z}} \end{pmatrix} \quad (4.20)$$

and

$$\mathbf{C} = \begin{pmatrix} \frac{1}{\lambda_{\widehat{\Theta}\widehat{\Theta}}^2\lambda_{\widehat{Z}\widehat{Z}}^2} & 0 & 0 \\ 0 & \lambda_{\widehat{\Theta}\widehat{\Theta}}^2 & 0 \\ 0 & 0 & \lambda_{\widehat{Z}\widehat{Z}}^2 \end{pmatrix}, \quad (4.21)$$

respectively. In Eqs.(4.20) and (4.21), $\lambda_{\widehat{\Theta}\widehat{\Theta}}$ is called the circumferential stretch, while $\lambda_{\widehat{Z}\widehat{Z}}$ is referred to as the axial stretch and they read, respectively, as:

$$\lambda_{\widehat{\Theta}\widehat{\Theta}} = \frac{r}{\widehat{R}} \quad \text{and} \quad \lambda_{\widehat{Z}\widehat{Z}} = \frac{L-L_0}{L_0} + 1, \quad (4.22)$$

where $r_i < r < r_e$ in \mathcal{B}_t and $R_i < \widehat{R} < R_e$ in \mathcal{B}_0 . Similarly to the case of uniaxial tensile stress, using the material parameters of Tab. 4.1, the strain energy functions of Eqs.(4.12)-(4.17) can be computed for different values of the circumferential and axial deformations (see Figs.(4.5)-(4.9)). It is observed that all the strain energy functions are convex functions for all states of deformations under consideration and the absolute minimum for all the models is yielded at $(\lambda_{\widehat{\Theta}\widehat{\Theta}}, \lambda_{\widehat{Z}\widehat{Z}}) = (1, 1)$, namely in the reference configuration \mathcal{B}_0 . It is of particular relevance the fact that, although the St. Venant-Kirchhoff law is not polyconvex for all the possible states of deformations, for the range and type of deformations considered and for the material parameters of Tricerri et al. [2014], $\widehat{\mathcal{W}}_{SVK}^{iso}$ is a convex function of the polyconvex invariants I_1 and I_2 . Indeed, this suggests that when solving inflation-extension problems on cylindrical geometry using the SVK model, the existence of displacement fields minimizing the potential function in Eq. (4.1) can be also expected when considering numerical simulations.

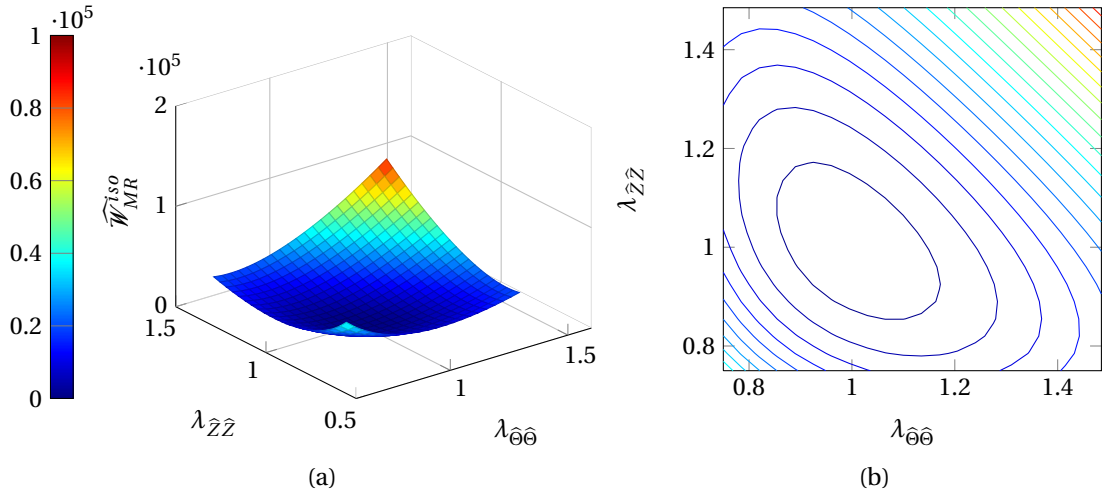


Figure 4.6: Strain energy function \widehat{W}_{MR}^{iso} [dyn / (s²cm²)] of Eq. (4.14). In this case $C_1 = C_2 = \frac{\mu}{2}$

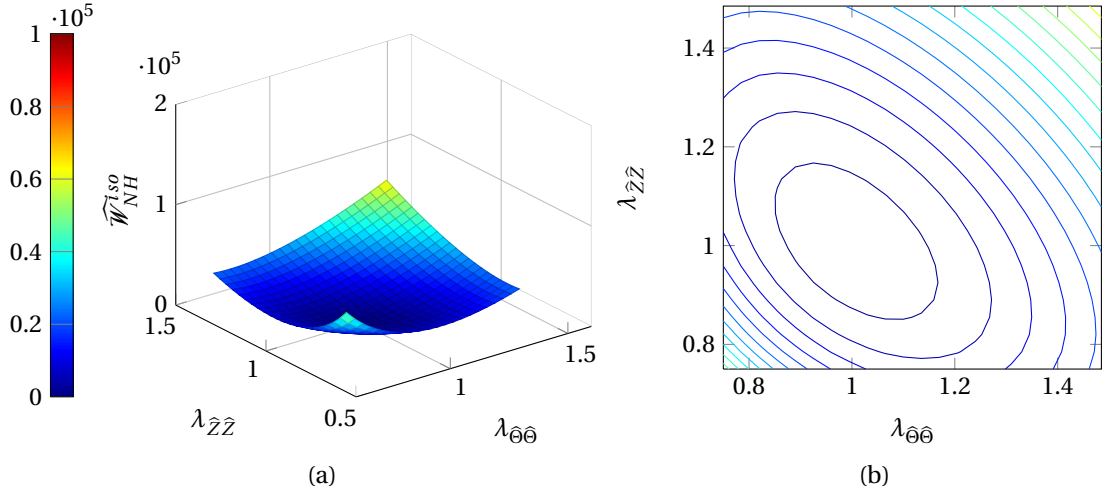


Figure 4.7: Strain energy function \widehat{W}_{NH}^{iso} [dyn / (s²cm²)] of Eq. (4.15). Material parameters from Tab. 4.1

Concerning the other constitutive models of Eqs.(4.14)-(4.17), it can be observed that the strain energy functions are all convex surfaces of the circumferential and axial deformations; this, as a consequence of the positiveness of the material parameters together with the polyconvexity of the invariants in Eqs.(4.14)-(4.17), guarantees the existence of minimizing solutions to inflation-extension problems. For this reason, the constitutive laws given by Eqs.(4.12)-(4.17) have been considered as possible modeling choices for the arterial tissue to simulate uniaxial tensile and inflation-extension tests.

4.2.2 Anisotropic constitutive laws

The anisotropic constitutive models that are considered in this work are of structurally motivated type for which the arterial tissue is represented as a fiber-reinforced material. The vessel wall is assumed to be composed of two main constituents: a background material (also referred to as the matrix material) representing the elastin in which one or more families of fibers, describing the collagen fibers, are

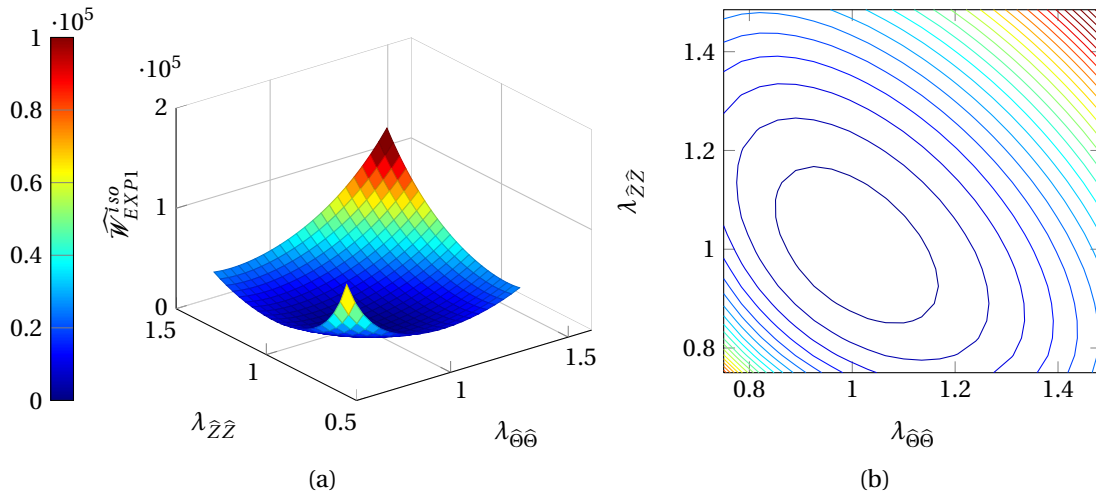


Figure 4.8: Strain energy function $\widehat{\mathcal{W}}_{EXP1}^{iso}$ [dyn / (s²cm²)] of Eq. (4.16). Material parameters from Tab. 4.1

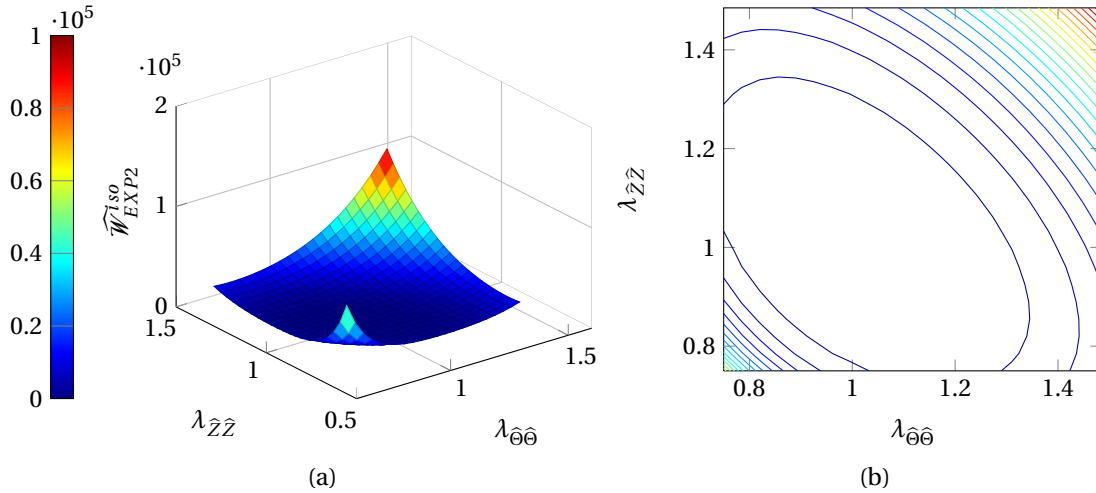


Figure 4.9: Strain energy function $\widehat{\mathcal{W}}_{EXP2}^{iso}$ [dyn / (s²cm²)] of Eq. (4.17). Material parameters from Tab. 4.1

immersed (see Sec. 2.1). The background material is assumed to behave as an isotropic body, while the families of fibers are supposed to be continuously arranged in the matrix endowing the body of a strongly directional (i.e. anisotropic) mechanical response. In the past decade, anisotropic laws have been proposed for different biomechanical applications on arteries or other living tissues, such as ligaments or cardiac tissue Calvo et al. [2007]; Holzapfel and Odgen [2006, 2009]. Within the context of mathematical modeling of the arterial tissue, the use of anisotropic models for fiber-reinforced materials is motivated by the strong fibrous nature of vessel wall, as discussed in Sec. 2.1. As shown in Fig. 4.3, not all the isotropic constitutive models (e.g. Mooney-Rivlin or neo-Hookean) are able to model the stiffening effect in the mechanical behavior of arteries for high deformations. On the contrary, since anisotropic constitutive laws consider both the elastin and collagen fibers, such stiffening effect can be better recovered from the mathematical modeling of the mechanical contribution of the collagen fibers to the overall mechanical response Holzapfel and Gasser [2000]; Li and Robertson [2009b]; Triccerri

et al. [2014]. More in detail, the latter is taken into account once the fibers are considered mechanically “active”. In literature, e.g. Holzapfel and Ogden [2010]; Calvo et al. [2007]; Dalong et al. [2012]; Balzani et al. [2012], when the tissue is modeled as a fiber-reinforced material, the fibrous component is assumed to be mainly aligned in the tangential plane of the vessel rather than along the radial direction, i.e. through the thickness of vessel wall. Such choice is supported by the experimental observations reported in e.g. Schriefl [2012].

For the sake of clarity, the remainder of the subsection is organized as follows. Firstly, the general form of an anisotropic model in the cases of one and multiple families of fibers are introduced. In this respect, it is worth pointing out that when a single family of fibers is immersed in the background material, the material is said to be transversely isotropic; on the other hand, when two families with the same mechanical properties are considered, the material is said orthotropic or locally orthotropic according to the angle formed by the two families of fibers Holzapfel [2000]. Afterwards, the strain energy function for a transversely isotropic material will be specialized according to the mathematical representation of the collagen fibers activation. With this aim, two classes of models are presented; firstly, the class of models for which the collagen fibers activation occurs at zero strains is introduced Holzapfel and Gasser [2000]; Gasser and Holzapfel [2006]; Calvo et al. [2007]; Balzani et al. [2006a]; Brands et al. [2008]; Brinkhues et al. [2013]; finally, the anisotropic models, also referred to as anisotropic multi-mechanism models, which describe the recruitment of the collagen fibers at finite strains are discussed Wulandana [2003]; Li [2009]; Li and Robertson [2009b]; Tricerri et al. [2014]. In this work, locally orthotropic constitutive laws are considered; however, in the following they will be simply referred to as anisotropic models and the corresponding strain energy functions will be specified throughout the section.

General form of a anisotropic model for arteries

Firstly, in this section the strain energy function for a transversely isotropic material is presented. From the mechanical point of view, the properties of a transversely isotropic body are symmetric with respect to a characteristic vector, indicated as $\boldsymbol{\tau}$, that is normal to a plane of isotropy, as in Fig. 4.10-(a). Similarly to isotropic materials, transversely isotropic bodies can be mathematically characterized in terms of their symmetry group $\mathcal{G}_{\mathcal{B}}$ which is $\mathcal{G}_{\mathcal{B}} = \{\mathbf{Q} \in \text{SO}(3) : \mathbf{Q}\boldsymbol{\tau} = \pm\boldsymbol{\tau}\}$ Raoult [2009]. For instance, for the cubic body in Fig. 4.10, by supposing that the characteristic vector is $\boldsymbol{\tau} = (1, 0, 0)$ and that plane of isotropy contains the \hat{Z} axis, the symmetry group is the set of all the rotation matrices \mathbf{Q} of the form:

$$\mathbf{Q} = \begin{pmatrix} \pm 1 & 0 & 0 \\ 0 & \cos \theta & -\sin \theta \\ 0 & \sin \theta & \cos \theta \end{pmatrix}, \quad (4.23)$$

for $\theta \in [0, 2\pi)$. It is worth pointing out that, when only a single family of fibers is immersed in the background material, the characteristic direction $\boldsymbol{\tau}$ is identified by the local alignment of the collagen fibers in \mathcal{B}_0 , described by $\hat{\boldsymbol{a}}$. On the other hand, when multiple families of fibers are immersed in the background material, the overall response of the body is not transversely isotropic anymore; indeed, for instance, when two families are considered the material is called orthotropic or locally orthotropic depending on the angle formed between the two vectors $\hat{\boldsymbol{a}}$ defining the local orientation of the fibers, see Fig. 4.10-(b). Specifically, for an orthotropic material the angle between the two vectors is 90° , while for a locally orthotropic material $\beta_{\hat{\boldsymbol{a}}}$ in Fig. 4.10-(b) can be different from 90° Holzapfel [2000]. When modeling fiber-reinforced materials, each family of fibers is supposed to be locally aligned along a characteristic direction (i.e. vector). Both in the reference and current configuration, the local direction

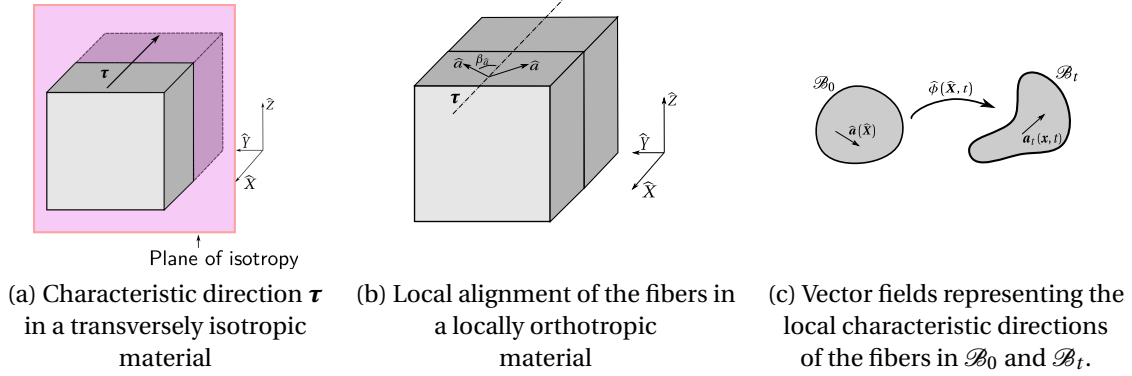


Figure 4.10: General representation of the characteristic direction $\boldsymbol{\tau}$ and of the vectorial fields $\hat{\boldsymbol{a}}$ in \mathcal{B}_0 and \boldsymbol{a}_t in \mathcal{B}_t

is mathematically described by means of a vectorial field which is indicated as $\hat{\boldsymbol{a}}$ in \mathcal{B}_0 and by \boldsymbol{a}_t in \mathcal{B}_t (see Fig. 4.10-(b)); similarly to the material density function $\rho_0(\hat{\boldsymbol{X}})$ in Sec. 3.2.1, the material field $\hat{\boldsymbol{a}}$ depends solely on the coordinates $\hat{\boldsymbol{X}}$, being referred to the reference configuration that is fixed in time. Without loss of generality, it can be supposed that $\hat{\boldsymbol{a}}$ and \boldsymbol{a}_t are unit vector fields on the corresponding configuration of \mathcal{B} Holzapfel [2000]; namely

$$\|\hat{\boldsymbol{a}}\| = 1 \quad \text{in } \mathcal{B}_0 \quad \text{and} \quad \|\boldsymbol{a}_t\| = 1 \quad \text{in } \mathcal{B}_t, \quad (4.24)$$

where $\|\cdot\|$ indicates the Euclidean norm in \mathbb{R}^3 Holzapfel [2000]. The local deformations of the fibers field (i.e. elongations or contractions) can be described by means of Eq. (3.5); indeed, the relation between the material distribution of fibers $\hat{\boldsymbol{a}} \in \mathcal{B}_0$ and its spatial counterpart $\boldsymbol{a}_t \in \mathcal{B}_t$ reads:

$$\lambda_a \boldsymbol{a}_t = \mathbf{F} \hat{\boldsymbol{a}}, \quad (4.25)$$

where $\lambda_a > 0$ measures the stretch (if $\lambda_a > 1$) or the contraction (if $\lambda_a < 1$) of the family of fibers along its characteristic direction $\hat{\boldsymbol{a}}$ due to the deformations of the body.

Similarly to isotropic bodies, the mechanical behavior of hyperelastic transversely isotropic materials can be characterized in terms of a scalar-valued strain energy function, indicated as $\widehat{\mathcal{W}}^{ti}$. In this case, because of the directional dependence of the mechanical behavior of the material on the deformations, the strain energy function is required to depend both on the right Cauchy-Green tensor \mathbf{C} and on the material vectorial field $\hat{\boldsymbol{a}}$. The material modeling principles of Sec. 3.3 must be satisfied, leading to the following general form of $\widehat{\mathcal{W}}^{ti}$:

$$\widehat{\mathcal{W}}^{ti} = \widehat{\mathcal{W}}^{ti}(\mathbf{C}, \hat{\boldsymbol{a}} \otimes \hat{\boldsymbol{a}}), \quad (4.26)$$

where $\boldsymbol{w} \otimes \boldsymbol{u}$ indicates the outer product between the two vectors \boldsymbol{w} and \boldsymbol{u} in \mathbb{R}^3 Holzapfel [2000] and the symmetric tensor $\mathbf{M} = (\hat{\boldsymbol{a}} \otimes \hat{\boldsymbol{a}})$ is usually referred to as the structural tensor of the family of collagen fibers Holzapfel [2000]; Spencer [1971]. In Holzapfel [2000]; Spencer [1971], it is shown that the form of the strain energy function $\widehat{\mathcal{W}}^{ti}$ in Eq. (4.26) is invariant under superimposed rigid motions of the body \mathcal{B} and that it satisfies the principles of material symmetry of Eq. (3.40). Furthermore, thanks to the dependency of $\widehat{\mathcal{W}}^{ti}$ on \mathbf{C} and \mathbf{M} , the function $\widehat{\mathcal{W}}^{ti}$ in Eq. (4.26) becomes an isotropic tensor function of its arguments Holzapfel [2000]; Balzani [2006]; Spencer [1971]; therefore, the representation theorems for isotropic tensor functions can still be applied and, similarly to isotropic constitutive models, $\widehat{\mathcal{W}}^{ti}$ in

4.2. Constitutive models for the healthy cerebral arterial tissue

Eq. (4.26) can be formulated in terms of the integrity basis of the tensors \mathbf{C} and \mathbf{M} Holzapfel [2000]; Spencer [1971]. The analogous of Eq. (4.9) for transversely isotropic constitutive models for a single family of collagen fibers-reinforced material is:

$$\widehat{\mathcal{W}} = \widehat{\mathcal{W}}(I_1, I_2, I_3, I_4, I_5), \quad (4.27)$$

where the set of invariants $(I_1, I_2, I_3, I_4, I_5)$ is called the integrity basis of \mathbf{C} and \mathbf{M} . In Eq. (4.27), I_4 and I_5 are called the pseudo invariants of \mathbf{C} and \mathbf{M} and they arise directly from the anisotropy of the body. They are defined, respectively, as:

$$I_4 = \mathbf{C} : (\widehat{\mathbf{a}} \otimes \widehat{\mathbf{a}}) = \text{Tr}(\mathbf{C}^T (\widehat{\mathbf{a}} \otimes \widehat{\mathbf{a}})) = \widehat{\mathbf{a}}^T \mathbf{C} \widehat{\mathbf{a}} = (\lambda_a)^2 \quad (4.28)$$

and

$$I_5 = \mathbf{C}^2 : \mathbf{M} = \text{Tr}(\mathbf{C}^2 \mathbf{M}) = \widehat{\mathbf{a}}^T \mathbf{C}^2 \widehat{\mathbf{a}}, \quad (4.29)$$

where $\mathbf{A} : \mathbf{B}$ indicates the scalar product between second order tensors in \mathbb{R}^3 Holzapfel [2000]. From the mechanical point of view, the fourth invariant I_4 corresponds to the square of the stretch λ_a of the body along the fiber direction $\widehat{\mathbf{a}}$, in the current configuration; I_5 measures the deformation of a family of collagen fibers under shear conditions Raoult [2009]. In the strain energy function $\widehat{\mathcal{W}}^{ti}$ of Eq. (4.27) for a single fiber-reinforced material, the mechanical contributions provided either by the background material and by the fibrous constituent must be taken into account. In the context of mathematical modeling of the arterial tissue by means of anisotropic models, it is worth pointing out that, a family of fibers actively contributes to the overall mechanical behavior only when it is stretched beyond a certain level, i.e. when its stretch is greater than a certain reference stretch, called the activation stretch; otherwise, the mechanical response of the material depends only on the mechanical behavior of the background material. In the following, such activation stretch is indicated as λ_A and the corresponding activation stretch by $I_{4,A} = (\lambda_A)^2$ (see Eq. (4.28)); then, the family of fibers is “active” when $I_4 > I_{4,A}$. Consequently, for either active and passive states of the family of collagen fibers, the strain energy function of Eq. (4.27) reads as follows:

$$\widehat{\mathcal{W}}(I_1, I_2, I_3, I_4, I_5) = \mathcal{U}(I_3) + \widehat{\mathcal{W}}^{ti}(I_1, I_2, I_4, I_5), \quad (4.30)$$

where,

$$\widehat{\mathcal{W}}^{ti} = \begin{cases} \widehat{\mathcal{W}}_{iso}^{ti}(I_1, I_2), & \text{if } I_4 \leq I_{4,A}, \\ \widehat{\mathcal{W}}_{iso}^{ti}(I_1, I_2) + \widehat{\mathcal{W}}_{fibers}^{ti}(I_4, I_5), & \text{if } I_4 > I_{4,A}, \end{cases} \quad (4.31)$$

where, for passive states of the family of collagen fibers, the strain energy function $\widehat{\mathcal{W}}_{iso}^{ti}$ describing the mechanical behavior of the elastin is of isotropic type, therefore $\widehat{\mathcal{W}}_{iso}^{ti} = \widehat{\mathcal{W}}^{iso}$, see Eq. (4.11); this is supported by the experimental observations of the isotropic response of the background material in fiber-reinforced materials such as the arterial tissue, e.g. Holzapfel and Gasser [2000]; Humphrey [2002]. As for Eq. (4.9), the contribution coming from the strain energy function $\mathcal{U}(I_3)$ is due to the deformations that would lead to changes in the volume of the body. For active states of the single family of fibers, the additive split of $\widehat{\mathcal{W}}^{ti}$ is supported by the experimental observations of the extremely weak interaction between the elastin and the collagen fibers Holzapfel and Gasser [2000]. In the more general case of N families of fibers immersed in the background material, although the overall mechanical response of the material is not transversely isotropic anymore, each i -th family of fibers, for $i = 1 \dots N$,

will be spatially distributed according to the vectorial fields $\hat{\mathbf{a}}^{(i)}$ in \mathcal{B}_0 and $\mathbf{a}_t^{(i)}$ in \mathcal{B}_t . Consequently, a set of N structural tensors $\mathbf{M}^{(i)} = \hat{\mathbf{a}}^{(i)} \otimes \hat{\mathbf{a}}^{(i)}$ for $i = 1, \dots, N$ is defined in order to measure the deformations associated to the i -th family of fibers. Similarly to Eqs. (4.28) and (4.29) two sets of pseudo invariants are defined, respectively, as:

$$\mathbb{I}_4 = \left\{ I_4^{(i)} \right\}_{i=1}^N, \text{ with } I_4^{(i)} = \mathbf{C} : \mathbf{M}^{(i)}, \quad (4.32)$$

and

$$\mathbb{I}_5 = \left\{ I_5^{(i)} \right\}_{i=1}^N, \text{ with } I_5^{(i)} = \mathbf{C}^2 : \mathbf{M}^{(i)}. \quad (4.33)$$

Eq. (4.31) can be generalized to the case of N families of fibers as follows:

$$\widehat{\mathcal{W}}^{aniso}(I_1, I_2, I_3, \mathbb{I}_4, \mathbb{I}_5) = \begin{cases} \widehat{\mathcal{W}}_{iso}^{aniso}(I_1, I_2), & \text{if } \mathbb{I}_4 \leq \mathbb{I}_{4,A}, \\ \widehat{\mathcal{W}}_{iso}^{aniso}(I_1, I_2) + \widehat{\mathcal{W}}_{fibers}^{aniso}(\mathbb{I}_4, \mathbb{I}_5), & \text{if } \mathbb{I}_4 > \mathbb{I}_{4,A}, \end{cases} \quad (4.34)$$

where the condition $\mathbb{I}_4 > \mathbb{I}_{4,A}$ refers only to those families, indicated by the index $i \in \mathbb{N}$ for $1 \leq i \leq N$, for which the condition $I_4^{(i)} > I_{4,A}^{(i)}$ is verified and the fiber family actively contributes to the mechanical response of the material. It is worth stressing the fact that in Eq. (4.34), the strain energy function is indicated as $\widehat{\mathcal{W}}^{aniso}$ since the response of the body is anisotropic and not transversely isotropic; therefore, $\widehat{\mathcal{W}}_{iso}^{aniso}(I_1, I_2)$ indicates the contribution of the elastin, while $\widehat{\mathcal{W}}_{fibers}^{aniso}(\mathbb{I}_4, \mathbb{I}_5)$ the one of the collagen fibers. The total response of the fibrous network, represented by $\widehat{\mathcal{W}}_{fibers}^{aniso}(\mathbb{I}_4, \mathbb{I}_5)$ in Eq. (4.34) is usually expressed as the sum of the strain energy functions of each family of fibers, indicated by $\widehat{\mathcal{W}}_{fibers}^{(i)}$, as follows:

$$\widehat{\mathcal{W}}_{fibers}^{aniso}(\mathbb{I}_4, \mathbb{I}_5) = \sum_{i=1}^N \widehat{\mathcal{W}}_{fibers}^{(i)}(I_4^{(i)}, I_5^{(i)}). \quad (4.35)$$

From the mechanical point of view, the additive split of $\widehat{\mathcal{W}}_{fibers}^{aniso}(\mathbb{I}_4, \mathbb{I}_5)$ is supported by the experimental observation of the weak interactions among the families of fibers Holzapfel and Gasser [2000].

Concerning the choice of the strain energy function for the background material, as mentioned before, isotropic constitutive models (as those in Eqs.(4.12)-(4.17)) are used; in literature, either the Mooney-Rivlin or the neo-Hookean model are usually employed Calvo et al. [2007]; Balzani et al. [2006a]; Gundiah et al. [2008, 2007]; Watton et al. [2009a]. In this work, based on either modeling and numerical reasons, the mechanical behavior of the elastin is described either by the first or the second order exponential models, that is

$$\widehat{\mathcal{W}}_{iso}^{aniso} = \widehat{\mathcal{W}}_{EXP1}^{iso} \quad \text{OR} \quad \widehat{\mathcal{W}}_{iso}^{aniso} = \widehat{\mathcal{W}}_{EXP2}^{iso}. \quad (4.36)$$

On the other hand, concerning the mechanical behavior of the single family of fibers $\widehat{\mathcal{W}}_{fibers}^{(i)}$, it is usually modeled by means of a second order exponential model, such as the one in Eq. (4.17), along the fibers direction Holzapfel and Gasser [2000]; Li and Robertson [2009b]; Calvo et al. [2007]; Brands et al. [2008]. Although a second order exponential law is a common choice (see e.g. Holzapfel and Gasser [2000]; Balzani et al. [2006a]; Li and Robertson [2009b]), its form depends on the mathematical description of the activation of the families of collagen fibers; the cases of recruitment of the collagen fibers either at zero or finite strains will be discussed in the remainder of the section. The second order exponential model for the single family of fibers is adequate in order to represent the stiffening effect

in the mechanical response of the arterial tissue that is associated to the contribution of the collagen fibers to the overall mechanical response of the vessel wall (see Sec. 2.2). It is important to remark that, the strain energy function in Eq. (4.34) must satisfy the polyconvexity condition for all states of deformations. This is verified if the constitutive laws for the background material $\widehat{\mathcal{W}}_{iso}^{aniso}$, the one for the collagen fibers $\widehat{\mathcal{W}}_{fibers}^{aniso}$ and the strain energy for the volumetric changes \mathcal{U} in Eq. (4.34) are polyconvex functions Balzani [2006]; Dacorogna [2000]. As shown in Dacorogna [2000], the polyconvexity of the strain energy function for the fiber-reinforcing component $\widehat{\mathcal{W}}_{fibers}^{aniso}$ is polyconvex if the strain energy function for the single family of fibers $\widehat{\mathcal{W}}_{fibers}^{(i)}$ is polyconvex. As already discussed in Sec. 4.2.1, the polyconvexity condition is satisfied for $\widehat{\mathcal{W}}_{iso}^{aniso}$ in Eq. (4.36), while the polyconvexity of $\widehat{\mathcal{W}}_{fibers}^{(i)}$ and of \mathcal{U} are discussed in the remainder of the section and in the next section, respectively; however, it can be anticipated that polyconvex strain energy functions $\widehat{\mathcal{W}}_{fibers}^{(i)}$ and \mathcal{U} are considered in this work.

Activation of the collagen fibers at zero strains

In the seminal work Holzapfel and Gasser [2000], an anisotropic constitutive model was proposed for arteries. This model is of particular relevance in the scientific community, being extensively used to represent the arterial tissue in different contexts; for instance, to numerically simulate balloon angioplasty or arterial clamping Holzapfel and Gasser [2007, 2002], to describe damaged arterial tissue Calvo et al. [2007]; Balzani et al. [2006b] and, recently, in the context of inverse problems in structural mechanics Kroon [2010]; Kroon and Holzapfel [2008]; Zeinali-Davarani et al. [2009]. According to Holzapfel and Gasser [2000], the collagen fibers are assumed to actively contribute to the mechanical response of the tissue whenever their stretch is greater than one that is the length of the collagen fibers in the reference configuration \mathcal{B}_0 , namely the configuration at zero strains, of the vessel wall. In particular, in Holzapfel and Gasser [2000], the vector field $\widehat{\mathbf{a}}$ describing the distribution in space of the collagen fibers is supposed to be a unitary field, as in Eq. (4.24). This implies that, according to Holzapfel and Gasser [2000], if N families of fibers are supposed to be immersed in the background material, for each family of collagen fibers the activation stretch $\lambda_A^{(i)}$ and the associated activation stretch $I_{4,A}^{(i)}$ in Eq. (4.34), for $i = 1, \dots, N$, are unitary. For this type of models, the strain energy function $\widehat{\mathcal{W}}^{aniso}$ reads:

$$\widehat{\mathcal{W}}^{aniso} = \widehat{\mathcal{W}}_{RC}^{aniso}(I_1, I_2, \mathbb{1}_4, \mathbb{1}_5) = \begin{cases} \widehat{\mathcal{W}}_{iso}^{aniso}(I_1, I_2), & \text{if } \mathbb{1}_4 \leq \mathbf{1}, \\ \widehat{\mathcal{W}}_{iso}^{aniso}(I_1, I_2) + \sum_{i=1}^N \widehat{\mathcal{W}}_{fibers}^{(i)}(\mathbb{1}_4, \mathbb{1}_5), & \text{if } \mathbb{1}_4 > \mathbf{1}, \end{cases} \quad (4.37)$$

where the subscript highlights the fact that the activation stretch of each family of fibers is the length in the reference configuration (RC) and $\mathbf{1}$ is a vector of entries equal to one, that is $\mathbf{1} = \{1\}_{i=1}^N$. As mentioned before, the strain energy function for the single family of fibers is a second order exponential along the fibers direction, namely:

$$\widehat{\mathcal{W}}_{fibers}^{(i)}(I_4^{(i)}, I_5^{(i)}) = \widehat{\mathcal{W}}_{EXP2-RC}^{(i)}(I_4^{(i)}) = \frac{\alpha^{(i)}}{2\gamma^{(i)}} \left(e^{\gamma^{(i)}(I_4^{(i)}-1)^2} - 1 \right), \quad (4.38)$$

where $\alpha^{(i)}$ and $\gamma^{(i)}$ are positive parameters representing the mechanical stiffness and the level of nonlinearity of the mechanical response of the i -th fibers family, respectively. As shown in Balzani [2006], the strain energy function of Eq. (4.38) is polyconvex for all possible states of deformation.

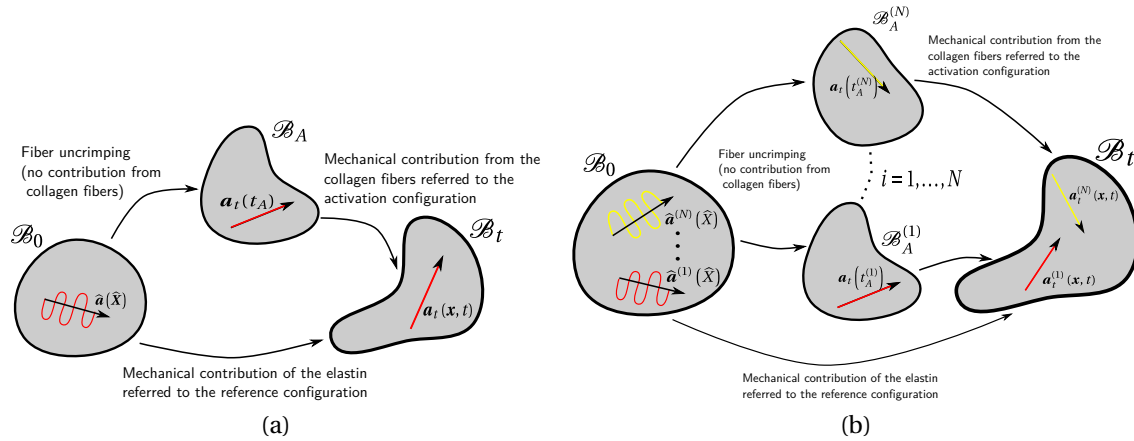


Figure 4.11: Schematic representation of the multi-mechanism model of Wulandana [2003]; Li [2009]. Single family of collagen fibers (a); N families of fibers (b)

Activation of the collagen fibers at finite strains

In Scott et al. [1972]; Burton [1954]; Roach and Burton [1957]; Hill et al. [2012] it is reported that the collagen fibers begin load-bearing, i.e. they contribute to the overall mechanical response of the tissue, at finite strains. Indeed, the recruitment of the collagen fibers at finite strains is considered as the underlying mechanism for the stiffening effect in the mechanical behavior of arteries for high deformations. A constitutive model that is able to describe the recruitment of the collagen fibers at finite strains and to characterize their mechanical response with respect to their activation stretch is called a *multi-mechanism model* Wulandana [2003]; Li [2009]; Robertson et al. [2009]; Wulandana and Robertson [2005]; Li and Robertson [2009b]. A multi-mechanism model was firstly introduced in Wulandana [2003]; Wulandana and Robertson [2005] assuming that either the mechanical response of the elastin and the one of the collagen fibers could be described by isotropic constitutive laws; afterwards, an anisotropic multi-mechanism law has been formulated in Li [2009]; Li and Robertson [2009b]. A detailed description of the kinematics of a multi-mechanism model can be found in Wulandana [2003]; Li [2009]; however, for the sake of clarity, the anisotropic multi-mechanism model of Li [2009] is briefly recalled here. Firstly, the case of a single family of collagen fibers immersed in the elastin is presented and, as a second step, its generalization to the general case of a finite number N of families is discussed. Let us consider a continuous body \mathcal{B} in which a single family of collagen fibers, represented by the material vector field \hat{a} , is immersed in the background material, as in Fig. 4.11-(a). As described in Li [2009]; Hill et al. [2012], it is supposed that, in the reference configuration \mathcal{B}_0 , the collagen fibers are in a wavy and crimped state which makes them not able to contribute to the overall mechanical response of the tissue. When small external loads are applied on \mathcal{B}_0 , although the collagen fibers start uncrimping, the mechanical response of the tissue can be described solely in terms of the mechanical contribution provided by the elastin. If the external loads increase a deformed configuration (indicated as \mathcal{B}_A in Fig. 4.11-(a)) at which the collagen fibers are completely uncrimped will be reached at a certain time t_A called the activation time; the corresponding deformed configuration, indicated as \mathcal{B}_A , is named the activation configuration associated to the family of collagen fibers. If the external loads increase further, for times $t > t_a$, the collagen fibers will be able to actively contribute to the overall mechanical response of the tissue and, therefore, the mechanical response of the arterial tissue will be determined by contributions of the elastin and collagen fibers. From the modeling point of view, it is worth pointing out the following aspects related

the multi-mechanism model proposed in Li [2009]:

- The activation of the family of collagen fibers is measured with respect to an activation stretch λ_A to which the activation stretch $I_{4,A}$ corresponds; more specifically, $I_{4,A} = I_4(t_A) = (\lambda_A)^2 = \hat{\mathbf{a}}^T \mathbf{C}(t_A) \hat{\mathbf{a}} > 1$. In the following the activation stretch for the multi-mechanism model is indicated as $I_{4,MM}$ in order to clearly distinguish it from the general activation stretch $I_{4,A}$ in Eqs. (4.31). The activation stretch λ_A is a characteristic quantity associated to a family of collagen fibers; for this reason, λ_A is a material parameter characterizing the mechanical response of the collagen fibers which should be determined from experimental measurements Hill et al. [2012].
- The mechanical contribution of the collagen fibers to the overall response of the tissue is measured with respect to the deformations of the body computed with respect to the activation configuration \mathcal{B}_A . Therefore, the strain energy function for the collagen fibers will depend on kinematic quantities (such as the deformation gradient tensor or the right Cauchy-Green tensor) that measure the deformations of the collagen fibers referred to \mathcal{B}_A . The deformation gradient defined with respect to \mathcal{B}_A at any time $t' = t - t_A > 0$ will be indicated as $\mathbf{F}^a(t')$ and defined as $\mathbf{F}^a(t') = \mathbf{F}(t_A)^{-1} \mathbf{F}(t)$, where $\mathbf{F}(t)$ is the deformation gradient referred to \mathcal{B}_0 at the time t Li [2009]. Consequently, the right Cauchy-Green tensor computed with respect to \mathcal{B}_A is defined as $\mathbf{C}^a(t') = (\mathbf{F}^a(t'))^T \mathbf{F}^a(t')$.
- When the collagen fibers are active, in order to properly measure their deformations, the fourth and the fifth pseudo invariants defined in Eqs. (4.28) and (4.29) must be referred to the configuration \mathcal{B}_A ; the structural tensor \mathbf{M} of Eq. (4.26) referred to \mathcal{B}_A reads as follows:

$$\mathbf{M}_A = \mathbf{a}_t(t_A) \otimes \mathbf{a}_t(t_A) \quad (4.39)$$

and, consequently, I_4 and I_5 referred to the activation configuration \mathcal{B}_A , they transform into

$$I_4^a(t') = \mathbf{C}^a(t') : \mathbf{M}_A = \frac{I_4(t)}{I_4(t_A)} \quad \text{and} \quad I_5^a(t') = (\mathbf{C}^a(t'))^2 : \mathbf{M}_A, \quad (4.40)$$

respectively Li [2009]. In Eq. (4.40), the time argument of the tensor \mathbf{C} and of the two pseudo invariants has been highlighted for clarity; $I_4(t)$ is the fourth invariant defined in Eq. (4.28) and $I_4^a(t')$ is referred to as the true stretch since it measures the stretch of the family of fibers with respect to the activation stretch $I_4(t_A)$ defined before Li [2009]; Li and Robertson [2009b].

- Since the elastin and the collagen fibers are assumed to behave as a purely elastic materials, if the external loads decrease and the collagen fibers return to a wavy and crimped state the mechanical response of the tissue will depend solely on the constitutive model chosen for the elastin.

The general form of the strain energy function of a transversely isotropic multi-mechanism model with one family of fibers can be formulated as follows:

$$\widehat{\mathcal{W}}_{MM}^{ti}(t, t') = \begin{cases} \widehat{\mathcal{W}}_{iso}^{ti}(I_1(t), I_2(t)), & \text{if } I_4(t) \leq I_{4,MM}, \\ \widehat{\mathcal{W}}_{iso}^{ti}(I_1(t), I_2(t)) + \widehat{\mathcal{W}}_{fibers}^{ti}(I_4^a(t-t_A), I_5^a(t-t_A)), & \text{if } I_4(t) > I_{4,MM}, \end{cases} \quad (4.41)$$

where $t > 0$ and $t' = t - t_A > 0$ and, for the sake of clarity, the time arguments of the invariants have been highlighted to specify the configuration with respect to which they are computed. For

$t < t_A$, the collagen fibers do not contribute to the mechanical response of the tissue, therefore the response to external loads depends solely on the strain energy function for the elastin $\widehat{\mathcal{W}}_{iso}^{ti}(I_1(t), I_2(t))$. It is important to point out that the strain energy function of Eq. (4.31) is referred to the reference configuration \mathcal{B}_0 of the body \mathcal{B} for both active and passive states of the collagen fibers; on the contrary, when the fibers are mechanically active for $I_4(t) > I_{4,MM}$, the constitutive law in Eq. (4.41) contains terms that are referred to either the reference configuration \mathcal{B}_0 ($\widehat{\mathcal{W}}_{iso}^{ti}$) or to the activation configuration \mathcal{B}_A , i.e. $\widehat{\mathcal{W}}_{fibers}^{ti}$. Although the activation stretch λ_A could be experimentally measured, the corresponding activation configuration cannot be determined (for instance it could be not unique); for this reason, the strain energy function for the family of fibers must be referred to the reference configuration \mathcal{B}_0 Holzapfel [2000]; Wulandana [2003]; Li [2009]. If Eq. (4.41) is referred uniquely to the reference configuration \mathcal{B}_0 , it is transformed as follows:

$$\widehat{\mathcal{W}}_{MM}^{ti}(t) = \begin{cases} \widehat{\mathcal{W}}_{iso}^{ti}(I_1(t), I_2(t)), & \text{if } I_4(t) \leq I_{4,MM}, \\ \widehat{\mathcal{W}}_{iso}^{ti}(I_1(t), I_2(t)) + J(t_A) \widehat{\mathcal{W}}_{fibers}^{ti}(I_4(t), I_5(t)), & \text{if } I_4(t) > I_{4,MM}, \end{cases} \quad (4.42)$$

where $J(t_A) = \det(\mathbf{F}(t_A))$ Li [2009].

In the more general case of N families of collagen fibers, each of them will be characterized by its activation configuration $\mathcal{B}_A^{(i)}$, for $i = 1, \dots, N$, and by its own activation stretch $\lambda_A^{(i)}$, as shown in Fig. 4.11-(b). Each i -th family of fibers, for $i = 1, \dots, N$, reaches the uncrimped state at a certain activation time $t_A^{(i)}$ and the corresponding activation configuration is indicated as $\mathcal{B}_A^{(i)}$. Similarly to the case of a single fiber family, sets of structural tensors and pseudo invariants is defined for each family of fibers (see Li [2009] for details) and the general form of the strain energy function reads:

$$\widehat{\mathcal{W}}_{MM}^{aniso}(t) = \begin{cases} \widehat{\mathcal{W}}_{iso}^{aniso}(I_1(t), I_2(t)), & \text{if } \mathbb{I}_4(t) \leq \mathbb{I}_{4,MM}, \\ \widehat{\mathcal{W}}_{iso}^{aniso}(I_1(t), I_2(t)) + \sum_{i=1}^N J(t_A^{(i)}) \widehat{\mathcal{W}}_{fibers}^{(i)}(I_4^{(i)}(t), I_5^{(i)}(t)), & \text{if } \mathbb{I}_4(t) > \mathbb{I}_{4,MM}, \end{cases} \quad (4.43)$$

where the set $\mathbb{I}_4(t)$ is defined in Eq. (4.32) and $\mathbb{I}_{4,MM} = \{I_{4,MM}^{(i)}\}$ is the set of the N activation stretches for the families of fibers. As in Li [2009]; Li and Robertson [2009b], the strain energy function for the single family of collagen fibers $\widehat{\mathcal{W}}_{fibers}^{(i)}$ referred to the activation configuration $\mathcal{B}_A^{(i)}$ is a second order exponential law along the fibers direction, that is:

$$\widehat{\mathcal{W}}_{fibers}^{(i)}(I_4^{(i)}(t), I_5^{(i)}(t)) = \widehat{\mathcal{W}}_{EXP2-MM}^{(i)}(I_4^{(i)}(t)) = \frac{\alpha^{(i)}}{2\gamma^{(i)}} \left(e^{\frac{\gamma^{(i)}}{I_4^{(i)}}(I_4^{(i)}(t) - I_{4,MM}^{(i)})^2} - 1 \right), \quad (4.44)$$

where, similarly to Eq. (4.38), $\alpha^{(i)}$ and $\gamma^{(i)}$ are positive material parameters measuring the mechanical properties of the i -th family of fibers.

It is worth noticing that the anisotropic models for which the activation of the collagen fibers occurs at zero strains can be deduced from the multi-mechanism model proposed in Li [2009] if $I_{4,MM} = 1$ in Eq. (4.44). Although the capability of the multi-mechanism model to describe the recruitment of the collagen fibers at finite strains, it has to be remarked that few works in literature have employed such models Dalong et al. [2012]; furthermore, details about their numerical discretization are not provided yet.

4.3. Modeling the nearly-incompressible behavior of arteries

As it will be discussed in Ch. 5, the numerical discretization of the multi-mechanism of Eq. (4.43) by means of continuous finite element spaces may induce numerical instabilities during the simulations of arterial wall mechanics. For this reason, the multi-mechanism model considered in Tricerri et al. [2014], for which

$$\widehat{\mathcal{W}}_{sMM}^{aniso}(t) = \begin{cases} \widehat{\mathcal{W}}^{iso}(I_1(t), I_2(t)), & \text{if } \mathbb{I}_4(t) \leq \mathbb{I}_{4,MM}, \\ \widehat{\mathcal{W}}^{iso}(I_1(t), I_2(t)) + \sum_{i=1}^N \widehat{\mathcal{W}}_{s, fibers}^{(i)}(I_4^{(i)}(t), I_5^{(i)}(t)), & \text{if } \mathbb{I}_4(t) > \mathbb{I}_{4,MM}, \end{cases} \quad (4.45)$$

is considered where the strain energy function for the single family of fibers is

$$\widehat{\mathcal{W}}_{s, fibers}^{(i)}(I_4^{(i)}(t), I_5^{(i)}(t)) = \widehat{\mathcal{W}}_{EXP2-sMM}^{(i)}(I_4^{(i)}(t)) = \frac{\alpha^{(i)}}{2\gamma^{(i)}} \left(e^{\gamma^{(i)}(I_4^{(i)}(t) - I_{4,MM}^{(i)})^2} - 1 \right). \quad (4.46)$$

Both the strain energy functions in Eq. (4.45) for background material and fibrous components are referred to the reference configuration \mathcal{B}_0 . Similarly to Eq. (4.38), the strain energy function $\widehat{\mathcal{W}}_{EXP2-sMM}^{(i)}$ is polyconvex for all possible states of deformation.

In order to show the convexity properties of the strain energy functions $\widehat{\mathcal{W}}_{EXP2-RC}^{(i)}$ and $\widehat{\mathcal{W}}_{EXP2-sMM}^{(i)}$ of Eqs. (4.38) and (4.46), let us consider the uniaxial tensile and inflation tests described in Sec. 4.2.1. Let us consider a single family of fibers immersed either in the cubic domain of Fig. 4.10 and in the cylindrical geometry of Fig. 4.4. The collagen fibers are directed along the \widehat{X} direction in the cubic domain, namely $\widehat{a} = (1, 0, 0)$, and along the circumferential direction in the cylindrical geometry, that is in cylindrical coordinates $\widehat{a} = (0, 1, 0)$. In both cases, the strain energy functions will depend solely on the deformations along the directions of the fibers; in fact the fourth invariant in the two cases reads as follows:

$$I_4 = \lambda_{\widehat{X}}^2 = \widehat{\lambda}^2 \quad \text{and} \quad I_4 = \lambda_{\widehat{\Theta}}^2 = \widehat{\lambda}^2, \quad (4.47)$$

where $\widehat{\lambda}$ indicates the deformations of the body. For the multi-mechanism model, it is supposed that the deformation at which the family of fibers starts load-bearing is $\lambda_A = \widehat{\lambda} = 1.5$. The strain energy functions $\widehat{\mathcal{W}}_{EXP2-RC}^{(i)}$ and $\widehat{\mathcal{W}}_{EXP2-sMM}^{(i)}$ are represented in Fig. 4.12 and, as expected, the qualitative behavior of the two functions is similar to the one observed in Fig. 4.3. It is worth pointing out that, in the case of the multi-mechanism strain energy function $\widehat{\mathcal{W}}_{EXP2-sMM}^{(i)}$, the strain energy function is zero until the activation stretch λ_A is reached; this represents the inability of collagen fibers to respond to external forces when they are in an inactive state. A more general case of two fibers families immersed in a cubic and cylindrical domain will be presented and discussed in Ch. 5, where the numerical validation of the constitutive models under consideration is addressed. A summary of the constitutive models that are considered in this work for the cerebral arterial tissue is presented in Tabs. 4.2 and 4.3.

4.3 Modeling the nearly-incompressible behavior of arteries

In the general formulations of the strain energy functions for isotropic and anisotropic bodies of Eqs. (4.11) and (4.31), $\mathcal{U}(I_3)$ models the response of the material to volume-changing deformations. In literature, biological tissues have been modeled as incompressible materials, i.e. a material for which the incompressibility condition (see Sec. 3.2.1) is satisfied for all possible deformations, in different contexts as arterial tissue Holzzapfel and Gasser [2000] or cardiac tissue modeling Holzzapfel and Odgen

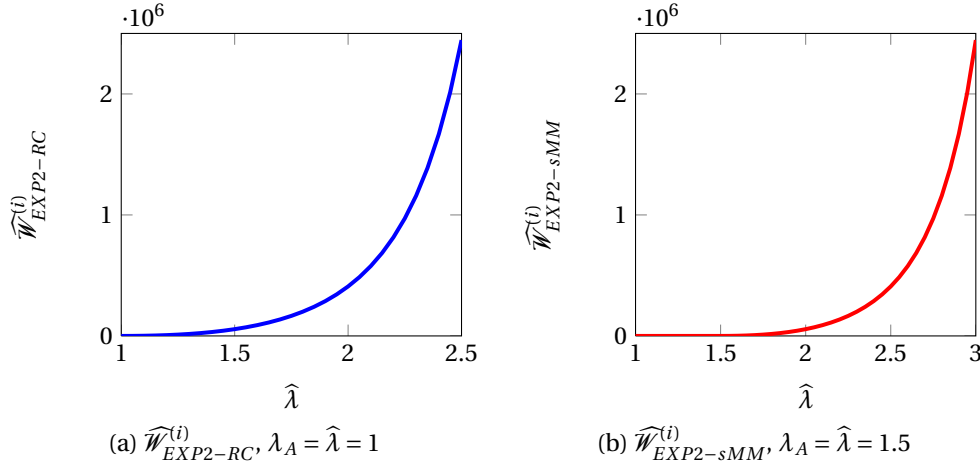


Figure 4.12: Strain energy functions $\widehat{\mathcal{W}}_{EXP2-RC}^{(i)}$ and $\widehat{\mathcal{W}}_{EXP2-sMM}^{(i)}$ [dyn / (s²cm²)] in the case of one family of collagen fibers immersed either in a cubic domain under the action of uniaxial tensile test or in a cylindrical geometry during inflation-extension tests

Model	Strain energy function	Polyconvexity for all \mathbf{F}
$\widehat{\mathcal{W}}_{SVK}^{iso}$	$\left(\frac{\lambda}{8} + \frac{\mu}{4}\right) I_1^2 - \left(\frac{3}{4}\lambda + \frac{\mu}{2}\right) I_1 - \frac{\mu}{2} I_2 + \frac{9}{8}\lambda + \frac{3}{4}\mu$	No
$\widehat{\mathcal{W}}_{MR}^{iso}$	$C_1(I_1 - 3) + C_2(I_2 - 3)$	Yes
$\widehat{\mathcal{W}}_{NH}^{iso}$	$\frac{\mu}{2}(I_1 - 3)$	Yes
$\widehat{\mathcal{W}}_{EXP1}^{iso}$	$\frac{\alpha_1}{2\gamma_1} \left(e^{\gamma_1(I_1-3)} - 1 \right)$	Yes
$\widehat{\mathcal{W}}_{EXP2}^{iso}$	$\frac{\alpha_2}{2\gamma_2} \left(e^{\gamma_2(I_1-3)^2} - 1 \right)$	Yes

Table 4.2: Constitutive models for the arterial tissue or the background material in anisotropic models

Model	Strain energy function	Polyconvexity for all \mathbf{F}
$\widehat{\mathcal{W}}_{EXP2-RC}^{(i)}$	$\frac{\alpha^{(i)}}{2\gamma^{(i)}} \left(e^{\gamma^{(i)}(I_4^{(i)}-1)^2} - 1 \right)$	Yes
$\widehat{\mathcal{W}}_{EXP2-sMM}^{(i)}$	$\frac{\alpha^{(i)}}{2\gamma^{(i)}} \left(e^{\gamma^{(i)}(I_4^{(i)}-I_{4,MM}^{(i)})^2} - 1 \right)$	Yes

Table 4.3: Constitutive models for the single family of collagen fibers. $I_{4,MM}^{(i)}$ is the activation stretch introduced in Eq. (4.46)

[2009]. For incompressible materials, the kinematic constraint $J = 1$ is inserted in the strain energy

4.3. Modeling the nearly-incompressible behavior of arteries

functions of Eqs. (4.11) and (4.31) by means of a Lagrange multiplier p ; for isotropic and anisotropic materials the strain energy function can be decomposed, respectively, as:

$$\begin{aligned}\widehat{\mathcal{W}}(I_1, I_2, I_3) &= \widehat{\mathcal{W}}^{iso}(I_1, I_2) - \mathcal{U}(I_3) = \widehat{\mathcal{W}}^{iso}(I_1, I_2) - p(J - 1) \quad \text{and} \\ \widehat{\mathcal{W}}(I_1, I_2, I_3, \mathbb{I}_4, \mathbb{I}_5) &= \widehat{\mathcal{W}}_{iso}^{aniso}(I_1, I_2) + \widehat{\mathcal{W}}_{fibers}^{aniso}(\mathbb{I}_4, \mathbb{I}_5) - \mathcal{U}(I_3) = \widehat{\mathcal{W}}_{iso}^{aniso}(I_1, I_2) + \widehat{\mathcal{W}}_{fibers}^{aniso}(\mathbb{I}_4, \mathbb{I}_5) - p(J - 1)\end{aligned}\quad (4.48)$$

where $\widehat{\mathcal{W}}^{iso}(I_1, I_2)$ and $\widehat{\mathcal{W}}^{aniso}(I_1, I_2, \mathbb{I}_4, \mathbb{I}_5)$ have been characterized in Secs. 4.2.1 and 4.2.2 and $\mathcal{U}(I_3) = -p(J - 1)$ with $J = \sqrt{I_3}$ (see Eq. (4.10)). The material scalar field p serves as a Lagrange multiplier which can be identified as the hydrostatic pressure Holzapfel [2000]; Odgen [1997]. The hydrostatic pressure field can only be determined from the balance principle of linear momentum (augmented of the necessary initial and boundary conditions) and it represents a workless reaction to the constraint $J = 1$ on the deformation field. Although the incompressibility assumption in Holzapfel and Gasser [2000], the experimental study carried out in Carew et al. [1968] showed that arterial tissue has a nearly incompressible (or quasi-incompressible) mechanical behavior during deformation processes. The mathematical description and the numerical simulation of nearly incompressible phenomena in arterial wall mechanics (and in solid mechanics in general) remains a challenging task, for instance, due to the occurrence either of locking phenomena or ill-conditioned linear systems during the numerical simulation of the arterial wall mechanics. In order to represent such mechanical behavior, different approaches have been proposed in literature (see for instance Glowinski and Le Tallec [1982, 1984]; Flory [1961]; Klass et al. [1999]). Among them, two techniques have been largely used: the so called \bar{F} -approach, described in Glowinski and Le Tallec [1982, 1984]; Elguedj et al. [2008]; Weiss et al. [1996]; Simo et al. [1985] and the technique, usually simply referred to as the volumetric-isochoric split, initially proposed in Flory [1961]. It is worth pointing out that both methodologies rely on a multiplicative decomposition of the deformation gradient \mathbf{F} and on a consequent decoupled form of the strain energy function similar to the one in Eq. (4.11); however, they strongly differ in the formulation of the mathematical problem governing the deformations of the arterial tissue under the action of external forces (see Eq. (3.26)). In the \bar{F} -approach, the nearly-incompressible condition is taken into account in the structural mechanics problem by means of the introduction of two scalar-valued functions, defined in \mathcal{B}_0 , in addition to the material displacement field $\hat{\mathbf{d}}$. The new functions represent the spatial distribution of the volume ratio J and a Lagrange multiplier to enforce the nearly-incompressibility constraint, respectively. The numerical discretization of the structural mechanics problem of Eq. (3.26), formulated according to the \bar{F} -approach, involves the use of mixed finite elements Brinkhues et al. [2013]; Auricchio et al. [2004] or high order continuous basis functions, such as e.g. in Isogeometric Analysis Elguedj et al. [2008]; Bazilevs et al. [2009], for the different vectorial and scalar fields; in addition, the functional spaces used to discretize the structural problem must satisfy the so called *Inf-Sup* condition Auricchio et al. [2004]; Quarteroni and Valli [1999b]. According to the second approach Flory [1961], the mathematical problem modeling the arterial wall mechanics is formulated solely in terms of the material displacement field $\hat{\mathbf{d}}$ Odgen [1997]; Flory [1961]; Sansour [2008]; the enforcement of the nearly incompressibility constraint relies on the penalization of the deformations of the arterial tissue that would lead to changes in its volume with respect to the one of the reference configuration \mathcal{B}_0 . The discretization and numerical solution of the resulting differential problem is usually carried out by means of standard finite elements Quarteroni and Valli [1999b] for which the formulation already satisfies the stability condition. In this work, the second approach has been preferred to the \bar{F} -approach due to the simpler numerical discretization of the structural mechanics problem and since it has already been employed with success in literature for the numerical simulations of the arterial wall mechanics, see e.g. Calvo et al. [2007]; Bazilevs et al. [2010]; Gasser et al. [2002]; Nobile

et al. [2013b]. This section is organized as follows. Sec. 4.3.1 deals with the volumetric-isochoric split of the deformation gradient \mathbf{F} and the associated additive split of the strain energy function $\widehat{\mathcal{W}}$. Sec. 4.3.2 presents a brief review of the different energy functions $\mathcal{U}(J)$ proposed in literature to describe the response of the tissue to volume-changing deformations in order to motivate the choice of $\mathcal{U}(J)$ adopted in this work. It also describes the mechanical implications related to the choice of $\mathcal{U}(J)$ on the representation of the nearly-incompressible behavior of the arterial tissue. In Sec. 4.3.3 the constitutive models introduced in Secs. 4.2.1 and 4.2.2 are reformulated according to the volumetric-isochoric split approach; moreover, the resulting definition of the mechanical stresses obtained from the new strain energy functions is critically discussed. Sec. 4.3.4 presents a three dimensional example of uniaxial tensile test on a cube in order to highlight the role of the volumetric and isochoric terms in the additive split of the strain energy function.

4.3.1 Volumetric-Isochoric split of the deformation gradient tensor

The mathematical representation of the nearly incompressible behavior of some elastic materials by means of the multiplicative decomposition of the deformation gradient tensor was firstly introduced in Flory [1961] and successfully applied within the context of finite strain elasticity (e.g. Simo et al. [1985]; Simo and Taylor [1991]). Indeed, such multiplicative decomposition was proved to reflect the correct physical behavior of isotropic materials, more specifically rubber materials, once used to define a corresponding split of the strain energy function Flory [1961]; Sansour [2008]. According to Flory [1961], the deformation gradient tensor \mathbf{F} of a continuous body \mathcal{B} is split into the product of two tensors as follows:

$$\mathbf{F} = \tilde{\mathbf{F}} \bar{\mathbf{F}} = (J^{1/3} \mathbf{I}) \bar{\mathbf{F}}, \quad (4.49)$$

where the tensor $\tilde{\mathbf{F}} := (J^{1/3} \mathbf{I})$ represents isotropic volume-changing (also referred to as volumetric) deformations, while the tensor $\bar{\mathbf{F}} := J^{-1/3} \mathbf{F}$, for which $\det(\bar{\mathbf{F}}) = 1$ describes volume-preserving (also called isochoric) deformations of \mathcal{B} . A schematic representation of the physical meaning of the two deformation tensors of Eq. (4.49) is presented in Fig. 4.13. When the deformation gradient \mathbf{F} is decomposed as in Eq. (4.49), also the right Cauchy-Green and Green-Lagrange tensors introduced in Sec. 3.1 can be split in a similar way; more precisely, introducing Eq. (4.49) into Eq. (3.8), the right Cauchy-Green tensor \mathbf{C} reads as follows:

$$\mathbf{C} = \tilde{\mathbf{C}} \bar{\mathbf{C}} = (J^{2/3} \mathbf{I}) \bar{\mathbf{C}}, \quad (4.50)$$

where the terms $\tilde{\mathbf{C}} := (J^{2/3} \mathbf{I})$ and $\bar{\mathbf{C}} = J^{-2/3} \mathbf{C}$, for which $\det(\bar{\mathbf{C}}) = 1$, have the same physical meaning of $\tilde{\mathbf{F}}$ and $\bar{\mathbf{F}}$ in Eq. (4.49), respectively. In Flory [1961], the multiplicative decomposition of \mathbf{F} is used in order to define a corresponding additive split of the strain energy function $\widehat{\mathcal{W}}$ characterizing the mechanical response of the body \mathcal{B} . More precisely, the additive split of $\widehat{\mathcal{W}}$ proposed in Flory [1961] reads as follows:

$$\widehat{\mathcal{W}} = \mathcal{U}(J) + \overline{\mathcal{W}}(\bar{\mathbf{C}}), \quad (4.51)$$

where $\overline{\mathcal{W}}(\bar{\mathbf{C}})$ indicates that the function $\overline{\mathcal{W}}$ depends on the principal invariants of $\bar{\mathbf{C}}$, for isotropic materials, and those ones of $\bar{\mathbf{C}}$ and the structural tensors \mathbf{M} in the case of anisotropic materials, see Sec. 4.3.3. As detailed in Sec. 4.3.3, when considering isotropic laws $\overline{\mathcal{W}}$ is the isochoric formulation of $\widehat{\mathcal{W}}(I_1, I_2)$, that is $\overline{\mathcal{W}} = \widehat{\mathcal{W}}^{iso}(\bar{I}_1, \bar{I}_2)$, while for anisotropic models $\overline{\mathcal{W}} = \widehat{\mathcal{W}}^{aniso}(\bar{I}_1, \bar{I}_2, \bar{I}_4, \bar{I}_5)$. From the

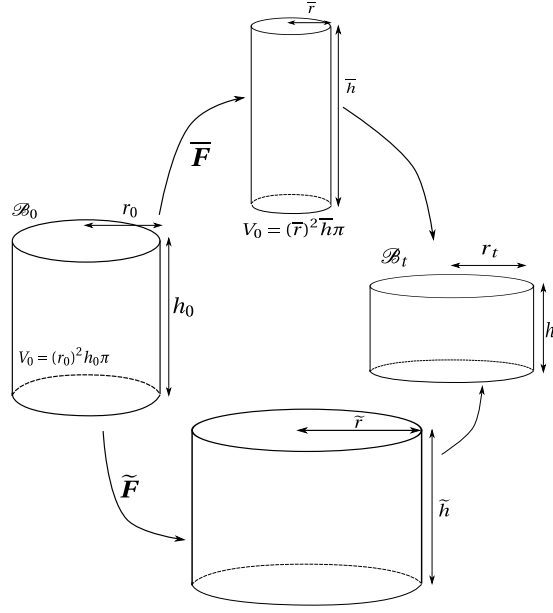


Figure 4.13: Graphical representation of the volume-changing and volume-preserving deformations described by the tensors $\tilde{\mathbf{F}}$ and $\bar{\mathbf{F}}$ in Eq. (4.49)

mechanical point of view, the isochoric strain energy function $\bar{\mathcal{W}}(\bar{\mathbf{C}})$ characterizes the mechanical response of the material for incompressible deformations, since $\det(\bar{\mathbf{C}}) = 1$, while the volumetric strain energy $\mathcal{U}(J)$ is introduced in Eq. (4.51) with the goal of penalizing the deformations of the material that would lead to changes in its volume, i.e. non volume-preserving (or compressible) deformations. From Eq. (4.51), it is clear that the mechanical response of a material is given by the mechanical contributions related to isochoric and volumetric deformations; therefore, in order to characterize the mechanical response of a material, both terms in Eq. (4.51) must be properly chosen. As discussed in Sec. 4.1, the strain energy function $\bar{\mathcal{W}}$ must satisfy the polyconvexity condition which in turn implies that both terms $\bar{\mathcal{W}}$ and \mathcal{U} in Eq. (4.51) must be polyconvex functions. Given the form of Eq. (4.51) and recalling the fact that the first Piola-Kirchhoff tensor is defined as the derivative of the strain energy function $\bar{\mathcal{W}}$ with respect to the deformation gradient tensor \mathbf{F} as in Eq. (3.41), the decoupled form of the first Piola-Kirchhoff tensor \mathbf{P} reads as follows:

$$\begin{aligned} \mathbf{P} = \tilde{\mathbf{P}} + \bar{\mathbf{P}} &= \frac{\partial \mathcal{U}(J)}{\partial \mathbf{F}} + \frac{\partial \bar{\mathcal{W}}(\bar{\mathbf{C}})}{\partial \mathbf{F}} = \\ &= 2\mathbf{F} \left(\frac{\partial \mathcal{U}(J)}{\partial \mathbf{C}} + \frac{\partial \bar{\mathcal{W}}(\bar{\mathbf{C}})}{\partial \mathbf{C}} \right), \end{aligned} \quad (4.52)$$

where $\tilde{\mathbf{P}}$ and $\bar{\mathbf{P}}$ are referred to as the volumetric and isochoric part of the first Piola-Kirchhoff tensor, respectively. The next two subsections are devoted to the characterization of the volumetric and isochoric strain energy functions and stress tensors; the choice of the volumetric strain energy function is presented in Sec. 4.3.2 while the constitutive models of Tabs. 4.2 and 4.3 are formulated in their isochoric form in Sec. 4.3.3. Secs. 4.3.2 and 4.3.3 also discuss the polyconvexity properties of the different strain energy functions.

4.3.2 Volumetric strain energy functions

In order to model the nearly-incompressible behavior of arteries, the volumetric constraint $U(J) = -p(J-1)$ in Eq. (4.48) is introduced in a relaxed form. More precisely, the general form of a volumetric strain energy function $\mathcal{U}(J)$ in Eq. (4.51) can be formulated as:

$$\mathcal{U}(J) = \kappa \widetilde{\mathcal{U}}(J), \quad (4.53)$$

where the function $\widetilde{\mathcal{U}}(J) \geq 0, \forall J > 0$, determines the response of the material to volume-changing deformations; κ , which can be interpreted as a bulk modulus, assumes the role of a user-specified penalty parameter that is suitably determined to weakly enforce the nearly-incompressible behavior of the material and the incompressible behavior of the material is recovered for $\kappa \rightarrow \infty$. It can be observed, by comparing the volumetric terms in Eqs. (4.48) and (4.53), that in the volumetric-isochoric split of $\widehat{\mathcal{W}}$ in Eq. (4.51), the Lagrange multiplier p is not present anymore and the constitutive law depends only on the deformations of \mathcal{B} . The function $\mathcal{U}(J)$ has to satisfy few requirements in order to be deemed suitable to penalize the volume-changing deformations; these are:

1. $\mathcal{U}(1) = \mathcal{U}'(1) = 0$;
2. \mathcal{U} is endowed with a unique minimum in $J = 1$;
3. $\mathcal{U}(J) \rightarrow \infty$ if $J \rightarrow 0$;
4. $\mathcal{U}(J)$ must be a convex function for all values of $J > 0$.

From the mechanical point of view, the first requirement implies that the strain energy function $\mathcal{U}(J)$ satisfies an energy- and stress-free reference configuration. As discussed in Sec. 4.2.1 this condition is important in order to guarantee that only deformations induce stresses. The last three requirements ensure that when solving the structural mechanics problem by minimizing the potential function in Eq. (4.1) the mechanical response of the body is such that the volume-changing deformations are minimized and the nearly-incompressible behavior is modeled. However, as it is discussed in Sec. 4.3.3 and e.g. in Brinkhues et al. [2013] the representation of the nearly-incompressible behavior is strongly affected by the choice of the penalization parameter κ in Eq. (4.53). As a final remark, since $\mathcal{U}(J)$ is required to be a convex function of a polyconvex function of \mathbf{F} , namely J , its polyconvexity for all possible deformations \mathbf{F} can be easily shown Dacorogna [2000]. In literature, different strain energy functions $\widetilde{\mathcal{U}}(J)$ have been proposed; see Hartmann and Neff [2003] for a review. In order to motivate the choice of the volumetric strain energy function adopted in this work, let us consider three functions $\widetilde{\mathcal{U}}(J)$ that can be found in literature: the polynomial function Li [2009]

$$\widetilde{\mathcal{U}}_1(J) = \frac{1}{2} (J-1)^2, \quad (4.54)$$

the function proposed in Simo and Taylor [1982]

$$\widetilde{\mathcal{U}}_2(J) = \frac{1}{4} ((J-1)^2 + \ln^2(J)), \quad (4.55)$$

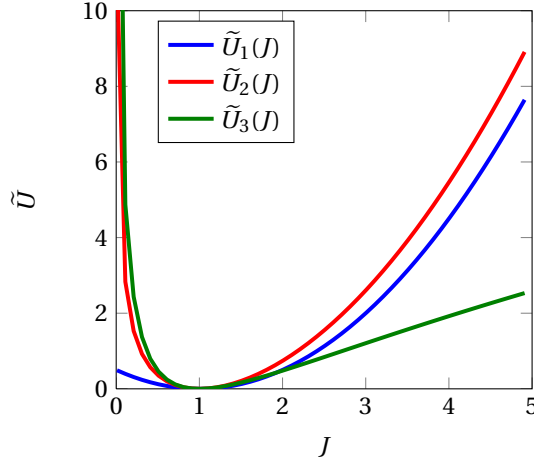


Figure 4.14: Representation of the volumetric strain energy functions [dyn / (s²cm²)] of Eqs. (4.54)-(4.56) for $0 < J \leq 5$

and the logarithmic function Calvo et al. [2007]; Balzani et al. [2012]

$$\tilde{\mathcal{U}}_3(J) = \frac{1}{2} \ln^2(J). \quad (4.56)$$

They are represented in Fig. 4.14; it can be observed that the constitutive model $\tilde{\mathcal{U}}_1(J)$ has a finite limit in the case of $J \rightarrow 0$, which violates the third requirement. Another important aspect of the volumetric function $\tilde{\mathcal{U}}_1(J)$ is that the deformations for which $J \rightarrow 0$ are not explicitly penalized in the model. In order to correct the characteristic behavior of $\tilde{\mathcal{U}}_1(J)$ for $J \rightarrow 0$, the function $\tilde{\mathcal{U}}_2(J)$ has been proposed in Simo and Taylor [1982]. Indeed, it explicitly penalizes the deformations for which $J \rightarrow 0$ and the ones that would lead to a volume ratio J different from one; it satisfies all the four requirements discussed before and provides the highest values of energy, i.e. values of penalization, among the three functions considered. On the other hand, the volumetric function $\tilde{\mathcal{U}}_3(J)$ is not convex for all the possible values of J , in particular for $J > e$. However, the function $\tilde{\mathcal{U}}_3(J)$ has been employed, for instance, in Balzani et al. [2006a,b]. Indeed, in Balzani et al. [2006a,b], the maximum value of the volume ratio J that is reported is $J = 1.03$ for which the volumetric strain energy function is still convex. To conclude, based on the considerations just presented, the volumetric strain energy function $\tilde{\mathcal{U}}_2(J)$ is employed for all the constitutive laws in this work; therefore in the following it will be assumed

$$\mathcal{U}(J) = \frac{\kappa}{4} (J-1)^2 + \ln^2(J) \quad (4.57)$$

and the corresponding volumetric stress tensor $\tilde{\mathbf{P}}$ of Eq. (4.52) reads as follows:

$$\tilde{\mathbf{P}} = 2\mathbf{F} \frac{\partial \mathcal{U}(J)}{\partial \mathbf{C}} = 2\mathbf{F} \left(\kappa \frac{\partial \tilde{\mathcal{U}}(J)}{\partial \mathbf{C}} \right) = \frac{\kappa}{2} (J^2 - J + \ln(J)) \mathbf{F}^{-T}. \quad (4.58)$$

4.3.3 Isochoric strain energy functions

In this section the isochoric strain energy function $\overline{\mathcal{W}}$ in Eq. (4.51) introduced in Flory [1961] to model nearly-incompressible materials is presented. The isochoric strain energy functions $\widehat{\overline{\mathcal{W}}}^{iso}(\bar{\mathbf{I}}_1, \bar{\mathbf{I}}_2)$ and

Model	Strain energy function	Polyconvexity for all \mathbf{F}
$\overline{\mathcal{W}}_{SVK}^{iso}$	$\left(\frac{\lambda}{8} + \frac{\mu}{4}\right)\bar{I}_1^2 - \left(\frac{3}{4}\lambda + \frac{\mu}{2}\right)\bar{I}_1 - \frac{\mu}{2}\bar{I}_2 + \frac{9}{8}\lambda + \frac{3}{4}\mu$	No
$\overline{\mathcal{W}}_{MR}^{iso}$	$C_1(\bar{I}_1 - 3) + C_2(\bar{I}_2 - 3)$	No
$\overline{\mathcal{W}}_{NH}^{iso}$	$\frac{\mu}{2}(\bar{I}_1 - 3)$	Yes
$\overline{\mathcal{W}}_{EXP1}^{iso}$	$\frac{\alpha_1}{2\gamma_1}\left(e^{\gamma_1(\bar{I}_1-3)} - 1\right)$	Yes
$\overline{\mathcal{W}}_{EXP2}^{iso}$	$\frac{\alpha_2}{2\gamma_2}\left(e^{\gamma_2(\bar{I}_1-3)^2} - 1\right)$	Yes

Table 4.4: Isochoric formulation of the constitutive models of Sec. 4.2.1.

$\widehat{\mathcal{W}}^{aniso}(\bar{I}_1, \bar{I}_2, \bar{I}_4, \bar{I}_5)$ for isotropic and anisotropic laws, respectively, are presented together with their polyconvexity properties which are also compared to those of the constitutive models of Secs. 4.2.1 and 4.2.2. The expressions of the isochoric parts of the first Piola-Kirchhoff tensors for the different constitutive models are also detailed.

Isochoric isotropic strain energy functions

As mentioned in Sec. 4.3.1, the isochoric strain energy function $\overline{\mathcal{W}}(\bar{\mathbf{C}})$ depends on the isochoric deformations. In the case of isotropic models, $\overline{\mathcal{W}}$ is an isotropic tensor function; therefore, as discussed in Sec. 4.2.1, it can be formulated in terms of the principal invariants of $\bar{\mathbf{C}}$ as follows:

$$\overline{\mathcal{W}}^{iso}(\bar{\mathbf{C}}) = \overline{\mathcal{W}}^{iso}(\bar{I}_1, \bar{I}_2, \bar{I}_3) = \overline{\mathcal{W}}^{iso}(\bar{I}_1, \bar{I}_2) \quad (4.59)$$

where, in the last equality, the dependency of $\overline{\mathcal{W}}$ on \bar{I}_3 has been dropped since $\det(\bar{\mathbf{C}}) = 1$ as in Eq. (4.50). The principal invariants $(\bar{I}_1, \bar{I}_2, \bar{I}_3)$ of $\bar{\mathbf{C}}$, also called the modified principal invariants of $\bar{\mathbf{C}}$, are defined, respectively, as:

$$\begin{aligned} \bar{I}_1 &= \text{Tr}(\bar{\mathbf{C}}) = J^{-2/3} \text{Tr}(\mathbf{C}) = J^{-2/3} I_1, \\ \bar{I}_2 &= \frac{1}{2} [\text{Tr}^2(\bar{\mathbf{C}}) - \text{Tr}(\bar{\mathbf{C}}^2)] = J^{-4/3} \frac{1}{2} [\text{Tr}^2(\mathbf{C}) - \text{Tr}(\mathbf{C}^2)] = J^{-4/3} I_2, \text{ and} \\ \bar{I}_3 &= \det(\bar{\mathbf{C}}) = J^{-2} \det(\mathbf{C}) = 1. \end{aligned} \quad (4.60)$$

According to the volumetric-isochoric approach described in Flory [1961], the isotropic constitutive laws of Sec. 4.2.1 are reformulated in terms of the modified invariants of $\bar{\mathbf{C}}$; their new formulation and polyconvexity properties are summarized in Tab. 4.4. It is worth pointing out that, as expected, the St. Venant-Kirchhoff model remains a non-polyconvex model. On the other hand, the isochoric formulation of the Mooney-Rivlin model leads to a strain energy function that is not polyconvex for all possible \mathbf{F} (see Tab. 4.2). This is due to the fact that the second modified invariant \bar{I}_2 is not a polyconvex function for all possible deformations Hartmann and Neff [2003]. However, both the St.

4.3. Modeling the nearly-incompressible behavior of arteries

Venant-Kirchhoff and the Mooney-Rivlin in the isochoric form have been employed in literature to describe either the arterial tissue Triccerri et al. [2014] or the elastin in an anisotropic model Calvo et al. [2007]. On the contrary, the first modified invariant of $\bar{\mathbf{C}}$ is a polyconvex function of \mathbf{F} , therefore, the polyconvexity properties of the neo-Hookean, first and second order exponential laws remain unchanged when they are formulated in the isochoric form. The isochoric first Piola-Kirchhoff tensor $\bar{\mathbf{P}} = \bar{\mathbf{P}}^{iso}$ can be determined from Eq. (4.52), as follows:

$$\begin{aligned} \bar{\mathbf{P}} = \bar{\mathbf{P}}^{iso} &= 2\mathbf{F} \frac{\partial \bar{\mathcal{W}}^{iso}(\bar{I}_1, \bar{I}_2)}{\partial \mathbf{C}} = 2\mathbf{F} \left(\frac{\partial \bar{\mathcal{W}}^{iso}(\bar{I}_1, \bar{I}_2)}{\partial \bar{I}_1} \frac{\partial \bar{I}_1}{\partial \mathbf{C}} + \frac{\partial \bar{\mathcal{W}}^{iso}(\bar{I}_1, \bar{I}_2)}{\partial \bar{I}_2} \frac{\partial \bar{I}_2}{\partial \mathbf{C}} \right) = \\ &= 2 \frac{\partial \bar{\mathcal{W}}^{iso}}{\partial \bar{I}_1} J^{-2/3} \left(\mathbf{F} - \frac{1}{3} I_1 \mathbf{F}^{-T} \right) + \\ &+ 2 \frac{\partial \bar{\mathcal{W}}^{iso}}{\partial \bar{I}_2} J^{-2/3} \left(\bar{I}_1 \mathbf{F} - \frac{1}{3} J^{-2/3} I_1^2 \mathbf{F}^{-T} - J^{-2/3} \mathbf{F} \mathbf{C} - \frac{1}{3} \text{Tr}(\mathbf{C}^2) \mathbf{F}^{-T} \right), \end{aligned} \quad (4.61)$$

where the standard results of derivation of isotropic tensor functions have been employed Holzapfel [2000]; Odgen [1997].

Isochoric anisotropic strain energy functions

The volumetric-isochoric split described in Sec. 4.3.1 can be employed to describe the nearly-incompressible behavior of arteries also when considering anisotropic constitutive models for the vessel wall. However, some controversy exists in the literature (see Sansour [2008]; Helfenstein et al. [2010]) on the application of the volumetric-isochoric split of \mathbf{F} , and the consequent additive split of $\bar{\mathcal{W}}$, in the case of anisotropic models. Hereafter, the isochoric form of the constitutive models of Sec. 4.2.2 is presented; afterwards, the different points of view that can be found in literature regarding the mathematical modeling of the nearly-incompressible behavior of arteries by means of anisotropic models are discussed.

The isochoric strain energy function $\bar{\mathcal{W}}$ in Eq. (4.51) in the case of anisotropic models with N families of fibers reads

$$\begin{aligned} \bar{\mathcal{W}}^{aniso}(\bar{\mathbf{C}}) &= \bar{\mathcal{W}}^{aniso}(\bar{I}_1, \bar{I}_2, \bar{\mathbb{I}}_4, \bar{\mathbb{I}}_5) \\ &= \begin{cases} \bar{\mathcal{W}}_{iso}^{aniso}(\bar{I}_1, \bar{I}_2), & \text{if } \bar{\mathbb{I}}_4 \leq \mathbb{I}_{4,A}, \\ \bar{\mathcal{W}}_{iso}^{aniso}(\bar{I}_1, \bar{I}_2) + \bar{\mathcal{W}}_{fibers}^{aniso}(\bar{\mathbb{I}}_4, \bar{\mathbb{I}}_5), & \text{if } \bar{\mathbb{I}}_4 > \mathbb{I}_{4,A}, \end{cases} \end{aligned} \quad (4.62)$$

where $\bar{\mathbb{I}}_4 = \left\{ \bar{I}_4^{(i)} \right\}_{i=1}^N$ and $\bar{\mathbb{I}}_5 = \left\{ \bar{I}_5^{(i)} \right\}_{i=1}^N$ are the set of the modified pseudo invariants of $\bar{\mathbf{C}}$ and $\mathbf{M}^{(i)}$ defined, respectively, as

$$\bar{I}_4^{(i)} = \bar{\mathbf{C}} : \mathbf{M}^{(i)} \quad (4.63)$$

and

$$\bar{I}_5^{(i)} = \bar{\mathbf{C}}^2 : \mathbf{M}^{(i)}, \quad (4.64)$$

with $\mathbf{M}^{(i)}$ being the structural tensor defined in Sec. 4.2.2. The isochoric form of the second order

Model	Strain energy function	Polyconvexity for all \mathbf{F}
$\widehat{\mathcal{W}}_{EXP2-RC}^{(i)}$	$\frac{\alpha^{(i)}}{2\gamma^{(i)}} \left(e^{\gamma^{(i)}(\bar{I}_4^{(i)}-1)^2} - 1 \right)$	Yes
$\widehat{\mathcal{W}}_{EXP2-sMM}^{(i)}$	$\frac{\alpha^{(i)}}{2\gamma^{(i)}} \left(e^{\gamma^{(i)}(\bar{I}_4^{(i)}-I_{4,MM}^{(i)})^2} - 1 \right)$	Yes

Table 4.5: Constitutive models for the single family of collagen fibers.

exponential law along the fibers direction of Tab. 4.3 is presented in Tab. 4.5. As shown in Balzani [2006]; Hartmann and Neff [2003]; Schröder and Neff [2003], the isochoric strain energy function in Tab. 4.5 are polyconvex for all \mathbf{F} being convex functions of the polyconvex modified pseudo invariant $\bar{I}_4^{(i)}$. The isochoric part of the first Piola-Kirchhoff stress tensor in Eq. (4.52) reads

$$\bar{\mathbf{P}} = \bar{\mathbf{P}}^{aniso} = \begin{cases} \bar{\mathbf{P}}_{iso}^{aniso}, & \text{if } \bar{\mathbb{I}}_4 \leq \mathbb{I}_{4,A}, \\ \bar{\mathbf{P}}_{iso}^{aniso} + \sum_{i=1}^N \bar{\mathbf{P}}_{fibers}^{(i)}, & \text{if } \bar{\mathbb{I}}_4 > \mathbb{I}_{4,A}, \end{cases} \quad (4.65)$$

where $\bar{\mathbf{P}}_{iso}^{ti} = \bar{\mathbf{P}}^{iso}$ in Eq. (4.61) and the isochoric first Piola-Kirchhoff stress tensor for the single family of fibers is defined as:

$$\bar{\mathbf{P}}_{fibers}^{(i)} = 2\mathbf{F} \left(\frac{\partial \bar{\mathcal{W}}_{fibers}^{(i)}}{\partial \mathbf{C}} \right) = 2\mathbf{F} \left(\frac{\partial \bar{\mathcal{W}}_{fibers}^{(i)}}{\partial \bar{I}_4^{(i)}} \frac{\partial \bar{I}_4^{(i)}}{\partial \mathbf{C}} \right) = 2 \frac{\partial \bar{\mathcal{W}}_{fibers}^{(i)}}{\partial \bar{I}_4^{(i)}} J^{-2/3} \left(\mathbf{F}\mathbf{M} - \frac{1}{3} I_4^{(i)} \mathbf{F}^{-T} \right). \quad (4.66)$$

When modeling fiber-reinforced materials, the fibers that are mechanically active (see Sec. 4.2.2) contribute to the overall mechanical response only along their local orientation that is described by the spatial vectorial field \mathbf{a}_t Holzzapfel [2000]. However, from Eq. (4.66), it can be observed that when the modified fourth invariant $\bar{I}_4^{(i)}$ is considered in the strain energy functions of Tab. 4.5 due to the term $\frac{1}{3} I_4^{(i)} \mathbf{F}^{-T}$, the mechanical response of the single family of fibers is not solely along the local orientation of the single family of fibers. Based on this observation, some authors, namely Sansour [2008]; Helfenstein et al. [2010], have proposed a different form of the isochoric strain energy function $\bar{\mathcal{W}}$ from the one in Eq. (4.62), that is

$$\begin{aligned} \bar{\mathcal{W}}^{aniso}(\bar{\mathbf{C}}) &= \bar{\mathcal{W}}^{aniso}(\bar{I}_1, \bar{I}_2, \mathbb{I}_4, \mathbb{I}_5) \\ &= \begin{cases} \bar{\mathcal{W}}_{iso}^{aniso}(\bar{I}_1, \bar{I}_2), & \text{if } \mathbb{I}_4 \leq \mathbb{I}_{4,A}, \\ \bar{\mathcal{W}}_{iso}^{aniso}(\bar{I}_1, \bar{I}_2) + \widehat{\mathcal{W}}_{fibers}^{aniso}(\mathbb{I}_4, \mathbb{I}_5), & \text{if } \mathbb{I}_4 > \mathbb{I}_{4,A}, \end{cases} \end{aligned} \quad (4.67)$$

where multiplicative splitting of the right Cauchy-Green tensor \mathbf{C} is considered only in the definition of \bar{I}_1 and \bar{I}_2 . In this work, for consistency with the isotropic case where the additive form strain energy function in Eq. (4.51) was formulated starting from the multiplicative decomposition of \mathbf{F} , the formulation of Eq. (4.62) has been preferred to the one in Eq. (4.67). In addition, such approach has already been used in literature for the modeling and numerical simulations of arteries Bazilevs et al. [2010]; Crosetto et al. [2012]. However, as it is discussed in Sec. 4.3.4, it is worth pointing out that

the choice of the volumetric-isochoric decomposition of the strain energy function $\overline{\mathcal{W}}^{aniso}$ induces relevant effects on the mathematical modeling of the nearly-incompressible behavior of arteries.

4.3.4 Remarks on the volumetric-isochoric split

This section addresses the relevance of the adequate choice of the penalization parameter κ on the mathematical modeling of the nearly-incompressible behavior of arteries. More precisely, the goal of the present analysis is to show that the quasi-incompressible behavior of the vessel wall can be effectively represented by means of the approach adopted in this work only when the order of magnitude of the penalization parameter is well-balanced in relation with the one of the characteristic material parameter of the constitutive model that is considered to describe the arterial tissue; therefore, it provides an indication of the adequate value of κ that should be used in the volumetric strain energy function of Eq. (4.48). The constitutive law describing the tissue (i.e. isotropic or anisotropic) influences the choice of the penalization parameter κ . In order to highlight the influence on the choice of κ of the constitutive model, the current analysis has been carried out either in the case of isotropic and anisotropic model; furthermore, in the latter case, the effect on the choice of κ of the two possible additive splits of the strain energy function $\widehat{\mathcal{W}}^{aniso}$, see Eqs. (4.62) and (4.67), is discussed. As a representative example, the static uniaxial tensile test on a cubic domain that has been described in Sec. 4.2.1 is considered. In this section, for convenience, the equations governing the deformation of the cubic domain in Fig. 4.2 are formulated in their spatial form; therefore, the balance principle of linear momentum reads as follows:

$$\begin{cases} \nabla \cdot \boldsymbol{\sigma} = \mathbf{0} & \text{in } \mathcal{B}_t, \\ \boldsymbol{\sigma} \mathbf{n} = \mathbf{s} & \text{on } \Gamma_{N,t}, \\ \mathbf{d} = \mathbf{0} & \text{on } \Gamma_{D,t}, \end{cases} \quad (4.68)$$

where \mathbf{d} is the spatial displacement field defined on the current configuration, $\Gamma_{N,t}$ is the boundary face of \mathcal{B}_t on which the tensile stress is applied (see Fig. 4.2) and $\Gamma_{D,t}$ is the boundary face of \mathcal{B}_t opposite to $\Gamma_{N,t}$ where homogeneous Dirichlet boundary conditions are imposed. The deformation of the cube along the direction of the applied load $\mathbf{s} = s\mathbf{E}_1$ is indicated by $\lambda_{\widehat{\chi}}$; in the static uniaxial tensile test, the only non-zero component of the Cauchy stress tensor $\boldsymbol{\sigma}$ is σ_{xx} for which $\sigma_{xx} = s$. In order to evaluate the effectiveness of a value of κ in Eq. (4.48), the stress component σ_{xx} obtained under the incompressibility assumption (i.e. when the strain energy function $\widehat{\mathcal{W}}$ is decoupled in the form of Eq. (4.48)) is compared with the one resulting from the additive volumetric isochoric split of $\widehat{\mathcal{W}}$. The material parameters of the constitutive laws considered in this section are consistent, in terms of order of magnitude, with the ones that can be found in Torii et al. [2008]; Delfino et al. [1997] for the cerebral arterial tissue; however, their values have been chosen as representative examples without aiming at representing the real mechanical properties of the tissue.

Firstly, let us assume that the cube in Fig. 4.2 is described by means of an isotropic model; for instance, the first order exponential model. The material parameters in Eq. (4.16) are $\alpha_1 = 4.47 \cdot 10^5$ dyn/cm² and $\gamma_1 = 8.35$, respectively. In the incompressible case, the deformation gradient \mathbf{F} admits the diagonal form $\mathbf{F} = \text{diag}\left(\lambda_{\widehat{\chi}}, \sqrt{\frac{1}{\lambda_{\widehat{\chi}}}}, \sqrt{\frac{1}{\lambda_{\widehat{\chi}}}}\right)$ from which the Cauchy stress tensor can be deduced. In particular, given the value of the applied tensile stress s , in order to determine σ_{xx} and the hydrostatic

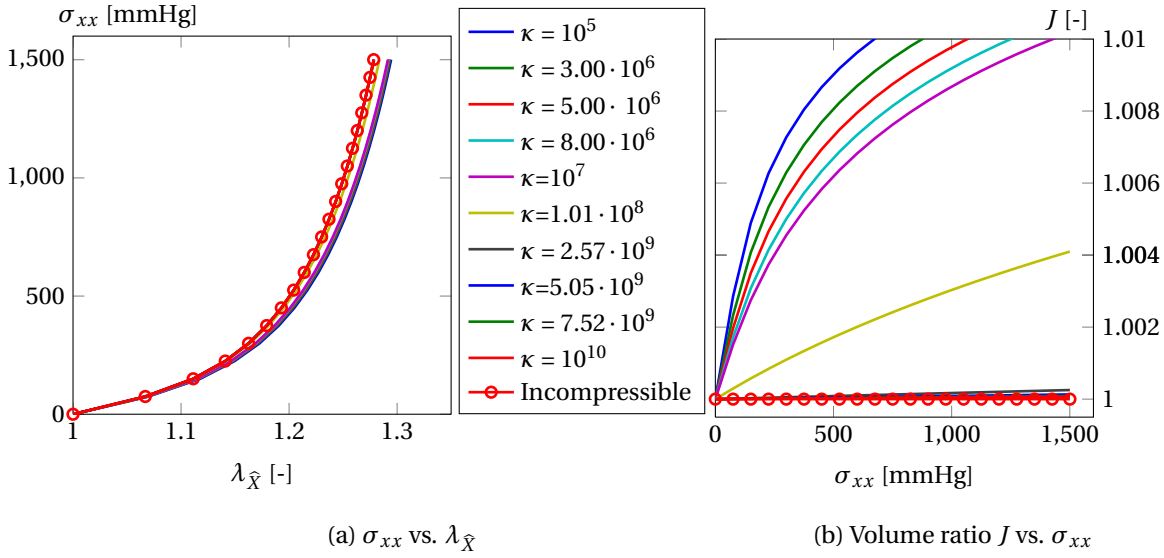


Figure 4.15: Stress-strain relation $\sigma_{xx} = \sigma_{xx}(\lambda_{\hat{X}})$ in the incompressible and nearly-incompressible case for the isotropic model EXP1; κ [dyn / cm²]

pressure field p in Eq. (4.48), the following nonlinear system has to be solved

$$\begin{cases} \sigma_{xx} = \alpha_1 e^{\gamma_1(I_1-3)} \lambda_{\hat{X}}^2 - p = s \\ \sigma_{yy} = \alpha_1 e^{\gamma_1(I_1-3)} \frac{1}{\lambda_{\hat{X}}} - p = 0, \end{cases} \quad (4.69)$$

where the second equation is due to fact that no external loads are applied on the lateral surface of the cube in Fig. 4.2 and $\left(I_1 = \lambda_{\hat{X}}^2 + \frac{2}{\lambda_{\hat{X}}}\right)$. By eliminating the hydrostatic pressure field from the second equation, for a given value of s , the stress-strain relation

$$\sigma_{xx}(\lambda_{\hat{X}}) - s = \alpha_1 e^{\gamma_1(I_1-3)} \left(\lambda_{\hat{X}}^2 - \frac{1}{\lambda_{\hat{X}}} \right) - s = 0 \quad (4.70)$$

is obtained; it is represented in Fig. 4.15(a). In the nearly incompressible case, the deformation gradient F and the right Cauchy-Green tensor C can be written as follows:

$$F = J^{1/3} \begin{pmatrix} \lambda_{\hat{X}} & 0 & 0 \\ 0 & \sqrt{\frac{1}{\lambda_{\hat{X}}}} & 0 \\ 0 & 0 & \sqrt{\frac{1}{\lambda_{\hat{X}}}} \end{pmatrix}, \quad \text{and} \quad C = J^{2/3} \begin{pmatrix} \lambda_{\hat{X}}^2 & 0 & 0 \\ 0 & \frac{1}{\lambda_{\hat{X}}} & 0 \\ 0 & 0 & \frac{1}{\lambda_{\hat{X}}} \end{pmatrix}. \quad (4.71)$$

The nonlinear system that governs the nearly-incompressible deformations reads

$$\begin{cases} \sigma_{xx} = \alpha_1 e^{\gamma_1(\bar{I}_1-3)} J^{-5/3} \left(J^{2/3} \lambda_{\hat{X}}^2 - \frac{1}{3} I_1 \right) + \frac{\kappa}{2} \left(J - 1 + \frac{\ln(J)}{J} \right) = s \\ \sigma_{yy} = \alpha_1 e^{\gamma_1(\bar{I}_1-3)} J^{-5/3} \left(\frac{J^{2/3}}{\lambda_{\hat{X}}} - \frac{1}{3} I_1 \right) + \frac{\kappa}{2} \left(J - 1 + \frac{\ln(J)}{J} \right) = 0, \end{cases} \quad (4.72)$$

4.3. Modeling the nearly-incompressible behavior of arteries

where $\bar{I}_1 = \left(\lambda_{\hat{X}}^2 + \frac{2}{\lambda_{\hat{X}}} \right)$ and $I_1 = J^{2/3} \bar{I}_1$. For each value of tensile stress s and penalization parameter κ , the stress-strain relation $\sigma_{xx} = \sigma_{xx}(\lambda_{\hat{X}})$ and corresponding value of the volume ratio J are represented in Fig. 4.15, respectively. It can be observed that for high values of tensile stress, namely $\sigma_{xx} > 500$ mmHg, and for κ lower than 10^8 , the nearly-incompressible form of the strain energy function models a material that is “softer” than the one modeled by the strain energy function in the incompressible form. In addition, the approximation of the incompressibility constraint $J = 1$ is quite poor, as shown in Fig. 4.15(b). However, a better representation of the nearly-incompressibility constraint is obtained if the order of magnitude of the bulk modulus is “large enough” compared to one of the highest parameter of the constitutive model, i.e. α_1 .

Let us now consider an anisotropic model; in particular let us suppose that only one family of fibers for which $\hat{\mathbf{a}} = (1, 0, 0)$ in \mathcal{B}_0 is immersed in the background material. Since a uniaxial tensile stress is considered and the direction of the applied load is parallel to the local alignment of the fibers, it can be shown that $\mathbf{a}_t = (1, 0, 0)$ in \mathcal{B}_t . In this work, a first order exponential law describes the elastin and the second order exponential law $\widehat{W}_{EXP2-RC}^{(i)}$ of Eq. (4.38) describes the single family of collagen fibers. The material parameters are $\alpha_1 = 4.47 \cdot 10^4$ and $\alpha^{(1)} = 10^5$ dyn/cm² while $\gamma_1 = 0.35$ and $\gamma^{(1)} = 2.5$. Under the incompressibility assumption, $I_4 = \lambda_{\hat{X}}^2$ and the stress-strain relation $\sigma_{xx}(\lambda_{\hat{X}})$ is determined by the nonlinear system:

$$\begin{cases} \sigma_{xx} = \alpha_1 e^{\gamma_1(I_1-3)} \lambda_{\hat{X}}^2 + 2\alpha^{(1)} e^{\gamma^{(1)}(I_4-1)^2} \lambda_{\hat{X}}^2 - p = s \\ \sigma_{yy} = \alpha_1 e^{\gamma_1(I_1-3)} \lambda_{\hat{X}}^2 - p = 0, \end{cases} \quad (4.73)$$

where it is worth pointing out that in the definition of the stress σ_{yy} there is no mechanical contribution from the family of fibers since they respond only to deformations along the $\hat{X} = x$ axis. The stress-strain relation $\sigma_{xx}(\lambda_{\hat{X}})$ is represented in Figs. (4.16) and (4.17). In the nearly incompressible case, if the decomposition of Eq. (4.62) is considered, for which $\bar{I}_4 = \lambda_{\hat{X}}^2$, the nonlinear system of Eq. (4.73) transforms into:

$$\begin{cases} \alpha_1 e^{\gamma_1(\bar{I}_1-3)} J^{-5/3} \left(J^{2/3} \lambda_{\hat{X}}^2 - \frac{1}{3} I_1 \right) + 2\alpha^{(1)} (\bar{I}_4 - 1) e^{\gamma^{(1)}(\bar{I}_4-1)^2} J^{-5/3} \left(\lambda_{\hat{X}}^2 - \frac{1}{3} I_4 \right) + \frac{\kappa}{2} \left(J - 1 + \frac{\ln(J)}{J} \right) = s \\ \alpha_1 e^{\gamma_1(\bar{I}_1-3)} J^{-5/3} \left(\frac{J^{2/3}}{\lambda_{\hat{X}}} - \frac{1}{3} I_1 \right) + 2\alpha^{(1)} (\bar{I}_4 - 1) e^{\gamma^{(1)}(\bar{I}_4-1)^2} J^{-5/3} \left(-\frac{1}{3} I_4 \right) + \frac{\kappa}{2} \left(J - 1 + \frac{\ln(J)}{J} \right) = 0, \end{cases} \quad (4.74)$$

while if the decomposition of Eq. (4.67) is adopted Eq. (4.73) transforms into:

$$\begin{cases} \alpha_1 e^{\gamma_1(\bar{I}_1-3)} J^{-5/3} \left(J^{2/3} \lambda_{\hat{X}}^2 - \frac{1}{3} I_1 \right) + 2\alpha^{(1)} (I_4 - 1) e^{\gamma^{(1)}(I_4-1)^2} \lambda_{\hat{X}}^2 + \frac{\kappa}{2} \left(J - 1 + \frac{\ln(J)}{J} \right) = t \\ \alpha_1 e^{\gamma_1(\bar{I}_1-3)} J^{-5/3} \left(\frac{J^{2/3}}{\lambda_{\hat{X}}} - \frac{1}{3} I_1 \right) + \frac{\kappa}{2} \left(J - 1 + \frac{\ln(J)}{J} \right) = 0. \end{cases} \quad (4.75)$$

The two systems in Eqs. (4.74) and (4.75) differ in the mechanical contribution of the collagen fibers to the stresses σ_{xx} and σ_{yy} . More precisely, if the modified pseudo invariant \bar{I}_4 is considered, due to the fact that it is related to isochoric changes, the term $\frac{1}{3} J^{-5/3} I_4$ appears in the definition of σ_{yy} . Therefore, from the mechanical point of view, the term $\frac{1}{3} J^{-5/3} I_4$ can be viewed as a consequence of the kinematic

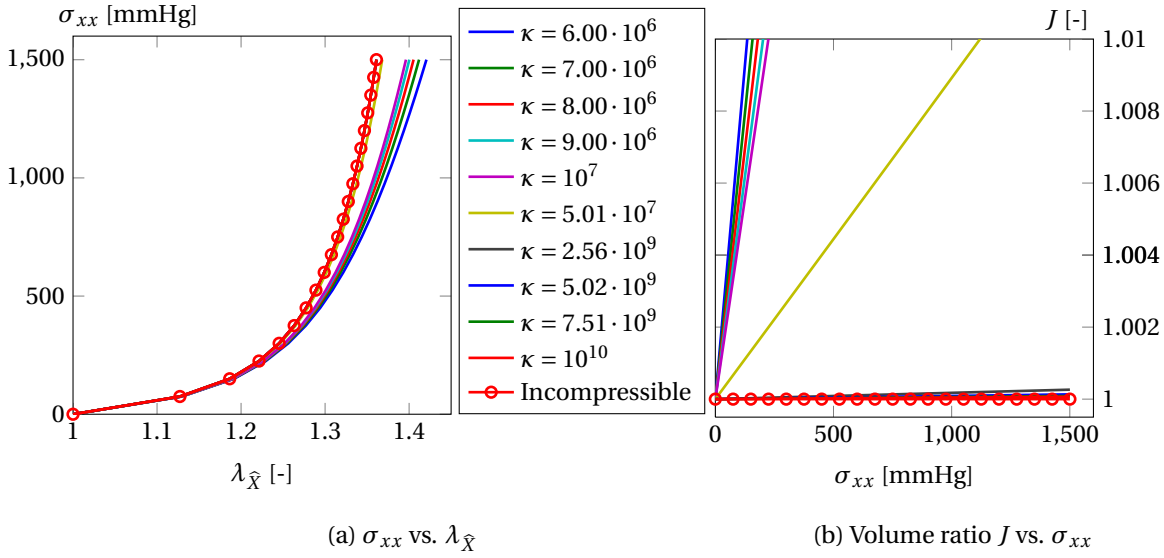


Figure 4.16: Anisotropic model (EXP1,EXP2-RC) with isochoric formulation of the fourth invariant $\bar{I}_4 = \bar{I}_4(\bar{\mathbf{C}})$

condition $\det(\bar{\mathbf{C}}) = 1$. On the other hand, similarly to Eq. (4.73) the contribution to the σ_{yy} stress of the collagen fibers is zero when the isochoric invariants are taken into account only in the isotropic part of the strain energy and I_4 is considered. The stress-strain relations and the volume ratios J associated to the two decompositions in Eqs. (4.62) and (4.67) for different values of the applied tensile stress are represented in Fig. 4.16 and Fig. 4.17, respectively. Similarly to what has been observed in Fig. 4.15, the nearly-incompressible behavior of the material can be effectively modeled only when κ is at least two orders of magnitude higher than the highest material parameters of the isochoric part of the strain energy function. However, as observed in Fig. 4.17, lower values of κ can be employed if the fourth invariant I_4 is considered instead of the modified fourth invariant \bar{I}_4 . This is due to the fact that, if the fourth invariant is adopted, the penalization term will be affecting only the deformation of the isotropic part of the strain energy function $\bar{\mathcal{W}}_{iso}^{aniso}(\bar{I}_1, \bar{I}_2)$ in which, for anisotropic materials, the order of magnitude of the highest material parameters is usually lower than the parameter characterizing the single family of collagen fibers.

4.3. Modeling the nearly-incompressible behavior of arteries

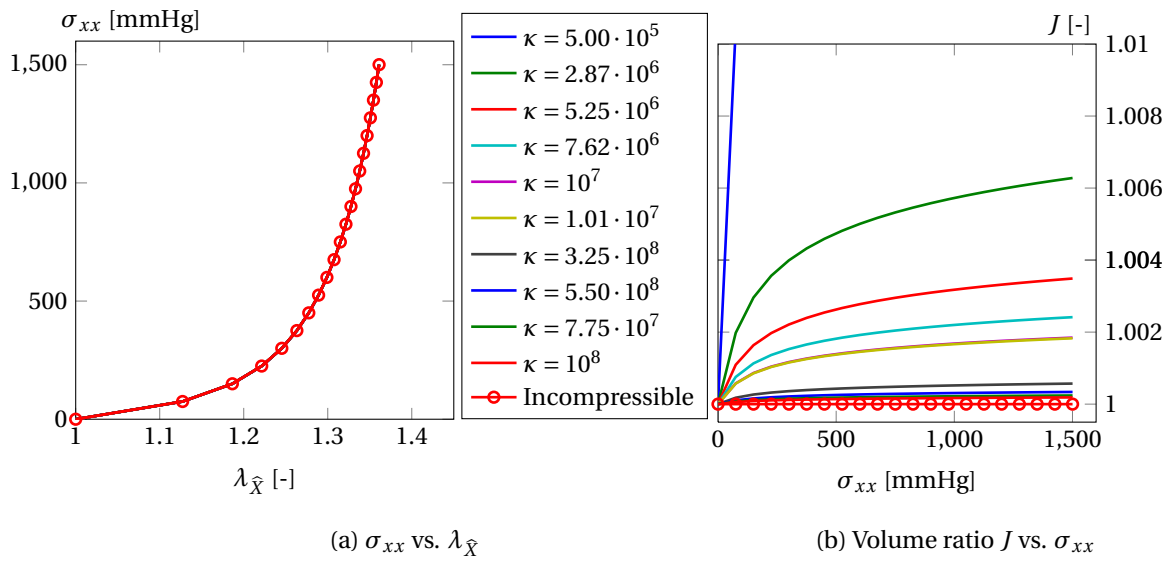


Figure 4.17: Anisotropic model (EXP1,EXP2-RC) with no isochoric formulation of the fourth invariant $I_4 = I_4(C)$

5 Numerical validation of constitutive models for the arterial tissue

The numerical simulation of the deformations of the arterial tissue under different loading configurations (namely physiological and pathological) aims at improving the current clinical knowledge by offering a flexible and reliable tool to the physicians. The characterization of the mechanical properties of the arterial tissue by means of experimental mechanical tests and the numerical validation with respect to experimental data of adequate constitutive models such as those of Ch. 4, represent two important steps toward the enhanced understanding of the arterial wall mechanics. Uniaxial or biaxial tests are usually employed to measure the mechanical properties of the arterial tissue, see e.g. Monson [2001]; Kenneth et al. [2008]; Sommer et al. [2010]; Bell et al. [2013]; simultaneously, numerical simulations of balloon angioplasty, arterial clamping, or inflation tests are carried out to analyze the capability of certain constitutive models to describe both healthy and unhealthy vessel walls Triccerri et al. [2014]; Calvo et al. [2007]; Dalong et al. [2012].

This chapter deals with the numerical validation of the isotropic and anisotropic constitutive models presented in Ch. 4 using finite elements simulations of static inflation tests on a cylindrical geometry representing a specimen of anterior cerebral artery. The experimental measurements of the stress-strain relation reported in Scott et al. [1972] are considered in order to estimate the material parameters for the different constitutive laws. The constitutive models employed in the numerical simulations are chosen among the ones discussed in Ch. 4 based on their capability to fit the experimental data. For each constitutive model, the stress-strain relation obtained from the numerical simulations is compared with the one resulting from the nonlinear approximation of the experimental data; finally, the volumetric-isochoric split to represent the nearly-incompressible behavior of arteries, presented in Sec. 4.3, is critically discussed based on the approximation of the incompressibility kinematic constraint.

This chapter is organized as follows. Sec. 5.1 deals with the numerical discretization of the structural mechanics problem governing the deformations of the arterial tissue; with this aim, the finite element method is briefly recalled and the discretization of the nonlinear problem by means of continuous piecewise polynomial basis functions is discussed. The resulting discrete nonlinear problem is solved by means of the Newton-Raphson method. In this regard, Sec. 5.1 also presents the linearization of the nonlinear discrete problem. Sec. 5.2 discusses different aspects related to the finite element numerical simulations of arterial tissue mechanics. More precisely, the topics addressed in Sec. 5.2 range from the efficient implementation of highly nonlinear models in a finite element library such as `LifeV` to numerical issues that may arise during numerical simulations of arterial wall mechanics. Sec. 5.3 shows the numerical validation of the implementation of the nonlinear constitutive models that will

describe the arterial tissue in Sec. 5.4. Finally, Sec. 5.4 addresses the numerical validation of some of the constitutive models introduced in Ch. 4 with respect to experimental measurements.

5.1 Numerical approximation: the Finite Element Method

The finite element method Quarteroni and Valli [1999b]; Hughes [2000]; Zienkiewicz et al. [2000]; Bonet and Wood [1997] is largely used in literature for the numerical simulations of the mechanics of different types of biological tissues, such as, for instance, cardiac tissue Rossi et al. [2013], ligaments Calvo et al. [2007], and arterial tissue Gasser and Holzapfel [2006]; Balzani et al. [2006b]. This section describes the numerical approximation of a general structural mechanics problem formulated in the strong form (i.e. in its differential form as problem (4.68)) by means of the finite element method; therefore, the weak (variational) formulation associated to the strong form and its numerical approximation are derived. When highly nonlinear laws such as those presented in Ch. 4 are used to model the arterial tissue, the numerical simulation of arterial wall mechanics involves the solution of highly nonlinear problems; with this aim, incremental/iterative solution techniques, such as the Newton-Raphson method, are applied to solve a sequence of linearized problems. Sec. 5.1.3 deals with the linearization of the nonlinear system of equations resulting from the discretization of the weak formulation of the differential problem.

5.1.1 Strong and weak formulations of the structural mechanics problem

In this section, the structural mechanics problem is formulated for a generic continuous body \mathcal{B} representing a specimen of arterial tissue. In particular, since the mechanical properties of the vessel wall are commonly measured by means of static mechanical tests (see e.g. Kenneth et al. [2008]; Sommer et al. [2010]), static structural mechanics problems are discussed here. Let us consider a continuous body \mathcal{B} whose boundary is indicated as $\partial\mathcal{B}$. In the absence of volume forces, such as gravity, the deformations of \mathcal{B} under the action of external forces are described by the static balance principle of linear momentum (see Eq. (3.26)); as commonly done within the context of solid mechanics Holzapfel [2000], the structural mechanics problem is set in its material form and endowed with suitable boundary conditions; consequently it reads:

$$\text{find } \hat{\mathbf{d}}: \mathcal{B}_0 \rightarrow \mathbb{R}^3 : \begin{cases} \hat{\nabla} \cdot \mathbf{P} = \mathbf{0} & \text{in } \mathcal{B}_0, \\ \mathbf{P} \hat{\mathbf{n}} = \hat{\mathbf{s}}_1 \hat{\mathbf{n}} & \text{on } \Gamma_{N1}, \\ \mathbf{P} \hat{\mathbf{n}} = \hat{\mathbf{s}}_2 \hat{\mathbf{n}} & \text{on } \Gamma_{N2}, \\ \hat{\mathbf{d}} = \mathbf{0} & \text{on } \Gamma_D, \end{cases} \quad (5.1)$$

here $\partial\mathcal{B}_0 = \Gamma_{N1} \cup \Gamma_{N2} \cup \Gamma_D$, Γ_{N1} and Γ_{N2} are the subsets of $\partial\mathcal{B}$ where external surface forces per unit of area act, i.e. where Neumann boundary conditions (BC) are applied, and Γ_D is the subset of $\partial\mathcal{B}$ where homogeneous Dirichlet BC are imposed. In problem (5.1), $\hat{\mathbf{s}}_1$ and $\hat{\mathbf{s}}_2$ are boundary data defined on the reference configuration \mathcal{B}_0 and $\hat{\mathbf{n}}$ is the outward directed unit normal vector to $\partial\mathcal{B}_0$. In problem (5.1) the first Piola-Kirchhoff tensor $\mathbf{P}(\hat{\mathbf{d}})$ is defined according to the volumetric-isochoric split discussed in Sec. 4.3.1 and it depends on the displacement field through the deformation gradient tensor \mathbf{F} as in Eqs. (4.52) and (3.41). In order to solve problem (5.1) by means of the Finite Element Method, let us introduce the Hilbert space of functions V defined as:

$$V = V(\mathcal{B}_0) = [H_{\Gamma_D}^1(\mathcal{B}_0)]^3 = \left\{ \hat{\boldsymbol{\psi}} \in [H^1(\mathcal{B}_0)]^3 \text{ s.t. } \hat{\boldsymbol{\psi}} = \mathbf{0} \text{ on } \Gamma_D \right\}. \quad (5.2)$$

The weak formulation of problem (5.1) is obtained by multiplying the equation of balance principle of linear momentum by an arbitrary vectorial test function $\hat{\boldsymbol{\psi}} \in V$ and integrating it, in the Lebesgue sense, in the reference configuration \mathcal{B}_0 ; due to the arbitrariness of the function $\hat{\boldsymbol{\psi}}$, the following equality holds:

$$\int_{\mathcal{B}_0} \hat{\boldsymbol{\nu}} \cdot \mathbf{P} \cdot \hat{\boldsymbol{\psi}} \, d\mathcal{B}_0 = \mathbf{0} \quad \forall \hat{\boldsymbol{\psi}} \in V, \quad (5.3)$$

where $\mathbf{a} \cdot \mathbf{b}$ indicates the scalar product between two vectors in \mathbb{R}^3 Holzapfel [2000]. By applying the divergence theorem in the volume integral of Eq. (5.3) and by considering that $\hat{\boldsymbol{\psi}} = \mathbf{0}$ on $\Gamma_D \forall \hat{\boldsymbol{\psi}} \in V$, the weak formulation of problem (5.1) reads:

find $\hat{\mathbf{d}} = \hat{\mathbf{d}}(\hat{\mathbf{X}}) \in V$:

$$\int_{\mathcal{B}_0} \mathbf{P} : \hat{\boldsymbol{\nu}} \hat{\boldsymbol{\psi}} \, d\mathcal{B}_0 = \oint_{\Gamma_{N1}} \hat{\mathbf{s}}_1 \hat{\mathbf{n}} \cdot \hat{\boldsymbol{\psi}} \, d\Gamma_{N1} + \oint_{\Gamma_{N2}} \hat{\mathbf{s}}_2 \hat{\mathbf{n}} \cdot \hat{\boldsymbol{\psi}} \, d\Gamma_{N2} \quad \forall \hat{\boldsymbol{\psi}} \in V. \quad (5.4)$$

In the next sections, for the sake of clarity, for each of the mechanical tests that are numerically simulated, the Neumann and the Dirichlet surfaces, namely Γ_{N_i} and Γ_D in problem (5.1) are specified.

5.1.2 Numerical discretization

In order to numerically solve the structural mechanics problem written in its weak form in Eq. (5.4), a suitable representation \mathcal{B}_0^h of the reference configuration \mathcal{B}_0 , also referred to as the computational domain, must be introduced at first. Given the reference configuration \mathcal{B}_0 , the computational domain \mathcal{B}_0^h is defined by means of a finite decomposition

$$\overline{\mathcal{B}_0} = \bigcup_{K \in \mathcal{T}_h} K, \quad (5.5)$$

where $\overline{\mathcal{B}_0}$ indicates the closure of \mathcal{B}_0 and \mathcal{T}_h is a triangulation of $\overline{\mathcal{B}_0}$ Quarteroni and Valli [1999b]. Afterwards, a finite dimensional space X_h^r of piecewise polynomials of degree r must be introduced on \mathcal{T}_h , namely:

$$X_h^r = X_h^r(\overline{\mathcal{B}_0}) = \left\{ \hat{\boldsymbol{\psi}}_h \in C^0(\overline{\mathcal{B}_0}) : \hat{\boldsymbol{\psi}}_{h|K} \in (\mathbb{P}_r)^3 \forall K \in \mathcal{T}_h \right\}. \quad (5.6)$$

In the definition of the polynomial space X_h^r the notation of Quarteroni and Valli [1999b] has been adopted; therefore, it can be anticipated that the computational domains considered in this work are the union of a finite number of tetrahedra K in \mathbb{R}^3 on which the polynomial space $(\mathbb{P}_r)^3$ is defined Quarteroni and Valli [1999b]. In this work, tetrahedral triangulations have been preferred to hexahedral ones (used for instance in Balzani [2006]; Gasser and Holzapfel [2006]) since the former can better approximate complex three-dimensional geometries, such as those representing anatomically realistic portions of the cerebral vasculature obtained from Magnetic Resonance Imaging (MRI) techniques, than the latter Crosetto [2011]. Eq. (5.4) is discretized by considering a finite dimensional space of functions V_h defined as $V_h := (X_h^r) \cap V \subset V$ in which the basis composed of Lagrangian basis functions $\{\hat{\boldsymbol{\psi}}_{h,A}\}_{A=1}^{N_h}$, where $N_h := \dim(V_h)$, is defined Quarteroni and Valli [1999b]. Each vectorial basis function has the form $\hat{\boldsymbol{\psi}}_{h,A} = (\hat{\psi}_{h,A} \mathbf{E}_1, \hat{\psi}_{h,A} \mathbf{E}_2, \hat{\psi}_{h,A} \mathbf{E}_3)$, where $\hat{\psi}_{h,A}$ is a scalar Lagrangian function of V_h defined on the triangulation \mathcal{B}_0^h and $(\mathbf{E}_1, \mathbf{E}_2, \mathbf{E}_3)$ is the Euclidean basis in \mathbb{R}^3 . The discrete representation $\hat{\mathbf{d}}_h \in V_h$ of

the material displacement field $\hat{\mathbf{d}} \in V$ in Eq. (5.4) reads

$$\hat{\mathbf{d}}_h(\hat{\mathbf{X}}) = \sum_{A=1}^{N_h} \sum_{j=1}^3 (\hat{\mathbf{d}}_{h,j})_A \hat{\psi}_{h,A}(\hat{\mathbf{X}}) \mathbf{E}_j, \quad (5.7)$$

whose j -th component is $\hat{d}_{h,j} := \sum_{A=1}^{N_h} (\hat{\mathbf{d}}_{h,j})_A \hat{\psi}_{h,A}$; the discretized weak formulation of Eq. (5.4) is written as:

find $\hat{\mathbf{d}}_h \in V_h$:

$$\int_{\mathcal{B}_0^h} \mathbf{P}(\mathbf{F}(\hat{\mathbf{d}}_h)) : \widehat{\nabla} \hat{\boldsymbol{\psi}}_h \, d\mathcal{B}_0^h = \oint_{\Gamma_{N1}^h} \hat{s}_1^h \hat{\mathbf{n}} \cdot \hat{\boldsymbol{\psi}}_h \, d\Gamma_{N1}^h + \oint_{\Gamma_{N2}^h} \hat{s}_2^h \hat{\mathbf{n}} \cdot \hat{\boldsymbol{\psi}}_h \, d\Gamma_{N2}^h \quad \forall \hat{\boldsymbol{\psi}}_h \in V_h, \quad (5.8)$$

where Γ_{Ni}^h is the approximation of Γ_{Ni} , for $i = 1, 2$, provided by the triangulation \mathcal{B}_0^h ; \hat{s}_1^h and \hat{s}_2^h are suitable approximations of the boundary data \hat{s}_1 and \hat{s}_2 on the corresponding surface, e.g. the L^2 -projection of the boundary data on piecewise polynomial spaces of functions $X_h^r(\overline{\Gamma_{N1}})$ and $X_h^r(\overline{\Gamma_{N2}})$, respectively. Similarly to Eq. (5.6), the two spaces of functions are defined as:

$$X_h^r(\overline{\Gamma_{Ni}}) = \left\{ \hat{\boldsymbol{\psi}}_h \in C^0(\overline{\Gamma_{Ni}}) : \hat{\boldsymbol{\psi}}_{h|K} \in (\mathbb{P}_r)^3 \, \forall K \in \mathcal{T}_h \cap \Gamma_{Ni} \right\} \quad \text{for } i = 1, 2. \quad (5.9)$$

5.1.3 Linearization of the nonlinear discrete structural problem

As anticipated before, when nonlinear constitutive models describe the vessel wall, the corresponding numerical solution of the structural mechanics problem (5.1) requires the use of incremental/iterative solution techniques. Indeed, in this work, the Newton-Raphson method has been employed to solve Eq. (5.8); the interested reader may refer to Quarteroni et al. [2007] for a detailed description of the method and of its convergence properties. The Newton-Raphson method relies mainly on the solution of (tangent) linear problems resulting from the linearization of Eq. (5.8).

Given the discrete weak formulation in Eq. (5.8), let us introduce the variational residual $\mathcal{R} : \mathbb{R}^{3N_h} \rightarrow \mathbb{R}^{3N_h}$ as:

$$\mathcal{R}(\hat{\mathbf{d}}_h)(\hat{\boldsymbol{\psi}}_h) = \int_{\mathcal{B}_0^h} \mathbf{P}(\mathbf{F}(\hat{\mathbf{d}}_h)) : \widehat{\nabla} \hat{\boldsymbol{\psi}}_h \, d\mathcal{B}_0^h - \oint_{\Gamma_{N1}^h} \hat{s}_1^h \hat{\mathbf{n}} \cdot \hat{\boldsymbol{\psi}}_h \, d\Gamma_{N1}^h - \oint_{\Gamma_{N2}^h} \hat{s}_2^h \hat{\mathbf{n}} \cdot \hat{\boldsymbol{\psi}}_h \, d\Gamma_{N2}^h \quad \forall \hat{\boldsymbol{\psi}}_h \in V_h, \quad (5.10)$$

where $\hat{\mathbf{d}}_h = ((\hat{\mathbf{d}}_{h,1})_1, \dots, (\hat{\mathbf{d}}_{h,1})_{N_h}, (\hat{\mathbf{d}}_{h,2})_1, \dots, (\hat{\mathbf{d}}_{h,2})_{N_h}, (\hat{\mathbf{d}}_{h,3})_1, \dots, (\hat{\mathbf{d}}_{h,3})_{N_h})$ is the vector of dimension $3N_h$ of the coefficients in Eq. (5.7). By comparing Eqs. (5.8) and (5.10), it is clear that solving the nonlinear equation $\mathcal{R}(\hat{\mathbf{d}}_h)(\hat{\boldsymbol{\psi}}_h) = 0 \quad \forall \hat{\boldsymbol{\psi}}_h \in V_h$ is equivalent to solve the discrete weak formulation of the structural mechanics problem. The iterative Newton-Raphson method can be briefly summarized as follows:

set	$\hat{\mathbf{d}}_h^{k=0},$
for	$k = 0, \dots,$
solve	$\mathcal{D}_{\hat{\mathbf{d}}_h} \mathcal{R}(\hat{\mathbf{d}}_h^k)(\hat{\boldsymbol{\psi}}_h, \delta \hat{\mathbf{d}}_h^k) = -\mathcal{R}(\hat{\mathbf{d}}_h^k)(\hat{\boldsymbol{\psi}}_h) \quad \forall \hat{\boldsymbol{\psi}}_h \in V_h,$
set	$\hat{\mathbf{d}}_h^{k+1} = \hat{\mathbf{d}}_h^k + \delta \hat{\mathbf{d}}_h^k,$
if stopping criteria satisfied	exit,
end	

(5.11)

where the index $k > 1 \in \mathbb{N}$ indicates the current iteration and the convergence is reached when $\|\mathcal{R}(\hat{\mathbf{d}}_h^k)(\hat{\boldsymbol{\psi}}_h)\|_\infty < tol_{abs} + \|\mathcal{R}(\hat{\mathbf{d}}_h^0)(\hat{\boldsymbol{\psi}}_h)\|_\infty tol_{rel}$, where $tol_{abs} > 0$ and $tol_{rel} > 0$ are two stopping tolerances and $\|\bullet\|$ indicates the Euclidean norm in \mathbb{R}^{3N_h} Quarteroni and Valli [1999b]. The operator $\mathcal{D}_{\hat{\mathbf{d}}}\mathcal{R}(\bullet)(\bullet, \bullet)$ represents the linearization, by means of the Gateaux derivatives, of the variational residual $\mathcal{R}(\bullet)(\bullet)$ in Eq. (5.10) with respect to the displacement field. As explained in Bonet and Wood [1997], the first derivative with respect to the material displacement field of $\mathcal{R}(\bullet)(\bullet)$, indicated as $\mathcal{D}_{\hat{\mathbf{d}}}\mathcal{R}(\bullet)(\bullet, \bullet)$, is defined as follows:

$$\mathcal{D}_{\hat{\mathbf{d}}}\mathcal{R}(\hat{\mathbf{d}}_h^k)(\hat{\boldsymbol{\psi}}_h, \delta\hat{\mathbf{d}}_h^k) = \int_{\mathcal{B}_0^h} \left(\mathcal{D}_{\mathbf{F}}\mathbf{P}(\mathbf{F}_h^k) : \hat{\nabla}(\delta\hat{\mathbf{d}}_h^k) \right) : \hat{\nabla}\hat{\boldsymbol{\psi}}_h d\mathcal{B}_0^h, \quad (5.12)$$

where $\mathcal{D}_{\mathbf{F}}\mathbf{P}(\mathbf{F}_h^k)$ represents the Gateaux derivative of the first Piola-Kirchhoff tensor with respect to the deformation gradient evaluated at the deformation state $\mathbf{F}_h^k = \hat{\nabla}\hat{\mathbf{d}}_h^k + \mathbf{I}$. In addition, in Eq. (5.12) it has been used that the external surface forces \hat{s}_1 and \hat{s}_2 are independent of the material displacement $\hat{\mathbf{d}}_h$. The linearized problem in Eq. (5.11) must be verified for each test function $\hat{\boldsymbol{\psi}}_h$ in V_h ; namely it has to be verified for each function $\hat{\boldsymbol{\psi}}_{h,A}$ of the Lagrangian basis of V_h . The linearization of the variational residual in Eq. (5.12) is a bilinear form in $\delta\hat{\mathbf{d}}_h^k$ and $\hat{\boldsymbol{\psi}}_h$; consequently, the linearized problem in Eq. (5.11) can be reformulated in the form of a linear system of equations as follows:

$$\mathcal{J}_{\mathbf{P}}(\hat{\mathbf{d}}_h^k)\delta\hat{\mathbf{d}}_h^k = -\mathcal{R}(\hat{\mathbf{d}}_h^k), \quad (5.13)$$

where $\mathcal{J}_{\mathbf{P}}(\hat{\mathbf{d}}_h^k) \in \mathbb{R}^{3N_h, 3N_h}$ is the tangent matrix of the first Piola-Kirchhoff tensor, defined as:

$$\left(\mathcal{J}_{\mathbf{P}}(\hat{\mathbf{d}}_h^k) \right)_{A,B} = \mathcal{J}_{\mathbf{P}}(\hat{\boldsymbol{\psi}}_{h,B}, \hat{\boldsymbol{\psi}}_{h,A}) = \int_{\mathcal{B}_0^h} \left(\mathcal{D}_{\mathbf{F}}\mathbf{P}(\mathbf{F}_h^k) : \hat{\nabla}(\hat{\boldsymbol{\psi}}_{h,B}) \right) : \hat{\nabla}\hat{\boldsymbol{\psi}}_{h,A} d\mathcal{B}_0^h, \quad (5.14)$$

where $\hat{\boldsymbol{\psi}}_{h,A}, \hat{\boldsymbol{\psi}}_{h,B}$ are basis functions of V_h , considered either as test and trial functions Quarteroni and Valli [1999b]; $\delta\hat{\mathbf{d}}_h^k \in \mathbb{R}^{3N_h}$ is the vector of coefficients

$$\delta\hat{\mathbf{d}}_h^k = \left((\delta\hat{d}_{h,1}^k)_1, \dots, (\delta\hat{d}_{h,1}^k)_{N_h}, (\delta\hat{d}_{h,2}^k)_1, \dots, (\delta\hat{d}_{h,2}^k)_{N_h}, (\delta\hat{d}_{h,3}^k)_1, \dots, (\delta\hat{d}_{h,3}^k)_{N_h} \right), \quad (5.15)$$

and the right hand side $\mathcal{R}(\hat{\mathbf{d}}_h^k) = \mathcal{R}(\hat{\mathbf{d}}_h^k)(\hat{\boldsymbol{\psi}}_{h,A}) \in \mathbb{R}^{3N_h}$ is obtained from the evaluation of the variational residual in Eq. (5.10) for all the basis functions $\hat{\boldsymbol{\psi}}_{h,A} \in V_h$.

5.2 Implementation and numerical aspects of simulations of arterial wall mechanics

This section addresses different aspects related to the numerical simulations of the arterial wall mechanics. Sec. 5.2.1 aims at describing the contributions that we have provided to the finite element library *LifeV Éco* [2010]. In Sec. 5.2.2, the numerical representation of the activation of the collagen fibers described in Sec. 4.2.2 is presented. In Sec. 5.2.3, a possible finite element implementation of the multi-mechanism model described in Li [2009] is critically discussed. To conclude, Sec. 5.2.4 deals with some aspects related to the numerical simulation of the arterial wall mechanics.

5.2.1 Efficient implementation of highly nonlinear constitutive models in LifeV

A numerical simulation of arterial wall mechanics might be very expensive especially if highly nonlinear anisotropic models describe the tissue Brinkhues et al. [2013]. Indeed, as discussed in Sec. 5.1.3, the numerical solution of the nonlinear discrete weak formulation given by Eq. (5.8) requires the updated evaluation of both the right hand side of the linearized problem in Eq. (5.11) and of the tangent matrix in Eq. (5.13) which is usually composed of different contributions depending on the nonlinearity of the constitutive law. The efficient implementation of highly nonlinear constitutive models plays therefore a crucial role in solving the mechanical problem in affordable computational times.

The constitutive models described in Ch. 4 have been implemented in the free open source library LifeV Éco [2010], a parallel finite element C++ library that implements state of the art of mathematical models and numerical methods for the solution of three-dimensional partial differential equations. LifeV targets a broad audience of researchers; for this reason, the organization and implementation of the different constitutive models have been driven by necessity of having a “user-oriented” library. It includes numerical methods and algorithms for the numerical simulation of complex engineering problems; indeed it has been extensively used for the numerical simulation of the human cardiovascular system, see e.g. Crosetto [2011]; Malossi [2012]; Pozzoli [2011], porous media Fumagalli [2012], cardiac tissue Rossi [2014], and other physical systems such as, for instance, free surface flows in orbitally shaken reactors Quinodoz [2012] and many others. The implementation efforts have led to the creation of the current structure module of LifeV. Its main features are flexibility and computational efficiency.

Flexibility has been achieved thanks to the implementation of a unified framework for the numerical simulations of structural mechanics problems. The organization of the structure module is depicted in Fig. 5.1. The numerical solution of problem (5.8) is managed by the *Solver Class* which, for instance, executes the Newton-Raphson method described in Sec. 5.1.3. As represented in Fig. 5.1, dynamic structural mechanics problems can be simulated thanks to the integration of the tools implementing time advancing schemes such as Backward Difference Formula (BDF) methods Quarteroni et al. [2007], provided by the core module of the library, inside the structure module. The different constitutive models have been implemented according to the so-called *Factory pattern* design described in Gamma et al. [1995] which provides a way to encapsulate a group of individual classes (see Stroustrup [2013]), each of them representing a single constitutive model, that have a common theme through a common abstract interface, implemented in an abstract class, the *Constitutive Model Class* in Fig. 5.1. Such abstract class can be used by external classes, such as the *Solver Class*, to solve the structural mechanics problem. The *Solver Class* creates an instance of the *Constitutive Model Class* Stroustrup [2013] and then uses the generic interface of the *Constitutive Model Class* to create the instance of the chosen constitutive model among the ones that are available. This pattern separates the details of implementation of a set of objects, i.e. constitutive models, from their general usage and relies on object composition Gamma et al. [1995]. Such organization of the structure module has led to a unified and flexible environment where each term of the strain energy function, i.e. the volumetric, the isochoric isotropic and, possibly, the isochoric model for the single family of collagen fibers, can be freely chosen by choosing a set of parameters when the simulation is started. The hierarchical relation between the different implementations of the constitutive models and the *Solver Class* is represented in Fig. 5.1. As a final remark, as represented in Fig. 5.1, the material parameters for the selected constitutive laws modeling the tissue are handled by the *Material Parameter Class* which is contained in the abstract interface *Constitutive Model Class*.

As discussed in Sec. 5.1.3, the numerical solution of a highly nonlinear system in Eq. (5.1) by means of the Newton technique requires the repeated evaluation of the tangent matrix Eq. (5.14) and of the

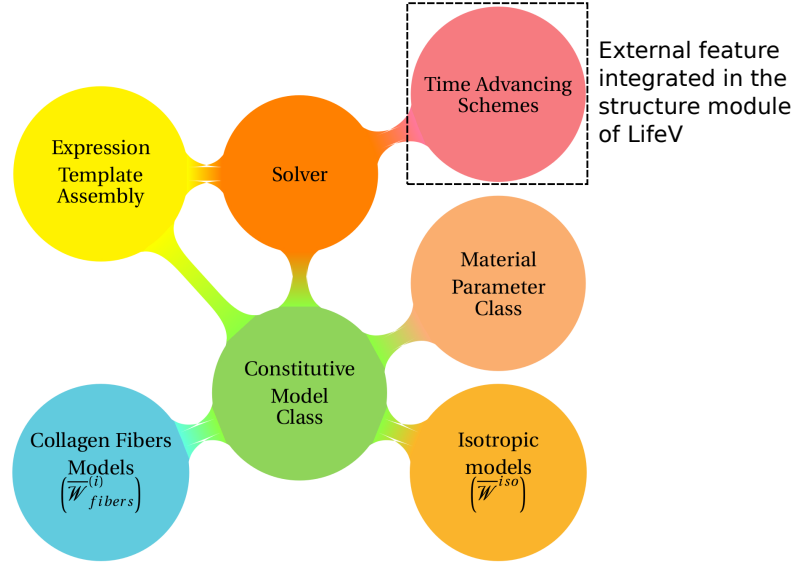


Figure 5.1: Organization of the structure module of the finite element library `LifeV`

right hand side $\mathcal{R}(\hat{\mathbf{a}}_h^k)(\hat{\boldsymbol{\psi}}_h)$ in Eq. (5.11). From the computational point of view, these two operations are among the most expensive ones together with the solution of the linearized problem by means of iterative methods (e.g. GMRES Saad [2003]); for this reason, as discussed in Quinodoz [2012]; Fischle [In Preparation], the implementation of efficient routines to assemble either $\mathcal{J}_P(\hat{\mathbf{a}}_h^k)(\hat{\boldsymbol{\psi}}_B, \hat{\boldsymbol{\psi}}_A)$ and $\mathcal{R}(\hat{\mathbf{a}}_h^k)(\hat{\boldsymbol{\psi}}_{h,A})$ is extremely important. The computational efficiency of the structure module has been achieved by means of the implementation of the finite element assembly routines for $\mathcal{J}_P(\hat{\mathbf{a}}_h^k)(\hat{\boldsymbol{\psi}}_B, \hat{\boldsymbol{\psi}}_A)$ and $\mathcal{R}(\hat{\mathbf{a}}_h^k)(\hat{\boldsymbol{\psi}}_{h,A})$ in the framework for finite element assembly, based on template meta-programming Di Pietro and Veneziani [2009], described in Quinodoz [2012]. Such framework is not detailed here; however, it is worth pointing out that, the work of Quinodoz [2012], initially developed for fluid dynamics applications, has been deeply extended in order to include the possibility of finite element assembly routines for structural mechanics problems. From the implementation point of view, the routines for the finite element assembly of the matrices and vectors have been implemented in the *Expression Template Assembly* framework indicated in Fig. 5.1; the correct execution of the assembly routines is controlled by the *Solver Class* and the *Constitutive Model Class*, as represented in Fig. 5.1.

Another important aspect in the numerical simulations of arterial wall mechanics is the evaluation of mechanical quantities, such as mechanical stresses, related to the deformations of the vessel wall. With this aim, based on the *Expression Template Assembly* framework, a set of computational tools for the evaluation of any scalar, vectorial or tensorial field defined on the computational domain \mathcal{B}_0^h has been implemented in `LifeV`. Such powerful set of tools, as the finite element assembly procedures, is computationally efficient and its use can range from post-processing of numerical simulations (for instance evaluating the Von Mises stress given a state of deformations) to automatic differentiation of functions.

5.2.2 Mathematical description of the collagen fibers activation

As mentioned in Sec. 4.2.2, when modeling the arterial wall tissue by means of anisotropic models, the mechanical contribution of the single family of collagen fibers occurs only if its stretch is higher than the activation stretch. More precisely, as discussed in Sec. 4.2.2, the i -th family of collagen fibers starts load-bearing if the activation condition $I_4^{(i)} > I_{4,A}^{(i)}$ in Eq. (4.34) is satisfied. The discretization and implementation, of the activation condition of the single family of collagen fibers is not addressed in literature. In this work, for anisotropic laws, the recruitment of the single family of collagen fibers is included in the definition of the isochoric part of the first Piola-Kirchhoff tensor (see Eq. (4.65)) by means of the following activation function

$$\xi(\bar{I}_4^{(i)}) = \frac{1}{\pi} \left(\arctan(\epsilon(\bar{I}_4^{(i)} - I_{4,A}^{(i)})) \right) + \frac{1}{2}, \quad (5.16)$$

where $\epsilon > 0$ is a dimensionless parameter which is suitably chosen to model the recruitment of the collagen fibers and, as in Sec. 4.2.2, $I_{4,A}^{(i)}$ represents the activation stretch of the i -th, for $i = 1, \dots, N$, family of fibers. Therefore, Eq. (4.65) is transformed in the following way:

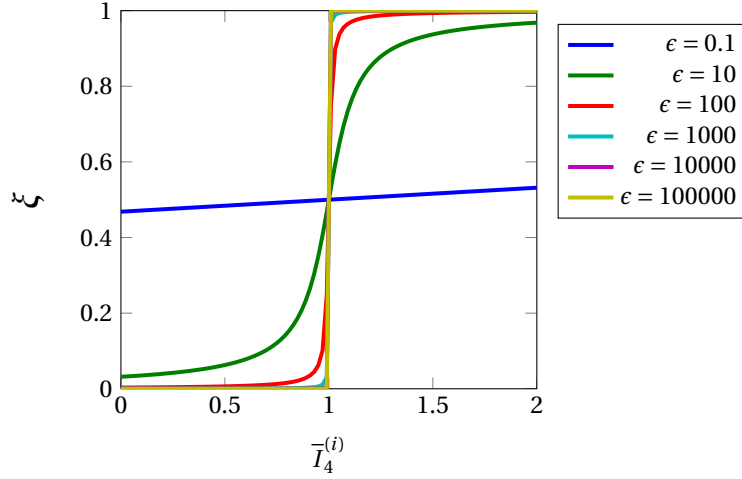
$$\bar{\mathbf{P}}^{aniso} = \bar{\mathbf{P}}_{iso}^{aniso} + \sum_{i=1}^N \xi(\bar{I}_4^{(i)}) \bar{\mathbf{P}}_{fibers}^{(i)} \quad (5.17)$$

in order to include the collagen fibers activation in the definition of the isochoric part of the first Piola-Kirchhoff tensor. We remark that the activation function $\xi(\bar{I}_4^{(i)})$ has been introduced into the definition of \mathbf{P} in order to avoid discontinuities in the first Piola-Kirchhoff stress tensor inside elements and across elements in the computation of the integrals defining the discrete weak formulation of the structural mechanics problem. Fig. 5.2 shows the activation function for different values of the parameter ϵ . For simplicity, it is assumed that $J = 1$, namely $\bar{I}_4^{(i)} = I_4^{(i)}$, and $I_{4,A}^{(i)} = 1$. It can be observed that it is necessary to choose an adequate value of ϵ in order to represent the abrupt recruitment of a single family of collagen fibers. For instance, since $0 < \xi < 1$ for all $I_4^{(i)}$, the value of ϵ can be set to achieve a certain level of mechanical activation given a fixed value of the stretch I_4 . Low values of ϵ are inadequate to model the abrupt recruitment of a family of collagen fibers; indeed, e.g. for $\epsilon = 0.1$ the activation function models the single family of collagen fibers as mechanically active even for strong compressive states, for instance for $0 < I_4^{(i)} < 0.5$. In the following, $\epsilon = 5 \cdot 10^5$ that corresponds to a level of mechanical activation $\xi = 0.9999$ at the stretch $I_4^{(i)} = 1.001$.

5.2.3 Finite element approximation of a multi-mechanism model

As anticipated in Sec. 4.2.2, the numerical discretization and finite element implementation of the multi-mechanism model in Wulandana [2003]; Li [2009] by means of continuous polynomial basis functions may induce numerical instabilities during the simulations. In this section, for the sake of simplicity, it is assumed that only one family of fibers is immersed in the background material; consequently, the super script indicating the family of fibers in Sec. 4.2.2 is omitted, i.e. $I_4^{(i)} = I_4$.

As presented in Sec. 4.2.2, the strain energy function characterizing the mechanical response of a family of fibers is referred to the activation configuration \mathcal{B}_A . Due to the change of reference configuration in Eq. (4.42), when the mechanical contribution of the family of fibers occurs, in order to properly compute the mechanical stresses, the deformation gradient \mathbf{F}^a , referred to \mathcal{B}_A , has to be


 Figure 5.2: Activation function $\xi\left(\bar{I}_4^{(i)}\right)$ of Eq. (5.17)

computed. More precisely, $\mathbf{F}^a(t')$, with $t' = t - t_A$, is defined as:

$$\mathbf{F}^a(t') = \mathbf{F}(t_A)^{-1} \mathbf{F}(t). \quad (5.18)$$

In Eq. (5.18), the deformation gradient at the activation time t_A reads as $\mathbf{F}(t_A) = \mathbf{F}(\hat{\mathbf{d}}_A) = \hat{\mathbf{v}}\hat{\mathbf{d}}(\hat{\mathbf{X}}, t_A) + \mathbf{I}$, where $\hat{\mathbf{d}}_A$ is the displacement field for which the activation condition $I_4 > I_{4,MM}$ is satisfied, see Sec. 4.2.2. It is worth pointing out that the activation displacement $\hat{\mathbf{d}}_A$ is not known a priori because it depends on the type of mechanical test that is numerically simulated. Therefore, between two successive iterations of the Newton-Raphson method (or, for instance, if dynamic structural mechanics simulations are considered, between two successive time steps) it is required to analyze the displacement field $\hat{\mathbf{d}}_h^k$ in order to find those points in \mathcal{B}_0^h (i.e. degrees of freedom defined by the finite element space X_h^r) for which the activation condition is satisfied; at those points, the displacement field must be saved in order to compute $\mathbf{F}(t_A)^{-1}$ in Eq. (5.18). It is worth pointing out that, from a general point of view, the displacement field for which $I_4 = I_{4,MM}$, indicated as $\hat{\mathbf{d}}_{MM}$, might not be found as a numerical solution of the structural problems between two successive iterations of the Newton-Raphson method and, therefore, the displacement field that is saved in order to compute $\mathbf{F}(t_A)^{-1}$ in Eq. (5.18) might not be exactly the displacement field at which the collagen fibers are activated. In addition, from a general point of view, it cannot be guaranteed that the activation condition will be satisfied simultaneously at all points in \mathcal{B}_0 , or equivalently in \mathcal{B}_0^h , at the same time. For a multi-mechanism model such as the one of Wulandana [2003]; Li [2009], the Newton-Raphson method in Eq. (5.11) can be modified as follows:

Set an initial guess $\hat{\mathbf{d}}_h^{k=0}$ for the solution of the nonlinear problem and iterate until convergence:

set	$\hat{\mathbf{d}}_h^{k=0}$,
for	$k = 0, \dots$,
solve	$\mathcal{D}_{\hat{\mathbf{d}}}\mathcal{R}(\hat{\mathbf{d}}_h^k, \hat{\mathbf{d}}_A^k)(\hat{\boldsymbol{\psi}}_h, \delta \hat{\mathbf{d}}_h^k) = -\mathcal{R}(\hat{\mathbf{d}}_h^k, \hat{\mathbf{d}}_A^k)(\hat{\boldsymbol{\psi}}_h) \quad \forall \hat{\boldsymbol{\psi}}_h$,
set	$\hat{\mathbf{d}}_h^{k+1} = \hat{\mathbf{d}}_h^k + \delta \hat{\mathbf{d}}_h^k$,
update	$\hat{\mathbf{d}}_A^{k+1} = \text{analyze}(\hat{\mathbf{d}}_h^{k+1})$
if stopping criteria satisfied	exit,
end	

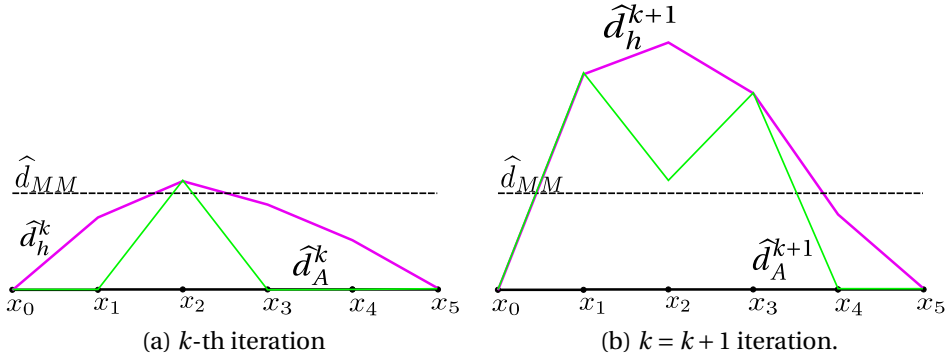


Figure 5.3: Evolution of the activation displacement $\hat{\mathbf{d}}_A$ between two successive iterations of the Newton-Raphson method for a one-dimensional case

(5.19)

In order to discuss the use of continuous polynomial functions to approximate Eq. (5.4) in the case of the multi-mechanism of Wulandana [2003]; Li [2009], let us consider a one-dimensional example represented in Fig. 5.3 and consider two successive iterations of the modified Newton-Raphson method described in Eq. (5.19). Let us assume that the displacement field for which the condition $I_4 = I_{4,MM}$ for a single family is known and, let us indicate it as $\hat{\mathbf{d}}_{MM}$. At the k -th iteration, the displacement field, indicated as $\hat{\mathbf{d}}_h^k$, is such that the activation displacement field $\hat{\mathbf{d}}_A^k$ is non zero only at the point x_2 of the discretized one-dimensional domain. Afterwards, at the iteration k , the tangent matrix $\mathcal{J}_P(\hat{\mathbf{d}}_h^k)$ in Eq. (5.14) is computed, which depends on $\mathbf{F}(t_A)^{-1} = \mathbf{F}(\hat{\mathbf{d}}_A^k)^{-1}$, and the linearized problem is solved again. Once the resolution of the linear system and the update steps in Eq. (5.19) are completed, the new finite element solution is indicated as $\hat{\mathbf{d}}_h^{k+1}$. The activation $\hat{\mathbf{d}}_A$ must be updated with respect to the solution $\hat{\mathbf{d}}_h^{k+1}$; in particular the values of $\hat{\mathbf{d}}_h^{k+1}$ at the points x_1, x_3 are now taken into account, while the value of $\hat{\mathbf{d}}_A$ at the point x_2 is not updated since at that point, the activation displacement was already achieved in the previous iteration. If the weak formulation in Eq. (5.4) is discretized by means of continuous polynomial functions, high oscillations in the deformation gradient $\mathbf{F}(t_A)^{-1}$ may appear and, in turn, they can lead to high numerical oscillations in the volume ratio $J(t_A)$ in Eq. (4.43), see e.g. Fig. 5.4-(d). It is worth pointing out that such oscillations might occur between neighboring elements in \mathcal{B}_0^h , as in Fig. 5.3, or even among the degrees of freedom of the same element.

In order to show the occurrence of numerical oscillations in the mechanical quantities that depend on the activation displacement $\hat{\mathbf{d}}_A$, for instance on the activation volume ratio $J(t_A) = J(\hat{\mathbf{d}}_A)$, let us consider a numerical simulation of an inflation test such as the one described in Secs. 4.2.1 and 5.4. We assume that, for a certain value of external forces applied on the internal surface of the cylinder, see Fig. 4.4 and Sec. 5.4 for details, the material displacement $\hat{\mathbf{d}}^h$ reads as in Fig. 5.4-(a). In addition, one single family of fibers which is supposed to form an angle $\beta = 42^\circ$ degrees with the circumferential direction \mathbf{E}_{\ominus} of the cylinder, is immersed in the background material and that its activation stretch $I_{4,MM} = 1.67$. Fig. 5.4-(b) presents the fiber stretch obtained from $\hat{\mathbf{d}}_h$; the corresponding activation displacement field $\hat{\mathbf{d}}_A$ and volume ratio $J(\hat{\mathbf{d}}_A)$ are represented in Figs. (5.4)-(c) and (5.4)-(d). As it can be observed, although the correct behavior of the solution in Fig. 5.4-(a) (see Sec. 5.4), significant oscillations and totally uncorrect values of the volume ratio can be observed in Fig. 5.4-(d). Fig. 5.5 is a three-dimensional representation of $\hat{\mathbf{d}}_h$, $\hat{\mathbf{d}}_A$, and of $J(\hat{\mathbf{d}}_A)$ in a central portion of the cylindrical domain considered in Sec. 5.4.

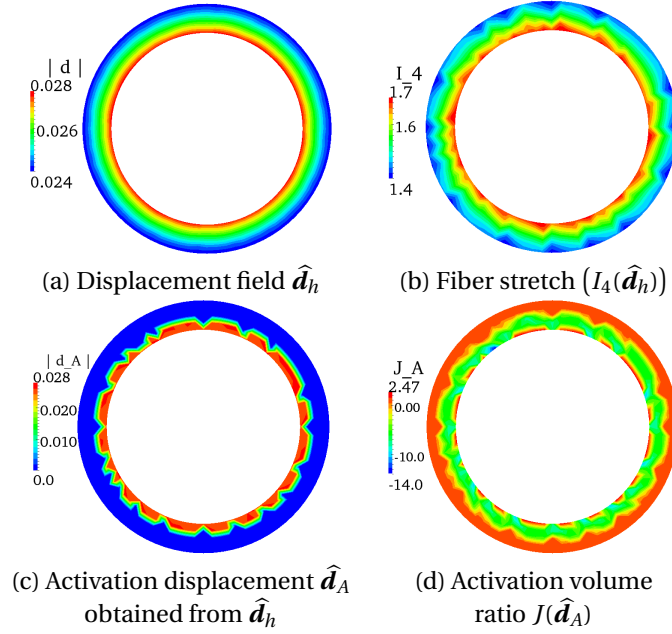


Figure 5.4: Displacement field

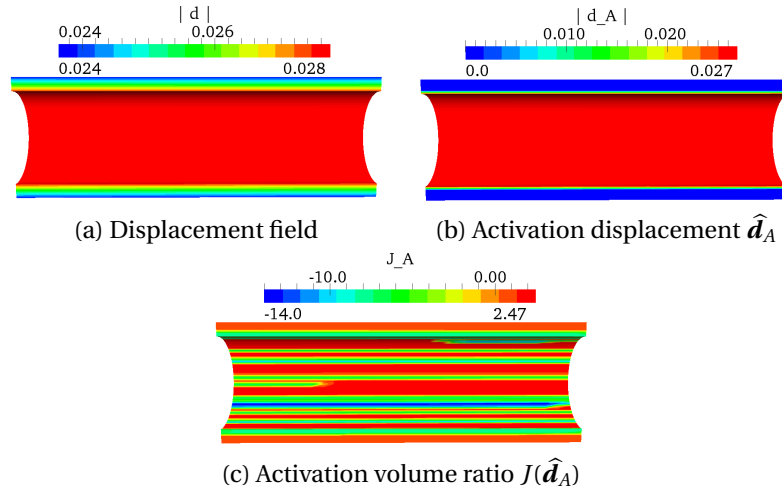


Figure 5.5: Central portion of the cylindrical domain considered in Sec. 5.4

The numerical oscillations on the activation volume ratio $J(\hat{\mathbf{d}}_A)$, presented in Figs. (5.4) and (5.5), induce numerical instabilities in the solution of the nonlinear discrete problem of Eq. (5.8) which in turn may lead to the divergence of the Newton-Raphson method. Specifically, such instabilities have been observed in all the numerical tests performed in the current numerical setting. An alternative approach to approximate the multi-mechanism of Wulandana [2003]; Li [2009] might involve the use of discontinuous finite elements to represent the activation displacement in order to allow multiple values of $\hat{\mathbf{d}}_A$ on the same degree of freedom. However, such alternative was out of the scope of the current work and, for this reason, it has not been investigated. For these reasons, as anticipated in Sec. 4.2.2, instead of the multi-mechanism model proposed in Wulandana [2003]; Li [2009], the simplified version of Eq. (4.46) has been employed in this work. Indeed, although such model represents a simplification

of the multi-mechanism model of Wulandana [2003]; Li [2009], it overcomes the numerical issues just presented and it can be discretized by means of continuous polynomial function. Furthermore, as presented in Sec. 5.4, it is able to describe the recruitment of the collagen fibers at finite strains avoiding the computation of the mechanical quantities referred to \mathcal{B}_0^A .

5.2.4 Remarks on the numerical solution of the nonlinear discrete problem

For the numerical simulation of static mechanical tests such as inflation tests on cylindrical specimen of arteries, in order to guarantee the convergence of the Newton-Raphson method for the solution of Eq. (5.8), the external loads are gradually increased up to the applied load of interest by means of a pseudo-time approach as in Tricceri et al. [2014]. Such technique is employed to properly initialize the Newton-Raphson method since its convergence properties strongly depend on the proximity of the initial guess to the final solution. However, by progressively increasing the applied load and solving the nonlinear problem might not be sufficient to achieve the convergence of the Newton-Raphson method; indeed, the adequate initialization of such iterative method is also sensitive to the constitutive model for the arterial tissue that is considered. In this section, it is shown that if the arterial tissue is described by the second order exponential model ($\overline{\mathcal{W}}_{EXP2}^{iso}$ in Tab. 4.4) in the numerical simulations of a mechanical test, in the range of small deformations, the Newton-Raphson method must be initialized using the numerical solution obtained by using other constitutive models (e.g. $\overline{\mathcal{W}}_{EXP1}^{iso}$) for the same mechanical test and for the same values of applied load.

In the experimental setting the external loads are applied on specimens of arterial tissue at rest. Therefore, when numerically simulating the experimental test such mechanical configuration of the arterial tissue is considered as the reference configuration of the specimen. Since in this work, possible pre-stress and pre-stretch Fung [1993] effects on the mechanical response of the tissue are neglected, the reference configuration is considered as the undeformed and stress-free configuration of the tissue. During the numerical simulations, for small values of external forces, the Newton-Raphson method can be initialized either with zero displacement, when the simulation is started, or by using the displacement field obtained from the previous applied loads. If $\overline{\mathcal{W}}_{EXP2}^{iso}$ describes the tissue, such initialization of the Newton-Raphson method is not enough to achieve the convergence of the iterative method. In order to explain the reasons of this problem, let us compare the linearization of the first Piola-Kirchhoff tensor obtained in the case of $\overline{\mathcal{W}}_{EXP2}^{iso}$ model and, for instance, in the case of the $\overline{\mathcal{W}}_{EXP1}^{iso}$ law. The EXP1 model has been considered as an example; indeed, the considerations that are presented hereafter are still valid for the other isotropic constitutive models of Tab. 4.4.

According to the additive split of $\widehat{\mathcal{W}}$ discussed in Sec. 4.3, the strain energy function for the EXP2 model reads:

$$\begin{aligned}\widehat{\mathcal{W}}_{EXP2}^{iso} &= \mathcal{U}_2(J) + \overline{\mathcal{W}}_{EXP2}^{iso} = \\ &= \frac{\kappa}{2} (J-1)^2 + \ln^2(J) + \frac{\alpha_2}{2\gamma_2} \left(e^{\gamma_2(\bar{I}_1-3)^2} - 1 \right),\end{aligned}\quad (5.20)$$

while for the EXP1 model it is:

$$\begin{aligned}\widehat{\mathcal{W}}_{EXP1}^{iso} &= \mathcal{U}_2(J) + \overline{\mathcal{W}}_{EXP1}^{iso} = \\ &= \frac{\kappa}{2} (J-1)^2 + \ln^2(J) + \frac{\alpha_1}{2\gamma_1} \left(e^{\gamma_1(\bar{I}_1-3)} - 1 \right).\end{aligned}\quad (5.21)$$

5.2. Implementation and numerical aspects of simulations of arterial wall mechanics

The corresponding first Piola-Kirchhoff stress tensors can be computed from Eq. (4.52) and read:

$$\begin{aligned} \mathbf{P}_{EXP2}^{iso} &= \tilde{\mathbf{P}} + \bar{\mathbf{P}}_{EXP2}^{iso} = \\ &= \frac{\kappa}{2} (J^2 - J + \ln(J)) \mathbf{F}^{-T} + 2\alpha_2 (\bar{I}_1 - 3) e^{\gamma_2 (\bar{I}_1 - 3)^2} J^{-2/3} \left(\mathbf{F} - \frac{1}{3} I_C \mathbf{F}^{-T} \right) \end{aligned} \quad (5.22)$$

and

$$\begin{aligned} \mathbf{P}_{EXP1}^{iso} &= \tilde{\mathbf{P}} + \bar{\mathbf{P}}_{EXP1}^{iso} = \\ &= \frac{\kappa}{2} (J^2 - J + \ln(J)) \mathbf{F}^{-T} + \alpha_1 e^{\gamma_1 (\bar{I}_1 - 3)} J^{-2/3} \left(\mathbf{F} - \frac{1}{3} I_C \mathbf{F}^{-T} \right), \end{aligned} \quad (5.23)$$

respectively. In Eqs. (5.22) and (5.23) the volumetric part of the first Piola-Kirchhoff tensor has been defined in Eq. (4.58). As discussed in Sec. 5.1.3, when considering the Newton-Raphson method, the evaluation of the linearized operator $(D_{\mathbf{F}} \mathbf{P}(\mathbf{F}_h^k) : \hat{\mathbf{v}} \hat{\boldsymbol{\psi}}_B)$ is required. For the EXP2 model, the linearized operator reads as follows:

$$\begin{aligned} (D_{\mathbf{F}} \mathbf{P}_{EXP2}^{iso}(\mathbf{F}_h^k) : \hat{\mathbf{v}} \hat{\boldsymbol{\psi}}_B) &= (D_{\mathbf{F}} \tilde{\mathbf{P}}(\mathbf{F}_h^k) : \hat{\mathbf{v}} \hat{\boldsymbol{\psi}}_B) + (D_{\mathbf{F}} \bar{\mathbf{P}}_{EXP2}^{iso}(\mathbf{F}_h^k) : \hat{\mathbf{v}} \hat{\boldsymbol{\psi}}_B) = \\ &= \frac{\kappa}{2} (D_{\mathbf{F}} (J^2 - J + \ln(J)) : \hat{\mathbf{v}} \hat{\boldsymbol{\psi}}_B) \mathbf{F}^{-T} + \frac{\kappa}{2} (J^2 - J + \ln(J)) D_{\mathbf{F}}(\mathbf{F}^{-T}) : \hat{\mathbf{v}} \hat{\boldsymbol{\psi}}_B + \\ &\quad + 2\alpha_2 D_{\mathbf{F}}(\bar{I}_C - 3) : \hat{\mathbf{v}} \hat{\boldsymbol{\psi}}_B \left[e^{\gamma_2 (\bar{I}_1 - 3)^2} J^{-2/3} \left(\mathbf{F} - \frac{1}{3} I_C \mathbf{F}^{-T} \right) \right] + \\ &\quad + 2\alpha_2 (\bar{I}_C - 3) D_{\mathbf{F}} \left(e^{\gamma_2 (\bar{I}_1 - 3)^2} J^{-2/3} \left(\mathbf{F} - \frac{1}{3} I_C \mathbf{F}^{-T} \right) \right) : \hat{\mathbf{v}} \hat{\boldsymbol{\psi}}_B, \end{aligned} \quad (5.24)$$

while for the EXP1 model it is:

$$\begin{aligned} (D_{\mathbf{F}} \mathbf{P}_{EXP1}^{iso}(\mathbf{F}_h^k) : \hat{\mathbf{v}} \hat{\boldsymbol{\psi}}_B) &= (D_{\mathbf{F}} \tilde{\mathbf{P}}(\mathbf{F}_h^k) : \hat{\mathbf{v}} \hat{\boldsymbol{\psi}}_B) + (D_{\mathbf{F}} \bar{\mathbf{P}}_{EXP1}^{iso}(\mathbf{F}_h^k) : \hat{\mathbf{v}} \hat{\boldsymbol{\psi}}_B) = \\ &= \frac{\kappa}{2} (D_{\mathbf{F}} (J^2 - J + \ln(J)) : \hat{\mathbf{v}} \hat{\boldsymbol{\psi}}_B) \mathbf{F}^{-T} + \frac{\kappa}{2} (J^2 - J + \ln(J)) D_{\mathbf{F}}(\mathbf{F}^{-T}) : \hat{\mathbf{v}} \hat{\boldsymbol{\psi}}_B + \\ &\quad + \alpha_1 D_{\mathbf{F}} \left(e^{\gamma_1 (\bar{I}_1 - 3)} J^{-2/3} \left(\mathbf{F} - \frac{1}{3} I_C \mathbf{F}^{-T} \right) \right) : \hat{\mathbf{v}} \hat{\boldsymbol{\psi}}_B. \end{aligned} \quad (5.25)$$

In Eqs. (5.24) and (5.25), due to the convexity properties of the volumetric strain energy function $\mathcal{U}_2(J)$, see Sec. 4.3.2, the first derivative of the volumetric part $D_{\mathbf{F}} \tilde{\mathbf{P}}(\mathbf{F}_h^k)$ is different from zero either at zero strains and also for small deformations. As it can be noticed from Eq. (5.24), at zero strains and for small deformations, the second order tensor $D_{\mathbf{F}} \mathbf{P}_{EXP2}^{iso}(\mathbf{F}_h^k) : \hat{\mathbf{v}} \hat{\boldsymbol{\psi}}_B$ is dominated by the volumetric term; this is due to the fact that at zero strains, namely for $\mathbf{F} = \mathbf{I}$ in Eqs. (5.24), the linearization of the isochoric part is zero, while for small deformations $(\bar{I}_C - 3) \approx 0$. On the contrary, for small deformations, the tangent matrix of the first Piola-Kirchhoff tensor \mathbf{P}_{EXP1}^{iso} is not dominated by the volumetric term since the linearization of the isochoric part of \mathbf{P}_{EXP1}^{iso} is different from zero. As discussed in Sec. 4.3, deformations of the material under the action of external forces are governed by the isochoric part of the strain energy function while volumetric deformations are strongly penalized by the choice of an adequate penalization parameter κ . Consequently, in the case of the EXP2 model, the fact that, for small deformations, the tangent matrix of \mathbf{P}_{EXP2}^{iso} is a volumetric dominated matrix leads to a poor convergence or to the divergence of the Newton-Raphson method since the unique deformations that the material undergoes are of volumetric type. Such considerations must be taken into account to properly initialize a numerical simulation using the EXP2 model. Indeed, if the EXP2 is employed, in order to retrieve the convergence of the Newton-Raphson method, the numerical simulation must

be initialized with the numerical solution obtained, for the same values of applied loads, with others constitutive models.

Another important aspect related to the numerical simulation of arterial wall mechanics is the influence of the penalization parameter κ in Eq. (4.53) on the solution of the linear system arising from the linearization of the weak formulation in Eq. (5.4). At each iteration of the Newton-Raphson method, the linearized problem is solved by means of iterative methods such as, for instance, the preconditioned GMRES method Saad [2003] and for symmetric matrices the conjugate gradient method Quarteroni et al. [2007]. When using the additive decomposition of the strain energy function $\widehat{\mathcal{W}}$ into its volumetric \mathcal{U} and isochoric $\overline{\mathcal{W}}$ parts to model the quasi-incompressible mechanical behavior of arteries, the performances of the iterative methods as GMRES are affected by the choice of the penalization parameter κ in Eq. (4.53). Indeed, it can significantly affect the convergence performances of the GMRES method due to the fact that the condition number of the Jacobian matrix in Eq. (5.14) tends to increase with the value of κ . In addition, when using linear finite elements, high values of the penalization parameter κ may lead to extremely poor convergence of the iterative method and, in turn, to poor convergence of the Newton-Raphson method (independently of the constitutive model) and eventually to locking phenomena Brinkhues et al. [2013]; Hughes [2000].

In the case of anisotropic constitutive laws, another parameter influencing the convergence of iterative methods for the solution of linearized systems is the activation parameter ϵ in Eq. (5.16). Indeed, for this type of models, the derivative of the activation function appears in the linearization of the first Piola-Kirchhoff tensor. In Fig. 5.2, it can be observed that, for values of ϵ for which the abrupt recruitment of the collagen fibers is modeled and, in the limit case, for $\epsilon \rightarrow \infty$, the derivative of the activation function tends to infinity around the activation stretch $I_{4,A}^{(i)}$. Therefore, for stretches of the collagen fibers around the activation stretch, the condition number of the linearized matrix of the first Piola-Kirchhoff tensor increases with ϵ . This, similarly to what has been remarked for the penalization parameter κ , may induce slow convergence of the iterative method for the linearized systems. On the other hand, for either small ($I_4^{(i)} \ll I_{4,A}^{(i)}$) or large ($I_4^{(i)} \gg I_{4,A}^{(i)}$) stretches, such effect on the condition number is negligible since the derivative of the activation function tends to zero.

5.3 Representative problems

In order to introduce the constitutive relations that will be used to model a specimen of cerebral artery in Sec. 5.4, this section focuses on the validation of some of the constitutive models of Ch. 4. However, in the structure module of `LifeV` the implementation and validation of the constitutive models of Ch. 4 and of other laws (e.g. the linear elastic or the anisotropic with distributed collagen fibers model described in Gasser and Holzapfel [2006]) are available.

In this section, the uniaxial tensile test on a cubic domain, described in Sec. 4.2.1, is considered. In order to reduce the computational burden of all numerical simulations, due to the type of mechanical test and to the symmetry of the domain, the deformations of only one quarter of the cube have been numerically simulated; therefore, symmetry boundary conditions have been used to mimic the presence of the remaining part of the domain, as represented in Fig. 5.6. The differential problem

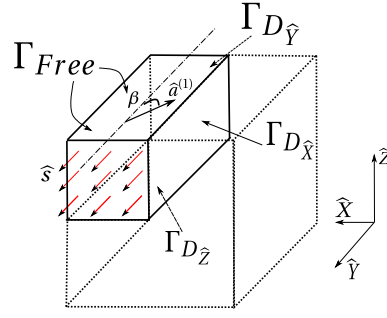


Figure 5.6: Representation of the uniaxial tensile test considered for validation.

governing the deformations of the cubic domain reads:

$$\text{find } \hat{\mathbf{d}}: \mathcal{B}_0 \rightarrow \mathbb{R}^3 : \begin{cases} \hat{\nabla} \cdot \mathbf{P} = \mathbf{0} & \text{in } \mathcal{B}_0, \\ \mathbf{P}\hat{\mathbf{n}} = \hat{s}\hat{\mathbf{Y}} & \text{on } \Gamma_s, \\ \mathbf{P}\hat{\mathbf{n}} = \mathbf{0} & \text{on } \Gamma_{Free}, \\ \hat{d}_{\hat{Y}} = 0 \text{ and } (\mathbf{P}\hat{\mathbf{n}}) \cdot \mathbf{E}_1 = (\mathbf{P}\hat{\mathbf{n}}) \cdot \mathbf{E}_3 = 0 & \text{on } \Gamma_{D_{\hat{Y}}}, \\ \hat{d}_{\hat{X}} = 0 \text{ and } (\mathbf{P}\hat{\mathbf{n}}) \cdot \mathbf{E}_2 = (\mathbf{P}\hat{\mathbf{n}}) \cdot \mathbf{E}_3 = 0 & \text{on } \Gamma_{D_{\hat{X}}}, \\ \hat{d}_{\hat{Z}} = 0 \text{ and } (\mathbf{P}\hat{\mathbf{n}}) \cdot \mathbf{E}_1 = (\mathbf{P}\hat{\mathbf{n}}) \cdot \mathbf{E}_2 = 0 & \text{on } \Gamma_{D_{\hat{Z}}}, \end{cases} \quad (5.26)$$

where $\mathbf{E}_2 = (0, 1, 0)$, Γ_s is the surface on which the tensile stress is applied, Γ_{Free} represents the two lateral surfaces on which no external forces act, while Γ_{D_i} , for $i = (\hat{X}, \hat{Y}, \hat{Z})$, are the surfaces on which Dirichlet boundary conditions are imposed in order to either constrain the movement of body along the direction of the tensile stress and to take into account the symmetry of the domain Hughes [2000]. As discussed in Sec. 4.2.1, for any value of the uniaxial tensile stress \hat{s} , the deformation gradient has a diagonal form. However, under the nearly-incompressibility assumption, it does not depend solely on the deformation of the body along the direction of the tensile stress, see Eq. (4.18). Indeed, as described hereafter, for isotropic models $\mathbf{F} = \mathbf{F}(\lambda_{\hat{Y}}, J)$, while for anisotropic models $\mathbf{F} = \mathbf{F}(\lambda_{\hat{X}}, \lambda_{\hat{Y}}, J)$. In order to validate the implementation of the constitutive models for different levels of deformation, different values of tensile stress \hat{s}_i , for $i = 1, \dots, N_s$ where N_s is the number of applied loads, have been considered. The validation process can be summarized in the following steps:

1. For each value \hat{s}_i of tensile stress, solve problem (5.26);
2. Extract, from the numerical solution $(\hat{\mathbf{d}}_h)_i$ the deformation $\lambda_{\hat{Y}_i}$ and define \mathbf{F} as in Eq. (5.27);
3. Compute the volume ratio J for which one of the other two diagonal components of the first Piola-Kirchhoff tensor $\mathbf{P}(\hat{\mathbf{d}})$ is zero, namely solve $\mathbf{P}(\hat{\mathbf{d}})_{\hat{X}\hat{X}} = \mathbf{P}(\lambda_{\hat{Y}_i}, J)_{\hat{X}\hat{X}} = 0$;
4. Compare the volume ratio J obtained from the solution of the above nonlinear equation $\mathbf{P}(\lambda_{\hat{Y}_i}, J)_{\hat{X}\hat{X}} = 0$ with the one obtained from the numerical simulation, indicated by J_i ;
5. Compute the component $(\mathbf{P}((\hat{\mathbf{d}}_h)_i)_{\hat{Y}\hat{Y}})_i = (\mathbf{P}_{\hat{Y}\hat{Y}}(\lambda_{\hat{Y}_i}, J_i))_i$ and compare it with the applied load \hat{s}_i . If the numerical results are correct, the equality $(\mathbf{P}_{\hat{Y}\hat{Y}}(\lambda_{\hat{Y}_i}, J_i))_i = \hat{s}_i$ should be satisfied.

The numerical validation has been carried out on a tetrahedral mesh composed of 6144 elements and using both linear (P1) and quadratic (P2) finite element spaces. The numerical results are shown in

Model ($\overline{\mathcal{W}}^{iso}$)	Parameters
$\overline{\mathcal{W}}_{SVK}^{iso}$	$E = 1.6438 \cdot 10^6, \nu = 0.4500$
$\overline{\mathcal{W}}_{EXP1}^{iso}$	$\alpha_1 = 4.4700 \cdot 10^5, \gamma_1 = 8.3500$
$\overline{\mathcal{W}}_{EXP2}^{iso}$	$\alpha_2 = 5.8111 \cdot 10^6, \gamma_2 = 4.0801$

Table 5.1: Material parameters for the isotropic models. E, α_1, α_2 [dyn/cm²]; ν, γ_1, γ_2 [-].

the case of $\mathbb{P}1$ elements for which the number of degrees of freedom (DOF), i.e. the dimension $3N_h$ of the vector of coefficients in Eq. (5.7), is 4131; in the following, firstly, the validation of isotropic models is presented, then the one of anisotropic models is shown. It is worth pointing out that, although the material parameters considered in the validation process have been set according to the ones found in literature, they do not represent the mechanical properties of any real specimen of arterial tissue. In the volumetric strain energy function of Eq. (4.57), the penalization parameter is $\kappa = 5.0 \cdot 10^8$ dyn/cm².

As it will be discussed in Sec. 5.4, the isotropic models for which the numerical validation is presented are the SVK, EXP1, and EXP2 models. The material parameters for the isochoric strain energy functions are presented in Tab. 5.1. In the case of isotropic constitutive models, under the nearly-incompressibility assumption, the deformation gradient \mathbf{F} reads:

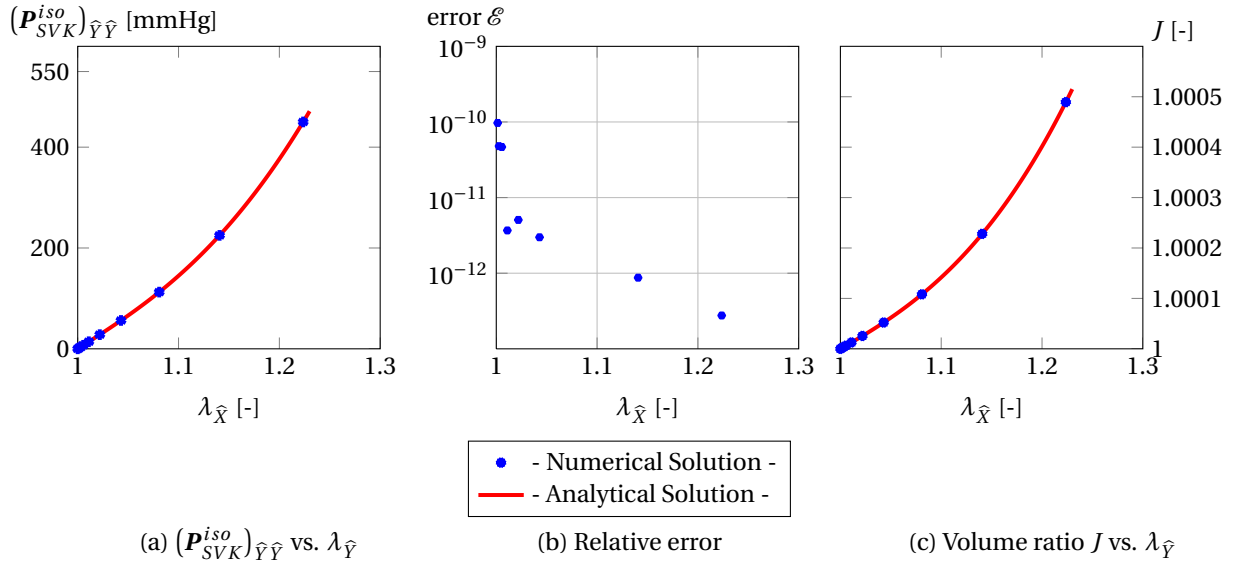
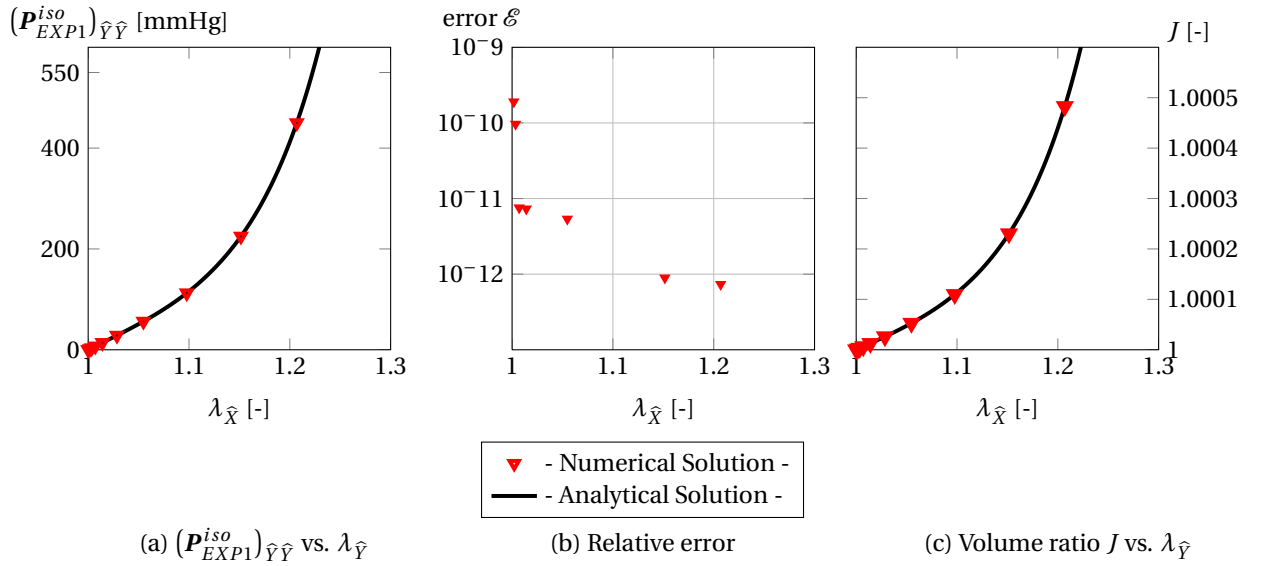
$$\mathbf{F} = \begin{pmatrix} \sqrt{\frac{J}{\lambda_{\hat{\gamma}}}} & 0 & 0 \\ 0 & \lambda_{\hat{\gamma}} & 0 \\ 0 & 0 & \sqrt{\frac{J}{\lambda_{\hat{\gamma}}}} \end{pmatrix}, \quad (5.27)$$

from which, by means of Eqs. (4.58) and (4.61), the first Piola-Kirchhoff tensor can be computed. Figs. (5.7)-(5.9) show the validation of the isotropic models; on the left and middle columns, the relation $\mathbf{P}_{\hat{\gamma}\hat{\gamma}}^{iso} = \mathbf{P}_{\hat{\gamma}\hat{\gamma}}^{iso}(\lambda_{\hat{\gamma}})$ and $J = J(\lambda_{\hat{\gamma}})$ are presented both for a continuous distribution of deformations $\lambda_{\hat{\gamma}}$ (indicated by the continuous curve) and for the deformations $\lambda_{\hat{\gamma}_i}$ measured for each uniaxial tensile test. On the right column, for each value of applied load \hat{s}_i , the relative error for each validation test is represented; the latter is defined as

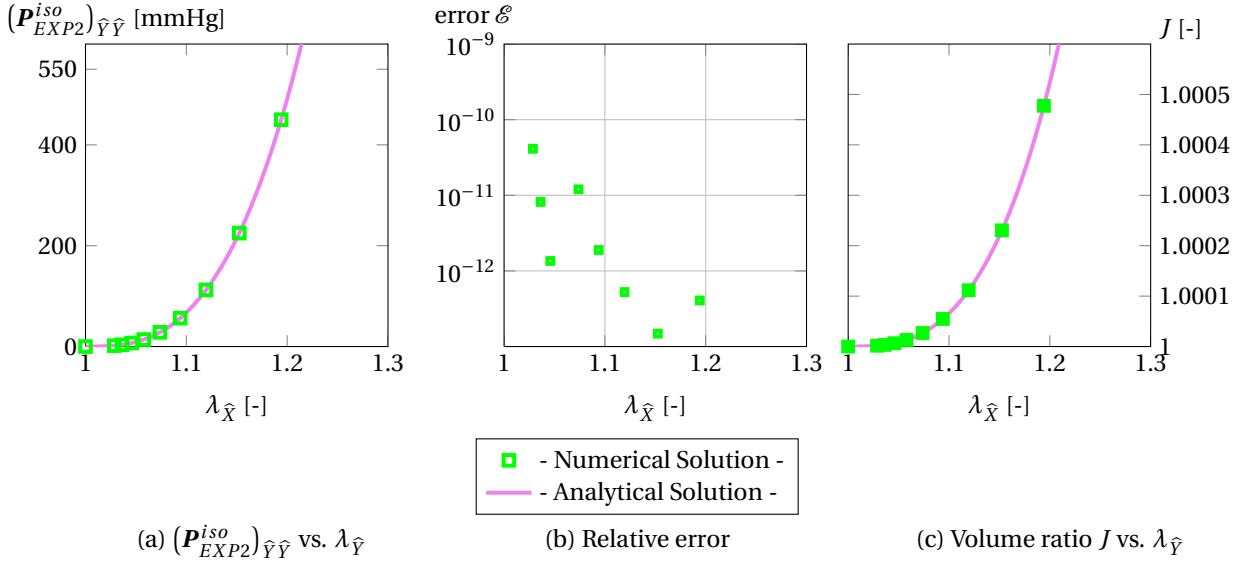
$$\mathcal{E} = \frac{\left| \left(\mathbf{P}_{\hat{\gamma}\hat{\gamma}}^{iso} \right)_i - \hat{s}_i \right|}{\hat{s}_i}, \quad (5.28)$$

where $\left(\mathbf{P}_{\hat{\gamma}\hat{\gamma}}^{iso} \right)_i = \mathbf{P}_{\hat{\gamma}\hat{\gamma}}^{iso} = \mathbf{P}_{\hat{\gamma}\hat{\gamma}}^{iso}(\lambda_{\hat{\gamma}_i}, J_i)$. From Figs. (5.7)-(5.9), it can be observed that for all the values of the applied load \hat{s}_i , the relative error between the imposed stress and the ones obtained from the numerical simulation is extremely small. In addition, also for the volume ratio J , the results obtained from the numerical simulations are overlapped on the continuous curve.

In Sec. 4.2.2 it has been anticipated that, in this work, either the EXP1 or EXP2 models are two possible modeling choices for the background material (i.e. the elastin); however, only the EXP1 model is considered. The reasons for this choice will be made more clear in Sec. 5.4. On the other hand, both the laws in Eqs. (4.38) and (4.46) are employed in the validation process for the description of the single family of collagen fibers. In literature, when anisotropic models are considered, two families of fibers


 Figure 5.7: Stress-strain relation $P_{\hat{Y}\hat{Y}}^{iso} = P_{\hat{Y}\hat{Y}}^{iso}(\lambda_{\hat{X}})$ for the SVK model

 Figure 5.8: Stress-strain relation $P_{\hat{Y}\hat{Y}}^{iso} = P_{\hat{Y}\hat{Y}}^{iso}(\lambda_{\hat{X}})$ for the EXP1 models

are usually assumed to be continuously immersed in the background material, as in e.g. Tricerri et al. [2014]; Balzani et al. [2006a]; Brinkhues et al. [2013]. Therefore, two families of fibers are considered in the validation process as well. In particular, they are assumed to form an angle $\beta^{(1)} = \frac{\pi}{6}$, and $|\beta^{(1)}| = |\beta^{(2)}|$ with respect to the \hat{Y} direction, as represented in Fig. 5.6 and the mechanical responses of the two families of fibers are supposed to be characterized by the same material parameters in Eqs. (4.38) and (4.46). The material parameters for the different isochoric strain energy functions are summarized in Tab. 5.2. In the following, an anisotropic model will be indicated by the couple of strain energy functions describing the background material and the single family of collagen fibers, e.g. (EXP1,


 Figure 5.9: Stress-strain relation $P_{\hat{Y}\hat{Y}}^{iso} = P_{\hat{Y}\hat{Y}}^{iso}(\lambda_{\hat{Y}})$ for the EXP2 models

EXP2-RC) if $\overline{\mathcal{W}}_{iso}^{aniso} = \overline{\mathcal{W}}_{EXP1}^{iso}$ and $\overline{\mathcal{W}}_{fibers}^{(i)} = \overline{\mathcal{W}}_{EXP2-RC}^{(i)}$ in Eq. (4.34). In Tab. 5.2, $\lambda_A^{(1)}$ and $\lambda_{MM}^{(1)}$ are the

Model ($\overline{\mathcal{W}}^{aniso}$)	Material Parameters
$\overline{\mathcal{W}}_{iso,EXP1}^{aniso}$	$\alpha_1 = 1.4740 \cdot 10^4$, $\gamma_1 = 0.8620$
$\overline{\mathcal{W}}_{fibers,RC}^{(i)}$	$\alpha^{(1)} = 2.0 \cdot 10^5$, $\gamma^{(1)} = 3.0$ $\beta^{(1)} = \frac{\pi}{6}$, $\lambda_A^{(1)} = 1$
$\overline{\mathcal{W}}_{fibers,sMM}^{(i)}$	$\alpha^{(1)} = 2.0 \cdot 10^5$, $\gamma^{(1)} = 3.0$ $\beta^{(1)} = \frac{\pi}{6}$, $\lambda_{MM}^{(1)} = 1.21$

Table 5.2: Material parameters for the isochoric strain energy functions composing the anisotropic (EXP1, EXP2-RC) and (EXP1, EXP2-sMM) models. α_1 , $\alpha^{(1)}$ [dyn/cm²]; $\beta^{(1)}$ [rad]; $\gamma_1, \gamma^{(1)}$, $\lambda_A^{(1)}$ [-].

activation stretches for the single family of collagen fibers, see Sec. 4.2.2. For the uniaxial tensile test, the stretch $I_4^{(i)}$ associated to the single family of fibers can be easily computed as

$$I_4^{(i)} = \lambda_{\hat{X}}^2 \sin(\beta^{(i)}) + \lambda_{\hat{Y}}^2 \cos(\beta^{(i)}), \quad (5.29)$$

where $\lambda_{\hat{X}}$ and $\lambda_{\hat{Y}}$ are the deformations along the two directions. In the case of anisotropic models, the deformation gradient tensor \mathbf{F} reads as follows:

$$\mathbf{F} = \begin{pmatrix} \lambda_{\hat{X}} & 0 & 0 \\ 0 & \lambda_{\hat{Y}} & 0 \\ 0 & 0 & \sqrt{\frac{J}{\lambda_{\hat{X}} \lambda_{\hat{Y}}}} \end{pmatrix}. \quad (5.30)$$

The validation process is similar to the one presented before; however, given a certain deformation $\lambda_{\hat{Y}}^*$, also the deformation $\lambda_{\hat{X}}$ obtained from the numerical simulations can be compared with the one

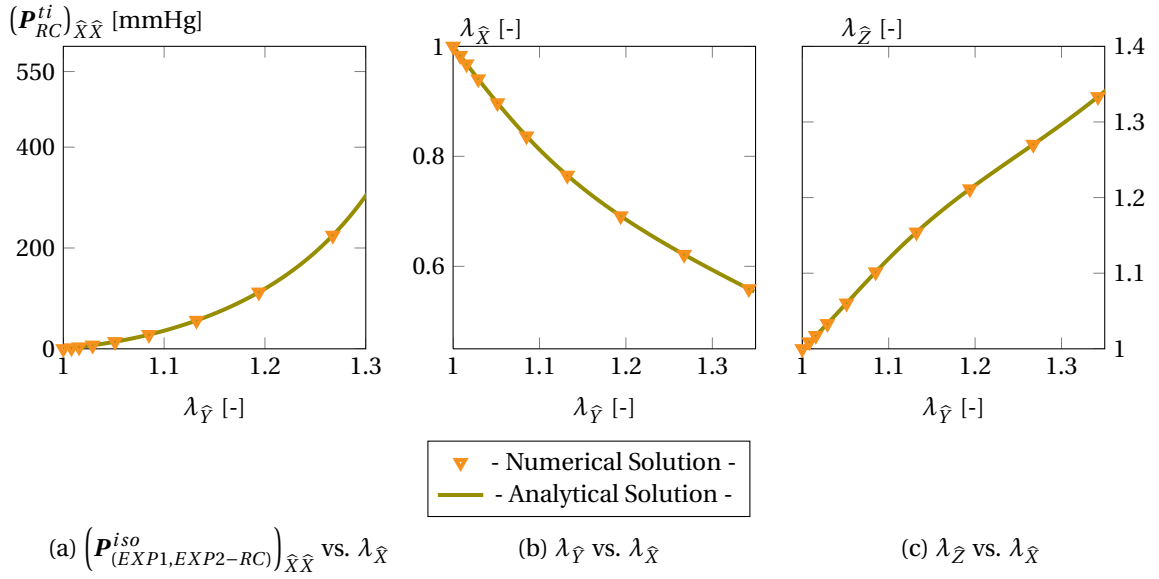


Figure 5.10: Stress-strain relation $P_{\hat{X}\hat{X}}^{iso} = P_{\hat{X}\hat{X}}^{iso}(\lambda_{\hat{X}})$ for the anisotropic (EXP1, EXP2-RC) model

obtained from the solution of the nonlinear system:

$$\begin{cases} \mathbf{P}_{\hat{X}\hat{X}}^{aniso}(\lambda_{\hat{X}}, \lambda_{\hat{Y}}^*, J) = 0 \\ \mathbf{P}_{\hat{Z}\hat{Z}}^{aniso}(\lambda_{\hat{X}}, \lambda_{\hat{Y}}^*, J) = 0. \end{cases} \quad (5.31)$$

Figs. (5.10) and (5.11) and Figs. (5.12) and (5.13) show the validation of the anisotropic models (EXP1, EXP2-RC) and of (EXP1, EXP2-sMM), respectively. As for the isotropic case, the deformations on the volume ratios J are overlapped on the curves obtained with a continuous distribution of deformations $\lambda_{\hat{Y}}$, and consequently, the relative errors defined in Eq. (5.28) have the same order of magnitude observed in the isotropic case. In particular, in Fig. 5.12 the abrupt change in the mechanical response is due to the abrupt recruitment of the collagen fibers.

From Figs. (5.10) and (5.12), it can be noticed that the cubic domain does not contract in the \hat{Z} direction. This is due to the particular choice of the material parameters and to the fact that the mechanical load is applied in the same plane where the fibers are defined. Indeed, in Eq. (5.30), for to the mechanical test under consideration, $\lambda_{\hat{Y}} > 1$ and $\lambda_{\hat{X}} < 1$. On the other hand, the condition

$$\frac{J}{\lambda_{\hat{X}}\lambda_{\hat{Y}}} < 1, \quad (5.32)$$

which would represent a contraction along the \hat{Z} direction, is not necessarily verified for all states of deformations. Let us assume that ideally $J = 1$, then a contraction along the \hat{Z} direction would occur if the condition $\frac{1}{\lambda_{\hat{Y}}} < \lambda_{\hat{X}}$ is verified. From the mechanical point of view, the deformation $\lambda_{\hat{Y}}$ depends on the mechanical characteristics of the fibers (i.e. the stiffer the single family of fibers, the smaller $\lambda_{\hat{Y}}$ for a certain value of applied load), while $\lambda_{\hat{X}}$ depends on the mechanical properties of the background material. For the material parameters in Tab. 5.2, since in practice $J > 1$, the condition in Eq. (5.32) is not verified, leading to the observed expansion along the \hat{Z} direction. For the sake of completeness,

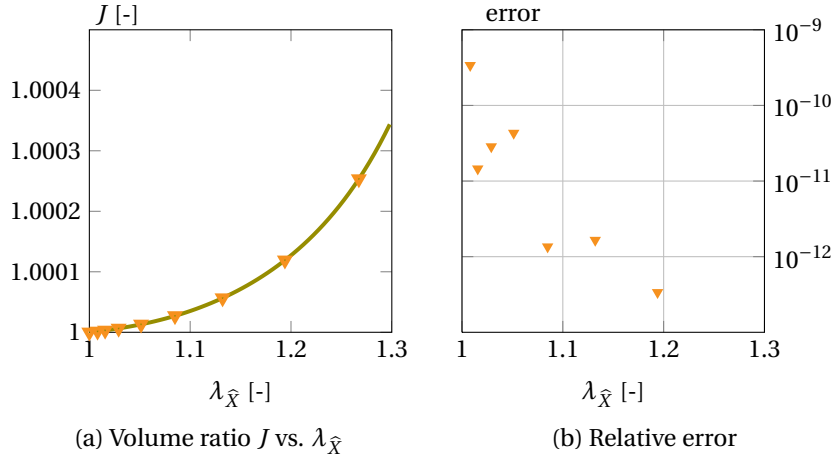


Figure 5.11: Stress-strain relation $P_{\hat{X}\hat{X}}^{iso} = P_{\hat{X}\hat{X}}^{iso}(\lambda_{\hat{X}})$ for the anisotropic (EXP1, EXP2-RC) model

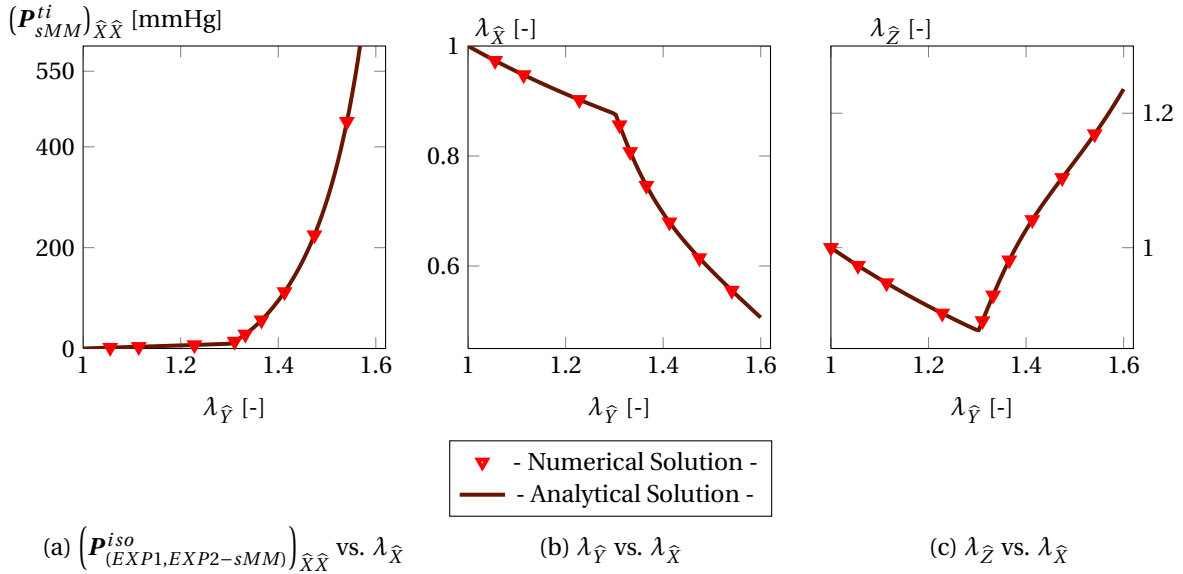


Figure 5.12: Stress-strain relation $P_{\hat{X}\hat{X}}^{iso} = P_{\hat{X}\hat{X}}^{iso}(\lambda_{\hat{X}})$ for the anisotropic (EXP1, EXP2-sMM) model

another test has been carried out. As a representative example, the anisotropic (EXP1, EXP2-RC) model is considered; however, the same conclusions can be drawn considering the (EXP1, EXP2-sMM) law. The same uniaxial tensile test as the one considered during the validation process has been performed, but the material parameters for the background material and collagen fibers have been swapped. The deformations of the domain are represented in Fig. 5.14; however, for the sake of brevity, graphs as the ones in Figs. (5.10)-(5.13) are not presented here. As it can be noticed, the cubic solid elongates along the \hat{Y} direction and shrinks along the other two directions; in particular, the deformations along the \hat{X} and \hat{Z} directions are different due to the presence of the collagen fibers.

In order to highlight the relevance of the efficient implementation of highly nonlinear constitutive models, the computational times required to assemble both $\mathcal{J}_{\mathbf{P}}(\hat{\mathbf{a}}_h^k)(\hat{\boldsymbol{\psi}}_B, \hat{\boldsymbol{\psi}}_A)$ and $\mathcal{R}(\hat{\mathbf{a}}_h^k)(\hat{\boldsymbol{\psi}}_h)$ in Eq. (5.13) by using the *Expression Template Assembly* routines (see Sec. 5.2 and Quinodoz [2012]) and

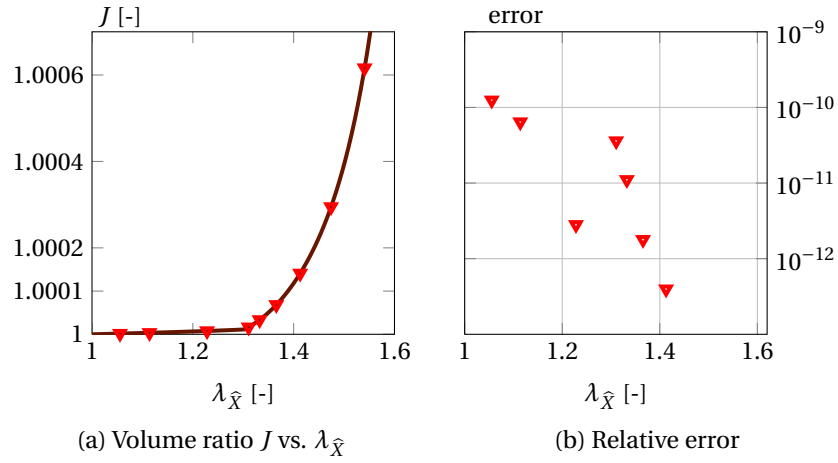


Figure 5.13: Stress-strain relation $P_{\hat{X}\hat{X}}^{iso} = P_{\hat{X}\hat{X}}^{iso}(\lambda_{\hat{X}})$ for the anisotropic (EXP1, EXP2-sMM) model

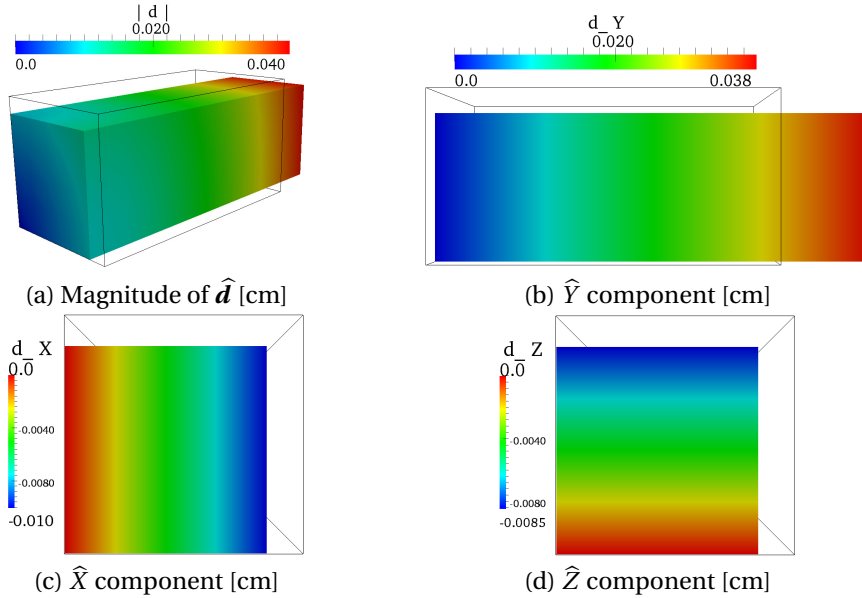


Figure 5.14: Deformation of the cube in Fig. 5.6 for which the material parameters of Tab. 5.2 for the elastin and collagen fibers have been swapped

the assembly procedures described, for instance, in Hughes [2000]; Zienkiewicz et al. [2000] have been compared. It is worth pointing out that, from the implementation point of view, the assembly techniques described in Hughes [2000]; Zienkiewicz et al. [2000] make strong use of nested loops over the single element and on its quadrature nodes to compute the integrals that define $\mathcal{J}_{\mathbf{P}}(\hat{\mathbf{a}}_h^k)(\hat{\boldsymbol{\psi}}_B, \hat{\boldsymbol{\psi}}_A)$ and $\mathcal{R}(\hat{\mathbf{a}}_h^k)(\hat{\boldsymbol{\psi}}_h)$; on the other hand, the routines based on the *Expression Template Assembly* strongly reduce the number of nested loops (see Quinodoz [2012] for details). For this reason, the computational time required to assemble $\mathcal{J}_{\mathbf{P}}(\hat{\mathbf{a}}_h^k)(\hat{\boldsymbol{\psi}}_B, \hat{\boldsymbol{\psi}}_A)$ and $\mathcal{R}(\hat{\mathbf{a}}_h^k)(\hat{\boldsymbol{\psi}}_h)$ with the *Expression Template Assembly* is reduced by a factor 0.5 with respect to the one needed when employing the procedures of Hughes [2000]; Zienkiewicz et al. [2000].

5.4 Numerical simulations of static inflation tests

This section deals with the numerical validation of some of the constitutive models discussed in Ch. 4 by means of numerical simulations of inflation tests on cylindrical specimens of arteries. The constitutive models, for which the numerical simulations are carried out, are chosen based on their capability of approximating the experimental measurements of the stress-strain relation of an anterior cerebral artery (ACA). Firstly, the experimental measurements and the determination of the material parameters are presented in Sec. 5.4.1. Afterwards, the numerical simulations of inflation tests are presented and conclusions are drawn in Sec. 5.4.2.

5.4.1 The set of experimental measurements and the least squares data fitting

In order to characterize the mechanical behavior of the healthy arterial tissue, it is necessary to estimate the material parameters of the isochoric constitutive models described in Sec. 4.3.3. In this work, the material parameters of each isochoric model are determined by computing the least-squares approximation Quarteroni et al. [2007] of experimental measurements of the stress-strain relation of cerebral arteries Scott et al. [1972]. In Scott et al. [1972] quasi-static inflation tests up to the transmural pressure ΔP , i.e. the difference between the pressures imposed on the external and internal surfaces of the vessel wall, of 200 mmHg on cylindrical specimens of healthy human anterior cerebral artery (ACA) are shown. The data in Scott et al. [1972] describe the deformations of the internal radius of the specimens of ACA, measured by the circumferential stretch in cylindrical coordinates defined in Eq. (4.22), according to the level of transmural pressure ΔP . Although in Scott et al. [1972] both healthy and unhealthy specimens of anterior cerebral arteries are considered, in this work only the experimental data on healthy arterial tissue are taken into account to estimate the material parameters for the different models. The data of Scott et al. [1972] are represented in Fig. 5.15; it can be observed that the mechanical response shows the typical nonlinear behavior of an healthy vessel, see Sec. 2.2. More precisely, the mechanical behavior is characterized by a nearly linear toe region at low strains and an exponential like region at high strains. As discussed in Sec. 2.2, the exponential like behavior for high strains is due to the recruitment of the collagen fibers at finite strains Scott et al. [1972]; Burton [1954]; Roach and Burton [1957]; Hill et al. [2012]. As already mentioned in Sec. 4.2, in this work the cerebral arterial tissue is modeled as composed of a unique layer of tissue. The goal of the current work is to validate the constitutive models under consideration in the case of a three-dimensional inflation test for which the material parameters are obtained from data fitting of experimental measurements. This choice is supported by the fact that, as pointed out in Dalong et al. [2012], there is no layer-specific experimental data published for the elastic properties of cerebral arteries. Consequently, in Dalong et al. [2012] the material parameters for the different arterial layers are artificially chosen according to the experimental data presented in Kenneth et al. [2008].

In order to estimate the material parameters, similarly to Wulandana and Robertson [2005]; Li and Robertson [2009b], the ACA is modeled as a cylindrical membrane of undeformed internal radius (R_0) and thickness (h) composed of an homogeneous and incompressible material, as represented in Fig. 5.16-(a). By virtue of the incompressibility assumption (i.e. $J = 1$), the volumetric function \mathcal{U} in Eq. (4.58) is identically zero, while the modified invariants of $\bar{\mathbf{C}}$ coincide with the principal invariants of \mathbf{C} , i.e. $\bar{\mathbf{C}} \equiv \mathbf{C}$ (see Eqs. (4.60), (4.63), and (4.64)). In Scott et al. [1972] the deformation of the internal radius is measured by the circumferential stretch, indicated by $\lambda_{\hat{\theta}\hat{\theta}}$, that is defined as $\lambda_{\hat{\theta}\hat{\theta}} = r/R_0$, with r being the deformed radius at a certain level of transmural pressure ΔP . In order to fit the experimental data, the nonlinear functions $\mathcal{F} = \mathcal{F}(\lambda_{\hat{\theta}\hat{\theta}})$ for isotropic and anisotropic models detailed hereafter, that

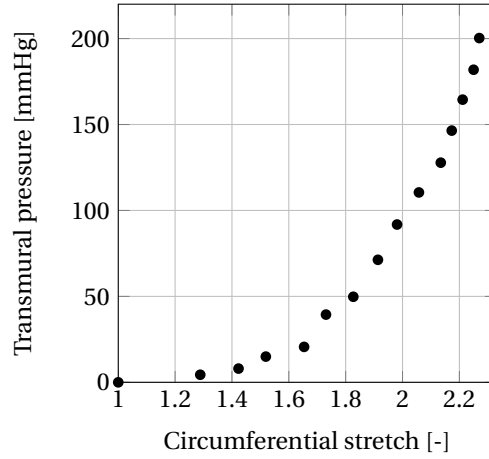


Figure 5.15: Experimental measurements of stress-strain relation from specimens of anterior cerebral arteries; data from Scott et al. [1972]. The measurements showed the typical exponential like behavior described in Sec. 2.2

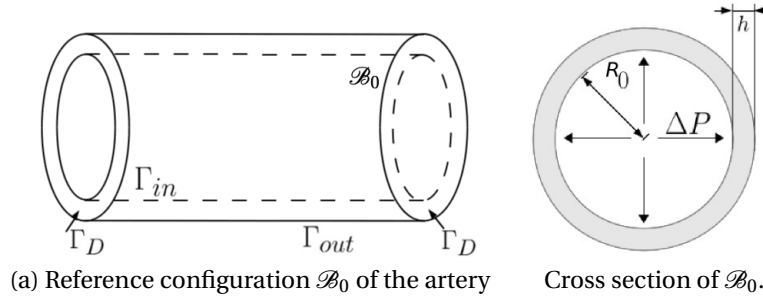


Figure 5.16: Computational domain \mathcal{B}_0 representing the arterial specimen and data of problem (5.1).

relate the membrane tension \mathcal{T} to the circumferential stretch $\lambda_{\hat{\theta}\hat{\theta}}$, are considered Li and Robertson [2009b]; Wulandana and Robertson [2005]; Naghdi and Tang [1977]; Naghdi [1984]. In addition, the membrane tension is related to the transmural pressure by means of the Young-Laplace equation, $\mathcal{T} = r \Delta P$ (Scott et al. [1972]). For a given constitutive model for the cerebral arterial tissue, the nonlinear approximation of the experimental data is computed by means of the Levenberg-Marquardt least-squares method Marquardt [1963].

Once the material parameters of a constitutive model have been estimated, the quality of the least-squares approximation is evaluated by means of the R^2 value Brown [2001] defined as:

$$R^2 = 1 - \frac{\sum_{i=1}^{n_s} (\mathcal{T}_i - \mathcal{T}(\lambda_{\hat{\theta}\hat{\theta},i}))^2}{\sum_{i=1}^{n_s} (\mathcal{T}_i - \overline{\mathcal{T}})^2}, \quad (5.33)$$

where n_s is the number of stress-strain experimental measurements $(\lambda_{\hat{\theta}\hat{\theta},i}, \mathcal{T}_i)$, for $i = 1, \dots, n_s$, $\overline{\mathcal{T}}$ is the mean measured membrane tension, and $\mathcal{T}(\lambda_{\hat{\theta}\hat{\theta},i})$ is the membrane tension evaluated at the measured deformation $\lambda_{\hat{\theta}\hat{\theta},i}$. The closer to one is the R^2 value corresponding to a constitutive model, the better is the data fitting.

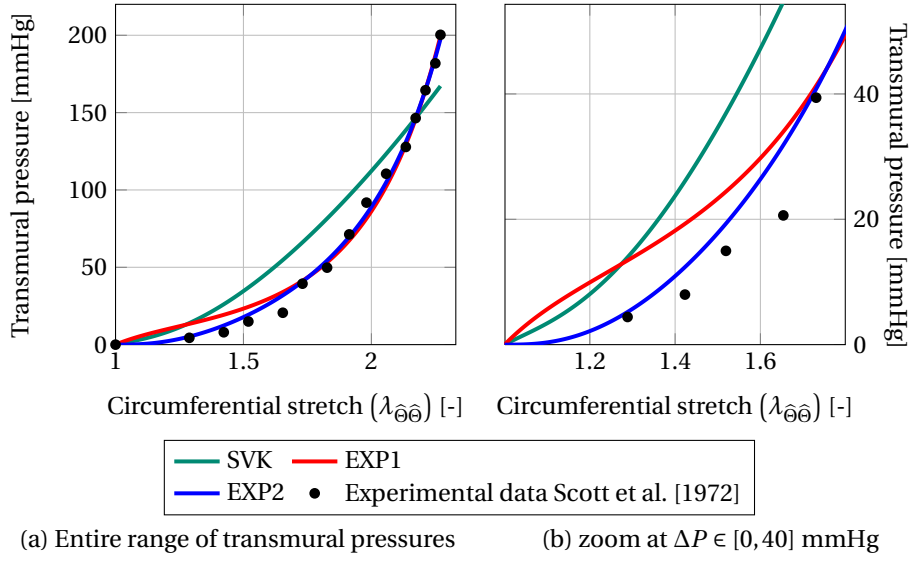


Figure 5.17: Least-squares approximation of the data in Scott et al. [1972] using the isotropic models. Full range of transmural pressures $\Delta P \in [0, 200]$ mmHg (left); zoom at low transmural pressures regime $\Delta P \in [0, 40]$ mmHg (right).

In the remainder of the section, the functions $\mathcal{T}(\lambda_{\hat{\theta}\hat{\theta}})$ used to approximate the experimental measurements for isotropic and anisotropic models are presented together with the values of the selected material parameters and the corresponding R^2 values. As discussed in Sec. 4.3.2, the penalization parameter κ in Eq. (4.57) is not involved in the parameter estimation procedure, since $J = 1$ and $\mathcal{U}_2(J) = -$, and set equal to $\kappa = 9.0 \cdot 10^6$ dyn/cm².

Determination of the material parameters for isotropic models

For isotropic models, under the incompressibility assumption (i.e. $J = 1$), Eq. (4.51) reduces to

$$\mathcal{W} = \overline{\mathcal{W}}^{iso}(\overline{I}_1, \overline{I}_2) = \mathcal{W}^{iso}(I_1, I_2). \quad (5.34)$$

According to Wulandana and Robertson [2005], in the case of isotropic constitutive models, the stress-strain function $\mathcal{T} = \mathcal{T}(\lambda_{\hat{\theta}\hat{\theta}})$ for the data fitting is

$$\mathcal{T}(\lambda_{\hat{\theta}\hat{\theta}}) = \frac{h}{\lambda_{\hat{\theta}\hat{\theta}}} \left(\lambda_{\hat{\theta}\hat{\theta}}^2 - \frac{1}{\lambda_{\hat{\theta}\hat{\theta}}^2} \right) \left(2 \frac{\partial \mathcal{W}^{iso}}{\partial I_1} + 2 \frac{\partial \mathcal{W}^{iso}}{\partial I_2} \right). \quad (5.35)$$

Fig. 5.17-(a) shows the least-squares approximation of the experimental data of Scott et al. [1972] by means of the function $\mathcal{T} = \mathcal{T}(\lambda_{\hat{\theta}\hat{\theta}})$ for the $(\mathcal{W}_{SVK}^{iso}, \mathcal{W}_{EXP1}^{iso}, \mathcal{W}_{EXP2}^{iso})$ isotropic constitutive models with the material parameters of Tab. 5.3. As indicated by the R^2 value in Tab. 5.3, in the case of the SVK model the experimental data are not properly approximated on the full range of transmural pressures. Conversely, the data fitting improves when the EXP1 and EXP2 models are considered. In these cases, as shown in Fig. 5.17-(a), for transmural pressures higher than 50 mmHg, small differences are observed between the two approximated stress-strain relations. On the other hand, see Fig. 5.17-(b), for low transmural pressures, the second order exponential (EXP2) model provides the best approximation of the data if compared with the other two isotropic models.

5.4. Numerical simulations of static inflation tests

Model (\mathcal{W}^{iso})	Parameters	R^2
\mathcal{W}_{SVK}^{iso}	$E = 1.1420 \cdot 10^5, \nu = 0.4500$	0.9338
\mathcal{W}_{EXP1}^{iso}	$\alpha_1 = 7.6350 \cdot 10^4, \gamma_1 = 0.7410$	0.9942
\mathcal{W}_{EXP2}^{iso}	$\alpha_2 = 6.8220 \cdot 10^4, \gamma_2 = 0.0609$	0.9971

Table 5.3: Material parameters and R^2 values for the isotropic models. E, α_1, α_2 [dyn/cm²]; ν, γ_1, γ_2 [-].

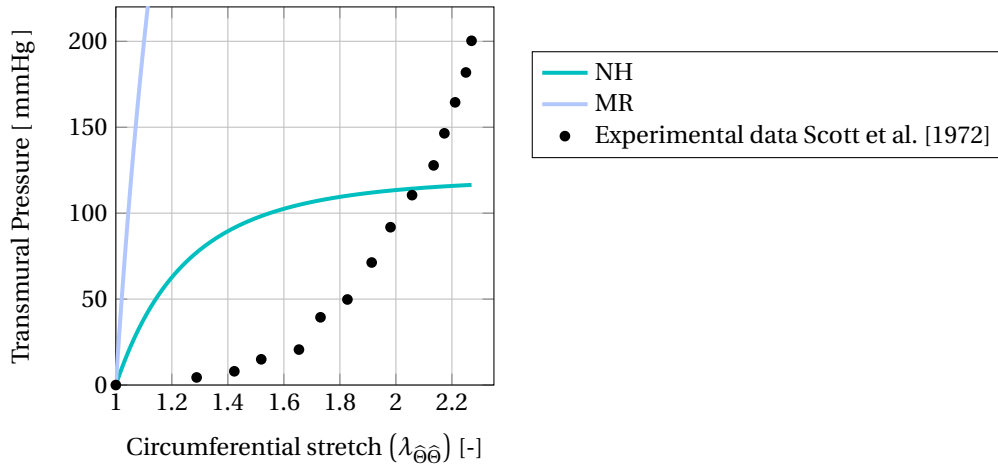


Figure 5.18: Least-squares approximation of the experimental measurements in Scott et al. [1972]

Model (\mathcal{W}^{iso})	Parameters	R^2
\mathcal{W}_{MR}^{iso}	$C_1 = 1.6479 \cdot 10^5, C_2 = 0.5480$	0.5021
\mathcal{W}_{NH}^{iso}	$E = 1.5622 \cdot 10^5, \nu = 0.4676$	0.5235

Table 5.4: Material parameters and R^2 values for the isotropic models. E, C_1, C_2 [dyn/cm²]; ν [-].

On the other hand, the Mooney-Rivlin and neo-hookean models ($\mathcal{W}_{MR}^{iso}, \mathcal{W}_{NH}^{iso}$) are not appropriate to approximate the experimental measurements, as represented in Fig. 5.18. This is due to the fact that the two strain energy functions in Eqs. (4.14) and (4.15) are first order polynomial functions of the invariants; therefore, the membrane tension in Eq. (5.35) depends solely on the term which is a concave function of the circumferential stretch. For the sake of completeness, the corresponding parameters and R^2 values are reported in Tab. 5.4. To conclude, the SVK, EXP1, and EXP2 will be employed in the numerical simulations presented in Sec. 5.4.2.

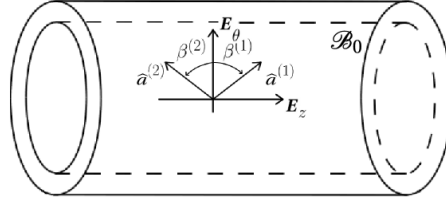


Figure 5.19: Directions $\hat{\mathbf{a}}^{(i)}$, $i = 1, 2$, of the families of collagen fibers in the reference configuration \mathcal{B}_0 of the specimen of artery

Determination of the material parameters for anisotropic models

Similarly to Eq. (5.34), under the incompressibility assumption (i.e. $J = 1$) the volumetric strain energy function in Eq. (4.51) is zero, therefore, Eq. (4.51) reduces to:

$$\mathcal{W} = \overline{\mathcal{W}}_{\text{aniso}}(\overline{I}_1, \overline{I}_2, \overline{I}_4, \overline{I}_5) = \mathcal{W}_{\text{iso}}^{\text{aniso}}(I_1, I_2) + \mathcal{W}_{\text{fibers}}^{\text{aniso}}(\mathbf{I}_4, \mathbf{I}_5). \quad (5.36)$$

As in other works where anisotropic models describe the arterial tissue (e.g. Li and Robertson [2009b]; Balzani et al. [2006a, 2012]), two families of collagen fibers oriented symmetrically with respect to the circumferential direction of the cylinder are assumed to be immersed in the background material, see Fig. 5.19. In addition, for anisotropic models, the material parameters $\alpha^{(i)}$ and $\gamma^{(i)}$ in Eqs. (4.38) and (4.46) are the same for all families of fibers. According to Li and Robertson [2009b], for the anisotropic models of Tab. 4.3 the function $\mathcal{F} = \mathcal{F}(\lambda_{\hat{\Theta}\hat{\Theta}})$ reads as :

$$\mathcal{F}(\lambda_{\hat{\Theta}\hat{\Theta}}) = \frac{h}{\lambda_{\hat{\Theta}\hat{\Theta}}} \left[2 \left(\lambda_{\hat{\Theta}\hat{\Theta}}^2 - \frac{1}{\lambda_{\hat{\Theta}\hat{\Theta}}^2} \right) \frac{\partial \mathcal{W}_{\text{iso}}^{\text{aniso}}}{\partial I_1} + \sum_{i=1}^2 2 \frac{\partial \mathcal{W}_{\text{fibers}}^{(i)}}{\partial I_4^{(i)}} \frac{\lambda_{\hat{\Theta}\hat{\Theta}}^2 \cos^2 \beta^{(i)}}{I_{4,A}^{(i)}} \right], \quad (5.37)$$

where $\beta^{(i)}$ is the angle between the characteristic direction of the i -th fiber family in the reference configuration \mathcal{B}_0 , indicated $\hat{\mathbf{a}}^{(i)}$, and the circumferential axis $\mathbf{E}_{\hat{\Theta}}$ (see Fig. 5.19). In Eq. (5.37), due to the representation of the arterial tissue as a membrane, the recruitment of the collagen fibers will occur simultaneously throughout the thickness of the vessel wall Wulandana and Robertson [2005]. In addition, it is considered that $\beta^{(1)} = -\beta^{(2)}$ and $I_{4,A}^{(1)} = I_{4,A}^{(2)}$. In order to include in the least-squares approximation the activation condition ($I_4^{(i)} > I_{4,A}^{(i)}$) of Eq. (4.34), the following modified form of Eq. (5.37) is considered:

$$\mathcal{F}(\lambda_{\hat{\Theta}\hat{\Theta}}) = \frac{h}{\lambda_{\hat{\Theta}\hat{\Theta}}} \left[2 \left(\lambda_{\hat{\Theta}\hat{\Theta}}^2 - \frac{1}{\lambda_{\hat{\Theta}\hat{\Theta}}^2} \right) \frac{\partial \mathcal{W}_{\text{iso}}^{\text{aniso}}}{\partial I_1} + \sum_{i=1}^2 2 \xi(I_4^{(i)}) \frac{\partial \mathcal{W}_{\text{fibers}}^{(i)}}{\partial I_4^{(i)}} \frac{\lambda_{\hat{\Theta}\hat{\Theta}}^2 \cos^2(\beta^{(i)})}{I_{4,A}^{(i)}} \right], \quad (5.38)$$

to relate the membrane tension to the circumferential stretch; in Eq. (5.38), $\xi(I_4^{(i)})$ is the activation function presented in Sec. 5.2.2. The activation stretch $I_{4,A}^{(i)}$ depends on the angle $\beta^{(i)}$ and on the circumferential stretch ($\lambda_{\hat{\Theta}\hat{\Theta}}^{A,(i)}$) at which the recruitment of the i -th family of collagen fibers occurs by means of the relation Li and Robertson [2009b]:

$$I_{4,A}^{(i)} = (\lambda_{\hat{\Theta}\hat{\Theta}}^{A,(i)})^2 \cos^2(\beta^{(i)}) + \sin^2(\beta^{(i)}), \quad (5.39)$$

and the additional condition $\lambda_{\hat{\theta}\hat{\theta}}^{A,(1)} = \lambda_{\hat{\theta}\hat{\theta}}^{A,(2)}$ is set. As discussed in Sec. 4.2.2, anisotropic models for which the collagen fibers are activated either at zero or finite strains are employed. In the first case (EXP2-RC model) such assumption implies that $\lambda_{\hat{\theta}\hat{\theta}}^{A,(i)} = 1$ and therefore $I_{4,A}^{(i)} = I_{4,RC}^{(i)} = 1$, for $i = 1, 2$. Conversely, for the multi-mechanism model (EXP2-sMM model) $\lambda_{\hat{\theta}\hat{\theta}}^{A,(i)} > 1$ and, therefore, $I_{4,A}^{(i)} = I_{4,MM}^{(i)} > 1$, for $i = 1, 2$, Li [2009]. In Li and Robertson [2009b]; Wulandana and Robertson [2005] an estimation of the circumferential stretch of activation in Eq. (5.39) is provided based on the measurements reported in Scott et al. [1972]. However, since experimental observations on the circumferential stretch of activation were not reported in Scott et al. [1972], $\lambda_{\hat{\theta}\hat{\theta}}^{A,(1)}$ is considered as an additional material parameter to be estimated for the EXP2-sMM model.

Tab. 5.5 summarizes the material parameters and R^2 values for each of the anisotropic models under consideration. In Tab. 5.5, $(\alpha_{iso}^{aniso}, \gamma_{iso}^{aniso})$ represent the material parameters characterizing the background material while $(\alpha^{(1)}, \gamma^{(1)}, \beta^{(1)}, \lambda_{\hat{\theta}\hat{\theta}}^{A,(1)})$ are the material parameters for the single family of collagen fibers. It is worth pointing out that the least-squares approximation of the data improves when anisotropic models are used with respect to isotropic models (Tab. 5.3). In addition, when the multi-mechanism model describes the collagen fibers, the approximation of the experimental data is further improved with respect to the EXP2-RC model. In Fig. 5.20, it can be observed that the recruitment of the collagen fibers at finite strains induces the sharp change in the membrane tension $\mathcal{F}(\lambda_{\hat{\theta}\hat{\theta}})$ around the circumferential stretch of activation $\lambda_{\hat{\theta}\hat{\theta}}^{A,(1)}$. Fig. 5.20-(a) shows the membrane tension $\mathcal{F}(\lambda_{\hat{\theta}\hat{\theta}})$ for the (EXP1, EXP2-RC) and (EXP1, EXP2-sMM) models. Fig. 5.20-(b) shows the function $\mathcal{F}(\lambda_{\hat{\theta}\hat{\theta}})$ when either the EXP1 or the EXP2 models describe the background material and the collagen fibers are represented by the EXP2-sMM model. In this case, the estimation of the circumferential stretch of activation $\lambda_{\hat{\theta}\hat{\theta}}^{A,(1)}$ is strongly affected by the choice of the model for the background material (see Fig. 5.20-(b) and Tab. 5.5). This is due to the fact that, as shown in Fig. 5.17-(b), the EXP2 model fits better than the EXP1 law the data in the low pressure regime; therefore, when using the EXP2 model for the background material, the collagen fibers are activated at a higher activation circumferential stretch to better fit in the high transmural pressure regime. The anisotropic multi-mechanism model (EXP2,

Model (\mathcal{W}_{ti})	Material Parameters	R^2
$\mathcal{W}_{EXP1}^{aniso} + \mathcal{W}_{EXP2-RC}^{(i)}$	$\alpha_{iso}^{aniso} = 1.7471 \cdot 10^4$, $\gamma_{iso}^{aniso} = 0.8620$ $\alpha^{(1)} = 1.4979 \cdot 10^5$, $\gamma^{(1)} = 0.5736$ $\beta^{(1)} = 56.52$	0.9951
$\mathcal{W}_{EXP2}^{aniso} + \mathcal{W}_{EXP2-RC}^{(i)}$	$\alpha_{iso}^{aniso} = 6.8220 \cdot 10^4$, $\gamma_{iso}^{aniso} = 0.8620$ $\alpha^{(1)} = 6.008 \cdot 10^{-6}$, $\gamma^{(1)} = 0.8211$ $\beta^{(1)} = 85.85$	0.9971
$\mathcal{W}_{EXP1}^{aniso} + \mathcal{W}_{EXP2-sMM}^{(i)}$	$\alpha_{iso}^{aniso} = 3.5270 \cdot 10^4$, $\gamma_{iso}^{aniso} = 0.3424$ $\alpha^{(1)} = 1.3370 \cdot 10^5$, $\gamma^{(1)} = 0.2141$ $\beta^{(1)} = 42.82$, $\lambda_{\hat{\theta}\hat{\theta}}^{A,(1)} = 1.5009$	0.9980
$\mathcal{W}_{EXP2}^{aniso} + \mathcal{W}_{EXP2-sMM}^{(i)}$	$\alpha_{iso}^{aniso} = 5.5420 \cdot 10^4$, $\gamma_{iso}^{aniso} = 3.0 \cdot 10^{-4}$ $\alpha^{(1)} = 1.3087 \cdot 10^5$, $\gamma^{(1)} = 0.5133$ $\beta^{(1)} = 47.27$, $\lambda_{\hat{\theta}\hat{\theta}}^{A,(1)} = 1.6538$	0.9985

Table 5.5: Parameters for the anisotropic models. α_{iso}^{aniso} , $\alpha^{(1)}$ [dyn/cm²]; $\beta^{(1)}$ [°]; γ_{iso}^{aniso} , $\gamma^{(1)}$, $\lambda_{\hat{\theta}\hat{\theta}}^{A,(1)}$ [-].

EXP2-sMM) model gives the best least-squares approximation of the experimental measurement; however, it will not be employed in the numerical simulations of healthy cerebral arterial tissue due to

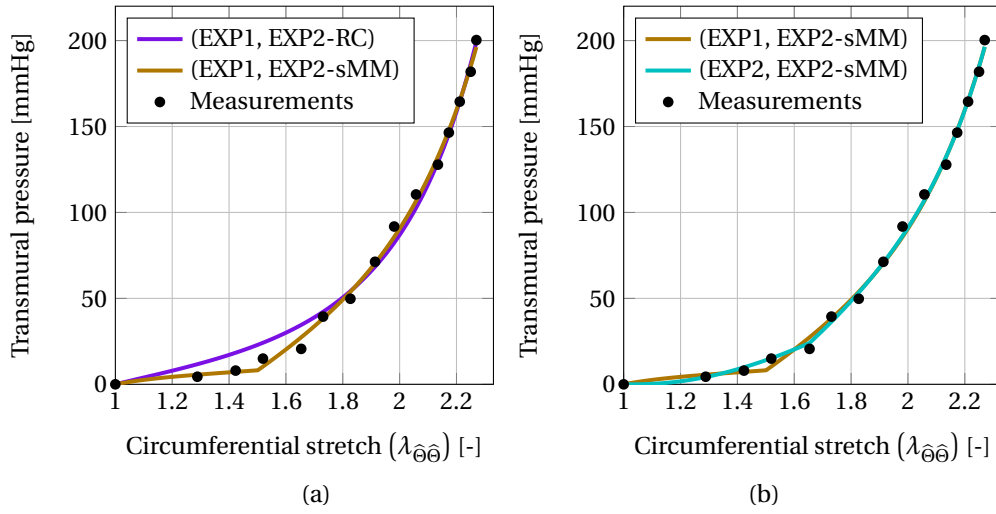


Figure 5.20: Least-squares approximation of the data in Scott et al. [1972] using the anisotropic models. Effects on the least-squares approximation of the experimental data of fixing either the constitutive law for the background material (case (a)) or the strain energy for the single family of fibers (b)

numerical issues related to the numerical solution of the structural mechanics problem (5.1) described in Secs. 5.2.3 and 5.2.4. The anisotropic models that will be considered in Sec. 5.4.2 are the (EXP1, EXP2-RC) and the multi-mechanism (EXP1, EXP2-sMM) law.

Concerning the estimation of the material parameters for the anisotropic models, it has to be remarked that the solution provided by the Levenberg-Marquardt method is strongly affected by the initial guess for the characteristic angle $\beta^{(1)}$, indicated by $\beta_0^{(1)}$, while the influence of the initial guesses for the remaining parameters is negligible. In Tab. 5.6 the material parameters for the anisotropic model composed of the couple (EXP1,EXP2-RC) resulting from different initial guesses of the $\beta^{(1)}$ are summarized. It is worth pointing out that, although the R^2 value of the least-squares approximation is not affected by $\beta_0^{(1)}$, the estimation of the material parameters of the anisotropic part of the strain energy function $\overline{\mathcal{W}}_{fibers}^{aniso}$ is strongly affected by the value of $\beta_0^{(1)}$. This indicates that, when using anisotropic models for the arterial tissue, the nonlinear least-squares approximation problem exhibits multiple local minima and highlights the importance of having experimental data of the characteristic directions of the collagen fibers in the vessel wall. Since no experimental observations of the collagen fibers were reported in Scott et al. [1972], as initial guess for the least-squares algorithm, $\beta_0^{(1)} = 45^\circ$ has been chosen. Finally, when $\beta_0^{(1)} = 90^\circ$ the collagen fibers are oriented along the axial direction of the cylinder; in this case, the R^2 value coincides with the one of the EXP1 model since the fibers are not stretched during the inflation tests, and therefore not activated for any value of the transmural pressure Li [2009].

5.4.2 Numerical simulations of inflation tests

This section presents numerical simulations of mechanical inflation tests on a computational domain representing a cylindrical specimen of anterior cerebral artery. The mechanical problem is defined in the computational domain \mathcal{B}_0 of Fig. 5.16- (a) that represents a cylindrical geometry of internal radius

5.4. Numerical simulations of static inflation tests

$\beta_0^{(1)}$	α_{iso}^{aniso}	γ_{iso}^{aniso}	$\alpha^{(1)}$	$\gamma^{(1)}$	$\beta^{(1)}$	R^2 value
30°	$1.7470 \cdot 10^4$	0.8620	$1.1263 \cdot 10^5$	0.4313	53.67°	0.9950
45°	$1.7470 \cdot 10^4$	0.8620	$1.4979 \cdot 10^5$	0.5736	56.51°	0.9950
60°	$1.7451 \cdot 10^4$	0.8620	$8.6011 \cdot 10^4$	3.2935	69.61°	0.9950
90°	$7.635 \cdot 10^4$	0.7411	0	0	90°	0.9942

Table 5.6: R^2 values obtained from the least-squares data fitting for anisotropic model (EXP1,EXP2-RC) for different values of $\beta_0^{(1)}$.

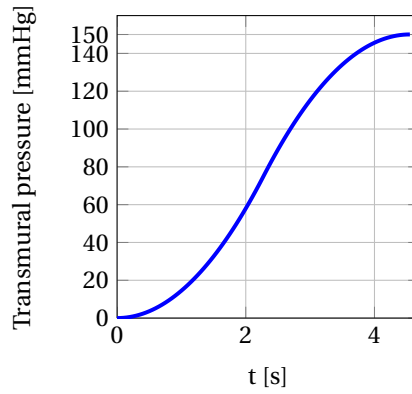


Figure 5.21: Inflating pseudo-time pressure profile $p(t)$ for problem (5.40)

R_0 and thickness h (as in Fig. 5.16-(b)). The problem reads:

$$\text{find } \hat{\mathbf{d}}: \mathcal{B}_0 \rightarrow \mathbb{R}^3 : \begin{cases} \hat{\nabla} \cdot (\mathbf{P}) = \mathbf{0} & \text{in } \mathcal{B}_0, \\ \mathbf{P} \hat{\mathbf{n}} = -p_{out} \hat{\mathbf{n}} & \text{on } \Gamma_{out}, \\ \mathbf{P} \hat{\mathbf{n}} = -p_{in} \hat{\mathbf{n}} & \text{on } \Gamma_{in}, \\ \hat{\mathbf{d}} = \mathbf{0} & \text{on } \Gamma_D, \end{cases} \quad (5.40)$$

where Γ_D is the subset of $\partial \mathcal{B}_0$. Here, homogeneous Dirichlet boundary conditions are imposed; the subsets Γ_{out} and Γ_{in} indicate the external and internal surfaces of the body and $\hat{\mathbf{n}}$ is the outward directed unit normal vector to the corresponding surface. p_{out} and p_{in} represent the pressures acting on Γ_{out} and Γ_{in} defining the transmural pressure $\Delta P = p_{in} - p_{out}$. It is assumed, for simplicity, that $p_{out} = 0$, thus yielding $\Delta P = p_{in}$ (see Fig. 5.16-(b)). The undeformed internal radius ($R_0 = 0.033$ cm) and the vessel wall thickness ($h = 0.010$ cm) of the tissue represented in Fig. 5.16-(b) correspond to the physiological dimensions of the anterior cerebral artery described in Scott et al. [1972]; Wulandana and Robertson [2005]. The length L of the cylindrical specimen is $L = 2$ cm. The range of transmural pressures considered to validate the different constitutive models is the physiological one occurring in cerebral arteries during one heart beat; therefore, $\Delta P \in [70, 150]$ mmHg Li [2009]. In order to achieve the convergence of the Newton-Raphson method for the values of transmural pressure of interest, the inflating pressure is gradually applied by means of the pseudo-time function $p(t)$ represented in Fig. 5.21. The linearized system in Eq. (5.11) is solved by means of the GMRES method Saad [2003] preconditioned with the Additive-Schwarz method Quarteroni and Valli [1999a]. The computational

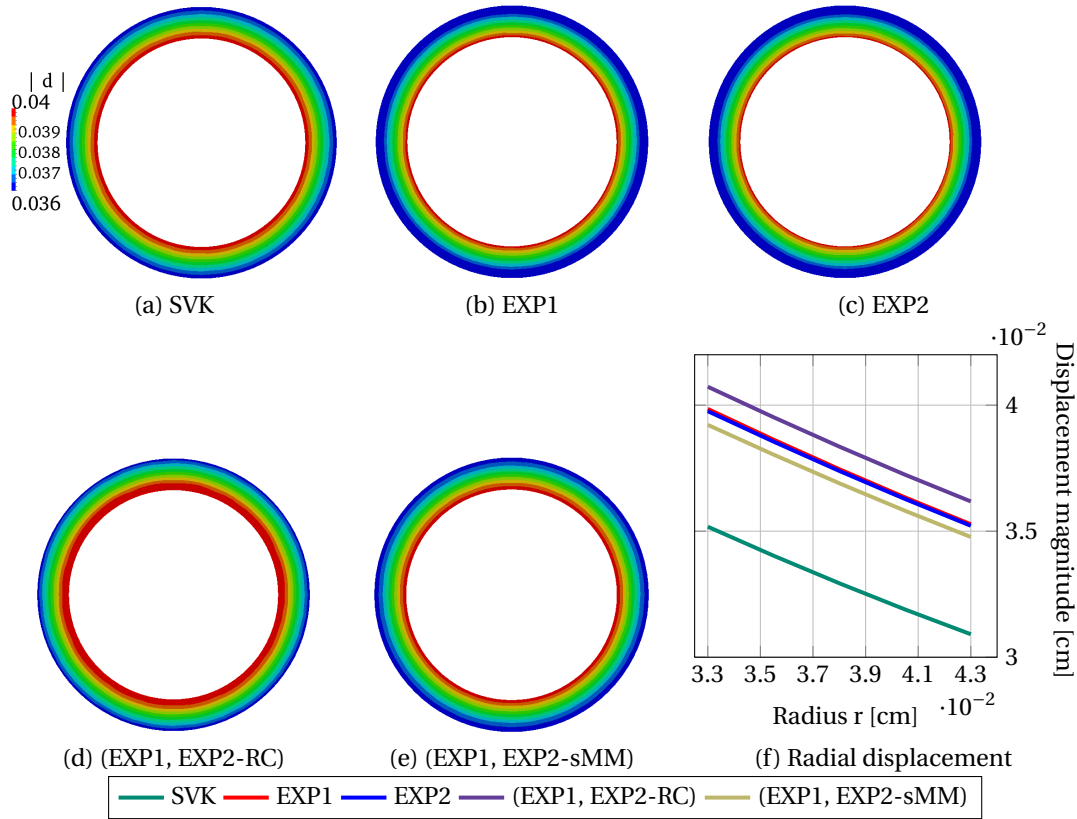


Figure 5.22: Displacement magnitude [cm] at the cross section at $z = 1$ cm and $\Delta P = 150$ mmHg for different material models

domain representing the cerebral artery (see Fig. 5.16) is discretized by a tetrahedral mesh composed of 384,000 elements with $\mathbb{P}1$ Lagrangian finite elements for which the total number of degrees of freedom (DOFs) when approximating Eq. (5.8) is 241,200. The numerical simulations have been run in parallel on 128 processors on the Cray XE6 supercomputer *Monte Rosa* at the Swiss national supercomputing center CSCS in Lugano, Switzerland.

Fig. 5.22 presents the magnitude of the displacement field at the cross section located at $z = 1$ cm for $\Delta P = 150$ mmHg for the constitutive models of Sec. 4.3.3. As expected, the contour lines of the displacement are concentric with the largest displacement occurring at the inner surface of the artery. The displacement magnitude in Figs. 5.22-(a)-(e) has been rescaled in order to show the correct qualitative behavior of all the numerical solutions; Fig. 5.22-(f) presents the radial displacement through the thickness of the vessel wall for all the constitutive models. Fig. 5.23 shows the stress-strain relations resulting from the least-squares approximation of the experimental measurements (see Sec. 5.4.1) and the ones obtained by the numerical simulations for the isotropic and anisotropic models, respectively. The circumferential stretch $\lambda_{\hat{\theta}\hat{\theta}}$ at the internal radius of the domain has been computed in order to compare it with the experimental measurement presented in Scott et al. [1972]. The circumferential stretch was obtained from the numerical results computing the magnitude of the displacement field on Γ_{in} at the cross section $z = 1$ cm such that the effects of Dirichlet boundary conditions applied on Γ_D (see Fig. 5.16-(a)) are negligible.

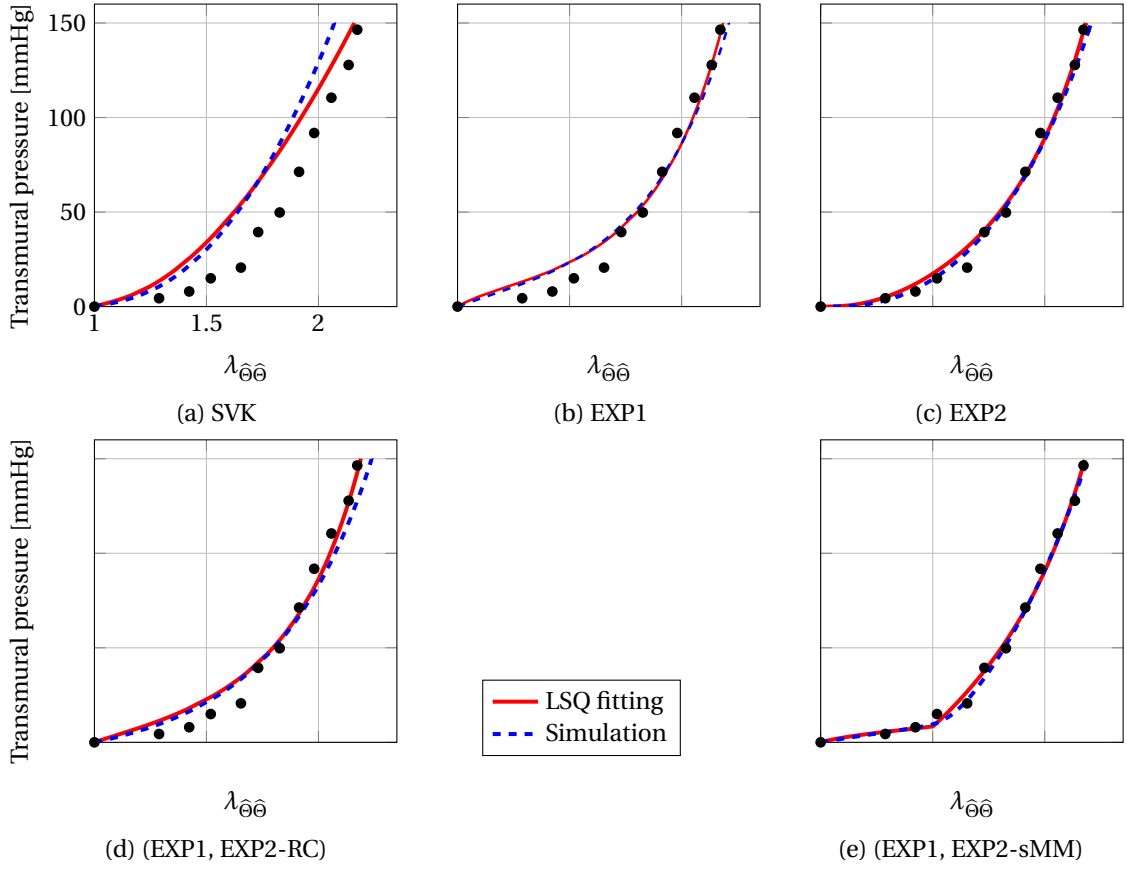


Figure 5.23: Stress-strain relation $\mathcal{T}(\lambda_{\hat{\theta}\hat{\theta}})$ and corresponding relation obtained from the numerical simulations for the models of Sec. 4.3.3. The dots represent the experimental data in Scott et al. [1972]

For the SVK isotropic model, as observed in Fig. 5.23-(a), with pressures $\Delta P \in [70, 150]$ the stress-strain relation obtained from the numerical simulations does not adequately reproduce the one predicted by the data fitting, especially for the high values of ΔP . Conversely, a good agreement between the numerical and least-squares fitted stress-strain relations is observed for the EXP1 and EXP2 models. Such difference among the isotropic models can be ascribed to the choice of the penalization parameter κ in Eq. (4.53). The larger is κ , the smaller is the body displacement under the action of external forces. Thus, a value for κ that represents a good compromise between the need to model the quasi-incompressible behavior of arteries and to obtain a meaningful displacement field for a certain constitutive model, e.g. the EXP1 and EXP2 models, may become inappropriate for another one, e.g. the SVK model. However, in this study, in order to have a consistent comparison of the numerical results among the different cases under consideration, the same value for the penalty parameter has been used in our numerical simulations. Figs. (5.23)-(d) and (5.23)-(e) show the stress-strain curves obtained from the least-squares approximation and numerical simulation for the (EXP1, EXP2-RC) and (EXP1, EXP2-sMM) models respectively. A good agreement between the simulated stress-strain relations and the corresponding functions $\mathcal{T}(\lambda_{\hat{\theta}\hat{\theta}})$ is observed. For the (EXP1, EXP2-RC) model the highest error occurs for high transmural pressures while for the multi-mechanism model, i.e. (EXP1, EXP2-sMM), the two curves overlap. However, in the latter case, the highest error occurs around the activation circumferential stretch. This is due to the fact that, in the data fitting, due to the membrane

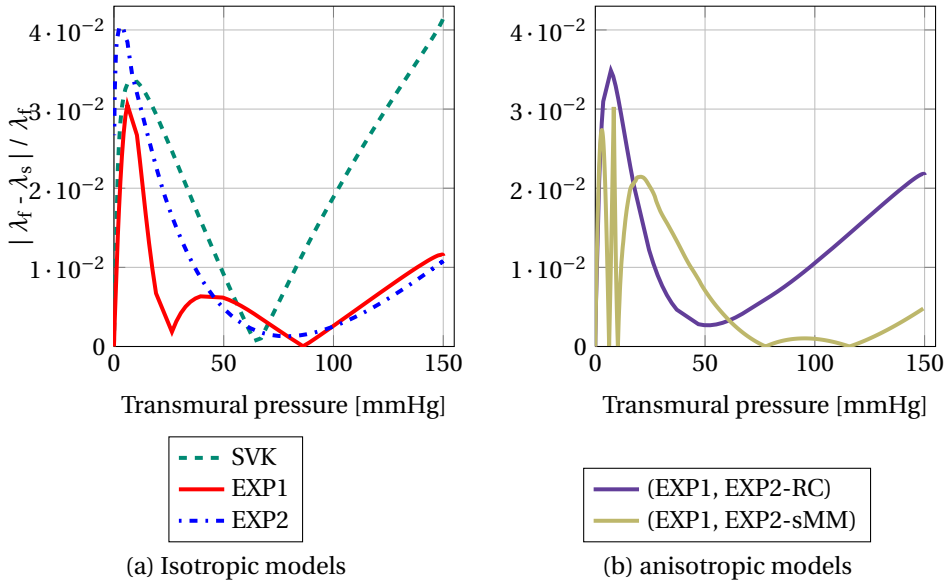


Figure 5.24: Relative error between the two stress-strain relations of Fig. 5.23 as a function of ΔP

modeling of the vessel wall, the recruitment of the collagen fibers is assumed to occur simultaneously throughout the thickness of the vessel wall; this assumption does not hold in the numerical simulations since the arterial wall is described as a full three-dimensional model.

Fig. 5.24 shows the relative error between the function $\mathcal{F}(\lambda_{\hat{\theta}\hat{\theta}})$ and the ones obtained from the numerical simulations. In the range of physiological transmural pressures, the maximum relative error is around 4% and it is observed for the isotropic SVK model. However, from the stress-strain measurements presented in Scott et al. [1972], the relative error between the function $\mathcal{F}(\lambda_{\hat{\theta}\hat{\theta}})$ and the numerically simulated stress-strain relations is compatible with (that is within the same range as) the one affecting the experimental measurements in Scott et al. [1972]. In the physiological range of pressures for the EXP1, EXP2 and the anisotropic models, the relative error is below 2.5% confirming the good approximation of the least-squares fitted stress-strain relation by the numerical simulations. In the low pressures regime (i.e. for $\Delta P \in [0, 20]$ mmHg) the high relative errors are due to the use of linear finite elements for the discretization of Eq. (5.4) and they are observed for all the constitutive models. Indeed, from the numerical point of view, high values of the penalty parameter κ can lead to incorrect displacement fields or to locking phenomena when discretizing Eq. (5.4) by means of $\mathbb{P}1$ finite elements Brinkhues et al. [2013]; Hughes [2000]. In this work, the value for κ has been set in order to simulate the nearly-incompressible behavior of blood vessels for $\Delta P \in [70, 150]$ mmHg; this may lead to displacements which are not circumferentially symmetric for low transmural pressures, as shown in Fig. 5.25 (left). However, such asymmetry can be addressed, for instance, by discretizing Eq. (5.4) by means of quadratic ($\mathbb{P}2$) finite elements, as shown in Fig. 5.25 (right). In this comparison, the isotropic EXP1 model is employed and, in order to have the same number of DOFs with the quadratic elements as in the linear case, a new mesh with 49,896 elements and 234,360 DOFs has been considered. In Fig. 5.25 it can be observed that for $\Delta P \in [70, 150]$ mmHg, the use of $\mathbb{P}2$ elements does not affect the circumferential stretch; we conclude that, the results presented in Fig. 5.23 are not significantly affected by the choice of the finite element space. Indeed, the vessel wall displacement on the internal surface of the domain measured in the case of $\mathbb{P}1$ and $\mathbb{P}2$ finite element spaces is the same. In addition, we remark that in the case of linear finite elements, the circumferential deformation reported in Fig. 5.23

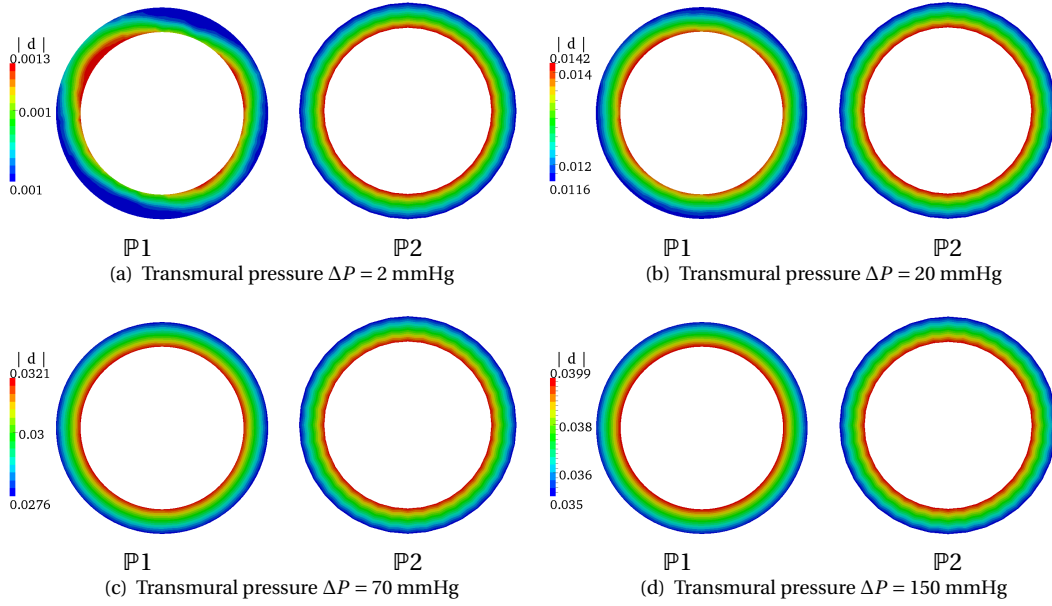


Figure 5.25: Displacement magnitude [cm] at different inflating pressures using the isotropic EXP1 model: using $\mathbb{P}1$ elements (#DOFs: 241,200)(left); using $\mathbb{P}2$ elements (#DOFs: 234,360)(right)

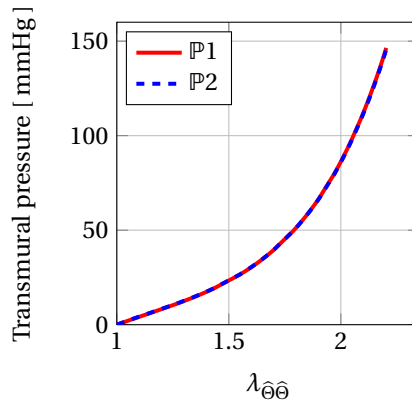


Figure 5.26: Stress-strain relation obtained using linear and quadratic finite elements

has been obtained by considering the maximum displacement on the internal surface for each value of transmural pressure. Therefore, the results presented in Fig. 5.23 might be slightly affected by the choice of the finite element space only in the low pressure regime that, however, is not of interest in this work. The isotropic EXP1 model has been employed and, in order to have an homogeneous comparison between the numerical simulations with linear and quadratic finite elements in terms of DOFs of the problem, a new triangulation of the domain (for which the number of tetrahedra and DOFs is 49,896 and 234,360 respectively) has been considered. In Fig. 5.25 the numerical solutions obtained in the two cases are presented for different values of transmural pressure (i.e. for $p \in [0, 150]$ mmHg) when using quadratic finite elements. In addition, see Fig. 5.26, the use of $\mathbb{P}2$ elements does not affect the circumferential stretch.

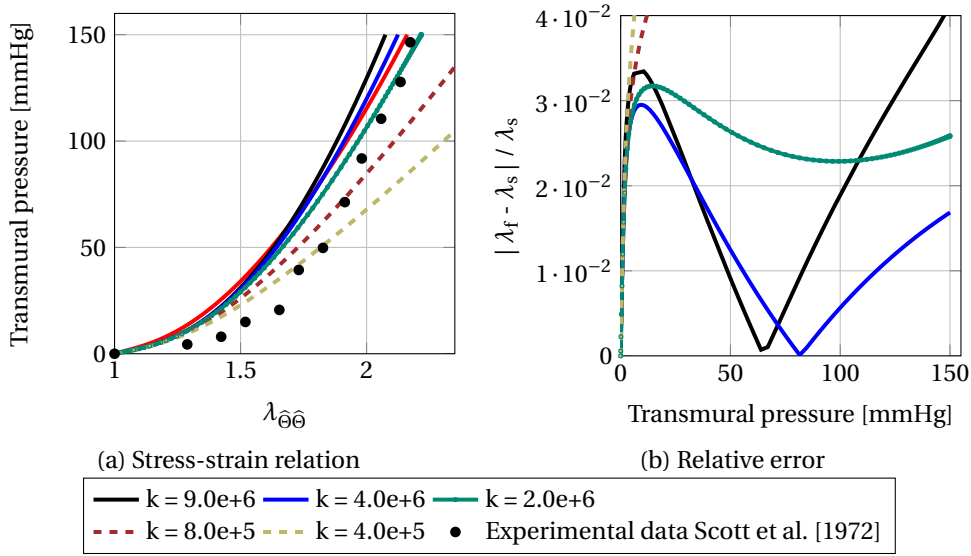


Figure 5.27: Stress-strain relations for different values of κ for the isotropic SVK model with the material parameters of Tab. 5.3.

In order to highlight the influence of the bulk modulus on the approximation of the circumferential stretch, Fig. 5.27-(a) shows the stress-strain relations obtained for different values of κ in Eq. (4.53) using the SVK model with the material parameters reported in Tab. 5.3. Fig. 5.27-(b) shows the influence of the penalization parameter on the computed displacement field and that, in this case, a different value of κ (i.e. $\kappa = 4.0 \cdot 10^6$ dyn/cm²) would have led to a better approximation of the function $\mathcal{T} = \mathcal{T}(\lambda_{\theta\hat{\theta}})$ in the range of transmural pressures of interest. It is worth pointing out that, as expected, lower values of the penalization parameters κ yield to bigger displacements than the ones observed for large values of κ . Similar considerations are valid also for the other isotropic constitutive models in Fig. 5.22. However, as reported in Fig. 5.24, the relative error between the numerical results and the curve obtained from the data fitting indicate that the value of bulk modulus employed in the numerical simulations is adequate in order to reproduce the stress-strain relation obtained from the least-squares approximation of the experimental measurements.

Fig. 5.28 shows the approximation of the incompressibility constraint at the cross section $z = 1$ cm at the inflating pressure of 150 mmHg for the constitutive models of Sec. 4.3.3. The largest error on the approximation of the volumetric constraint ($J = 1$) occurs at the internal surface of the artery where the displacement is higher. The smallest error, around 4.5%, is obtained for the SVK model due to the smaller radial displacement (see Fig. 5.23-(a)) of the vessel with respect to those obtained with the other constitutive laws. As presented in Fig. 5.27, the choice of the penalization parameter κ strongly affects the numerical results for the SVK model. Fig. 5.29 shows the Jacobian J at the cross section $z = 1$ cm at the inflating pressure of 150 mmHg for two different values of κ ($\kappa = 4.0 \cdot 10^6$ and $\kappa = 9.0 \cdot 10^6$ dyn/cm²) using the SVK model. In Fig. 5.29, the Jacobian J is presented only for the values of κ such that the error on the incompressibility constraint is lower than 20%. For the SVK model, Fig. 5.29 shows that for $\Delta P \in [70, 150]$ mmHg, $\kappa = 4.0 \cdot 10^6$ dyn/cm² leads to a better approximation of the stress-strain relation $\mathcal{T}(\lambda_r)$ by means of the numerical simulations; however, such choice for the penalization parameter yields a poor approximation of the incompressibility constraint. For the constitutive models of Sec. 4.3.3 the biggest error is reported for the anisotropic models, as in Fig. 5.28. Indeed, as discussed in Sec. 4.3.4, for anisotropic models, the value of the penalization parameter

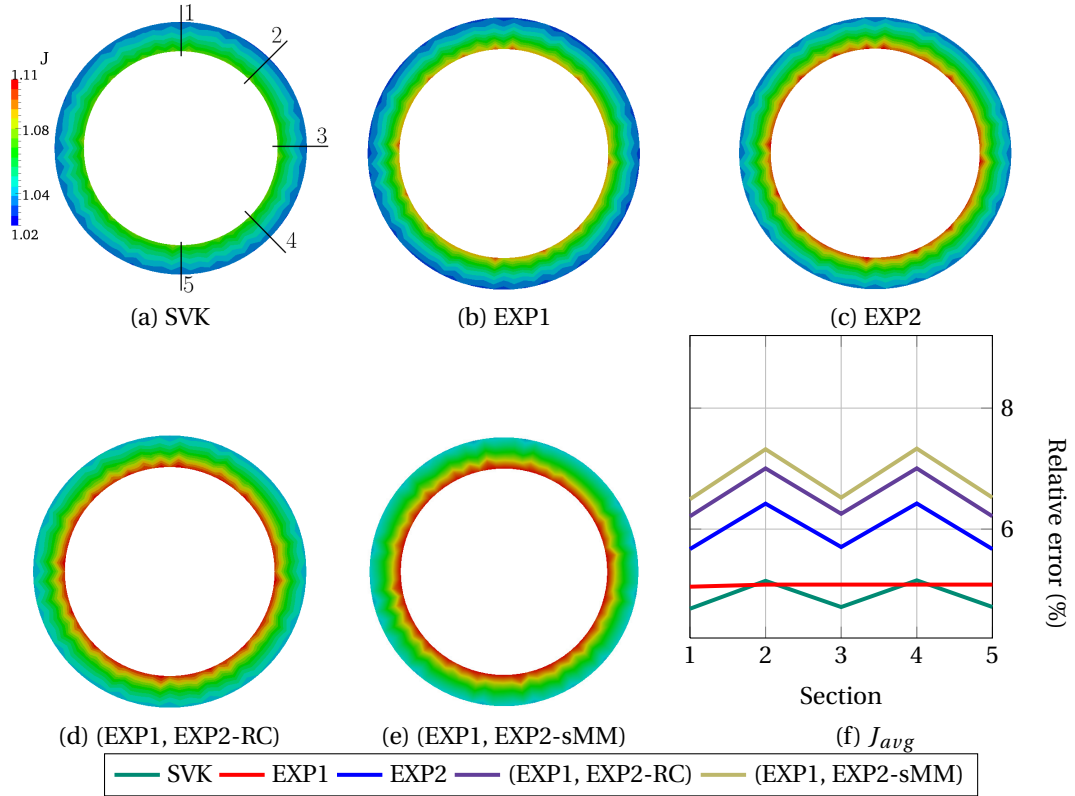


Figure 5.28: Volume ratio J and J_{avg} at $z = 1$ cm, $\Delta P = 150$ mmHg for the different material models; $\kappa = 9.0 \cdot 10^6$ dyn/cm².

should be chosen according to the characteristic parameter for the mechanical stiffness of the collagen fibers. This suggests that, once again, the value of the penalty parameter κ used for the numerical simulations should be tuned according to the constitutive law used to describe the tissue. Fig. 5.28-(f) shows the relative error (percentage) on the incompressibility constraint for $\Delta P = 150$ mmHg. More specifically, in Fig. 5.28-(f) the relative error is defined as $Er = 100(J_{avg} - 1)$, where J_{avg} is the average of the volume ratio along each one of the directions depicted in Fig. 5.28-(a). The oscillations reported in Fig. 5.28-(f) highlight the mesh dependence of the numerical results. Indeed, we observe that the Jacobian J in Fig. 5.28 is computed at the highest transmural pressure for which the numerical solution obtained with linear and quadratic finite elements is the same. However, the Jacobian J depends on the spatial gradient of the displacement field which in the case of Lagrangian basis function is strongly affected by the spatial orientation of the tetrahedra in the mesh. Thus, the oscillations in Fig. 5.28-(f) cannot be addressed by employing $\mathbb{P}2$ finite element in the discretization of the weak formulation. The averaged Jacobians J_{avg} in Fig. 5.28-(f) indicate that the value of κ used in the numerical simulations leads to an acceptable approximation of the incompressibility constraint with the maximum relative error being approximately 7%. In order to evaluate the mesh dependency on the approximation of the incompressibility constraint, numerical simulations of static inflation tests have been carried out for two additional meshes: one coarser and one finer than the reference mesh. For this numerical comparison, the isotropic EXP1 model describes the arterial tissue and $\mathbb{P}1$ finite elements discretize the weak formulation in Eq. (5.4). The coarser mesh is composed of 108,000 elements while the finer one is composed of 2,960,640 tetrahedra, yielding to 72,480 and 1,852,800 DOFs, respectively. Fig. 5.30 shows the approximation of the incompressibility constraint at the cross section $z = 1$ cm at the inflating

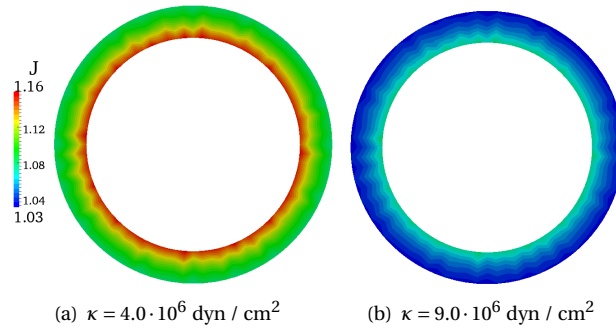


Figure 5.29: Volume ratio J for different values of the penalization parameter κ for the SVK model at the pressure $\Delta P = 150 \text{ mmHg}$.

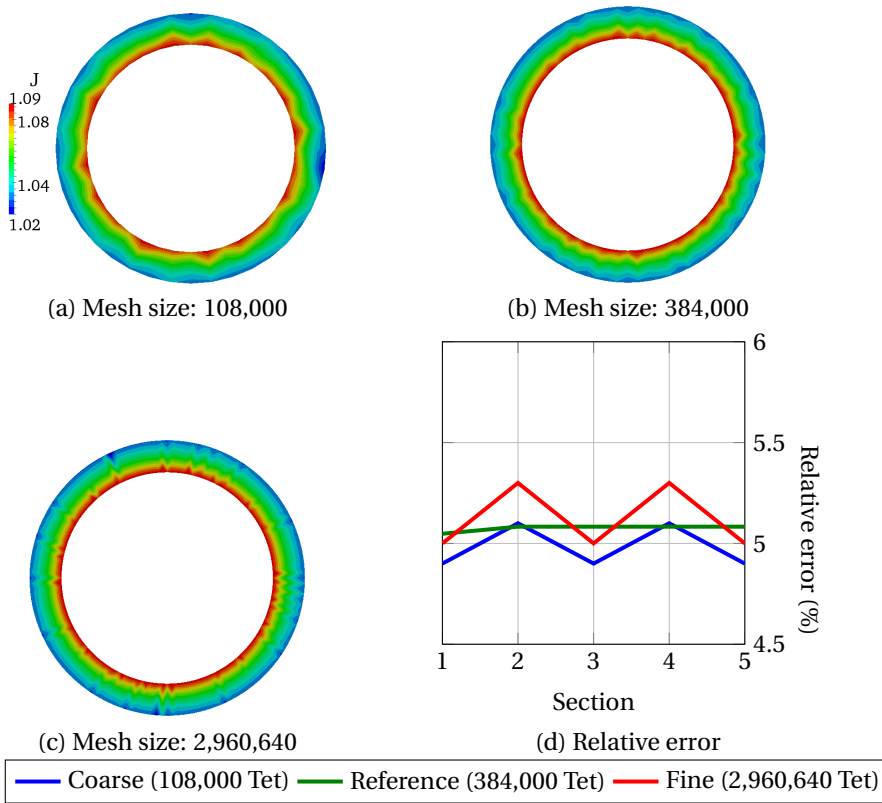


Figure 5.30: Volume ratio J for different meshes of the computational domain.

pressure of 150 mmHg. Mesh refining effects are not noticeable in the numerical solution suggesting that the approximation of the condition $J = 1$ is mainly affected by the choice of the penalty parameter κ .

Figs. (5.31)-(5.36) present the displacement field, the isochoric stretch $\bar{T}_4^{(1)}$ and the corresponding value of the activation function at the cross section $z = 1$. In Figs. (5.31)-(5.36), only the stretch and activation of one of the two families is shown; indeed, as it can be deduced from Eq. (5.39), for each value of displacement field, either the isochoric stretch or the activation function have the same values for both families of fibers. In Figs. (5.33)-(5.36), the activation stretch for the multi-mechanism model is

5.4. Numerical simulations of static inflation tests

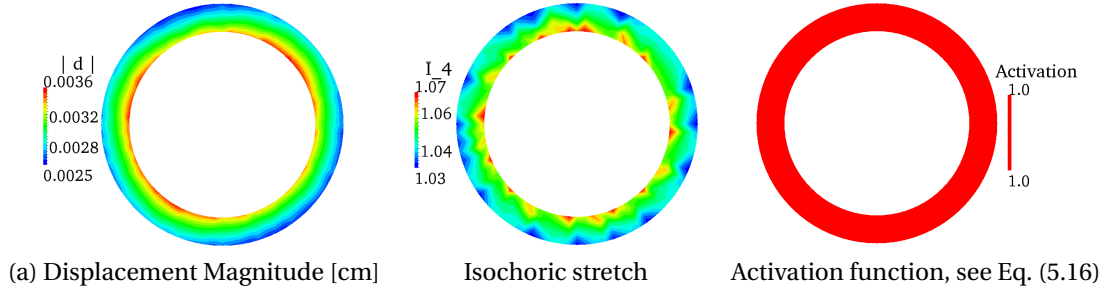


Figure 5.31: Displacement magnitude [cm], isochoric stretch $\bar{I}_4^{(1)}$ and mechanical activation of a single family of collagen fibers for inflation test; (EXP1, EXP2-RC) constitutive model. $\Delta P = 8.425$ mmHg; cross section $z = 1$

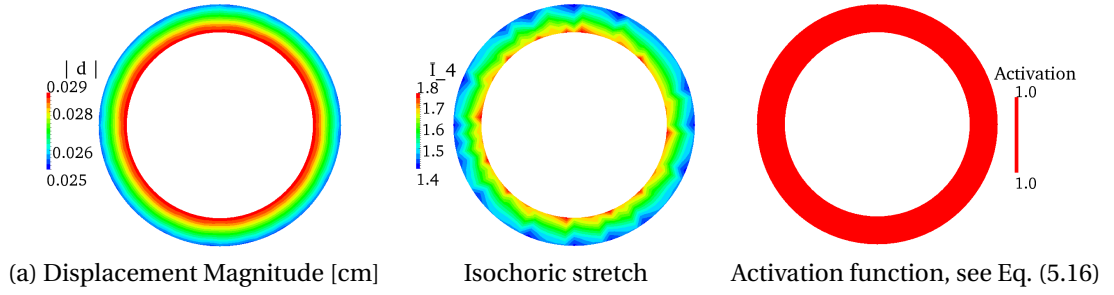


Figure 5.32: Displacement magnitude [cm], isochoric stretch $\bar{I}_4^{(1)}$ and mechanical activation of a single family of collagen fibers for inflation test; (EXP1, EXP2-RC) constitutive model. $\Delta P = 67.27$ mmHg; cross section $z = 1$

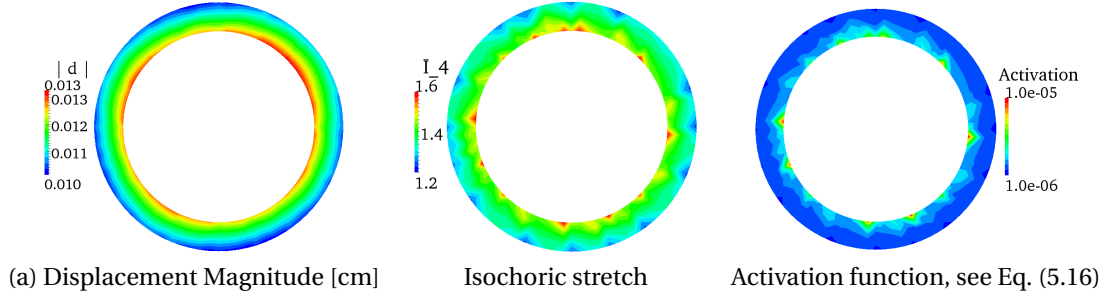


Figure 5.33: Displacement magnitude [cm], isochoric stretch $\bar{I}_4^{(1)}$ and mechanical activation of a single family of collagen fibers for inflation test; (EXP1, EXP2-sMM) constitutive model. $\Delta P = 8.425$ mmHg; activation stretch $I_{4,MM}^{(1)} = 1.6700$ and cross section $z = 1$

$I_{4,MM}^{(1)} = 1.6700$. For inflation tests and the characteristic direction of the collagen fibers obtained from the data fitting, the fibers are stretched ($\lambda_{\bar{a}} > 1$ in Eq. (4.25)) for all states of deformations, or equivalently for all values of transmural pressure ΔP . For this reason, in the case of the (EXP1, EXP2-RC) model, the activation function is always one stretch of the collagen fibers is greater than one for inflation tests. On the other hand, in Figs. (5.33) and (5.36) it can be observed that the collagen fibers are progressively activated through the thickness of the vessel wall as the transmural pressure ΔP increases.

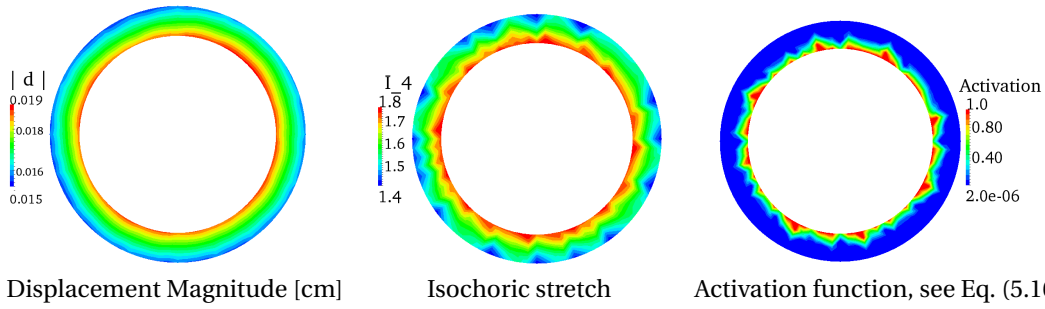


Figure 5.34: Displacement magnitude [cm], isochoric stretch $\bar{I}_4^{(1)}$ and mechanical activation of a single family of collagen fibers for inflation test; (EXP1, EXP2-sMM) constitutive model. $\Delta P = 13.66$ mmHg; activation stretch $I_{4,MM}^{(1)} = 1.6700$. Cross section $z = 1$

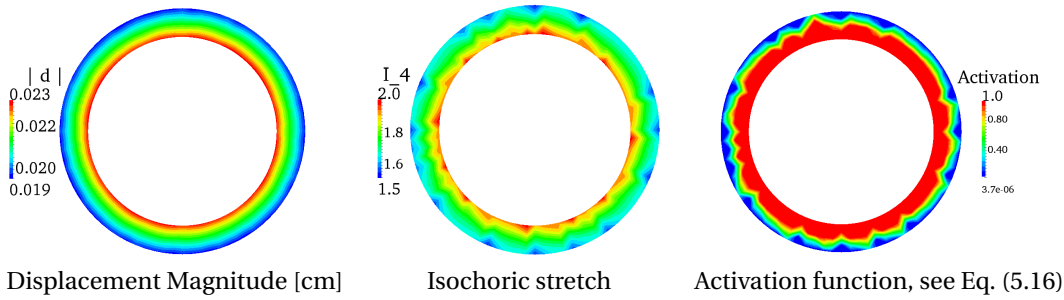


Figure 5.35: Displacement magnitude [cm], isochoric stretch $\bar{I}_4^{(1)}$ and mechanical activation of a single family of collagen fibers for inflation test; (EXP1, EXP2-sMM) constitutive model. $\Delta P = 30$ mmHg; activation stretch $I_{4,MM}^{(1)} = 1.6700$ and cross section $z = 1$

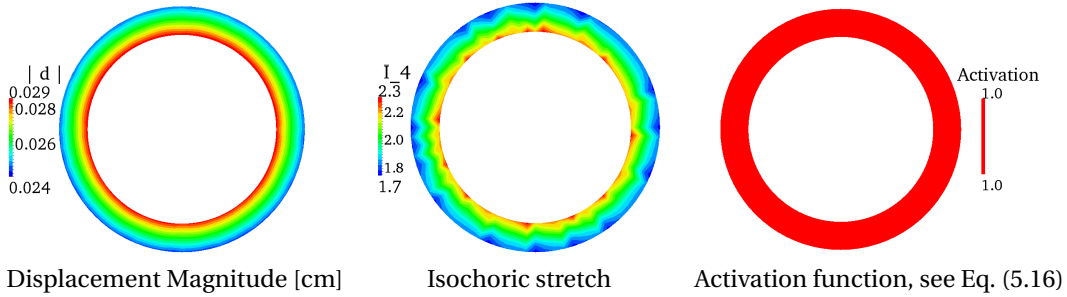


Figure 5.36: Displacement magnitude [cm], isochoric stretch $\bar{I}_4^{(1)}$ and mechanical activation of a single collagen fibers for inflation test; (EXP1, EXP2-sMM) constitutive model. $\Delta P = 67.27$ mmHg; activation stretch $I_{4,MM}^{(1)} = 1.6700$; cross section $z = 1$

5.4.3 Conclusions

The numerical validation of the isotropic and anisotropic constitutive models for the mechanical characterization of healthy cerebral arterial tissue has highlighted both modeling and numerical aspects that should be considered when simulating the arterial wall mechanics. From the modeling point of view, the least squares approximation and the numerical results suggests that, according to the range of transmural pressures of interest, a suitably calibrated isotropic model (as e.g. EXP1 or EXP2)

can lead, in terms of the data fitting quality, to equivalent results to an anisotropic one, i.e. the (EXP1, EXP2-RC) model. In addition, the possibility of modeling the recruitment of the collagen fibers at finite strains (EXP1, EXP2-sMM) instead of at zero strains leads to a better approximation of the experimental measurements with a good agreement of the numerical results. As mentioned in Sec. 5.2.4, in view of the numerical simulations, the choice of the constitutive law among the isotropic models should be made in order to take into account numerical issues that can arise; e.g. the initialization of the nonlinear solver and the influence of the penalty parameter in Eq. (4.53) according to the constitutive model. Moreover, the numerical results obtained using the EXP1 and EXP2 indicate that when experimental observations of the characteristic directions of collagen fibers are not available on human specimen of arteries, an isotropic model can be a viable alternative to an anisotropic model; this has the advantage of reducing the number of material parameters that need to be estimated and the computational cost of the assembling of the tangent matrix of the first Piola-Kirchhoff tensor. Concerning the numerical aspects, the multiplicative decomposition of the deformation gradient F (and the resulting additive splitting of the strain energy function $\widehat{\mathcal{W}}$ in Eq. (4.51)) leads to an acceptable approximation of the incompressibility condition $J = 1$ with $\mathbb{P}1$ finite elements. It is worth pointing out that, as discussed in Sec. 4.3.4, in order to better simulate the quasi-incompressible behavior of arteries, large values of the penalization parameter κ in the volumetric strain energy should be employed, specially for anisotropic laws, and second order $\mathbb{P}2$ finite elements should be considered to discretize the weak formulation of structural mechanics problem. However, from the computational point of view, the use of $\mathbb{P}2$ finite elements is extremely expensive, especially when highly nonlinear constitutive laws model the arterial tissue; for this reason, in this work, linear finite elements have been preferred to the second order ones.

Fluid-Structure Interaction Problems **Part II** **for the Cardiovascular System**

6 Mathematical Modeling of Fluid-Structure Interaction problems

The cardiovascular system consists of the heart, blood vessels, and approximately five liters of blood that flow in the dense network of arteries, veins, and capillaries. It is responsible for providing oxygen, nutrients, and hormones, as well as transporting cellular waste products throughout the body, and enabling the various organs of their correct functioning, see e.g. Nichols and O'Rourke [1998] and Ch.1 in Formaggia et al. [2009]. Due to its high biological relevance, the study of the cardiovascular system is longstanding. Indeed, together with the mechanical characterization of the arterial, venous and cardiac tissue Fung [1993], also the analysis of the blood flow in vessels is extremely important in order to characterize physiological and, possibly, pathological phenomena such as flow separation or recirculation and, as further step, estimate their effects on the arterial wall under different conditions of the body, e.g. at rest or during exercise. Indeed, as discussed for arteries in Sec. 2.1, it is known that blood vessels deform and react to the mechanical loads due to the blood flow (also referred to hemodynamical forces) originated from the pumping action of the heart. The ability of blood vessels to passively and actively respond to hemodynamical forces is usually referred to as the compliance of vessels and the consequent mechanical interactions between the blood flow and vessel play a key role in the regulation of the blood flow along the arterial tree. Furthermore, as described in e.g. McGloughlin [2011], in pathological cases, the blood-vessel interactions have a fundamental role in the onset and development of cardiovascular diseases. For this reason, in the last decades, the advancements in the power of modern computers, the progress in imaging and geometry extraction techniques as well as the development of adequate numerical methods and algorithms have led to a wide application of mathematical models and numerical simulations to the study of the cardiovascular system. In particular, the modeling and simulation of the blood flow in compliant arteries has gained increasing attention due to the high social impact of cardiovascular diseases, as atherosclerosis and aneurysms, in industrialized societies Murray and Lopez [1996]. Together with experimental studies and observations, numerical simulations aim at endowing the researchers with important tools for the interpretation and analysis of the circulatory system functionality, both in physiological and pathological situations.

This part of the work focuses on the mathematical modeling and numerical simulation of the blood flow in deformable arteries taking into account their mechanical interactions. When studying such complex coupled systems, the mathematical models for the blood ("the fluid") and for the arterial wall ("the structure") should describe the main features of their mechanical behavior in the condition of interest. Blood is a concentrated suspension of cellular elements including red blood cells, white blood cells, and platelets that are suspended in plasma; the interested reader may refer to Robertson et al. [2008] for a detailed description of the different cellular and non-cellular components of the blood. In addition to the driving force of the heart and to the arterial and venous network, the normal

blood circulation depends on the main mechanical properties of the blood, which are: shear thinning viscosity, viscoelasticity and thixotropy Fung [1993]; Robertson et al. [2008]; Chien et al. [1970]. The shear-thinning viscosity of blood is essentially due to the ability of the red blood cells to aggregate to form three-dimensional microstructures under low shear rates and to deform at high shear rates. As discussed in Robertson et al. [2008], the aggregation of the red blood cells may play an important role on the mechanical characteristics of the blood in regions of stable recirculation or stagnant flow which may occur either in case of cardiovascular diseases (e.g. aneurysms) or in the venous system. Therefore, when modeling the blood flow in healthy arteries, blood can be considered as a Newtonian fluid with constant viscosity. This assumption is commonly accepted in literature when modeling blood flow in large vessels such as the aorta (e.g. Nichols and O'Rourke [1998]; Crosetto [2011]; Malossi [2012]; Pozzoli [2011]; Formaggia et al. [2009]; Zakaria et al. [2008]; Ottesen et al. [2004]) and in cerebral arteries (e.g. Valencia et al. [2013]; Bazilevs et al. [2010]; Cebal et al. [2011]; Valencia and Solis [2006]; Bazilevs et al. [2010]). In literature, see Cebal et al. [2011]; Janela et al. [2010b]; Cebal et al. [2003, 2005], both Newtonian and generalized Newtonian models for the blood viscosity (see Robertson et al. [2008]) are considered. The numerical results, obtained from simulations of the blood flow in computational domains representing anatomically realistic portions of the cerebral vasculature, indicate that the effects of the modeling choice for the blood flow viscosity on the flow patterns and hemodynamical indicators such as, for instance, Wall Shear Stress (WSS) or Oscillatory Shear Index (OSI) are negligible. For this reason, in this work, the blood flow is modeled as a Newtonian fluid with constant viscosity. Regarding the constitutive models that can be employed for the description of the arterial wall, see Ch. 4 and Ch. 5.

In order to investigate the flow patterns in arteries, computational fluid dynamics (CFD) simulations represent a valuable tool in support of medical decisions since they allow to identify pathological situations as e.g. flow-separation or recirculation in specific parts of the cardiovascular system Formaggia et al. [2009]. Indeed, from the analysis of steady and unsteady flow simulations in anatomically accurate geometries of blood vessels, a set hemodynamical indicators, as the WSS, can be readily obtained. CFD simulations have been extensively employed for the study of the blood circulation in different portions of the cardiovascular system both in physiological and pathological conditions; see e.g. Zakaria et al. [2008]; Malek et al. [1999]; Oshima et al. [2005]; Lou et al. [2008]; Mantha et al. [2006]; Castro et al. [2006]; Baek et al. [2010]; Gambaruto and João [2012]. The study of the blood circulation by means of CFD simulations consists of different steps; namely, the vessel reconstruction from anatomical images, the generation of the computational domain, the CFD simulation, and the post-processing and visualization of the numerical results (see Cebal et al. [2005]; Oshima et al. [2001]). As discussed in Cebal et al. [2005]; Oshima et al. [2001], the first three steps strongly influence the numerical results. The reconstruction of the portion of the cardiovascular system of interest is usually derived from medical images acquired with different techniques such as e.g. Computer Tomography, Magnetic Resonance Imaging (MRI), or 3D Rotational Angiography. The quality of the reconstruction of the anatomic shape of a blood vessel depends on the resolution of the acquired medical images and on the knowledge and experience of the technician analyzing the images; see Cebal et al. [2005]; Oshima et al. [2001] and Ch.4 and Ch.5 of Formaggia et al. [2009]. Indeed, during the reconstruction process, image filtering and smoothing techniques are required in order to extract and regularize the contours of the vessel lumen in the acquired images. From this, it follows that the quality of the triangulation of the computational domain (i.e. the mesh) representing the vessel lumen strongly influences the numerical results Crosetto [2011]. Within the context of CFD simulations in rigid arteries, the blood flow is described by means of the Navier-Stokes equations which must be endowed with a set of appropriate boundary and initial conditions. For the correct simulation of the blood flow in arteries, the adequate definition of boundary conditions for the inlet and outlet boundary surfaces

of the computational domain is fundamental. Indeed, as shown in Marzo et al. [2009, 2010], the flow patterns inside the computational domain may be strongly affected by the choice of the boundary conditions. Due to improvements in the measuring techniques such as Doppler Ultrasound, experimental measurements of the blood flow rate during one heart beat in different parts of the arterial tree are now available Reymond [2011]; Hart and Haluszkiewicz [2000]; Matsuo et al. [2011]; consequently, the imposed boundary conditions aim at reproducing such physiological flow rates either by imposing velocity profiles, such as the Womersely profile Nichols and O'Rourke [1998], or by means of defective boundary conditions, for instance when flow rates are imposed Heywood et al. [1996]; Formaggia et al. [2006a]. The reliability of CFD simulations for prediction of blood flow dynamics was validated using particle image velocimetry measurements on idealized and realistic models Hoi et al. [2006]; Ford et al. [2008]. However, the estimation of some hemodynamical indicators that are commonly related to the development of cardiovascular diseases, such as WSS or WSS Gradient (WSSG), is strongly affected by the assumption of rigid vessel wall Xiang et al. [2012]. For instance, the WSS might be overestimated in CFD simulations compared to the one computed in three-dimensional Fluid-Structure Interaction (FSI) simulations.

As mentioned before, arteries are compliant and their deformations affect the dynamics of blood flow and the computation of important derived quantities. For this reason, the mathematical modeling and numerical simulations of the coupled physical system composed of blood flow and vessel wall plays an important role, together with experimental observations, in the study of the cardiovascular system. Within the context of Fluid-Structure Interaction modeling, the Navier-Stokes equations (also referred to as the fluid equations) describe the blood flow, while the conservation equation of linear momentum (or, alternatively, the solid equation), see Sec. 3.2.2, governs the deformations of the arterial wall under the action of the hemodynamical forces Formaggia et al. [2009]. As anticipated in Sec. 3.2, the fluid equations are commonly formulated in the spatial (Eulerian) form, while on the other hand the solid equation is formulated in the material (Lagrangian) form. The two subsystems are coupled by means of an Arbitrary Lagrangian-Eulerian (ALE) formulation Formaggia et al. [2009]; Nobile [2001]. More precisely, the ALE formulation of the Navier-Stokes equations is considered in order to take into account the movement of the fluid domain, which is derived from the displacement of the vessel wall, described by means of an additional set of equations together with the fluid and solid problems. The advantage of formulating the FSI problem in an ALE formulation with respect to a fully spatial or material formulation is that the coupling conditions for the two subsystems, i.e. the boundary conditions for the single sub-problem that represent the interactions between the fluid and structure, are formulated in the same form of the problem to which they refer. As discussed in Crosetto [2011], the FSI problem is nonlinear due to the Navier-Stokes equations, the constitutive models for the arterial wall and the formulation of the fluid equations in the ALE form. In order to numerically simulate the dynamics of the coupled system, different solution strategies have been developed. In literature, two strategies are commonly employed to solve the FSI problem: the so-called modular (or partitioned) and nonmodular (or monolithic) techniques Formaggia et al. [2009]; Crosetto et al. [2011]. From the implementation point of view, the former have the advantage of being relatively simple to implement since existing solvers for the single subsystem can be reused; conversely, the latter requires the implementation of ad-hoc methods and algorithms for the numerical simulations, and their efficacy in solving the coupled FSI problem relies on the use of adequate preconditioning techniques for the monolithic linear system Crosetto [2011]. When partitioned strategies are employed, weakly and strongly coupled algorithms are available Pozzoli [2011]; Nobile [2001]; Küttler et al. [2010]. Weakly coupled schemes (see Ch. 9 in Formaggia et al. [2009]) may be affected by stability issues due to the added mass effect Causin et al. [2005], while strongly coupled strategies may be characterized by an high number of iterations between the two fluid and solid system, therefore high CPU times,

to compute the solution of the coupled problem Formaggia et al. [2009]; Küttler et al. [2010]. On the other hand, in monolithic strategies the coupled FSI problem is solved as a whole; therefore, the coupling of the two subsystems is directly enforced in the nonlinear monolithic problem which makes them not sensitive to the added mass effect. Furthermore, although monolithic techniques may be computationally expensive, due to the fact that the FSI problem is solved entirely at each time, they require less CPU time to converge to the numerical solution compared to partitioned schemes; for this reason, a monolithic approach is employed in this work. The interested reader may refer to Crosetto [2011]; Pozzoli [2011]; Formaggia et al. [2009]; Nobile [2001]; Crosetto et al. [2011]; Küttler et al. [2010]; Causin et al. [2005]; Fernández and Moubachir [2005] and references therein for an extensive and detailed discussion on the available solution strategies to solve FSI problems in hemodynamics and on their properties. As for CFD simulations, also the use of adequate boundary conditions is extremely important to simulate the blood flow in physiological conditions. Indeed, while inlet boundary conditions are imposed in order to reproduce the physiological waveforms, the choice of both outflow boundary conditions and boundary conditions for the external surface of the vessel wall can have significant influence on the numerical results. Outflow boundary conditions are imposed to mimic the continuation of the arterial network downstream the computational domain Malossi [2012]; Formaggia et al. [2001]; Vignon-Clementel et al. [2010]; Vignon-Clementel [2006]; Nobile et al. [2013a]; Janela et al. [2010a]; in this work, resistance BCs are imposed on the outlet surface of the fluid domain in order to attain physiological values of pressure inside the computational fluid domain. Concerning the external surface of the solid domain, pure elastic or viscoelastic Robin boundary conditions are commonly imposed to simulate the effects of the perivascular tissue on the deformations of the arterial wall Crosetto [2011]; Malossi [2012]; Moireau et al. [2012]. Here, pure elastic Robin conditions are considered to constrain the displacement of the solid domain to physiological values.

Although the mathematical modeling and numerical approximation of FSI problems in hemodynamics are well established topics in literature Crosetto [2011]; Malossi [2012]; Formaggia et al. [2009]; Nobile [2001], for the sake of clarity, this chapter presents the mathematical problem describing the blood flow in compliant arteries; the description of the FSI problem presented in this chapter is oriented to the discussion that will follow in the remainder of the work. Sec. 6.1 presents the FSI problem describing the blood flow in compliant arteries. In particular, it briefly discusses the ALE approach used to couple the fluid and solid equations. Sec. 6.2 discusses the discretization in space and time of the coupled problem and the solution strategy to solve the discrete problem.

6.1 Mathematical formulation of the Fluid-Structure Interaction Problem

As discussed in Sec. 3.2, the governing equations for the blood flow and arterial wall motion are formulated in the spatial (Eulerian) and material (Lagrangian) coordinates, respectively. The former are defined in a fixed volume representing the domain of interest (i.e. the vessel lumen) Formaggia et al. [2009], while the latter are defined in the reference configuration which evolves in time, see Sec. 3.2. In FSI problems in hemodynamics, the generic domain representing the portion of the vascular system under consideration can be represented as in Fig. 6.1. Here the vessel lumen, i.e. the fluid domain, is indicated as \mathcal{F} , the fluid-wall interface is indicated by Γ , while \mathcal{B} represents the solid domain. The fluid-structure (FS) interface Γ is also referred to as the physical boundary of the fluid domain, while the lateral extremities are called the artificial boundaries since they delimit the portion of the vascular system of interest. Similarly to Sec. 3.1, in Fig. 6.1, $(\mathcal{F}_0, \Gamma_0)$ and $(\mathcal{F}_t, \Gamma_t)$ represent the reference and current configurations of the vessel lumen and fluid-wall interface, respectively. As shown in Fig. 6.1,

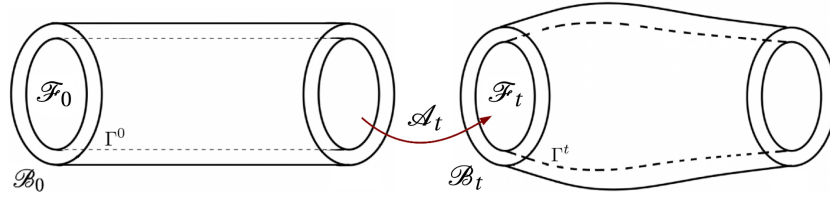


Figure 6.1: Representation of a generic domain of interest in FSI problems

an Eulerian description of the blood flow is not adequate since the fluid domain cannot be fixed in time as it follows the displacement of the vessel wall and, on the other hand, a Lagrangian description is not adequate either. In order to solve the Navier-Stokes equations in a moving domain the ALE formulation of the fluid equations is introduced Formaggia et al. [2009]. As in Sec. 3.1, where the motion of a continuous body from \mathcal{B}_0 to \mathcal{B}_t in Lagrangian coordinates is described by the diffeomorphism $\hat{\phi}$, in the ALE frame of reference the movement of the fluid domain is described by means of the motion map:

$$\mathcal{A} : \mathcal{F}_0 \times \mathbb{R}^+ \rightarrow \mathcal{F}_t \subset \mathbb{R}^3 \quad \text{s.t.} \quad \mathbf{x} = \mathcal{A}(\mathbf{X}, t), \quad (6.1)$$

where, \mathbf{X} and \mathbf{x} indicate the position of a point \mathbf{P} in \mathcal{F}_0 and \mathcal{F}_t , respectively; similarly to Sec. 3.1, the displacement of the fluid domain described by $\mathcal{A}(\bullet, \bullet)$ is indicated as $\hat{\mathbf{d}}_{\mathcal{F}} = \mathbf{x} - \mathbf{X}$, for any $\mathbf{X} \in \mathcal{F}_0$. It is worth pointing out that, from a general point of view, the reference configuration with respect to which the ALE map is defined can be any arbitrary configuration of \mathcal{F} different from the one obtained for the coupled system at rest, see Formaggia et al. [2009]. In the following, the ALE map will be shortly indicated as \mathcal{A}_t in order to highlight that, for any given time t , it describes the motion of the fluid domain from the reference to the current configuration. More precisely, as explained in Crosetto [2011]; Formaggia et al. [2009], the ALE motion map $\mathcal{A}(\bullet, \bullet)$ is employed to describe the movement of the fluid-structure interface Γ , while it keeps fixed the artificial boundaries, as in Fig. 6.1. These constraints on the displacement of the fluid domain involve only the boundaries of \mathcal{F} ; therefore, the displacement inside the fluid domain is arbitrary Formaggia et al. [2009]; Crosetto [2011]. It is worth reminding that, given the displacement $\hat{\mathbf{d}}_{\mathcal{F}}$ of \mathcal{F} , then the velocity of the fluid domain, also referred to as the ALE velocity, is defined as $\mathbf{w}_{\mathcal{F}} = \frac{\partial \hat{\mathbf{d}}_{\mathcal{F}}}{\partial t} = \frac{\partial \mathcal{A}}{\partial t}(\mathbf{X}, t)$ for any $\mathbf{X} \in \mathcal{F}_0$. By means of the ALE velocity, it is possible to relate the time derivatives of Eulerian spatial and vectorial fields defined on the current configuration \mathcal{F}_t with respect to the ALE motion. As shown in Formaggia et al. [2009], such time derivative is called the ALE time derivative of an Eulerian field $q(\mathbf{x}, t)$ and it is defined as:

$$\left. \frac{\partial q}{\partial t} \right|_{\mathcal{A}_t} = \mathbf{w}_{\mathcal{F}} \cdot \nabla q + \frac{\partial q}{\partial t}, \quad (6.2)$$

where $\left. \frac{\partial q}{\partial t} \right|_{\mathcal{A}_t} = \frac{d}{dt} q(\mathcal{A}(\mathbf{X}, t), t)$.

As previously stated, in this work the blood is modeled as an incompressible fluid whose velocity \mathbf{u} and pressure p inside the vessel lumen are governed by the Navier-Stokes equations; namely, the

balance principles of mass and linear momentum in the spatial form, see Secs. 3.2.1 and 3.2.2, i.e.

$$\left\{ \begin{array}{l} \nabla \cdot \mathbf{u} = 0 \quad \text{in } \mathcal{F}, \\ \rho_f \frac{\partial \mathbf{u}}{\partial t} + \rho_f (\mathbf{u} \cdot \nabla) \mathbf{u} - \nabla \cdot (\mu_f (\nabla \mathbf{u} + (\nabla \mathbf{u})^T)) + \nabla p = 0 \quad \text{in } \mathcal{F}, \end{array} \right. \quad (6.3)$$

where the material derivative of the spatial velocity field $\frac{D}{Dt} \mathbf{u} = \frac{\partial \mathbf{u}}{\partial t} + (\mathbf{u} \cdot \nabla) \mathbf{u}$ and the definition of the Cauchy stress tensor for a Newtonian fluid with constant viscosity, $\boldsymbol{\sigma}_f = \mu_f (\nabla \mathbf{u} + (\nabla \mathbf{u})^T) - p \mathbf{I}$, have been inserted in the balance principle of linear momentum; see Eq. (3.25). Since the Navier-Stokes equations in Eq. (6.3) are presented in their spatial form, we recall that the domain \mathcal{F} on which they are defined is the generic fixed fluid domain, i.e. vessel lumen; in Eq. (6.3), ρ_f and μ_f the density and dynamic viscosity characterizing the blood, respectively. The Navier-Stokes equations in Eq. (6.3) have been formulated in the absence of body forces, such as gravity, which may influence the blood flow; however, such assumption is commonly accepted in literature when studying the vascular system (see e.g. Bazilevs et al. [2010]; Crosetto [2011]; Malossi [2012]; Formaggia et al. [2009]). By means of Eq. (6.2), the Navier-Stokes equations are then recast in a moving fluid domain \mathcal{F}_t ; more precisely, the system of PDEs governing the blood flow in compliant arteries reads as follow:

$$\left\{ \begin{array}{l} \nabla \cdot \mathbf{u} = 0 \quad \text{in } \mathcal{F}_t, \\ \rho_f \frac{\partial \mathbf{u}}{\partial t} \Big|_{\mathcal{A}_t} + \rho_f ((\mathbf{u} - \mathbf{w}_{\mathcal{F}}) \cdot \nabla) \mathbf{u} - \nabla \cdot (\mu_f (\nabla \mathbf{u} + (\nabla \mathbf{u})^T)) + \nabla p = 0 \quad \text{in } \mathcal{F}_t, \end{array} \right. \quad (6.4)$$

where \mathcal{F}_t is the deformed, i.e. current, configuration of the fluid domain. As already mentioned, the deformations of the arterial wall under the action of the blood flow are described by means of the balance principle of linear momentum in the Lagrangian form, see Eq. (3.26). The fluid and solid problems of Eqs. (6.4) and (3.26) must be coupled ensuring a global energy balance. This is achieved by imposing three interface coupling conditions on the fluid-structure interface Γ through:

- the continuity of the fluid and solid velocities (kinematic condition);
- the continuity of the stresses transmitted from the solid to the fluid domain and viceversa (dynamic condition);
- the continuity of the solid and fluid displacements (adherence condition).

The last coupling condition is introduced by the ALE formulation of the fluid equations and, consequently, the system of equations modeling the coupled FSI system together with the coupling conditions reads:

$$\begin{aligned} \nabla \cdot \mathbf{u} &= 0 && \text{in } \mathcal{F}_t, \\ \rho_f \frac{\partial \mathbf{u}}{\partial t} \Big|_{\mathcal{A}_t} + \rho_f ((\mathbf{u} - \mathbf{w}_{\mathcal{F}}) \cdot \nabla) \mathbf{u} - \nabla \cdot (\mu_f (\nabla \mathbf{u} + (\nabla \mathbf{u})^T)) + \nabla p &= 0 && \text{in } \mathcal{F}_t, \\ \rho_s \frac{\partial \hat{\mathbf{d}}}{\partial t} - \hat{\nabla} \cdot (\mathbf{P}(\hat{\mathbf{d}})) &= 0 && \text{in } \mathcal{B}_0, \\ \mathbf{u} &= \hat{\mathbf{v}} && \text{on } \Gamma_t, \end{aligned} \quad (6.5)$$

$$\left(J_{\mathcal{A}_t} \boldsymbol{\sigma}_f \mathbf{F}_{\mathcal{A}_t}^{-T} \right) \hat{\mathbf{n}}_{\mathcal{F}} = \mathbf{P} \hat{\mathbf{n}} \quad \text{on } \Gamma_0, \quad (6.6)$$

$$\hat{\mathbf{d}}_{|\Gamma_0} = \hat{\mathbf{d}}_{\mathcal{F}_t|\Gamma_0} \quad \text{on } \Gamma_0, \quad (6.7)$$

6.1. Mathematical formulation of the Fluid-Structure Interaction Problem

where the last three equations represent the coupling conditions listed above. We remark that the boundary conditions that have to be imposed on the artificial boundaries of the fluid and solid domain (e.g. inlet, outlet and external surface of the fluid and solid domain, respectively, see Fig. 6.1) are not specified in the system above; indeed they strongly depend on the FSI problem of interest and they will be detailed in the next chapters in order to better specify the simulations settings that have been considered. As in Ch. 3, $\hat{\mathbf{d}}$ and $\hat{\mathbf{v}}$ represent the material displacement and velocity fields of the arterial wall, respectively; $\mathbf{F}_{\mathcal{A}_t}^{-T}$ and $J_{\mathcal{A}_t}$ are the adjoint (see Sec. 4.1) and the determinant of the deformation gradient tensor defined from the ALE motion map, $\hat{\mathbf{n}}$ and $\hat{\mathbf{n}}_{\mathcal{F}}$ are the outward directed unit normal vectors to the solid domain \mathcal{B}_0 and the fluid domain \mathcal{F}_0 , respectively, and $\hat{\mathbf{d}}_{|\Gamma_0}$ indicates the restriction of the displacement of the arterial wall on the fluid-wall interface Γ_0 in the reference configuration. As mentioned before, the coupling conditions are formulated in the same frame of reference of the problem to which they refer. Indeed, the continuity of the velocities, Eq. (6.5), is formulated on the current configuration of the fluid-solid interface, Γ_t , while the continuity of the stresses and the geometric adherence, in Eqs. (6.6) and (6.7) respectively, on the reference configuration Γ_0 ; see Fig. 6.1.

As mentioned before, the ALE map is such that the continuity of the displacements, also referred to as the geometric adherence condition, is satisfied together with the boundary conditions imposed on the inlet and outlet surface of the fluid domain for which $\hat{\mathbf{d}}_{\mathcal{F}} = \mathbf{0}$. As discussed in Formaggia et al. [2009], the ALE map can be arbitrary inside the fluid domain; more precisely, it can be any extension $\hat{\mathbf{d}}_{\mathcal{F}} = \text{Ext}(\hat{\mathbf{d}}_{|\Gamma_0})$ of $\hat{\mathbf{d}}_{|\Gamma_0}$ in \mathcal{F}_0 . For instance, in this work, the extension operator is given in terms of an harmonic extension of the interface displacement by solving:

$$\left\{ \begin{array}{ll} -\Delta \hat{\mathbf{d}}_{\mathcal{F}} = \mathbf{0} & \text{in } \mathcal{F}_0, \\ \hat{\mathbf{d}}_{\mathcal{F}} = \mathbf{0} & \text{on } \Gamma_{0,in} \cup \Gamma_{0,out}, \\ \hat{\mathbf{d}}_{\mathcal{F}} = \hat{\mathbf{d}}_{|\Gamma_0} & \text{on } \Gamma_0, \end{array} \right. \quad (6.8)$$

where $\Gamma_{0,in}$ and $\Gamma_{0,out}$ indicate the generic inlet and outlet surfaces in the reference configuration \mathcal{F}_0 of the fluid domain, respectively. The interested reader may refer to Wick [2011] and references therein for a discussion about different methods to extend the interface displacement inside the fluid domain and the corresponding properties. In the following, for the sake of brevity, when the numerical discretization and solution technique of the coupled FSI problem are described, the notation used in Crosetto et al. [2011] to indicate the fluid, solid and geometric problems is employed. The fluid problem, together with the continuity of the velocity condition, is shortly represented as:

$$\mathbf{F}(\mathbf{u}, p, \hat{\mathbf{d}}_{\mathcal{F}}) = \mathbf{0} \quad \text{in } \mathcal{F}_t; \quad (6.9)$$

similarly, the solid problem with the continuity of the stresses is indicated as:

$$\mathbf{S}(\hat{\mathbf{d}}, \mathbf{u}, p) = \mathbf{0} \quad \text{in } \mathcal{B}_0, \quad (6.10)$$

and, finally, the geometric problem (6.8) with the geometric adherence condition is represented as:

$$\mathbf{G}(\hat{\mathbf{d}}, \hat{\mathbf{d}}_{\mathcal{F}}) = \mathbf{0} \quad \text{in } \mathcal{F}_0. \quad (6.11)$$

The above problems are complemented with suitable initial and boundary conditions; in this work, the same type of initial and boundary conditions have been considered for all the numerical

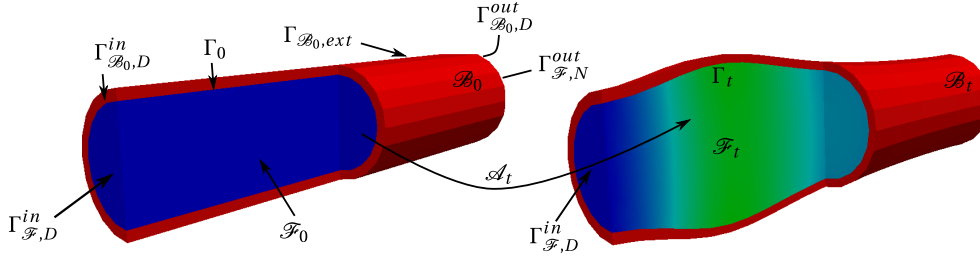


Figure 6.2: Representation of a generic domain of interest where the boundary surfaces and domain are specified for the boundary conditions in Eqs. (6.12)-(6.16)

simulations. More precisely, the initial conditions represent the FSI system at rest, i.e. in the absence of blood flow, while the boundary conditions are specified hereafter. After introducing the general form of the different boundary conditions in this section, the different functions characterizing the set of boundary conditions will be specified case by case in the next chapters. Let us consider the fluid and solid domains represented in Fig. 6.2; the following set of boundary conditions is imposed on the lateral and external surfaces of the fluid and solid domain, in Eqs. (6.9)-(6.11):

- for the fluid problem:

$$\mathbf{u} = \mathbf{g} \quad \text{on } \Gamma_{\mathcal{F},D}^{in}, \quad (6.12)$$

$$\boldsymbol{\sigma}_{\mathcal{F}} \mathbf{n}_{\mathcal{F}} = RQ(\mathbf{u}) \mathbf{n}_{\mathcal{F}} \quad \text{on } \Gamma_{\mathcal{F},N}^{out}. \quad (6.13)$$

- for the solid problem:

$$\hat{\mathbf{d}} = \mathbf{0} \quad \text{on } \Gamma_{\mathcal{B}_0,D}^{in} \cup \Gamma_{\mathcal{B}_0,D}^{out}, \quad (6.14)$$

$$\mathbf{P} \hat{\mathbf{n}} + K \hat{\mathbf{d}} = \mathbf{h} \quad \text{on } \Gamma_{\mathcal{B}_0,ext}. \quad (6.15)$$

- for the geometric problem:

$$\hat{\mathbf{d}}_{\mathcal{F}} = \mathbf{0} \quad \text{on } \Gamma_{\mathcal{F},D}^{in} \cup \Gamma_{\mathcal{F},N}^{out}. \quad (6.16)$$

Eqs. (6.12) and (6.13) represent an inlet velocity profile, usually derived from physiological measurements of blood flow rates at the inlet of the computational domain Crosetto [2011]; Malossi [2012], and a resistance boundary condition to mimic the presence of the vasculature network downstream the computational domain Formaggia et al. [2001]; Vignon-Clementel et al. [2010]; in Eq. (6.13), R represents the resistance coefficient describing the continuation of the vasculature network, while $Q(\mathbf{u})$ is the blood flow measured at the outlet surface of the computational domain, see Vignon-Clementel et al. [2010]; Reymond et al. [2010] and references therein. Concerning the solid domain, zero displacement is imposed on the lateral surfaces of the arterial wall, Eq. (6.14), while a pure elastic Robin boundary condition is imposed, in Eq. (6.15), on the external wall to mimic the effect of the surrounding tissues on the deformations of the vessel wall. Eq. (6.16) prescribes zero displacement on the artificial boundaries, similarly to Eq. (6.8). In the next section, it will be assumed that all the boundary data that define the boundary conditions in Eqs. (6.12)-(6.16) have the necessary regularity properties required by the variational formulation of the coupled FSI problem, see e.g. Crosetto [2011]; Formaggia et al. [2009]; Nobile [2001]. This property will also allow the individual sub-problems (when considered standing

alone, within segregated iterative methods) to make sense Pozzoli [2011]; Formaggia et al. [2009].

6.2 Space-Time discretization and solution of the FSI problem

The coupled FSI problem is approximated by means of the finite element method Quarteroni and Valli [1999b]. In this section, for the sake of clarity, the weak formulation of the FSI problem that will be considered in the numerical simulations is presented, see Crosetto [2011]; Formaggia et al. [2009]; Nobile [2001] and references therein for more insights.

In order to derive the variational formulation of the FSI problem from its strong form, adequate function spaces have to be chosen. In this work, similarly to Crosetto [2011], we set:

$$V_{\mathbf{u}} = \{ \mathbf{u} = \hat{\mathbf{u}} \circ \mathcal{A}_t^{-1} \mid \hat{\mathbf{u}} \in [H^1(\mathcal{F}_0)]^3 \}, \quad (6.17)$$

$$V_p = \{ p = \hat{p} \circ \mathcal{A}_t^{-1} \mid \hat{p} \in L^2(\mathcal{F}_0) \}, \quad (6.18)$$

$$V_{\hat{\mathbf{d}}} = \{ \hat{\mathbf{d}} \in [H^1(\mathcal{B}_0)]^3, \mid \hat{\mathbf{d}} = \mathbf{0} \text{ on } \Gamma_D = \Gamma_{\mathcal{B}_0,D}^{in} \cup \Gamma_{\mathcal{B}_0,D}^{out} \}, \quad (6.19)$$

$$V_{\hat{\mathbf{v}}} = \{ \hat{\mathbf{v}} \in [H^1(\mathcal{B}_0)]^3 \mid \hat{\mathbf{v}} = \mathbf{0} \text{ on } \Gamma_D = \Gamma_{\mathcal{B}_0,D}^{in} \cup \Gamma_{\mathcal{B}_0,D}^{out} \}, \quad (6.20)$$

$$V_{\hat{\mathbf{d}}_{\mathcal{F}}} = \{ \hat{\mathbf{d}}_{\mathcal{F}} \in [H^1(\mathcal{F}_0)]^3 \mid \hat{\mathbf{d}}_{\mathcal{F}} = \mathbf{0} \text{ on } \Gamma_{\mathcal{F},D}^{in} \cup \Gamma_{\mathcal{F},D}^{out} \}. \quad (6.21)$$

By following Crosetto [2011]; Nobile [2001], a global variational formulation of the FSI problem is obtained by imposing in a weak sense the continuity of the stresses on the fluid-structure interface. Such condition is imposed by balancing the variational residuals of the two momentum equations restricted to the interface. If the following space of functions $W = \{ (\mathbf{v}_{\mathcal{F}}, \mathbf{v}_{\mathcal{S}}) \in V_{\mathcal{F}} \times V_{\hat{\mathbf{v}}} \mid \text{tr}_{\Gamma_0}(\mathbf{v}_{\mathcal{F}} \circ \mathcal{A}_t) = \text{tr}_{\Gamma_0}(\mathbf{v}_{\mathcal{S}}) \}$, where $\text{tr}(\bullet)$ indicates the trace operator, is chosen the weak stresses continuity condition is satisfied Crosetto [2011]; Nobile [2001] and the weak form of the coupled Navier-Stokes, solid and geometric problems reads as:

find $\mathbf{u} \in V_{\mathbf{u}}$, $p \in V_p$, $\hat{\mathbf{d}} \in V_{\hat{\mathbf{d}}}$, and $\hat{\mathbf{d}}_{\mathcal{F}} \in V_{\hat{\mathbf{d}}_{\mathcal{F}}}$:

$$\begin{aligned} & \int_{\mathcal{F}_0} \left(\rho_f \frac{\partial \mathbf{u}}{\partial t} \Big|_{\mathcal{A}_t} \cdot \mathbf{v}_{\mathcal{F}} \right) + (\rho_f (\mathbf{u} - \mathbf{w}_{\mathcal{F}}) \nabla \mathbf{u}) \cdot \mathbf{v}_{\mathcal{F}} - \boldsymbol{\sigma}_{\mathcal{F}} : \nabla \mathbf{v}_{\mathcal{F}} \, d\mathcal{F}_0 + \\ & + \int_{\mathcal{B}_0} \rho_s \frac{\partial^2 \hat{\mathbf{d}}}{\partial t^2} \cdot \mathbf{v}_{\mathcal{S}} + \mathbf{P} : \widehat{\nabla} \mathbf{v}_{\mathcal{S}} \, d\mathcal{B}_0 + \oint_{\Gamma_{\mathcal{B}_0,ext}} k \hat{\mathbf{d}} \cdot \mathbf{v}_{\mathcal{S}} \, d\Gamma_{\mathcal{B}_0,ext} = \\ & = \oint_{\Gamma_{\mathcal{F},N}^{out}} RQ(\mathbf{u}) \mathbf{n}_{\mathcal{F}} \cdot \mathbf{v}_{\mathcal{F}} \, d\Gamma_{\mathcal{F},N}^{out} + \oint_{\Gamma_{\mathcal{B}_0,ext}} \mathbf{h} \cdot \mathbf{v}_{\mathcal{S}} \, d\Gamma_{\mathcal{B}_0,ext} \quad \forall (\mathbf{v}_{\mathcal{F}}, \mathbf{v}_{\mathcal{S}}) \in W, \forall t \in (0, T), \end{aligned} \quad (6.22)$$

$$\int_{\mathcal{F}_t} \nabla \mathbf{u} \mathbf{q} \, d\mathcal{F}_t = 0 \quad \forall \mathbf{q} \in V_p, \forall t \in (0, T), \quad (6.23)$$

$$\int_{\mathcal{F}_0} \widehat{\nabla} \hat{\mathbf{d}}_{\mathcal{F}} : \widehat{\nabla} \mathbf{v}_g \, d\mathcal{F}_0 = 0 \quad \forall \mathbf{v}_g \in V_{\hat{\mathbf{d}}_{\mathcal{F}}}, \forall t \in (0, T). \quad (6.24)$$

$$(6.25)$$

It is worth pointing out that, although the condition representing the continuity of the stresses is enforced in a weak sense, the continuity of the velocity is imposed in a strong way discretizing directly Eq. (6.5). The strong nonlinearity of the weak formulation of the FSI problem is due to the presence of the convective term in the Navier-Stokes equation, the use of nonlinear constitutive models for the arterial wall and the dependence of the fluid displacement $\hat{\mathbf{d}}_{\mathcal{F}}$ on the one of the structure.

The variational formulation in Eq. (6.25) is discretized in time by means of the second order BDF

method Quarteroni et al. [2007]. The nonlinearities in the FSI problem can be discretized in time according to different techniques, as discussed in Crosetto [2011]. In this work, the so called *Fully Implicit* (FI) method of Crosetto [2011] is employed; therefore, the nonlinear terms in the fluid and solid equations are discretized implicitly as well as the boundary terms that depend on the solution, i.e. the outflow $Q(\mathbf{u})$ in Eq. (6.22) and the Robin boundary condition on $\Gamma_{\mathcal{B}_0,ext}$. As discussed in Crosetto [2011], the Fully Implicit strategy leads to a more accurate and robust time discretization of the FSI problem compared to the one obtained by means of other strategies, such as the Geometric-Convective Explicit (GCE) for which the advection nonlinear term, depending on the fluid and ALE velocities \mathbf{u} and $\mathbf{w}_{\mathcal{F}}$, in the Navier-Stokes equations is linearized Crosetto [2011]; however, from the computational point of view, a Fully Implicit monolithic approach is the most expensive between the different techniques (i.e. FI or GCE) described in Crosetto [2011]. It is worth pointing out that the stability of the overall time discretization of the monolithic system does not depend solely on the method to treat the nonlinearities; indeed, other factors, such as the choice of the time step or the explicit vs. implicit imposition of the boundary conditions on the FSI system play an important role as well Crosetto [2011]; Nobile et al. [2013b]; Janela et al. [2010c].

The weak formulation of the FSI problem is discretized in space by choosing suitable finite element spaces to discretize the space in Eqs. (6.17)-(6.21). In this regard, let us assume that two conforming triangulations \mathcal{F}_0^h and \mathcal{B}_0^h have been introduced to approximate the fluid and solid domains \mathcal{F}_0 and \mathcal{B}_0 , respectively; more precisely, triangulations \mathcal{F}_0^h and \mathcal{B}_0^h with matching grid of the fluid-solid interface Γ in Fig. 6.1 are considered. This choice has the advantage of avoiding interpolation procedures of the solid and fluid velocities when the velocity continuity condition is imposed. Afterward, we suppose that finite element spaces are detailed in the next chapters. In order to present the nonlinear monolithic system that must be solved at each time step in order to simulate the dynamics of the coupled FSI system, let us suppose that the discrete finite element solution at the time t^n (with $t^n = n\Delta T$, for $n = 0, \dots, N_t$, where ΔT is the time step in the BDF method and N_t is the total number of time steps for which $T = N_t\Delta T$ in Eq. (6.25)) has been computed and it is indicated by the vector $(\mathbf{v}_h^n, \hat{\mathbf{a}}_h^n, (\hat{\mathbf{a}}_{\mathcal{F}})_h^n)$, where $\mathbf{v}_h^n = (\mathbf{u}_h^n, p_h^n)$ indicates the solution of the fluid problem, while $\hat{\mathbf{a}}_h^n$ and $(\hat{\mathbf{a}}_{\mathcal{F}})_h^n$ are the solutions of the solid and geometric problems, respectively. The nonlinear monolithic system that is solved at each time step in order to compute the fluid (\mathbf{v}_h^{n+1}) , solid $(\hat{\mathbf{a}}_h^n)$, and geometric $((\hat{\mathbf{a}}_{\mathcal{F}})_h^n)$ solutions from the ones obtained at the previous time step is presented in Crosetto [2011] and it is recalled here for the

sake of completeness; it reads:

$$\begin{pmatrix}
 (F_h)_{\mathcal{F}_t\mathcal{F}_t} & (F_h)_{\mathcal{F}_t\Gamma_t} & 0 & 0 & 0 & 0 & 0 \\
 (F_h)_{\Gamma_t\mathcal{F}_t} & (F_h)_{\Gamma_t\Gamma_t} & 0 & 0 & \mathbf{I} & 0 & 0 \\
 \hline
 0 & 0 & (S_h)_{\mathcal{B}_0\mathcal{B}_0} & (S_h)_{\mathcal{B}_0\Gamma_0} & 0 & 0 & 0 \\
 0 & 0 & (S_h)_{\Gamma_0\mathcal{B}_0} & (S_h)_{\Gamma_0\Gamma_0} & -\mathbf{I} & 0 & 0 \\
 \hline
 0 & \mathbf{I} & 0 & -\mathbf{I}/\delta t & 0 & 0 & 0 \\
 \hline
 0 & 0 & 0 & 0 & 0 & (G_h)_{\mathcal{F}_0\mathcal{F}_0} & (G_h)_{\mathcal{F}_0\Gamma_0} \\
 0 & 0 & 0 & -\mathbf{I} & 0 & 0 & \mathbf{I}
 \end{pmatrix}
 \begin{pmatrix}
 (\mathbf{v}_h^{n+1})_{\mathcal{F}_t\mathcal{F}_t} \\
 (\mathbf{v}_h^{n+1})_{\mathcal{F}_t\Gamma_t} \\
 \hline
 (\widehat{\mathbf{d}}_h^{n+1})_{\mathcal{B}_0\mathcal{B}_0} \\
 (\widehat{\mathbf{d}}_h^{n+1})_{\mathcal{B}_0\Gamma_0} \\
 \hline
 \lambda_{\Gamma_0\Gamma_0}^{n+1} \\
 (\widehat{\mathbf{d}}_{\mathcal{F}}^{n+1})_{h,\mathcal{F}_0\mathcal{F}} \\
 (\widehat{\mathbf{d}}_{\mathcal{F}}^{n+1})_{h,\mathcal{F}_0\Gamma_0}
 \end{pmatrix}
 =
 \begin{pmatrix}
 (\mathbf{r}_{F_h}^{n+1})_{\mathcal{F}_t\mathcal{F}_t} \\
 (\mathbf{r}_{F_h}^{n+1})_{\mathcal{F}_t\Gamma_t} \\
 \hline
 (\mathbf{r}_{S_h}^{n+1})_{\mathcal{B}_0\mathcal{B}_0} \\
 (\mathbf{r}_{S_h}^{n+1})_{\mathcal{B}_0\Gamma_0} \\
 \hline
 (-\mathbf{I}/\delta t)(\widehat{\mathbf{d}}_h^{n+1})_{\mathcal{B}_0\Gamma_0} \\
 \hline
 0 \\
 0
 \end{pmatrix}, \quad (6.26)$$

where the right hand side depends on the forcing terms evaluated at the time t^{n+1} and on the solutions at the previous time steps according to the time discretization scheme. In Eq. (6.26), F_h , S_h , and G_h are the fluid, solid, and geometric discrete operators associated to the residuals of Eqs. (6.9)-(6.11) in which the finite element approximation of the unknown fields has been introduced; in particular, the block matrices $(F_h)_{A,B}$ are defined from the finite element discretization of the Navier-Stokes equations where the indexes A and B indicate the Lagrangian test and trial functions corresponding to a degree of freedom belonging to either the interior of \mathcal{F}_t or the interface Γ_t ; similar meaning for the matrices $(S_h)_{A,B}$ and $(G_h)_{A,B}$. From a general point of view, the diagonal blocks are obtained from the finite element discretization of the single sub-problem while the off-diagonal components enforce the coupling conditions. As discussed in Crosetto [2011], the component $\lambda_{\Gamma_0\Gamma_0}^{n+1}$ is a vector whose dimension is equal to the number of degrees of freedom lying on the fluid-wall interface and it represents a Lagrange multiplier to enforce the stresses continuity condition in a weak sense.

In order to solve the nonlinear system Eq. (6.26) the Newton-Raphson method is employed; thus, similarly to Sec. 5.1.3, the linearization of Eq. (6.26) is necessary. More precisely, when considering the linearized problem as in Eq. (5.11); thus, given the solution at the k -th iteration of the Newton-Raphson method $(\mathbf{v}_h^{n,k}, \widehat{\mathbf{d}}_h^{n,k}, (\widehat{\mathbf{d}}_{\mathcal{F}}^{n,k})_h)$, the correction step $(\delta \mathbf{v}_h^k, \delta \widehat{\mathbf{d}}_h^k, \delta (\widehat{\mathbf{d}}_{\mathcal{F}}^k)_h)$ is determined by the solution of the following linearized problem:

$$\begin{pmatrix}
 D_{\mathbf{v}}F & D_{\widehat{\mathbf{d}}}F & D_{\widehat{\mathbf{d}}_{\mathcal{F}}}F \\
 D_{\mathbf{v}}S & D_{\widehat{\mathbf{d}}}S & D_{\widehat{\mathbf{d}}_{\mathcal{F}}}S \\
 0 & D_{\widehat{\mathbf{d}}}G & D_{\widehat{\mathbf{d}}_{\mathcal{F}}}G
 \end{pmatrix}
 \begin{pmatrix}
 \delta \mathbf{v}_h^k \\
 \delta \widehat{\mathbf{d}}_h^k \\
 \delta (\widehat{\mathbf{d}}_{\mathcal{F}}^k)_h
 \end{pmatrix}
 =
 \begin{pmatrix}
 -\mathcal{R}_F(\mathbf{v}_h^k, \widehat{\mathbf{d}}_h^k, (\widehat{\mathbf{d}}_{\mathcal{F}}^k)_h) \\
 -\mathcal{R}_S(\mathbf{v}_h^k, \widehat{\mathbf{d}}_h^k, (\widehat{\mathbf{d}}_{\mathcal{F}}^k)_h) \\
 -\mathcal{R}_G(\widehat{\mathbf{d}}_h^k, (\widehat{\mathbf{d}}_{\mathcal{F}}^k)_h)
 \end{pmatrix} \quad (6.27)$$

where $\mathbf{v} = (\mathbf{u}, p)$ and $D_i \mathcal{P}(\bullet, \bullet, \bullet)$ indicates the Gateaux derivative of the operator \mathcal{P} defining each sub-problem, i.e. $\mathcal{P} = F, S, G$ where F, S, G are defined in Eqs. (6.9)-(6.11), with respect to the i -th component i of the monolithic solution, i.e. $i = (\mathbf{v}, \widehat{\mathbf{d}}, \widehat{\mathbf{d}}_{\mathcal{F}})$. In Eq. (6.27) $\mathcal{R}_{\mathcal{P}}(\bullet, \bullet, \bullet)$, for $\mathcal{P} = F, S, G$, denote the variational residual defined from each of the three sub-problems, see Crosetto [2011]. For

a more detailed definition of the linearized operator in Eq. (6.27), the interested reader may refer to Malossi [2012]. The derivative of the fluid operator F with respect to the displacement of the fluid domain $D_{\hat{a}_f}$ are usually referred as the shape derivatives Crosetto [2011]; Fernández and Moubachir [2005]. As discussed in Crosetto [2011]; Fernández and Moubachir [2005], their correct computation and implementation is not straightforward and, for some applications, they are neglected from the tangent matrix in Eq. (6.27). However, poor convergence of the Newton-Raphson method might be observed when that block in the tangent matrix is not considered, see e.g. Fernández and Moubachir [2005]. For this reason, in this work, they have been considered in the tangent matrix of the linearized problem.

7 Applications to hemodynamics: healthy cerebral vessels

In literature, numerical simulations on cylindrical and toroidal geometries representing idealized blood vessels have been employed to study, for instance, the convergence properties of iterative solution strategies of the FSI problem Pozzoli [2011]; Fernández and Moubachir [2005]; Gerbeau and Vidrascu [2003] or to design and analyze coupling strategies for three-dimensional and reduced FSI models Malossi [2012]; Janela et al. [2010a]; Formaggia et al. [2006b]. Similarly, they can be employed to analyze the influence of the modeling choice of the arterial wall on the numerical results.

This chapter presents the numerical simulations of the blood flow in cylindrical and toroidal geometries of arteries for different modeling choices of the arterial wall; more precisely, the material parameters of the constitutive models characterize the mechanical behavior of healthy cerebral arterial tissue, see Sec. 5.4.1. The aim of the current analysis is to simulate the physiological mechanical forces that act on the vessel wall during one heart beat and to evaluate the effects of the constitutive model (either isotropic or anisotropic) on the spatial distribution of mechanical quantities, e.g. the stresses, that are commonly considered as important indicators in the study of the mechanical behavior of healthy arterial tissue. For this reason, in order to reproduce physiologic hemodynamical conditions, the computational domains under consideration reproduce the physiological dimensions of healthy cerebral vessels (as in Sec. 5.4.2) and the boundary conditions imposed on the solid and fluid domains are derived from *in vivo* measurements.

This chapter is organized as follows. Sec. 7.1 describes the simulations setting, i.e. the set of boundary and initial conditions for the FSI problem under consideration. Sec. 7.2 presents the numerical results obtained for two idealized geometries of blood vessels and their critical analysis; more precisely, Secs. 7.2.1 and 7.2.2 discuss the FSI numerical simulations carried out on a straight cylinder, while Sec. 7.2.3 presents the results obtained in the case of a toroidal geometry.

7.1 Problem setting

In this section, the notation of Fig. 6.2 is adopted in order to indicate specific subsets of the computational domain and of its boundary (e.g. inlet or outlet surfaces). The size of the computational domain is the physiological one for the anterior cerebral artery considered in Scott et al. [1972], for which both the isotropic and anisotropic constitutive models of Ch. 4 have been numerically validated, see Sec. 5.4. For this reason, the material parameters of the constitutive models that are considered in the next section are those summarized in Tabs. 5.3 and 5.5. In addition, the density ρ_f and dynamic viscosity

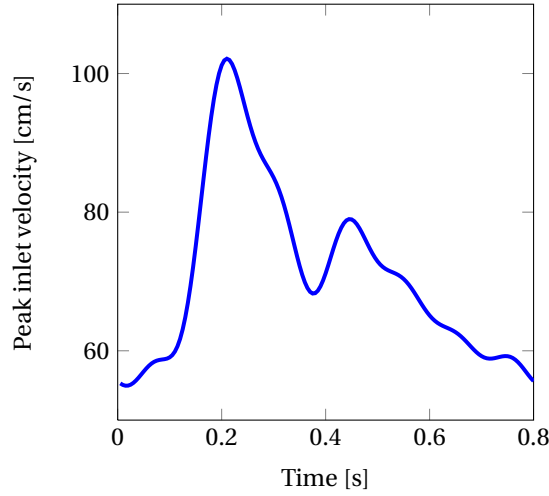


Figure 7.1: Peak velocity of the inlet parabolic profile imposed on the boundary $\Gamma_{\mathcal{F},D}^{in}$ of the fluid domain

μ_f of the blood are $\rho_f = 1.0 \text{ g/cm}^3$ and $\mu_f = 0.035 \text{ g / (cm}\cdot\text{s)}$, respectively, while the density of the arterial wall $\rho_s = 1.2 \text{ g/cm}^3$ as e.g. in Crosetto [2011]; Malossi [2012]. As mentioned in Sec. 6.2, the three sub-problems are discretized in time by means of a second order BDF method.

At the inlet surface $\Gamma_{\mathcal{F},D}^{in}$ of the fluid domain, a parabolic velocity profile centered with respect to $\Gamma_{\mathcal{F},D}^{in}$ is imposed along the inward directed normal unit vector to $\Gamma_{\mathcal{F},D}^{in}$. The time evolution (represented in Fig. 7.1) of the peak velocity of the parabolic profile is computed from a physiological flux profile measured on an Internal Carotid Artery (ICA) Baek et al. [2010]. More in detail, the physiological flux employed in Baek et al. [2010] has been rescaled with respect to the cross section area of the geometries under consideration and the applied parabolic profile is such that, at each time t , the total inlet flux through $\Gamma_{\mathcal{F},D}^{in}$ is equal to the rescaled flux. It is worth pointing out that the velocity values of the inlet profile reported in Fig. 7.1 are consistent with the experimental measurements reported in literature for the cerebral vasculature Hart and Haluzkiewicz [2000]; Matsuo et al. [2011]; Ogoh et al. [2005]. A resistance boundary condition is imposed at the outlet surface $\Gamma_{\mathcal{F},N}^{out}$ of the fluid domain, see Eq. (6.13). The resistance R in Eq. (6.13) is chosen to attain physiological values of blood pressure inside the fluid domain, as done in e.g. Torii et al. [2008]; Bazilevs et al. [2010]; Reymond et al. [2010]; Bazilev et al. [2010]; Torii et al. [2006, 2009]. In addition, the dependence of the resistance boundary condition on the flux Q measured on $\Gamma_{\mathcal{F},N}^{out}$ is treated implicitly Malossi [2012]; in the numerical simulations presented hereafter $R = 1.032 \cdot 10^6 \text{ dyn} \cdot \text{s} / \text{cm}^5$.

An elastic Robin boundary condition as the one in Eq. (6.15) is applied on the external surface of the solid domain $\Gamma_{\mathcal{B}_0,ext}$. In this case, in Eq. (6.15) we set $\mathbf{h} = \mathbf{0}$, while the elastic coefficient K is determined such that physiological radial deformations of the vessel wall are obtained Draney et al. [2002]; we set, $K = 10^7 \text{ dyn/cm}^3$. Elastic Robin boundary conditions have been employed in e.g. Crosetto [2011]; Crosetto et al. [2011], while in Malossi [2012]; Moireau et al. [2012]; Malossi and Bonemann [2013] a viscoelastic Robin boundary condition is applied. As pointed out in Crosetto [2011]; Crosetto et al. [2011], physiological displacements of the arterial wall can be obtained by considering elastic Robin boundary conditions. For this reason, due to the lack of experimental data to estimate the mechanical coefficients in the viscoelastic Robin conditions of Malossi [2012]; Moireau et al. [2012]; Malossi and Bonemann [2013] for the cerebral vasculature, pure elastic Robin boundary condition have been

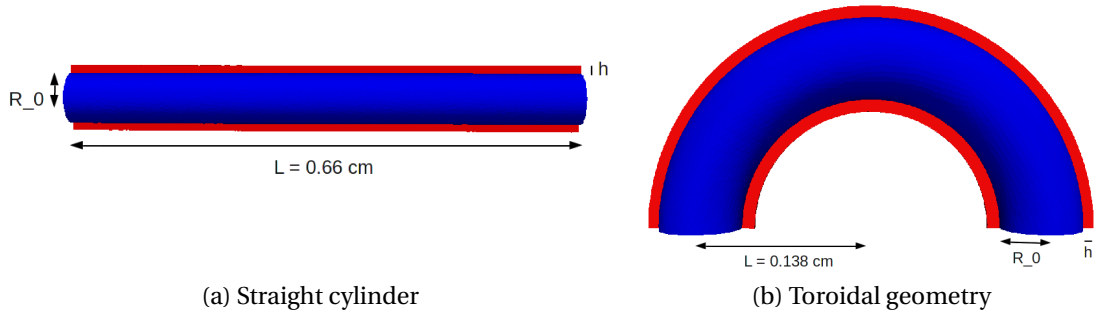


Figure 7.2: Idealized geometries of blood vessels. The internal radius R_0 and wall thickness h represent the characteristic dimensions of the anterior cerebral artery Scott et al. [1972]

preferred to viscoelastic Robin conditions on the external surface.

In this work, the FSI numerical simulations have been carried out by using the FSI monolithic solver implemented in *LifeV* and described in Crosetto [2011]. More precisely, in order to use the nonlinear constitutive models described in Ch. 5, the framework for managing the different constitutive models described in Sec. 5.2.1 has been integrated in the FSI module of *LifeV*. The numerical simulations have been run in parallel on 128 processors on the Cray XE6 supercomputer *Monte Rosa* at the Swiss national supercomputing center CSCS in Lugano, Switzerland.

7.2 Numerical simulations on idealized blood vessels

This section presents the FSI numerical simulations that have been carried out for two different geometries representing idealized blood vessels: a straight cylindrical and a toroidal domain, see Fig. 7.2. The internal radius and wall thickness of the vessels are the same as in Sec. 5.4, namely $R_0 = 0.033$ cm and $h = 0.01$ cm, respectively. It is worth pointing out that, for the time evolution of the peak inlet velocity represented in Fig. 7.1, the characteristic dimensions of the fluid domains in Fig. 7.2, and the fluid density and dynamic viscosity, we have that the Reynolds number in the fluid domain varies between 53 and 103 during one heart beat. This, as it is shown in the next sections, yields a laminar blood flow in the fluid domain during the full heart beat. Sec. 7.2.1 deals with the numerical simulations on the cylindrical geometry in Fig. 7.2, while Sec. 7.2.3 presents the ones on the toroidal domain; details regarding the spatial discretization of the computational domains and the dimensions of the finite element monolithic problem are provided in the following sections. Concerning the finite element spaces employed for the discretization of the weak formulation of Eq. (6.25), the fluid problem is discretized by means of the Inf-Sup stable pair $\mathbb{P}1\text{Bubble}-\mathbb{P}1$ of finite elements Quarteroni and Valli [1999b], while the solid and the geometric problems are discretized using linear $\mathbb{P}1$ finite elements.

7.2.1 FSI simulations on a straight cylinder

In this case, the FSI numerical simulations have been carried out on two different sets of triangulations of the fluid and solid domains. The motivation for this choice is described in Sec. 7.2.2 and it is related to the description of the mechanical activation of collagen fibers throughout the vessel wall. The two sets of meshes under consideration differ from each other on the triangulation of the fluid-structure interface Γ . More precisely, the meshes in the first set (indicated as Set 1) are built from an unstructured

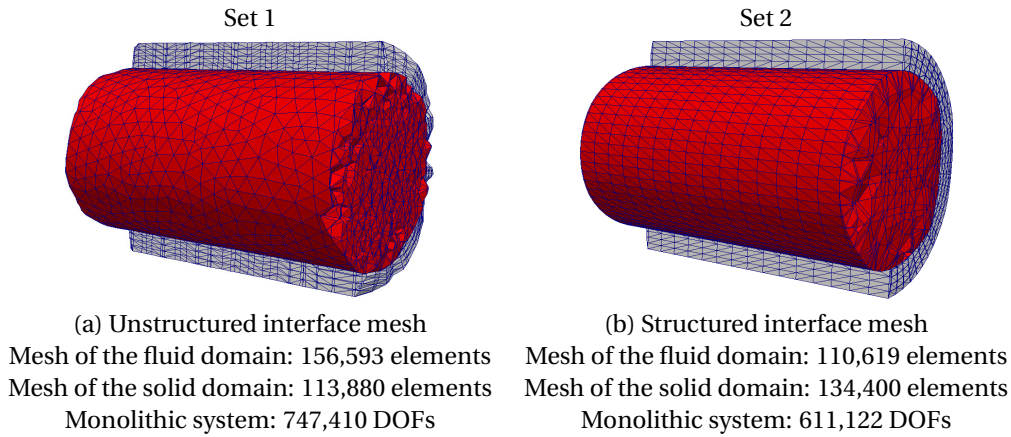


Figure 7.3: Two sets of meshes of the cylindrical geometries employed in the numerical simulations

Constitutive model	Set of meshes
SVK	Set 1
EXP1	Set 1
EXP2	Set 1
(EXP1, EXP2-RC)	Set 1
(EXP1, EXP2-sMM)	Set 2

Table 7.1: Set of meshes employed in the numerical simulations for the different constitutive models for the vessel wall

triangulation of Γ , while the second ones (i.e. Set 2) are built from a structured mesh of the fluid-structured interface, as reported in Fig. 7.3. As it will be described in Sec. 7.2.2, Set 2 has been employed in the numerical simulations only when the anisotropic (EXP1, EXP2-sMM) law describes the vessel wall, see Tab. 7.1. However, in order to have a fair comparison of the numerical results in terms of the DOFs of the FSI monolithic problem among the different simulations under consideration, the fluid and solid meshes in Set 1 and Set 2 are composed of a similar number of tetrahedra; the details regarding the different meshes in the two sets are presented in Fig. 7.3.

In order to extract the numerical results for the current analysis, two complete heart beats have been numerically simulated for all the cases under consideration. Indeed, as presented in Fig. 7.4(a), due to the laminar flow occurring inside the fluid domain, the periodic regime in the fluid pressure and velocity field are attained during the second heart beat. Fig. 7.4(b) shows the time evolution of the mean blood pressure at the cross section $z = 0.33$ cm measured for the different constitutive models. It can be observed the strong pulsatile behavior as reported in Ferguson [1972a]; in addition, it is worth pointing out that, the minimum value of the pressure, $p = 75$ mmHg, and pressure range are consistent with the experimental observations reported in den Heijer et al. [2003] and the values considered in Valencia et al. [2013]; Torii et al. [2007] in physiological numerical simulations of cerebral circulation. The time evolution of the mean blood pressure at $z = 0.33$ cm is very similar for all the numerical simulations performed with the different constitutive models. This suggests that, in this case, the constitutive model for the arterial wall does not strongly affect the hemodynamics inside the vessel lumen and viceversa.

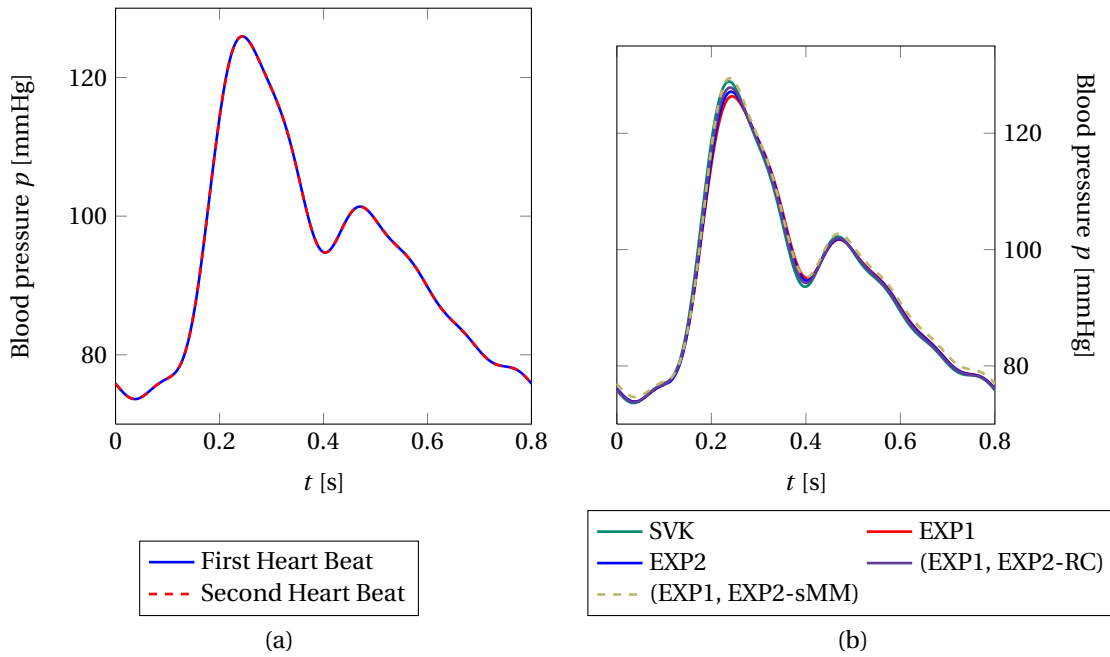


Figure 7.4: Blood pressure p vs time at the cross section $z = 0.33$ cm; (a) periodic regime between the first and second heart beat; (b) pressure profiles for the different constitutive models

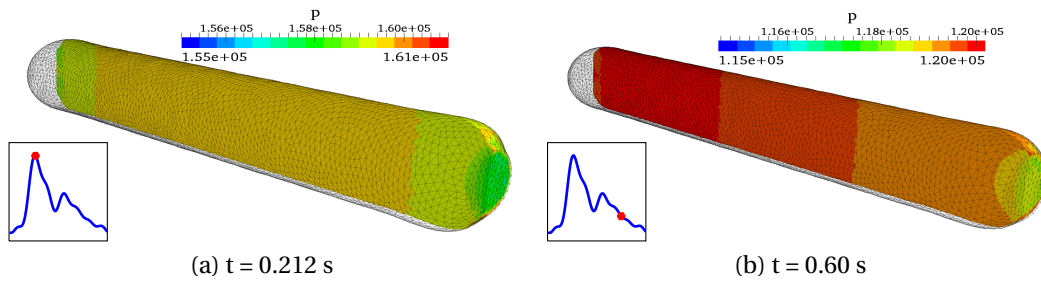


Figure 7.5: Blood pressure p [dyn / cm²] in the deformed fluid domain. Constitutive model for the arterial wall: EXP1

Fig. 7.5 presents the blood pressure p in the deformed fluid domain at the time $t = 0.212$ s, corresponding to the systolic peak of the inflow fluid velocity profile, and at time $t = 0.60$ s during the diastolic phase. Since similar results were obtained with all the constitutive laws, for the sake of brevity, only the spatial distribution of the fluid pressure p in the case of the EXP1 model for the vessel wall is shown. It can be observed that the pressure field p presents a very low spatial gradient along the axis of the cylindrical geometry. This is due to the high resistance R that is considered for the outlet boundary conditions which induces physiological values of blood pressure in the fluid domain.

Fig. 7.6 shows the magnitude of the fluid velocity \mathbf{u} at different cross sections of the fluid domain in the case of the EXP1 constitutive model for the arterial wall; similar results were obtained also with the other constitutive models. In Fig. 7.6, each cross section is deformed according to the vectorial field \mathbf{u} . As it can be observed, the fluid velocity profile is parabolic at all the cross sections considered, that is a laminar flow is established. In addition, the magnitude of the fluid velocity increases at the outlet surface of the fluid domain. This effect is induced by the low Reynolds number attained during

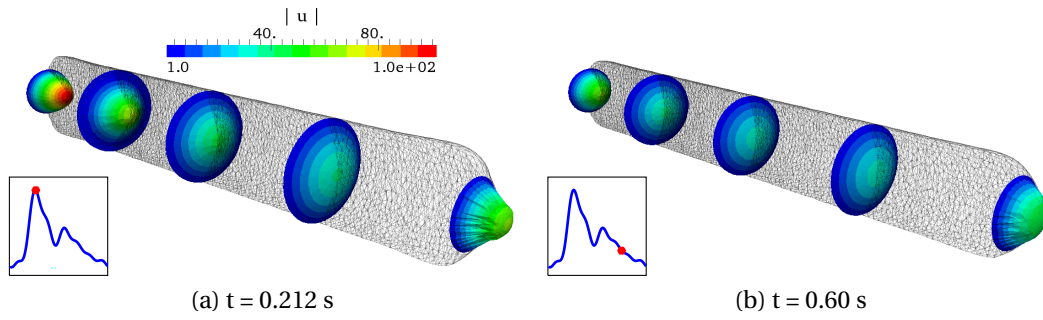


Figure 7.6: Magnitude of the blood flow velocity \mathbf{u} [cm / s] in the deformed fluid domain. Constitutive model for the arterial wall: EXP1

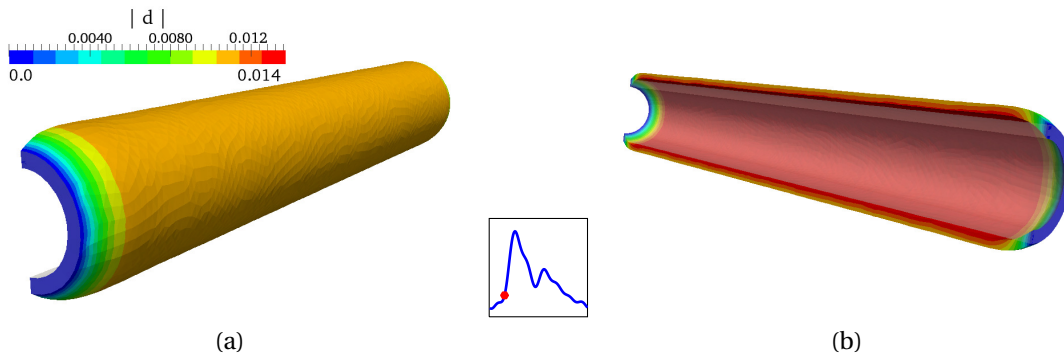


Figure 7.7: Displacement $\hat{\mathbf{d}}$ [cm] of the vessel wall. (a) External view; (b) Internal view. Time $t = 0.100$ s. Constitutive model EXP1. The gray overlay represents the undeformed domain.

the heart beat and the homogeneous Dirichlet boundary conditions imposed on the fluid domain displacement on $\Gamma_{\mathcal{F},D}^{out}$; indeed, it is due to the smaller cross-section surface of the outlet boundary $\Gamma_{\mathcal{F},D}^{out}$ with respect to the surface of an internal cross-section of the fluid domain.

Figs. 7.7-7.9 show the deformations of the vessel wall at three different times of the heart beat. As for the fluid velocity and pressure, similar results were obtained among the numerical simulations; therefore, in Figs. 7.7-7.9, the deformations of the solid domain are presented only in the case of the isotropic EXP1 law. During the heart beat, the vessel wall deforms mainly in the radial direction rather than along the axial direction of the domain. In addition, the characteristic propagation of the pressure wave from the inlet toward the outlet of the fluid domain often obtained within the context of FSI numerical simulations on idealized geometries of vessels (e.g. Formaggia et al. [2009]; Fernández and Moubachir [2005]; Janela et al. [2010c]) is not observed. Indeed, the development of such pressure wave strongly depends on the boundary conditions imposed both at the outlet and external surfaces of the fluid and solid domains, respectively. Thus, the pressure wave propagation does not occur due to the high resistance R applied on $\Gamma_{\mathcal{F},D}^{out}$ and to the elastic Robin boundary conditions imposed on $\Gamma_{\mathcal{B}_0,ext}$. The displacement magnitude of the vessel wall obtained for the different models at time $t = 0.212$ s is presented in Figs. 7.10-(a)-(e). The displacement magnitude in Figs. 7.10-(a)-(e) has been rescaled in order to show the qualitative behavior of all the numerical solutions. As already mentioned for Figs. (7.7)-(7.9), the qualitative behavior of the numerical solution is the same as the one reported in Fig. 5.22 for static inflation tests where the deformations of the vessel wall were purely along the radial direction of the domain. In addition, as expected, the largest displacement occurs at the inner

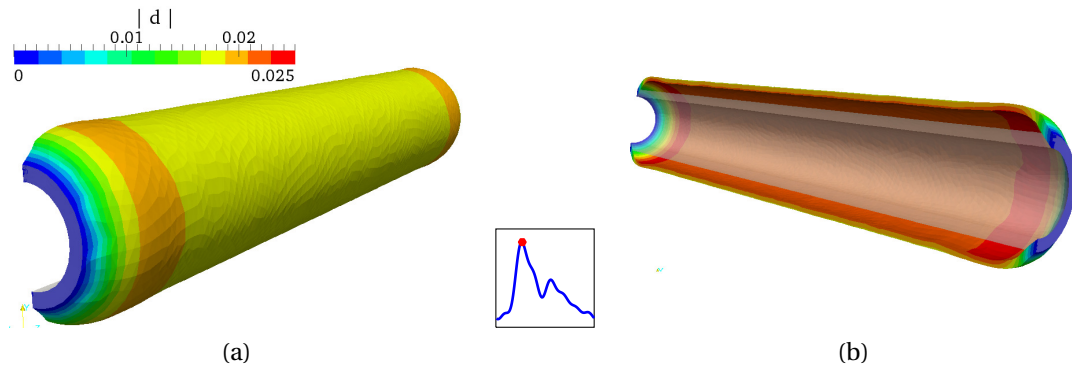


Figure 7.8: Displacement $\hat{\mathbf{d}}$ [cm] of the vessel wall. (a) External view; (b) Internal view. Time $t = 0.212$ s. Constitutive model EXP1. The gray overlay represents the undeformed domain.

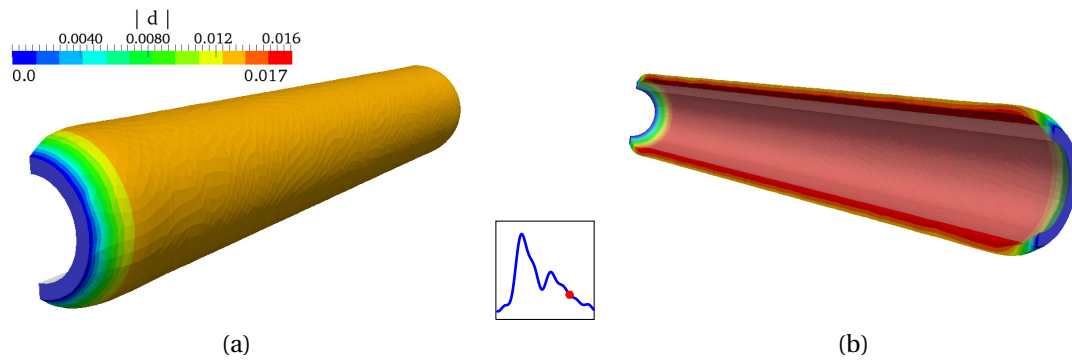


Figure 7.9: Displacement $\hat{\mathbf{d}}$ [cm] of the vessel wall. (a) External view; (b) Internal view. Time $t = 0.60$ s. Constitutive model EXP1. The gray overlay represents the undeformed domain.

surface of the artery. Fig. 7.10-(f) presents the radial displacement at one point of the internal surface of the vessel wall along the heart beat. In Fig. 7.10-(f), for each constitutive model, the maximum and minimum values in the radial displacement indicate a change in the vessel radius of approximately 27% of the undeformed internal radius R_0 during the heart beat. This value is consistent with the experimental measurements reported in Giller et al. [1993] for the anterior cerebral artery. In addition, Fig. 7.10-(f) shows that the choice of the constitutive model for the arterial tissue significantly affects the resulting vessel wall displacement. More specifically, the use of the SVK model leads to the smallest vessel wall displacements, whereas the highest displacements are registered for the EXP2 law; more precisely, the displacement predicted by the EXP2 model is around 11% higher than the one obtained with the SVK model during the heart beat. It is worth pointing out that the deformations of the vessel wall depend not only on the mechanical loads due to the blood flow but also the mechanical pressure applied on the external surface of the vessel wall defined by the Robin boundary condition. Therefore, in order to explain the numerical results presented in Fig. 7.10-(f), the effective transmural pressure given by the difference of the two mechanical loads must be considered. More specifically, the effective transmural pressure measured during the heart beat varies between $\Delta P = 3$ mmHg and $\Delta P = 15$ mmHg. As discussed in Sec. 5.4.1, for this range of transmural pressures, for the material parameters of Tabs. (5.3) and (5.5), the SVK and EXP2 model represent the most and the least rigid material, respectively (see Fig. 5.17-(a)). The same argument holds for the differences in the numerical results among the two anisotropic models, see Fig. 5.20-(a).

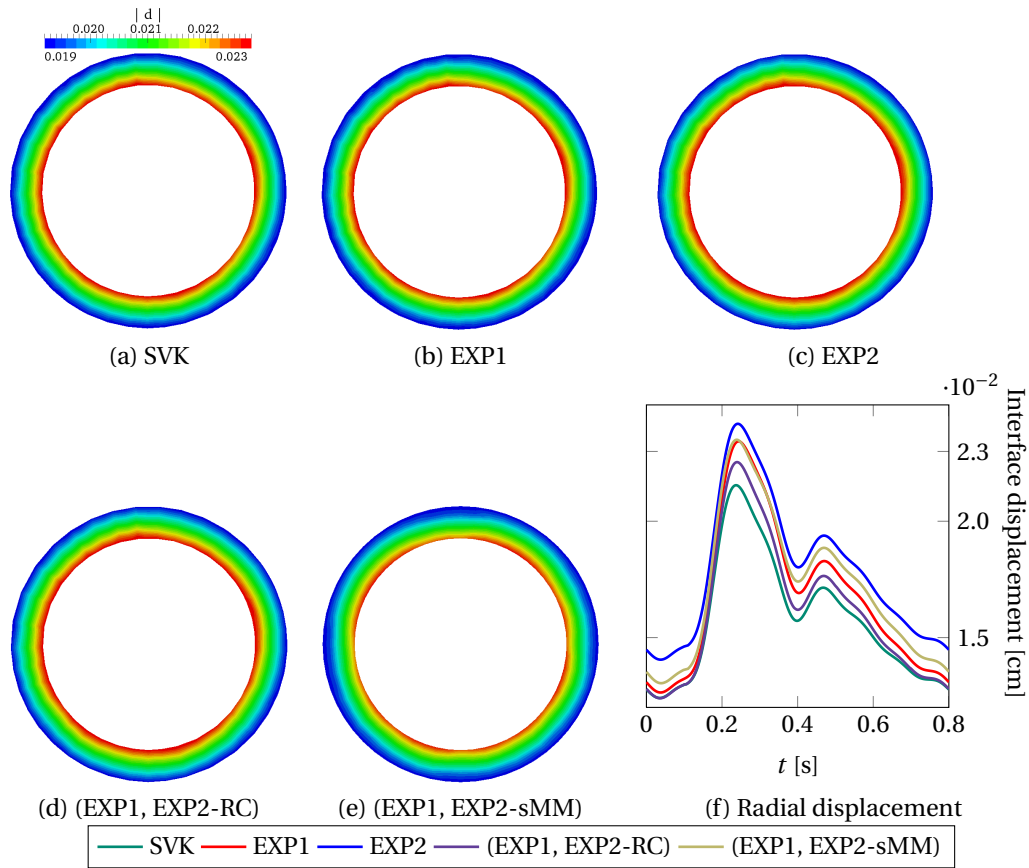


Figure 7.10: Displacement \hat{d} [cm] of the vessel wall at the cross section $z = 0.33$ cm for the different constitutive models.

When anisotropic constitutive laws for the vessel wall are employed, it is interesting to investigate the deformations of the collagen fibers during the heart beat to estimate their contribution to the mechanical response of the vessel wall. In order to qualitatively present the dynamics of the collagen fibers orientation during the heart beat, the (EXP1, EXP2-sMM) model is considered; however, a similar dynamics has been observed also in the case of the (EXP1, EXP2-RC) model. Fig. 7.11 shows the two families of fibers passing through the points lying on the intersection between the vertical plane $z = 0.33$ and the straight line $y = 0$. As reported in Tab. 5.5, the characteristic angle $\beta^{(i)}$, for $i = 1, 2$, between the local alignment of each family and the circumferential direction is $|\beta^1| = |\beta^2| = 42.82^\circ$. In Fig. 7.11, the collagen fibers are presented in their undeformed state, i.e. for zero displacement of the vessel wall. On the other hand, Fig. 7.12 shows the deformations of the collagen fibers during the heart beat. The variation of their local direction is highlighted in Figs. (7.12)-(b) and (7.13); the angle between the local alignment of the single family of collagen fibers and the circumferential direction decreases as the radial displacement increases. In particular, in Fig. 7.12, the position of the collagen fibers at the beginning and the end of the heart beat is represented by the purple curves; the corresponding characteristic angle with respect to the circumferential direction measures $|\beta_{ref-HB}^{(1)}| = |\beta_{ref-HB}^{(2)}| = 35.70$ rad. As expected, the maximum variation in the local alignment of the collagen fibers in the heart beat with respect to β_{ref-HB} is observed in correspondence with the systolic peak of the inlet velocity profile, for which the measured angle is $|\beta_{systole}^{(1)}| = |\beta_{systole}^{(2)}| = 33.071^\circ$ rad. Therefore, in the case of the (EXP1, EXP2-sMM) model, for physiological diastolic and systolic blood pressures, the change in the local orientation of the

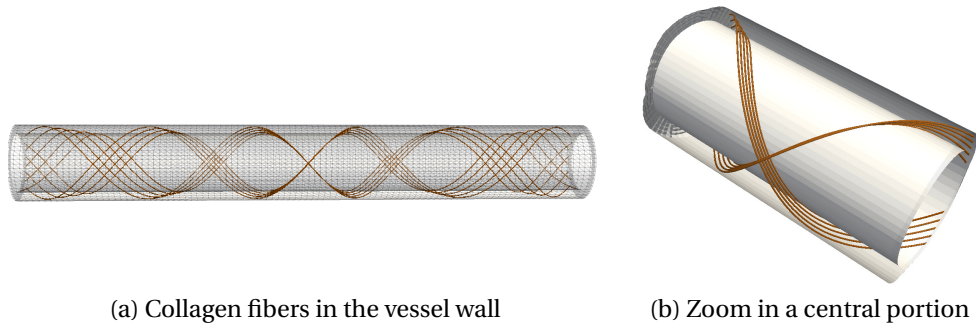


Figure 7.11: Representation of the collagen fibers in the reference configuration \mathcal{B}_0 of the arterial wall. Constitutive model: (EXP1, EXP2-sMM), see Tab. 5.5

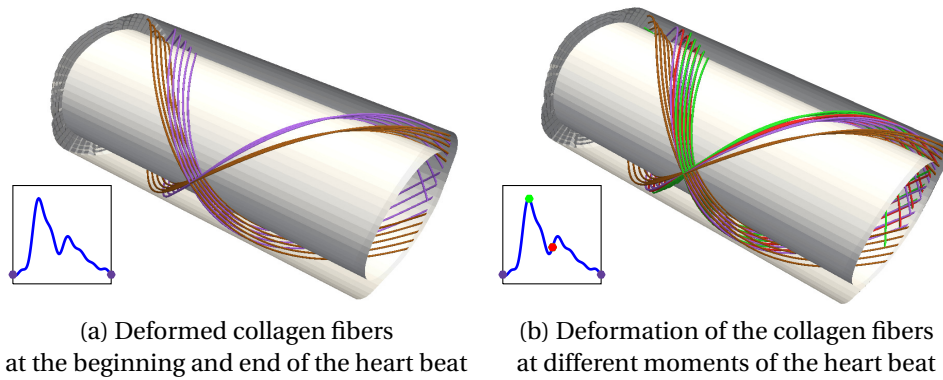


Figure 7.12: Representation of the deformed collagen fibers at different times during the heart beat. Constitutive model: (EXP1, EXP2-sMM)

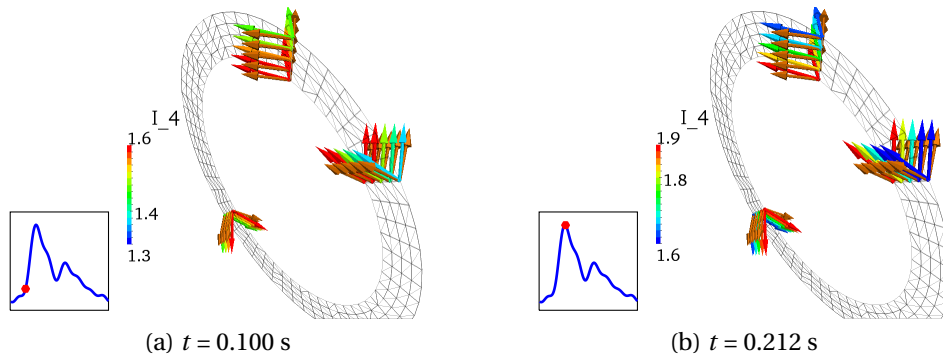


Figure 7.13: Local alignment of the collagen fibers at the cross section $z = 0.33$ cm. The brown arrows represent the collagen fibers in the reference configuration of the vessel wall. Constitutive model: (EXP1, EXP2-sMM)

collagen fibers is about the 7% of β_{ref-HB} . As already mentioned, similar results have been obtained in the case of the (EXP1, EXP2-RC) model for which $|\beta^1| = |\beta^2| = 56.52$, $|\beta_{ref-HB}^{(1)}| = |\beta_{ref-HB}^{(2)}| = 0.8964$, and $|\beta_{systole}^{(1)}| = |\beta_{systole}^{(2)}| = 47.11^\circ$; therefore the maximum variation is about 8% of $|\beta_{ref-HB}^{(1)}|$. On the other hand, the variation between $\beta^{(1)}$ and $\beta_{ref-HB}^{(1)}$ (or, similarly, $\beta^{(2)}$ and $\beta_{ref-HB}^{(2)}$) cannot be considered as an indicative measure of the deformations of the collagen fibers, since it strongly depends

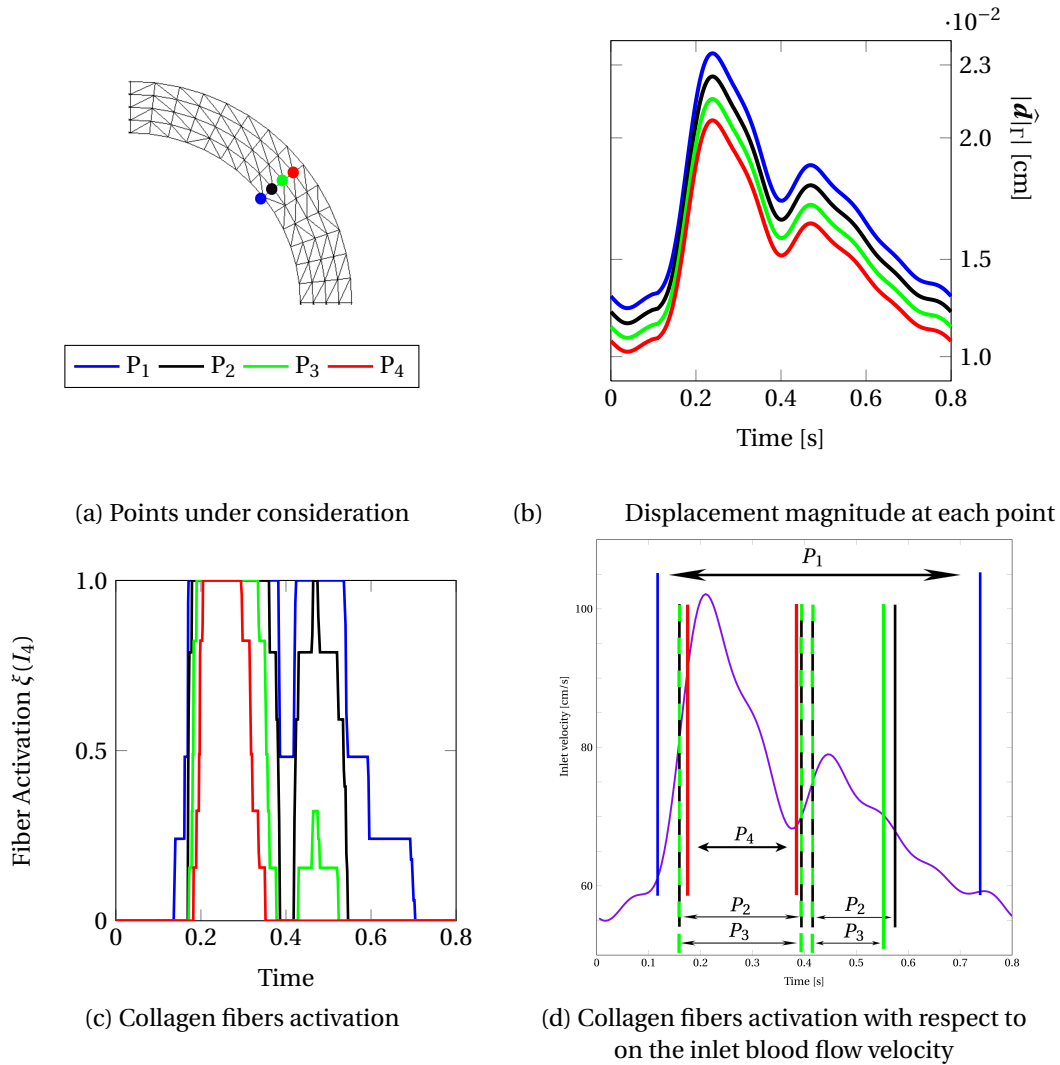


Figure 7.14: Displacement and activation times through the thickness of the vessel wall for the multi-mechanism model (EXP1, EXP2-sMM)

on the diastolic pressure attained in the numerical simulations. As presented in Fig. 7.13, the highest stretch of the collagen fibers occurs at the internal surface of the vessel wall in correspondence with the highest displacement. As a final remark, it is worth pointing out that the local orientations of the two families of fibers remain symmetric with respect to the circumferential direction of the cylinder since, as presented in Figs. (7.7)-(7.9), the vessel wall deforms along the radial direction.

When the anisotropic multi-mechanism model is employed in the numerical simulations, the progressive activation and deactivation of the collagen fibers through the thickness of the vessel wall is observed. In order to show the time evolution of the mechanical activation of the collagen fibers through the thickness of the arterial wall, in Fig. 7.14-(a) four points along the radial direction of the domain are considered at $z = 0.33$ cm. Figs. (7.14)-(b)-(c) present the displacement and the mechanical activation of the collagen fibers for each one of the four points under consideration. As the arterial tissue displacement decreases moving along the radial direction from the internal toward the external

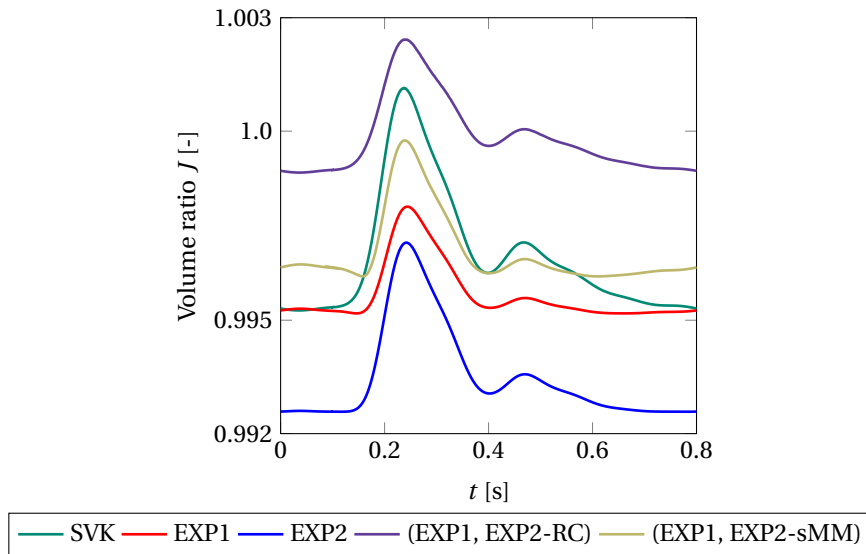


Figure 7.15: Mean volume ratio J on the cross section at $z = 0.33$ cm of the solid domain

surface of the domain, the total amount of time for which the collagen fibers are active during the heart beat decreases. It is worth pointing out that, the qualitative piecewise constant in time behavior of the activation functions in Fig. 7.14-(c) is due to the high value of the activation parameter $\epsilon = 5.0 \cdot 10^5$ chosen in Eq. (5.16) which leads to a highly steep activation function around the activation stretch; see Fig. 5.2. Fig. 7.14-(d) reports the activation time intervals for each of the four points presented in Fig. 7.14-(a) on the physiological inlet velocity profile. It can be observed that at the innermost point P_1 , the collagen fibers are mechanically active for almost the entire duration of the heart beat, while at P_4 , the outermost point under consideration, the collagen fibers activation occurs only during the systolic peak. On the other hand, at the points P_2 and P_3 internal to the arterial wall, the collagen fibers actively contribute to the mechanical response of the tissue during both the systolic and the diastolic phase of the heart beat. This numerical result may indicate the relevance of modeling the recruitment of the collagen fibers at finite strains to highlight the protective role of the fibers in the outermost layers of the arterial tissue. On the other hand, in the case under consideration, we recall that the collagen fibers are always mechanically active during the heart beat for the (EXP1, EXP2-RC) model; therefore, their progressive activation cannot be captured when considering such constitutive law.

Fig. 7.15 shows the approximation of the incompressibility constraint $J = 1$ for all the constitutive laws under consideration during the heart beat; the maximum error, about 0.8% is obtained with the EXP2 model. However, the approximation of the incompressibility condition is acceptable over the whole heart beat. It is worth pointing out that, the numerical result presented in Fig. 7.15 is due to the fact that the approximation of the condition $J = 1$ is related to the value of the effective transmural pressure between the internal and external surfaces of the solid domain. As already discussed, the application of elastic Robin boundary condition on $\Gamma_{\mathcal{B}_0, ext}$ that equilibrates the mechanical loads due to the blood flow leads to low effective transmural pressures for which the error on the kinematic condition $J = 1$ is small.

Figs. (7.16)-(7.21) show the spatial distribution of the Von Mises stress obtained with the different constitutive models at different times of the heart beat in a central portion of the solid domain. As it can be observed, at the beginning of the systolic phase (Figs. (7.16) and (7.17)) the highest values of

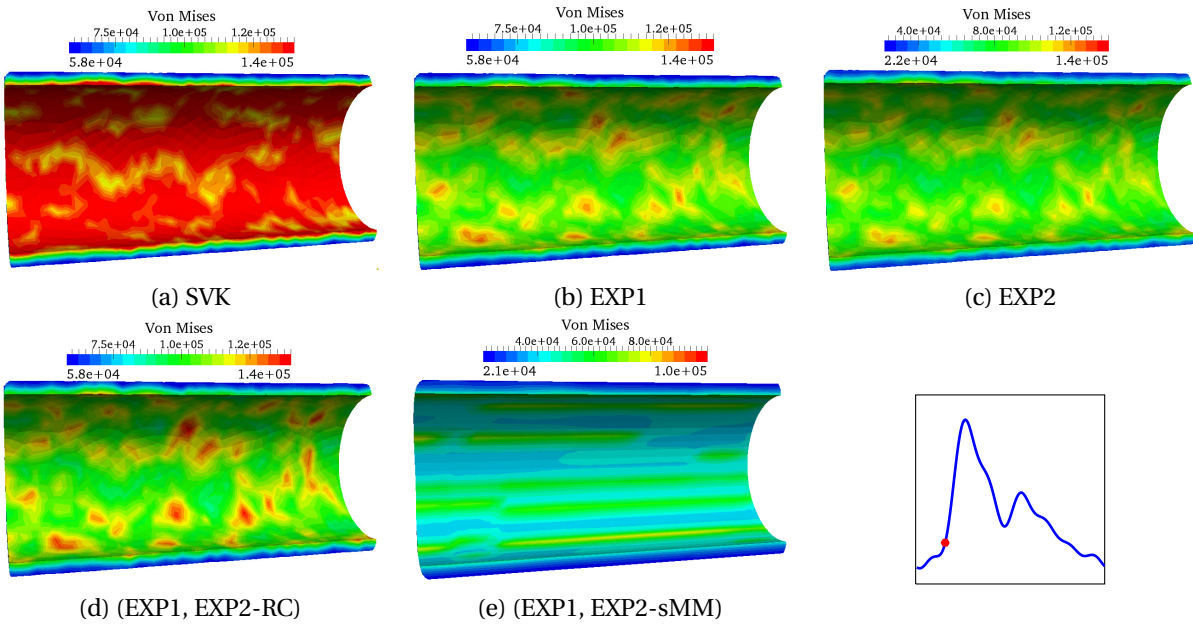


Figure 7.16: Von Mises stress for the different constitutive models at the time $t = 0.100$ s. Internal view

the Von Mises stresses are obtained for the SVK model. This result is consistent with both the data fitting presented in Fig. 5.17-(a) and the solid displacement presented in Fig. 7.10-(f); indeed, the SVK model describes the most rigid material among all the constitutive laws under consideration. On the other hand, the lowest values of Von Mises stress are obtained for the anisotropic (EXP1, EXP2-sMM) law. This is due to the fact that the Von Mises stress has been computed at $t = 0.1$ s for which the collagen fibers are partially activated, see Fig. 7.14-(c); therefore, although for the (EXP1, EXP2-sMM) model, the vessel wall displacement is similar to the ones obtained with the other constitutive models (see Fig. 7.10-(f)), the Von Mises stress is lower since parameter α_{iso}^{aniso} , that describes the mechanical stiffness of the isotropic part, in the (EXP1, EXP2-sMM) model is lower than the ones in the other constitutive models. At the systolic peak, see Figs. (7.18) and (7.19), the spatial distribution of the Von Mises stress does not present significant differences among the different cases under consideration. Indeed, similarly to Figs. (7.16) and (7.17), the SVK and the EXP2 models describe the most and the least rigid material, respectively. On the other hand, as reported in Figs. (5.17) and (5.20)(a), the EXP1 and the two anisotropic models predict similar values of the Von Mises stress. During the diastolic phase, see Figs. (7.20) and (7.21), the Von Mises stress in the case of the (EXP1, EXP2-sMM) model is lower than the one predicted by the other constitutive laws due to the deactivation of the fibers, similarly to what is reported in Figs. (7.16) and (7.17). In particular, it is worth pointing out that, when the multi-mechanism (EXP1, EXP2-sMM) model is employed in the numerical simulations, the variation of the Von Mises stress through the thickness vessel wall is strongly affected by the activation and deactivation of the collagen fibers. Indeed, in Figs. (7.16) and (7.17) and Figs. (7.20) and (7.21) the Von Mises stress along the radial direction is lower than the ones reported for the other models due to the non-active state of the collagen fibers through the arterial tissue, see Fig. 7.14-(d). On the other hand, the distribution of the Von Mises stress at the systolic peak measured for the (EXP1, EXP2-sMM) model is similar to the ones obtained for the remaining laws.

7.2. Numerical simulations on idealized blood vessels

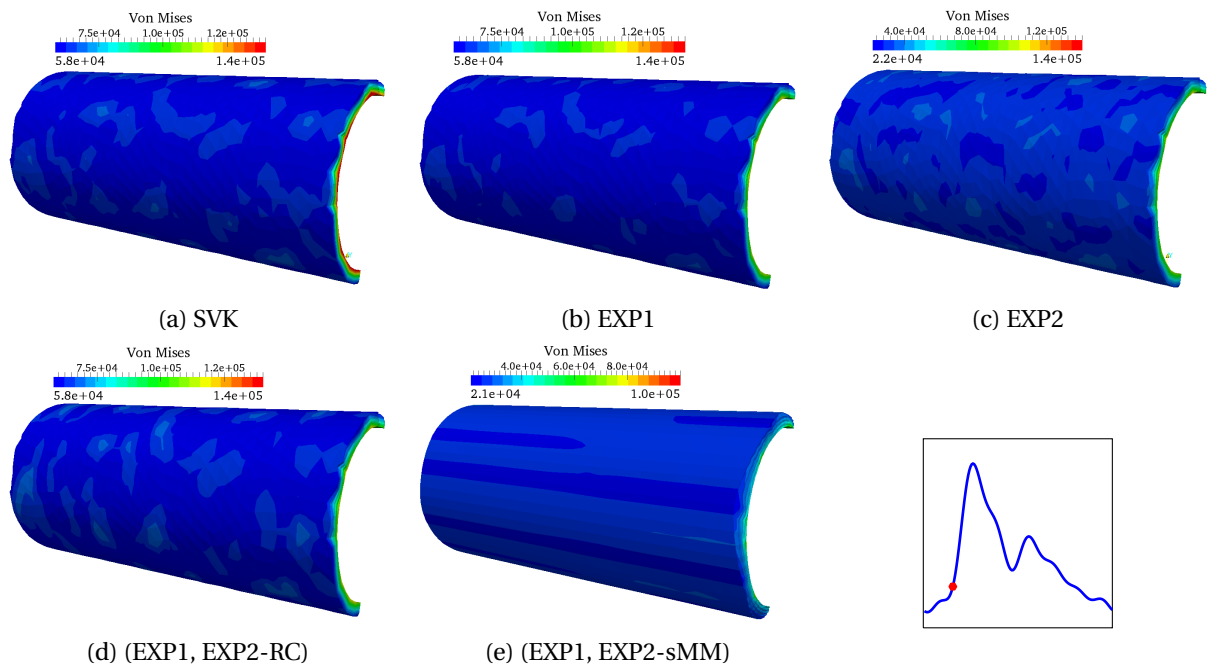


Figure 7.17: Von Mises stress for the different constitutive models at the time $t = 0.100$ s. External view

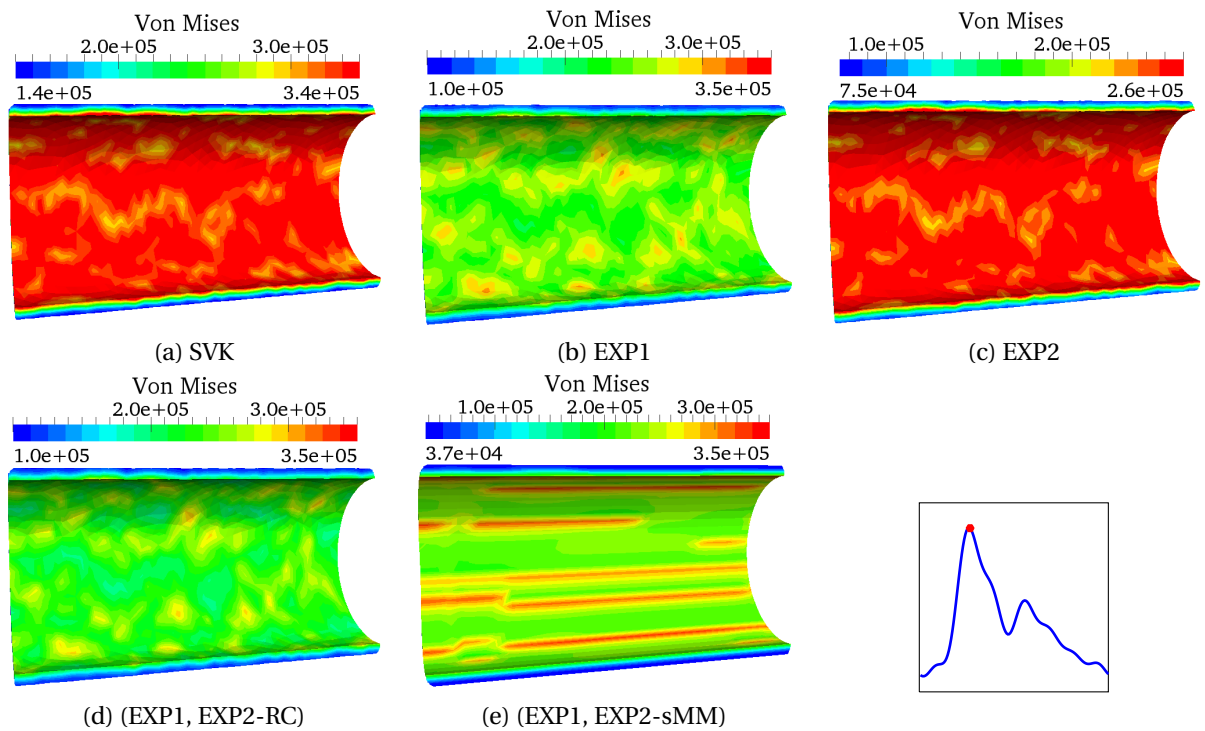


Figure 7.18: Von Mises stress for the different constitutive models at the time $t = 0.212$ s. Internal view.

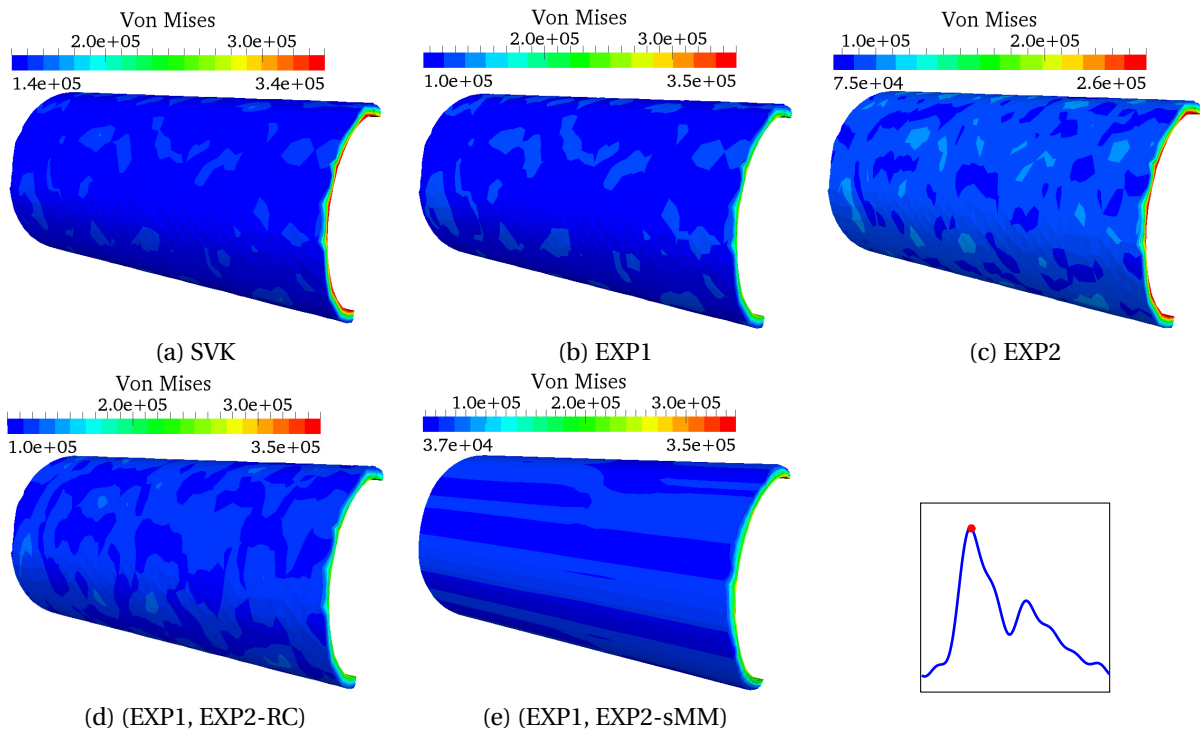


Figure 7.19: Von Mises stress for the different constitutive models at the time $t = 0.212$ s. External view.

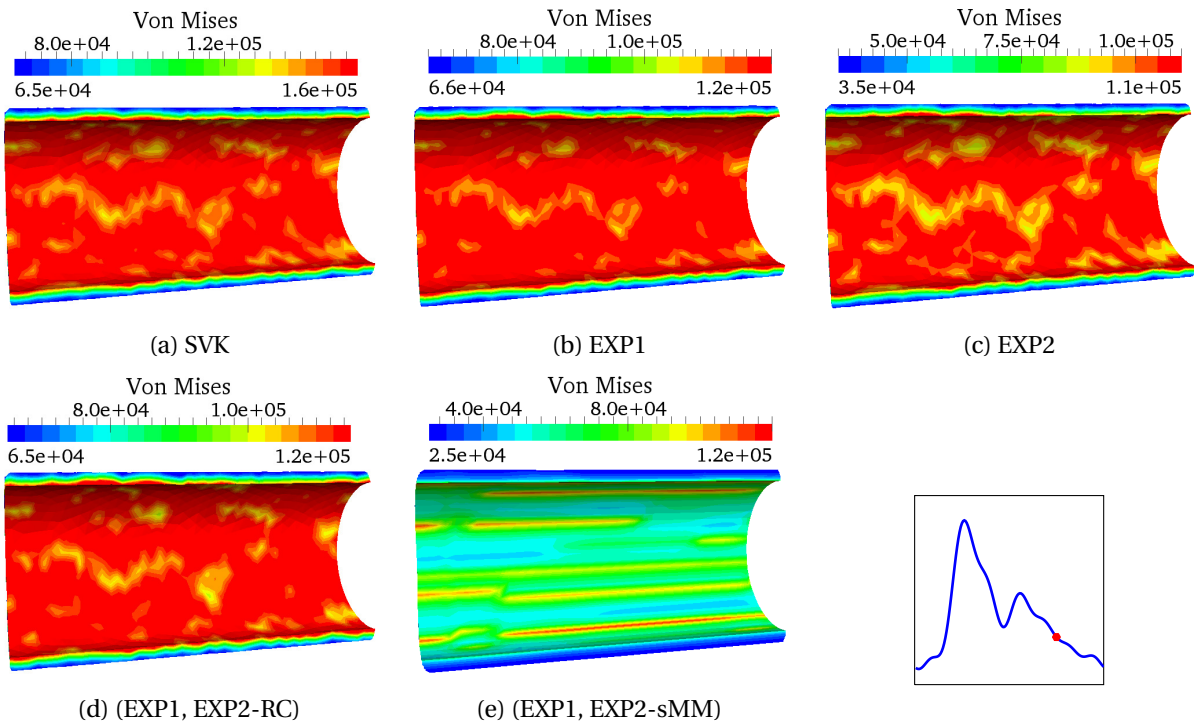


Figure 7.20: Von Mises stress for the different constitutive models at the time $t = 0.600$ s. Internal view.

7.2. Numerical simulations on idealized blood vessels

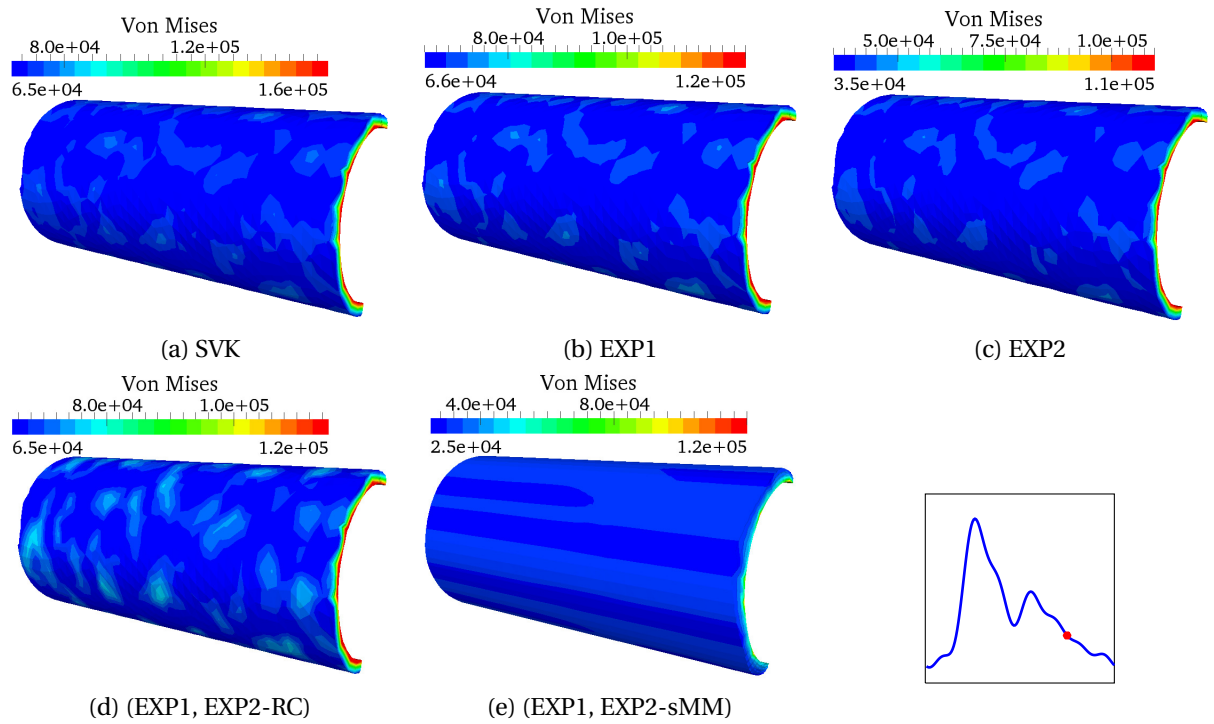


Figure 7.21: Von Mises stress for the different constitutive models at the time $t = 0.600$ s. External view.

7.2.2 On the collagen fibers activation in FSI numerical simulations

In this section we report and discuss the numerical issues that have been encountered when FSI numerical simulations with the multi-mechanism model (EXP1, EXP2-sMM) have been carried out on the idealized cylindrical geometry of anterior cerebral artery. Indeed, when such constitutive law is employed with the material parameters in Tab. 5.5, stagnation in the Newton-Raphson method of the FSI monolithic system in Eq. (6.26) has been observed. It is important to emphasize that this phenomenon is mainly related to the non-uniform activation of the collagen fibers throughout the vessel wall during the systolic phase of the heart beat. Indeed, when the other constitutive models considered in Sec. 7.2.1 are employed with the material parameters in Tab. 5.5, the stagnation of the Newton-Raphson method does not occur. In this work, the numerical challenges posed by the use of the multi-mechanism model within the context of FSI numerical simulations have been addressed by means of two different heuristic approaches. The first, as mentioned in Sec. 7.2.1, involves the use of solid and fluid meshes with structured triangulations of the fluid-structure interface, while the second consists in using small values of the penalization parameters κ in the volumetric strain energy function in Eq. (4.57), as well as of small activation parameters ϵ in Eq. (5.16). Both approaches are effective in order to overcome the stagnation of the Newton-Raphson method; however, as presented hereafter, when the second technique is employed, its effects on the numerical results are evident, eventually leading to non-physical results.

In Fig. 7.22, the activation function of the two families of collagen fibers is shown at different times of the heart beat. At the first row, the activation function is presented on the unstructured solid mesh of Set 1, while the activation function is presented at the same times but on the structured solid mesh of Set 2 at the second row. In the case of the unstructured mesh, at time $t = 0.158$ s, when the collagen fibers start to activate on the internal surface of the domain, the activation function is highly oscillating while in the case of the structured interface mesh it shows a more uniform distribution on the same surface. In the case of unstructured interface mesh, the high oscillations in the activation function induce oscillations in the computation of the mechanical stresses that are transmitted between the two sub-domains. This, in turn leads to the stagnation of the Newton-Raphson method. On the other hand, the use of structured interface meshes reduces the numerical oscillations in the transmission of the mechanical stresses and restores the convergence of the Newton-Raphson method.

The alternative heuristic approach that has been adopted in this work relies on the relaxation of the nearly-incompressibility constraint, by choosing small values of the penalization parameter κ in Eq. (4.57), as well as on the use of low activation parameters ϵ in the case of unstructured interface mesh. In particular, for the numerical results presented in Figs. (7.23)-(7.25), the penalization and activation parameters have been reduced from $\kappa = 9.0 \cdot 10^6$ to $\kappa = 5.0 \cdot 10^5$ and from $\epsilon = 5.0 \cdot 10^5$ to $\epsilon = 50$, respectively. Regarding the mathematical description of the collagen fibers, it is worth pointing out that for $\epsilon = 50$ in Eq. (5.16) the collagen fibers are modeled as mechanically active for stretches significantly smaller than the activation stretch. For instance, for $\epsilon = 5.0 \cdot 10^5$ the collagen fibers are mechanically active only for stretches bigger than the activation stretch, while for $\epsilon = 50$ a family actively contributes to the overall mechanical response of the tissue, with a level of mechanical activation of 4%, already for a stretch 20% smaller than the activation stretch, see Fig. 5.2; this, in turn, affects the vessel wall displacement during the heart beat. Results are presented in Figs. (7.24) and (7.25). Fig. 7.23 shows the approximation of the volume ratio J at the systolic peak of the heart beat. As already discussed in Sec. 4.3, in the case of lower bulk modulus the error on the kinematic constraint is higher than the one measured for $\kappa = 9.0 \cdot 10^6$. As presented in Figs. (7.24) and (7.25), although this approach is effective to overcome the numerical stagnation of the Newton method, its effects on the arterial wall displacement are not negligible compared to the other constitutive models under consideration.

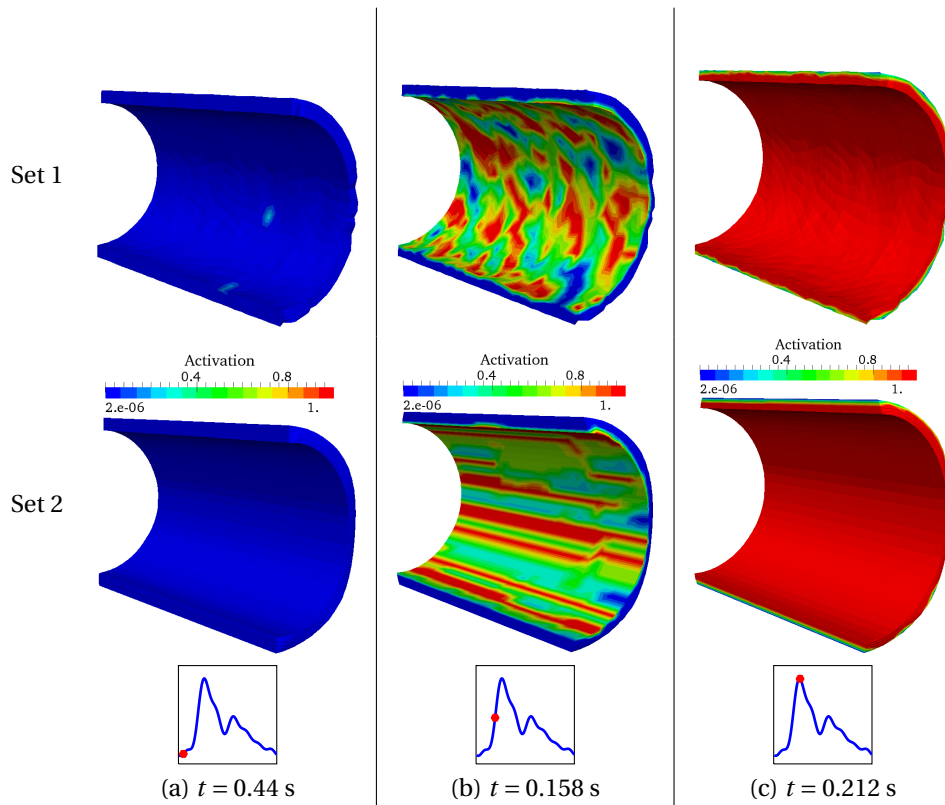


Figure 7.22: Activation function for the (EXP1, EXP2-sMM) model at different times of the heart beat in the case of structured and unstructured meshes. Internal view

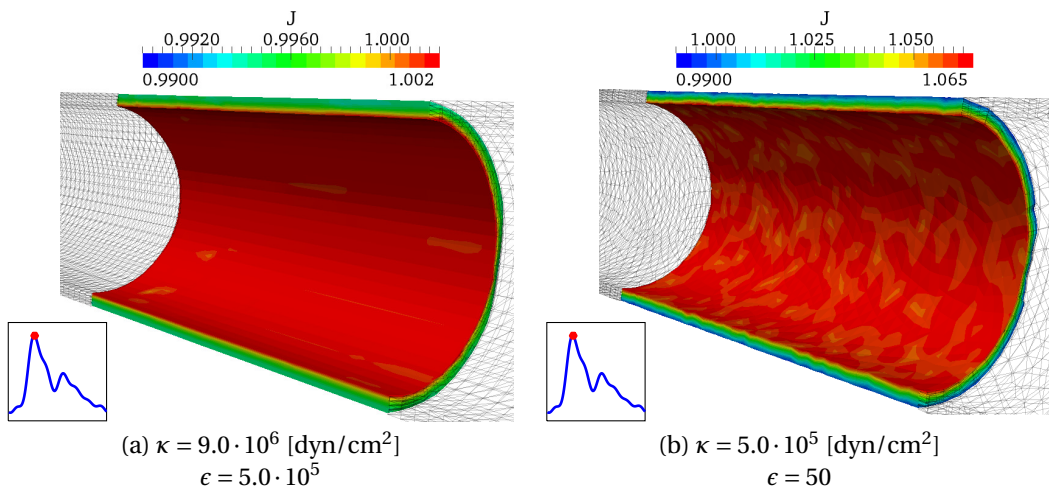


Figure 7.23: Volume ratio J at the time $t = 0.212$ c on a central portion of the solid domain for the values of the bulk modulus and activation parameter ϵ under consideration

Tab. 7.2 details the number of iteration of the Newton-Raphson method according to the modeling choice for the vessel wall. It is worth specifying that the time step Δt of the time discretization of the weak formulation is $\Delta t = 0.001$ s, the numerical simulations have been run on 128 processors, and the

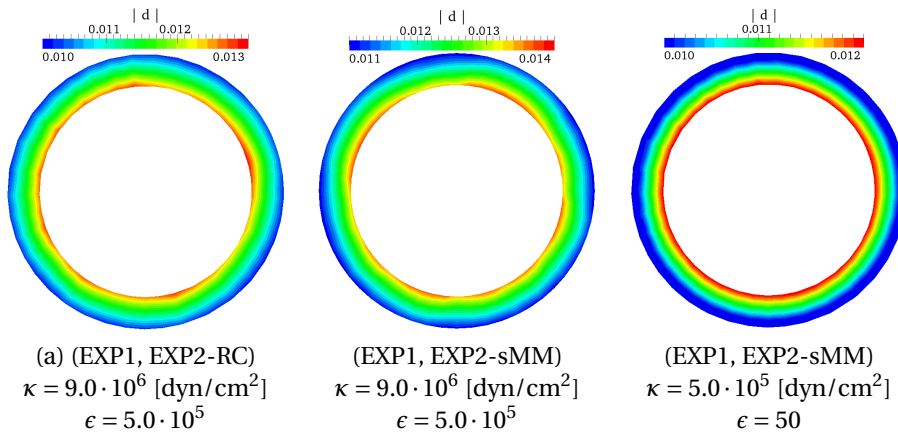


Figure 7.24: Displacement $\hat{\mathbf{d}}$ of the vessel wall at the cross section $z = 0.33$ cm at the time $t = 0.100$ s for different values of bulk modulus

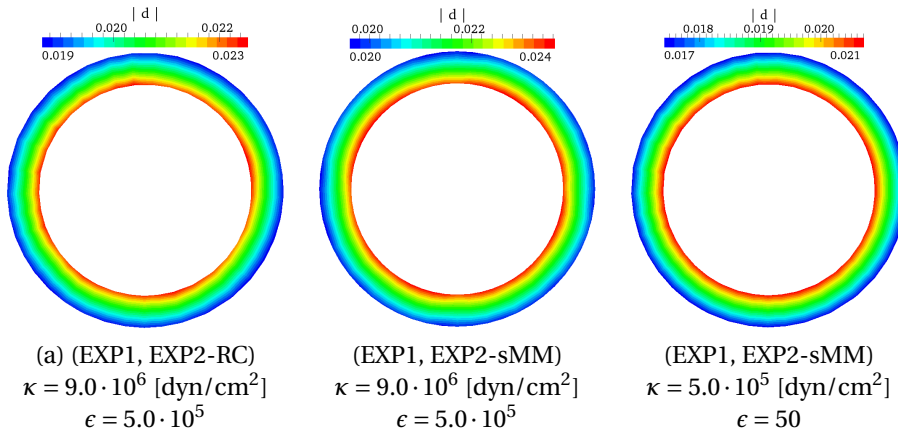


Figure 7.25: Displacement $\hat{\mathbf{d}}$ of the vessel wall at the cross section $z = 0.33$ cm at the time $t = 0.212$ s for different values of bulk modulus

linearized monolithic system of Eq. (6.27) has been solved by means of the GMRES method Saad [2003] preconditioned with the Additive-Schwarz method Quarteroni and Valli [1999a]. In Tab. 7.2, in the case of isotropic constitutive laws, the number of Newton-Raphson iterations has been reported only for the EXP2 model since similar results were registered for all isotropic constitutive laws. As it can be observed, from a general point of view, in the case of anisotropic constitutive laws, a higher number of iterations is required to reach the desired tolerance of the Newton-Raphson method with respect to one reported for isotropic laws. In addition, the use of the multi-mechanism model induces an additional increase in the number of iterations. However, at the systolic peak of the blood flow, it can be observed that the number of iterations is the same as the ones reported for the anisotropic (EXP1, EXP2-RC) model; this can be explained by the fact that at the systolic peak for both mathematical models, the collagen fibers are mechanically active throughout the whole vessel wall thickness; see Fig. 7.14. As already discussed in this section, when the (EXP1, EXP2-sMM) law is employed on Set 1 of meshes with the material parameters of Sec. 5.4.1, the Newton-Raphson method does not converge to the desired tolerance. To conclude, in order to highlight the high computational cost of the numerical simulations presented in Sec. 7.2.1, it is important to refer that the computational time required to simulate one heart beat with an isotropic model is 16 hours, while in the case of the anisotropic (EXP1, EXP2-RC)

7.2. Numerical simulations on idealized blood vessels

Time [s]	EXP2 on Set 1	(EXP1, EXP2-RC) on Set 1	(EXP1, EXP2-sMM) on Set 2	(EXP1, EXP2-sMM) on Set 1	(EXP1, EXP2-sMM) on Set 1 and small κ and ϵ
0.100	1	2	4	2	2
0.212	3	6	6	-	6
0.400	2	5	8	-	7
0.700	1	3	5	-	5

Table 7.2: Number of Newton-Raphson iterations required to solve the nonlinear FSI monolithic system according to the constitutive models for the vessel wall at different times

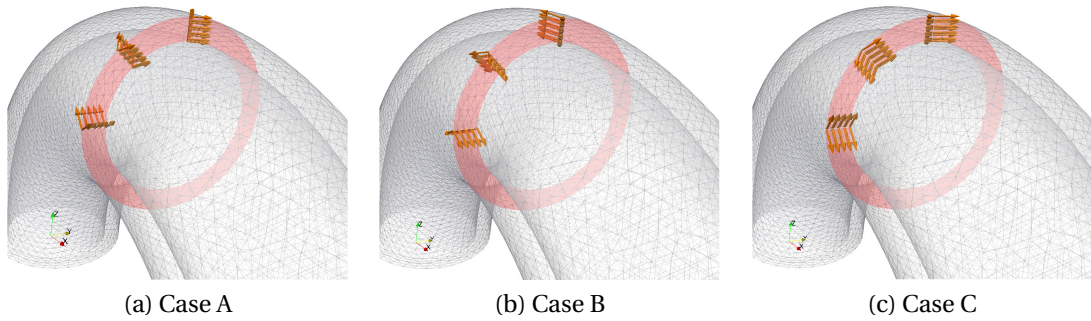


Figure 7.26: Vectorial representation of the two families of fibers in the (EXP1, EXP2-RC) model on one cross section of the solid domain for the sensitivity study on the vessel wall displacement with respect to the collagen fibers orientation.

and (EXP1, EXP2-sMM) laws it increases up to 58 and 72 hours, respectively.

7.2.3 FSI simulations on a toroidal vessel geometry

Numerical simulations of the coupled FSI problem have been also carried out on a toroidal geometry of blood vessel, represented in Fig. 7.2. The same material parameters for the arterial wall models considered in Sec. 7.2.1 are employed. In order to reproduce the same physiological blood flow and pressures, and arterial wall displacement during the heart beat, the same set of boundary conditions described in Sec. 7.1 is considered. The fluid and solid meshes are composed of 176,641 and 106,212 linear tetrahedral elements, respectively. The finite elements spaces for the fluid, solid and geometric problems are the ones mentioned in Sec. 7.1 for which the total number of DOFs of the FSI monolithic system is 822,695. In order to reduce the computational burden, due to the similarities that this case presents with respect to the one described in Sec. 7.2.1, the dynamics of the FSI coupled system has been simulated only in the cases of the isotropic EXP2 and the anisotropic (EXP1, EXP2-RC) laws. In the case of the (EXP1, EXP2-RC), it is assumed that the characteristic direction of the two families of collagen fibers forms with the main radial direction of the torus the angle is $|\beta^{(1)}| = |\beta^{(2)}| = 56.52^\circ$ as in Sec. 7.2.1, see Fig. 7.26-(a).

Fig. 7.27 shows the blood pressure at two different time instants of the heart beat. Similarly to Fig. 7.5, the minimum diastolic pressure is 75 mmHg, while the maximum systolic pressure is 130 mmHg. In particular, during the heart beat, the maximum blood pressure is not registered at the inlet surface of

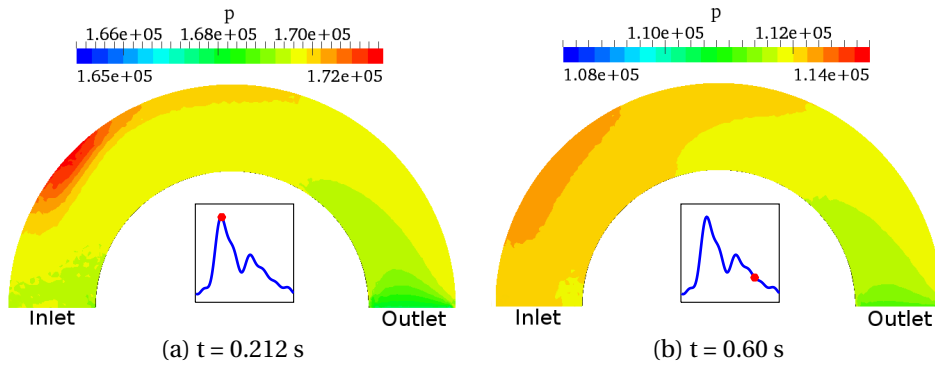


Figure 7.27: Blood pressure p [dyn / cm²] in the deformed fluid domain. Constitutive model for the arterial wall: EXP2

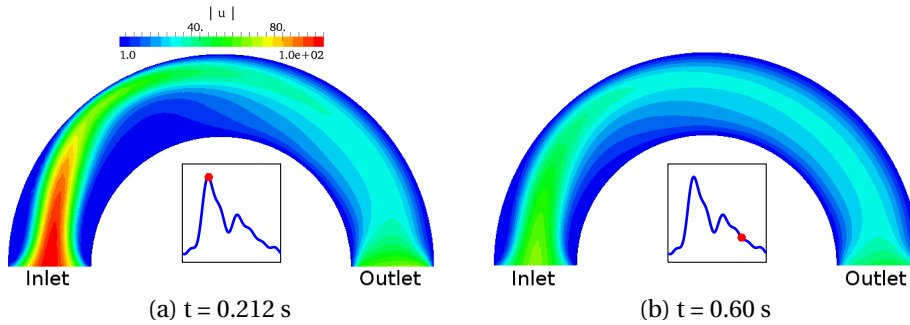


Figure 7.28: Magnitude of the blood flow velocity \mathbf{u} [cm / s] in the undeformed fluid domain. Constitutive model for the arterial wall: EXP2

the domain, but it occurs inside the fluid domain, as shown in Figs. (7.27) and (7.28). As reported in Sec. 7.2.1, the propagation of the pressure wave from the inlet to the outlet surface of the domain is not observed due to the combined effect of the high resistance applied on the outlet surface and to the imposition of the Robin boundary condition on the external wall of the vessel. In addition, due to the external Robin boundary conditions, the vessel wall displacement measured during the heart beat is mainly along the radial direction in the local toroidal set of coordinates, see Fig. 7.29. As it can be noticed, the displacement magnitude is consistent with the one reported in Fig. 7.10-(f) for the case of the straight cylinder. In particular, in the case of the isotropic EXP2 model, the displacement of the blood vessel is symmetric with respect to a cut along the main circumferential direction of the torus (see Fig. 7.30); the same type of symmetry was observed in Fernández and Moubachir [2005] where an isotropic linear elastic constitutive model was employed. On the other hand, the use of the anisotropic model (EXP1, EXP2-RC) leads to an asymmetric vessel wall displacements during the heart beat. This phenomenon is highlighted in Fig. 7.31 at two different times of the heart beat. As it can be noticed, although the displacement measured in the case of the (EXP1, EXP2-RC) law is lower than the one obtained with the EXP2 model (as described also in Sec. 7.2.1), the vessel wall displacement is strongly affected by the presence of the collagenous component in the arterial tissue. In particular, as reported in Fig. 7.31 and on the first row of Fig. 7.32, the asymmetry in the arterial wall displacement is oriented according to the direction (i.e. clockwise or counterclockwise) of the parametrization in the circumferential direction on the main radial cut of the solid domain. Indeed, Fig. 7.26-(a) the orientation of collagen fibers indicate a counterclockwise parametrization of the main

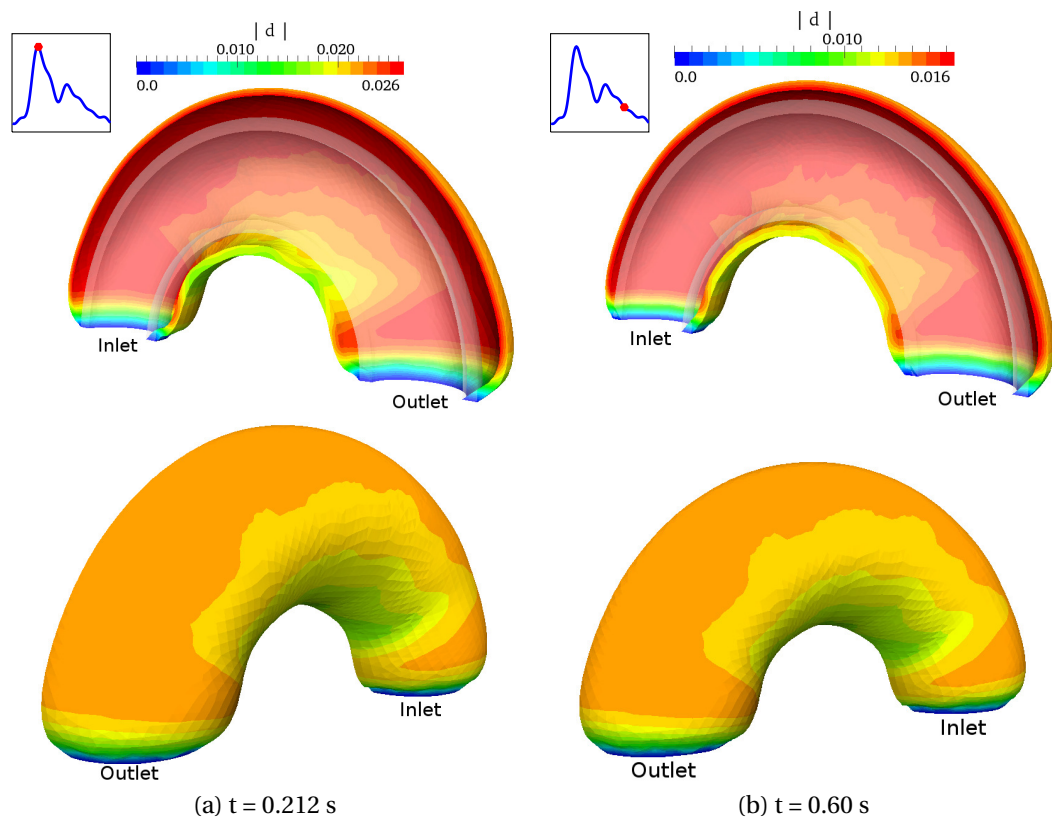


Figure 7.29: Magnitude of the vessel wall displacement \hat{d} [cm] in the undeformed fluid domain. Constitutive model for the arterial wall: EXP2. In the first row, the gray overlay represents the undeformed domain.

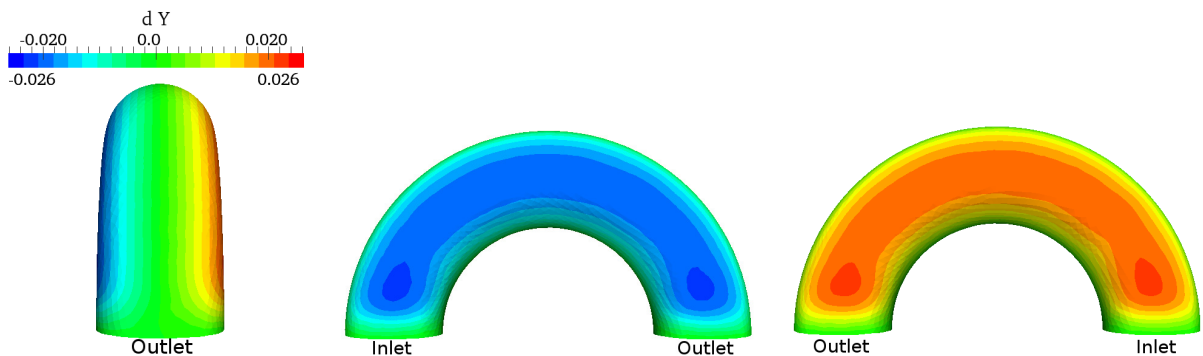


Figure 7.30: Component along the y axis of the arterial wall displacement \hat{d} [cm] at the systolic peak, $t = 0.212$ s

radial cut of the geometry and, as reported on right column of Fig. 7.31, the maximum vessel wall displacement is attained on the lateral side of the domain coherent with such parametrization. For the sake of completeness, in order to confirm that such mechanical behavior of the vessel wall is due to the employment of an anisotropic model, a sensitivity study has been carried out with respect to the direction of the collagen fibers. Specifically, two other cases have been considered; these are shown in

Fig. 7.26-(b) and (c). As it can be observed in Fig. 7.26-(b) and (c), in the two additional cases under consideration, the parametrization of the section in the main radial direction has been inverted with respect to Case A in Fig. 7.26 and rotated of 90° degrees. For all three cases, the two families of fibers are characterized by the same angle, reported in Tab. 5.5, with respect to the local and main circumferential directions. The vessel wall displacement for the cases presented in Fig. 7.26 are reported in Fig. 7.32. In the first two cases, i.e. for Case A and B in Fig. 7.32, the maximum of the vessel wall displacement is attained on one side of the solid domain. On the other hand, the symmetry of the solid displacement $\hat{\mathbf{d}}$ with respect to the y axis is attained in the Case C, namely when the symmetry of the collagen fibers with respect to the y axis is considered. It is worth pointing out that, the strong dependency of the blood vessel displacement on the spatial orientation of the collagen fibers will in turn affect the spatial distribution of the mechanical stresses inside the vessel wall during the heart beat.

The numerical results presented in this sections highlighted different aspects that must be considered when simulating the coupled blood flow-arterial wall system. Firstly, the simulations on the cylindrical and toroidal geometries show that the choice of the constitutive model for the arterial wall does not strongly affect the fluid dynamics inside the vessel lumen, at least for the small values of the Reynolds number typical of the cerebral arteries. On the other hand, non negligible differences have been reported regarding the displacement fields predicted by the different constitutive models. More precisely, in the case of the cylindrical geometry, although the similar qualitative behavior of all the numerical solutions, it has been observed that in the physiological range of blood pressures and velocities, the SVK model (largely used in FSI numerical simulations of the cardiovascular system) predicts the smallest vessel wall displacement, while on the other hand the EXP2 model yields the highest values. This is explained by considering the effective transmural pressure that occurs during the heart beat between the internal and external surfaces of the vessel lumen; in view of this, the results obtained on the straight cylinder are coherent with what was predicted by the data fitting. However, similar values of the Von Mises stresses were measured inside the vessel wall for all the constitutive models. On the contrary, the simulations on the toroidal geometry show that the effects of the constitutive model for the vessel wall on the numerical solutions are evident both from a qualitative and quantitative point of view. More specifically, in the case of the anisotropic model (EXP1, EXP2-RC), the spatial orientation of the collagen fibers has a significant influence on the displacement of the arterial tissue and, therefore, in the evaluation of the mechanical stresses that are commonly related to the possible onset and development of cardiovascular diseases. These results indicate that the choice of the constitutive model for the vessel wall should take into account both the need of correctly describing the dynamics of the artery during the heart beat and the type of vessel that is being considered. In addition, the results presented in this section stress the need of a proper validation of the FSI numerical results with respect to FSI experiments on in vitro idealized models of vessels.

7.2.4 Conclusions

The numerical simulation on the cylindrical geometry with the multi-mechanism model showed the progressive activation and deactivation of the collagen fibers throughout the vessel wall during the cardiac cycle. It has been shown that, the collagen fibers situated on the internal surface of the vessel wall are mechanically active for the largest part of the heart beat, while the ones located on the external parts of the tissue reach the active state only during the peak of the systolic phase. Such constitutive model has never been used in literature within the context of FSI numerical simulations and it seems to be a valuable option to study the role of the collagen fibers in the vessel wall dynamics. In this respect, the use of multi-layer models for the arterial tissue would represent a further step in the numerical

the simulations with the multi-mechanism model show that the use of such constitutive law is critical within the context of FSI problems in hemodynamics. The numerical challenges have been solved by means of two heuristic approaches; however, both of them present their limitations when FSI simulations are considered. Indeed, structured triangulations of the fluid-solid interface cannot be employed when anatomically realistic geometries of vessels, and eventually aneurysms, are considered; on the other hand, the relaxation of the nearly incompressibility constraint and of the modelization of the abrupt recruitment of the collagen fibers strongly affect the vessel wall dynamics during the heart beat.

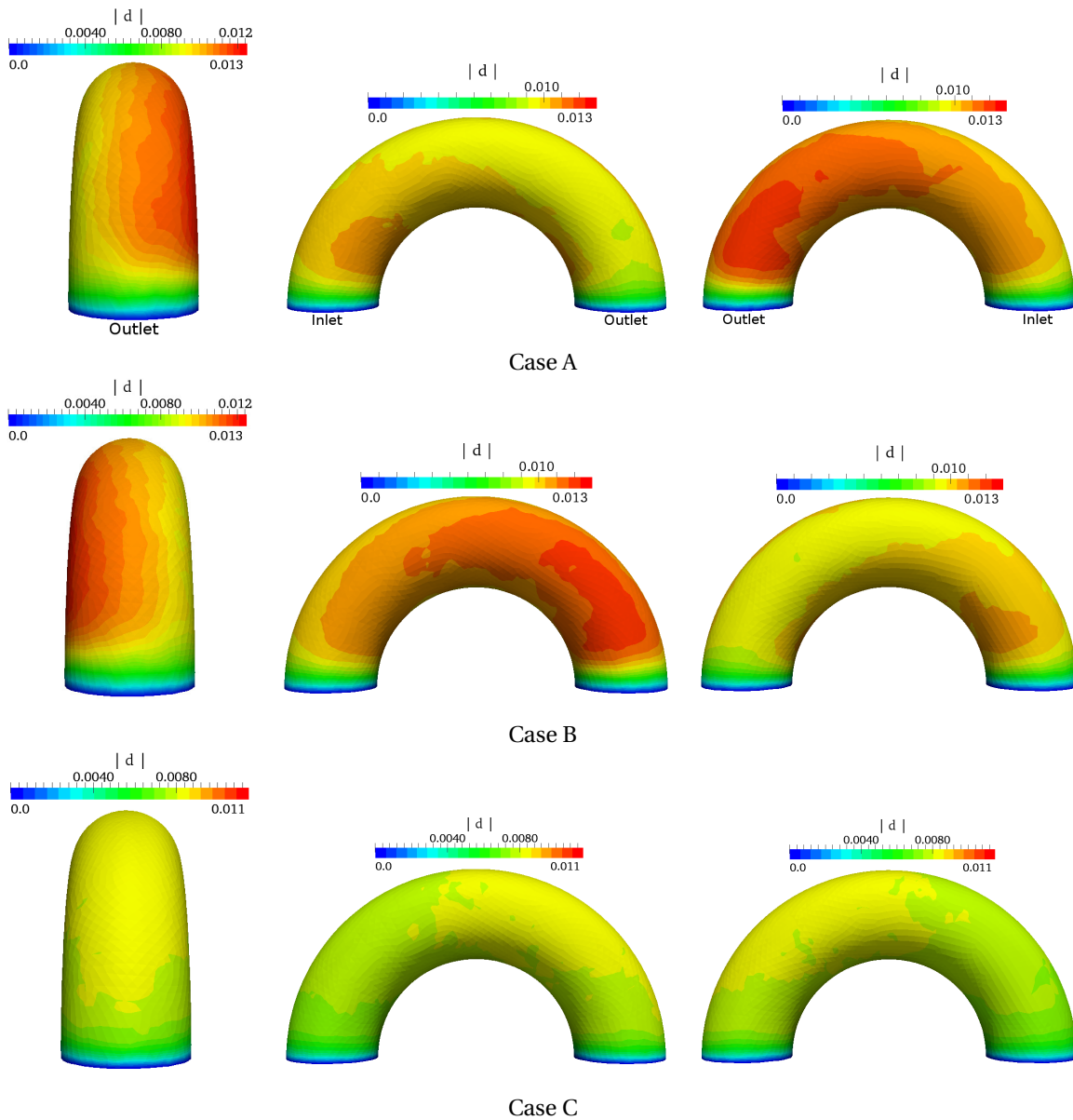


Figure 7.32: Vessel wall displacement in the case of the (EXP1, EXP2-RC) model with different orientation of the collagen fibers. Different views. Time $t = 0.100$ s.

Biomechanics of unhealthy arterial tissue **Part III**

8 Mathematical modeling and numerical simulations of unhealthy arterial tissue

The mechanical response of arteries changes during life time depending on different factors. Short-term changes in the mechanical properties of the arterial tissue are due for instance to injuries caused by trauma; on the other hand, the long-term evolution of the mechanical behavior of arteries is linked to physiological and, possibly, pathological processes. As discussed in Sec. 2.1, the natural thickening of the tunica intima that occurs during aging induces a long-term transformation in the overall mechanical response of the tissue Holzapfel and Gasser [2000]. Alternatively, the onset and development of cardiovascular diseases such as atherosclerosis or aneurysms represent pathological situations in which the changes in the mechanical properties of arteries are driven by multiple factors. Together with the mathematical modeling of the arterial tissue and blood flow dynamics in compliant arteries, the mathematical description of such long-term evolution has gained increasing attention over the last decades in the biomechanical community Ateshian and Humphrey [2012]. For the study of the evolution of the mechanical properties of the tissue in the case of cardiovascular diseases, two different approaches have been considered in literature, see Ateshian and Humphrey [2012]; Ambrosi et al. [2011]; Weisbecker et al. [2011]. The former Ateshian and Humphrey [2012]; Ambrosi et al. [2011]; Taber [1995]; Humphrey and Rajagopal [2002a] considers the biological growth and structural remodeling of the tissue, while the latter Li [2009]; Calvo et al. [2007]; Dalong et al. [2012]; Weisbecker et al. [2011]; Li and Robertson [2009a]; Balzani et al. [2013]; Famaey et al. [2012] focuses on the description of the mechanical degradation of the properties of arteries that characterizes unhealthy conditions of the tissue as happens during the formation and enlargement of aneurysms.

Growth and remodeling models aim at describing the natural biological processes leading to changes in the mass of the tissue (i.e. growth) and in its structure (i.e. remodeling); see e.g. Ateshian and Humphrey [2012]; Ambrosi et al. [2011]; Taber [1995]; Humphrey and Rajagopal [2002a]. As discussed in Ambrosi et al. [2011], growth and remodeling models can be formulated within the context of the continuum mechanics or the mixtures theory; in the latter case, a set of governing equations for the single constituents (e.g. elastin, collagen fibers and smooth muscle cells) as well as their interactions must be formulated. Indeed, these models must take into account the fact that each constituent possesses different properties and can turn over at different rates and to varying extents. In e.g. Baek et al. [2006]; Kroon and Holzapfel [2007]; Chatziprodromou et al. [2007]; Watton et al. [2009b], the growth and remodeling of the cerebral aneurysmal tissue are proposed. In these works, the models are formulated in the case of axisymmetric fusiform and saccular aneurysms and the variations of mass

and structure of the tissue are described by means of specific models. More precisely, in Baek et al. [2006] the model is based on a constrained mixture theory and different constituents are considered, while the models in Kroon and Holzapfel [2007]; Chatziprodromou et al. [2007] are formulated from the continuum mechanics theory. In Kroon and Holzapfel [2007] the collagen fibers are assumed to be the unique constituent of the tissue, while in Chatziprodromou et al. [2007] the tissue is modeled as an isotropic material. In Chatziprodromou et al. [2007], the study of growth and remodeling of saccular cerebral aneurysm is carried out by considering fluid-structure interaction simulations on an idealized geometry of blood vessel in which a localized weakening of the mechanical properties of the tissue is introduced in a bounded portion of the computational domain representing the vessel wall. In Chatziprodromou et al. [2007], the effects of different levels of weakening on the spatial distribution on pressure, velocity, solid displacement, WSS and Von Mises stresses fields are analyzed. However, the growth of a saccular cerebral aneurysm is modeled under the assumption of constant blood inflow and no perianeurysmal tissue is taken into account. The studies presented in Baek et al. [2006]; Kroon and Holzapfel [2007]; Chatziprodromou et al. [2007]; Watton et al. [2009b] show the capability of growth and remodeling models to describe the enlargement and remodeling occurring inside the aneurysm dome; however, as pointed out in Ambrosi et al. [2011]; Watton et al. [2009b], there is a pressing need for further experimental studies on aneurysmal tissue in order to shed light on the chemical and mechanical processes that guide the evolution of aneurysms.

In pathological conditions of the arterial tissue, the mechanical properties of the arterial wall may be degraded either by the natural course of the illness or by the iatrogenic tissue damage caused by medical interventions such as angiography or arterial clamping. For this reason, the mathematical modeling of the degradation of the mechanical properties of arteries, more generally referred to as arterial tissue damage, represents a valuable technique for the characterization of the mechanical behavior of unhealthy arterial tissue. It is worth pointing out that the degradation of the mechanical properties of arteries is a microscopic phenomenon Balzani et al. [2013], which is then described at the macroscopic level following the approach, proposed in Simo [1987]; Kachanov [1958], based on the concept of internal state variable. In addition, the damage models for the arterial tissue proposed in literature, e.g. Li [2009]; Calvo et al. [2007]; Dalong et al. [2012]; Weisbecker et al. [2011]; Li and Robertson [2009a]; Balzani et al. [2013]; Famaey et al. [2012], have been considered in the numerical simulations of angiography and arterial clamping rather than for fluid-structure interaction (FSI) simulations of the blood-flow in compliant arteries. This can be explained by considering the fact that the iatrogenic damage caused by medical interventions can be assumed to be related only to the deformations of the vessel registered during the surgery and on the fact that the time scales characterizing the operation and the creation of damage are comparable. On the other hand, within the context of aneurysms, the factors leading to the mechanical degradation of the properties of the vessel wall are of different types (e.g. mechanical, chemical, enzymatic Li and Robertson [2009a]; Sforza et al. [2009]) and the characteristic time scale for onset and enlargement of an aneurysm (months or years) is much higher than that of the phenomenon that is numerically simulated, i.e. the blood-flow during one heart beat (few seconds). However, in Li [2009]; Li and Robertson [2009a] a damage model that considers high WSS as a possible factor leading to the weakening of the tissue is presented.

In this work we study the effects on the vessel wall deformations and stresses of different levels of mechanical weakening of the tissue according to the constitutive model describing the artery. The study is carried out in the case of numerical simulations of inflation tests with the final aim of considering unhealthy arterial tissue within the context of FSI simulations, see Ch. 7.2. In particular, in the FSI case, the effects on hemodynamical indicators such as WSS are analyzed.

This chapter is organized as follows. Sec. 8.1 shortly introduces the most common cardiovascular

disease occurring in the brain: the cerebral aneurysm; in addition, it describes the histopathology of a cerebral aneurysm and discusses the different factors that are commonly related to the course of this disease. Next, in Sec. 8.2, some of the damage models proposed in literature Dalong et al. [2012]; Li and Robertson [2009a]; Balzani et al. [2013] for the arterial tissue are presented together with the approach employed in this work to represent the arterial tissue weakening. Due to the incomparable time scales of the blood flow and damage progression in the aneurysm wall, the approach adopted in this work to describe the weakening of the arterial tissue assumes the levels of weakening as known, rather than considering continuous damage functions. Finally, Sec. 8.3 presents numerical simulations of static inflation tests on unhealthy cerebral arterial tissue; the effect of the level of weakening together with the modeling choice for the arterial wall is discussed.

8.1 Cerebral aneurysms and their histopathology

Cerebral aneurysms (CA) are pathological localized dilatations of the cerebrovascular wall resulting from an acquired, or less frequently a congenital, weakness in the arterial tissue McGloughlin [2011]; Stehbens [1989]. CA are in direct communication with the lumen and therefore the blood flow. CA are frequently located near arterial bifurcations or curved areas of cerebral arteries in proximity or in the Circle of Willis, that is the main vascular network that supplies blood to the brain; see Fig. 8.1-(a). CA can be classified according to their etiology, morphology, size and location. Morphologically, cerebral aneurysms are of three types: saccular, fusiform, or dissecting aneurysms McGloughlin [2011]. Saccular aneurysms, that account for the 80-90% of cerebral aneurysms, are sac-like deformations of the vessel wall; on the other hand, fusiform and dissecting aneurysms have a much lower annual incidence compared to saccular aneurysms; see McGloughlin [2011] and references therein. For this reason, in this work we will focus on the study of the first type of aneurysms.

Epidemiology studies reveal that millions of people may harbor at least one cerebral aneurysm Caranci et al. [2013] and that intracranial aneurysms account for about 80% of all nontraumatic subarachnoid hemorrhage. When the rupture of a cerebral aneurysm occurs, the incidence of patient death is over 50%, while of the survivors, 25% of the patients suffer severe disability and the rest are at an increased risk for stroke, recurrent bleeding, or other complications McGloughlin [2011]. This highlights the importance of studying this cardiovascular diseases in order to better understand the degenerative processes that may lead to the rupture of a CA and, possibly, improve the current clinical treatments, for instance, by analyzing the effects of the implantation of stents or coils inside the vessel lumen in the proximity of the aneurysm Jeong and Rhee [2012]. The most common locations for CA are the anterior circulation, i.e. close to the anterior cerebral artery and anterior communicating artery, at the junction of the internal carotid and the posterior communicating arteries, the middle cerebral artery and the basilar artery, as in Fig. 8.1, see e.g. McGloughlin [2011]; Humphrey and Canham [2000]; Wire et al. [2003]; Jeong et al. [2009]. As presented in Fig. 8.1-(a), two main parts can be identified in a saccular aneurysm: the neck, the part that links the sac-like deformation to the parent vessel, and the dome, namely the out-pouching dilatation. The natural course of a saccular cerebral aneurysm is composed of at least three main phases: pathogenesis, enlargement, and, possibly, rupture.

The diagnosis of a cerebral aneurysm is extremely important to planify the most adequate treatment in order to prevent its rupture. However, as pointed out in Sforza et al. [2009]; Humphrey and Canham [2000], most of the aneurysms are asymptomatic until rupture. For this reason, unruptured aneurysms may be diagnosed during investigation of clinical symptoms relative to cranial nerve compression or fortuitously found during routine CT or MR imaging check-ups for unrelated health issues; in addition,

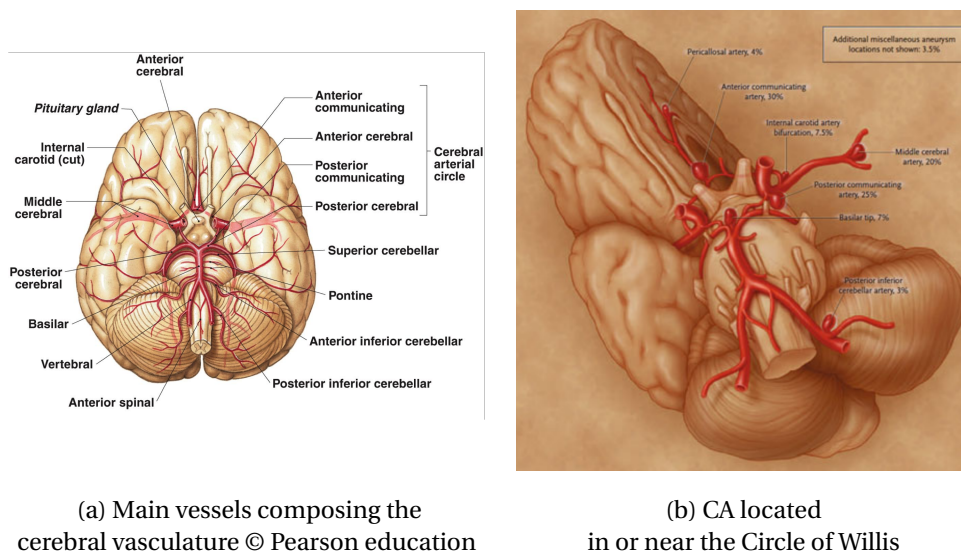


Figure 8.1: Main cerebral vascular network and examples of CA; (a) Circle of Willis; (b) Sketch of CA Brisman et al. [2006].

they might be diagnosed in the case of subarachnoid hemorrhage caused by the rupture of another existing aneurysm, or during screening in the presence of positive family history of ruptured aneurysms Jeong and Rhee [2012]; San Millán Ruiz et al. [2006]. Indeed, although the exact etiology of CA remains unclear Caranci et al. [2013], it is commonly accepted that different genetic, life-style related, chemical and mechanical factors play a role in the onset and development of CA. Among the genetic factors, it has been observed that the occurrence of intracranial aneurysms is higher in women than in men as well as in people with a positive familial history rather than in people for which cerebral aneurysms have not occurred in close relatives McGloughlin [2011]; Caranci et al. [2013]; in addition, ambient factors such as smoking, excessive alcohol consumption and hypertension seem to be related to the onset of CA. As discussed in Sforza et al. [2009]; Jeong and Rhee [2012]; Cebra et al. [2005], mechanical and chemical factors are strictly related; indeed hemodynamic forces and flow characteristics, such as recirculation, secondary flow, and jet impingement, are considered to be major mechanical factors related to the genesis of CA due to their effect on the natural remodeling of the vessel wall. For instance, repetitive flow impingement against the vessel wall under pulsatile flows may induce fatigue, thus potentially causing morphological and functional change in the endothelium. Among the hemodynamic forces that are considered as driving factors for the onset and development of aneurysms, the WSS is the most important one since endothelial cells actively sense and respond to WSS Nixon et al. [2010]. Indeed, as discussed in Sforza et al. [2009]; Jeong and Rhee [2012] and references therein, WSS is a determinant factor for the vessel wall structural remodeling via the production of vasoactive substances such as nitric oxide. Therefore, in abnormal conditions of blood flow, if the WSS increases in a limited region of the vessel wall, it can potentially cause a local damage to the arterial wall due to degenerative changes in the endothelium. In addition to high values of WSS, also WSS Gradient (WSSG) and temporal directional variation in WSS play an important role in the initiation of CA. However, the formation of intracranial aneurysms is believed to be related to an interaction between high-flow hemodynamic forces, for instance due to hypertension, and the arterial wall.

The process of enlargement of a cerebral aneurysm is still unclear. Indeed, despite the general agreement on the mechanisms of aneurysms initiation, there is a significant controversy regarding its development Jeong and Rhee [2012]; Humphrey and Canham [2000]. The two main theories focus

on high-flow effects and low-flow effects, respectively; however, both of them consider the chemical processes induced by the blood-flow in the aneurysm dome as leading factors for the enlargement phase. The first theory considers high WSS as a cause of endothelial injury and vessel wall mechanical degradation. Abnormal high values of WSS are thought to lead to a loss in the arterial tone (i.e. level of mechanical tension within the artery). In Cebal et al. [2011], it is shown that ruptured aneurysms are more likely to have complex flow patterns with small impingement regions which are characterized by elevated WSS. On the other hand, the low-flow effects hypothesis relies on the effects on localized blood-flow stagnation against the wall in the dome. Blood-flow stagnation induces a dysfunction in the production of nitric oxide which results in the aggregation of red blood cells, leukocytes along the intimal surface. This process may cause intimal damage, leading to the infiltration of white blood cells inside the aneurysmal tissue. In Shojima et al. [2004]; Boussel and McCulloch [2008], experimental and computational studies showed a possible correlation between aneurysm growth and low values of WSS compared to the ones measured in the surroundings vasculature. However, despite the controversy about the role of hemodynamic forces during CA development, there is a general agreement on the fact that the process of aneurysm enlargement is characterized by apoptosis of smooth muscle cells and by a pathological rate of collagen fibers turn over in the aneurysm dome. As discussed in Kroon and Holzapfel [2007]; Humphrey and Canham [2000] this may result in an enhanced presence of immature collagen, which is weaker than mature collagen found in healthy arterial tissue, leading to a softer tissue.

The rupture of a cerebral aneurysm occurs when the wall tension exceeds the mechanical strength of the tissue. The most important factors employed to predict the rupture of a cerebral aneurysm are its size, aspect ratio, and position in the Circle of Willis Wire et al. [2003]; Jeong et al. [2009]. The size of an aneurysm refers to the maximum dimension in the dome, while the aspect ratio is defined as the ratio between the size of the aneurysm and the width of the neck, see Fig. 8.2-(a). Different ranges of values of aspect ratio can be found in literature as indicators of possible rupture Wire et al. [2003]; Jeong et al. [2009]; it has been estimated that the critical size of aneurysms to which rupture may occur varies between 3 and 10 mm Wire et al. [2003]; Jeong et al. [2009]; Crompton [1966]; Kassel and Torner [1983]. These factors do not account for the mechanical properties of the aneurysmal tissue Humphrey and Canham [2000]. Indeed, as described in Humphrey and Canham [2000] and references therein, the rupture occurs at the fundus of the aneurysm, see Fig. 8.2-(a). In Humphrey and Canham [2000]; Abruzzo et al. [1998] it is reported that a high percentage of aneurysms presents small variations in the wall thickness between the neck and the fundus; nevertheless, as measured for instance in Valencia et al. [2013]; Sherif et al. [2014], the thickness of the aneurysmal wall is lower than the one found in the parent vessel. As for the enlargement, hemodynamics and abnormal wall remodeling play a key role also in the rupture. As discussed in Cebal et al. [2011], stable complex flow patterns, i.e. exhibiting flow separation and vorticity during the whole heart beat, high flow concentration at the neck corresponding to small flow impingement areas in the dome characterize the hemodynamics of ruptured aneurysms. Simultaneously, hypertensive blood pressure causes significant changes in the spatial distribution of WSS on the wall, see e.g. Torii et al. [2006]. Although not commonly considered as an important aspect in order to determine whether an aneurysm will rupture or not, it is worth remarking that also the perianeurysmal environment has been investigated as possible indicator. Indeed, it has been shown that when CA develop contact constraints during its growth, the hemodynamics is strongly influenced by the resulting shape Sforza et al. [2012] making it prone to rupture San Millán Ruiz et al. [2006]; Sforza et al. [2012]. In order to prevent subarachnoid hemorrhages due to rupture, different medical procedures are currently available, such as coiling or stenting; the interested reader may refer to e.g. McLaughlin [2011]; Augsburger [2008] for a detailed description of the different techniques, their efficacy, and a discussion on the support that numerical simulations of blood flow in arteries can

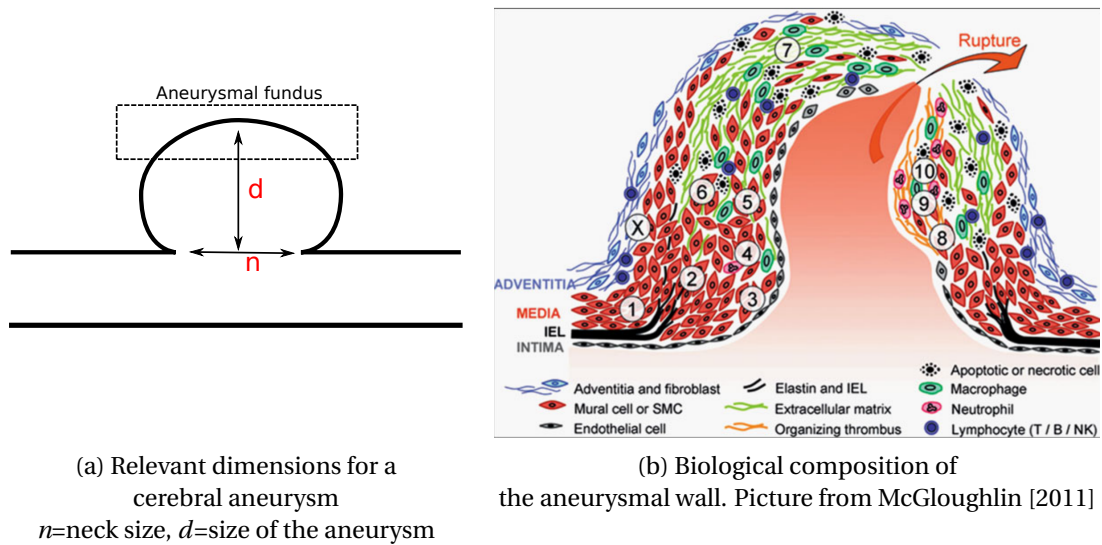


Figure 8.2: Important spatial dimensions and biological composition of the aneurysmal wall. In (b) the absence of internal elastic lamina and media inside the dome is highlighted.

provide to the design and implantation of medical devices.

From the histological point of view, the characteristics of the tissue of a CA, as wall thickness, composition, and mechanical behavior, vary according to the portion of the aneurysm that is being considered. As presented in Li [2009]; Humphrey and Canham [2000], the variation in the wall thickness between the neck and the fundus can be explained by considering that the pathological collagen fiber remodeling takes place mostly in the dome rather than at the neck Kroon and Holzapfel [2007]. The tissue of an intracranial aneurysm is structurally different from a healthy arterial tissue. As described in Scott et al. [1972]; Sforza et al. [2009]; Humphrey and Canham [2000]; Ferguson [1972b]; Campbell and Roach [1981]; Humphrey and Taylor [2008], the internal elastic lamina and the elastin network in the tunica media become markedly degraded or fragmented during the onset of a cerebral aneurysm. Indeed, for most of the cerebral aneurysms, the transition from the parent vessel Humphrey and Canham [2000] to aneurysm is characterized by a sharp break in the media layer Campbell and Roach [1981]; Sekhar and Heros [1981], therefore it is thought that the aneurysm stems from the intima and adventitia layers; see Fig. 8.2-(b). At the orifice, the media terminates and the internal elastic lamina is fragmented, while in the aneurysm dome the tissue is mainly composed of collagen fibers. In addition, the collagen fibers at the neck do not present a strong spatial organization, such as in healthy arteries, they differ in length and caliber and are in a wavy state. On the other hand, in the dome, they present a strong spatial orientation; they are straightened and organized in distinct laminae; see Humphrey and Canham [2000] and references therein. For this reason, the mechanical behavior of the aneurysmal wall is determined by the stiffness of the collagen fibers. However, in spite of such composition, the mechanical failure of the aneurysmal wall occurs at smaller deformations and tensions than the ones measured for the neck Steiger et al. [1986]. This, as already mentioned before, can be explained by the fact that immature collagen fibers can be found in the dome resulting in a softer tissue compared to the one at the neck Humphrey and Canham [2000].

8.2 Mathematical modeling of arterial tissue weakening

As discussed in Sec. 8.1, an intracranial aneurysm originates from an unhealthy state of the artery due to an initial damage of the internal elastic lamina and media layers. The approach employed in this work to describe unhealthy cerebral arterial tissue has been already considered in different works in literature for the description of damaged arteries (e.g. Calvo et al. [2007]; Li and Robertson [2009a]; Dalong et al. [2012]; Weisbecker et al. [2011]; Famaey et al. [2012]); it is based on the mathematical mode firstly proposed in Kachanov [1958] and then considered in e.g. Simo [1987] for non-biological materials. This technique is based on the concept of internal state variable, i.e. a quantity that can capture the mechanical history of a material and can be used to predict variations in the mechanical properties such as softening or, possibly, failure. Such changes are modeled by means of a dimensionless internal variable $D \in [0, 1]$ that represents the mechanical integrity of the body Calvo et al. [2007]; Li and Robertson [2009a]; Dalong et al. [2012]; Weisbecker et al. [2011]; more precisely, the progressive degradation of the mechanical properties of the tissue is taken into account by inserting in the strain energy function $\widehat{\mathcal{W}}$ characterizing the healthy arterial tissue the term $(1 - D)$. In Calvo et al. [2007]; Li and Robertson [2009a]; Dalong et al. [2012]; Famaey et al. [2012] the factor $(1 - D)$ multiplies the full strain energy function, or part of it; therefore it can be viewed as a term representing the degradation of properties of the tissue such as, for instance, its mechanical strength. The same approach was already employed e.g. in Simo [1987]. Alternatively, in the anisotropic model of Balzani et al. [2012], the factor $(1 - D)$ multiplies the scalar quantity measuring the collagen fibers deformation in order to model residual strains.

In this work, unhealthy arterial tissue is assumed to be characterized by a lower mechanical stiffness compared to the one of healthy tissue according to a specific material law at hand; with this aim, we employ the approach considered in Calvo et al. [2007]; Li and Robertson [2009a]; Dalong et al. [2012]; Famaey et al. [2012]. If the arterial tissue behaves as an isotropic material, the general form of the strain energy function reads

$$\widehat{\mathcal{W}}^{iso,D} = \widehat{\mathcal{W}}^{iso}(I_1, I_2, I_3; D) = (1 - D)\widehat{\mathcal{W}}^{iso}(I_1, I_2, I_3), \quad (8.1)$$

where $\widehat{\mathcal{W}}^{iso}(I_1, I_2, I_3)$ is the effective strain energy of the healthy tissue that has been discussed in Ch. 4. Similarly, if anisotropic strain energy functions $\widehat{\mathcal{W}}^{aniso}$, as those in Sec. 4.2.2, model the tissue, the multiplicative factor $(1 - D)$ may affect either a unique component of the strain energy function, e.g. when assuming that the damage occurs only for the elastin or the collagen fibers, or both of them Calvo et al. [2007]; Li and Robertson [2009a]; Dalong et al. [2012]; Famaey et al. [2012]. When it is supposed that both elastin and collagen might be damaged during deformation processes, the anisotropic strain energy function describing unhealthy arterial tissue reads

$$\widehat{\mathcal{W}}^{aniso,D} = \widehat{\mathcal{W}}^{aniso}(I_1, I_2, I_3, I_4, I_5; D_{iso}; D^{(1)}, \dots, D^{(N)}) = \quad (8.2)$$

$$= (1 - D_{iso})\widehat{\mathcal{W}}_{iso}^{aniso}(I_1, I_2, I_3) + \sum_{i=1}^N (1 - D^{(i)})\widehat{\mathcal{W}}_{fibers}^{(i)}(I_4^{(i)}, I_5^{(i)}), \quad (8.3)$$

where $\widehat{\mathcal{W}}_{iso}^{aniso}(I_1, I_2, I_3)$ and $\widehat{\mathcal{W}}_{fibers}^{(i)}(I_4^{(i)}, I_5^{(i)})$ are the constitutive laws for the elastin and the single family of collagen fibers, respectively (see Sec. 4.2.2), and $D_{iso}, D^{(1)}, \dots, D^{(N)} \in [0, 1]$ are the internal variables employed to model the degradation of the mechanical properties of the different constituents. It is worth pointing out that each of the dimensionless variables $D_{iso}, D^{(1)}, \dots, D^{(N)}$ may be characterized in terms of different indicators. From Eqs. (8.1) and (8.3), it can be observed that the mechanical integrity of the material (or the single component) is represented by the value $D = 0$, while the full

mechanical failure occurs for $D = 1$. As discussed in Sec. 8.1, different factors are known to induce damage on the tissue; therefore, in order to describe the influence of such factors on the healthy state of the tissue damage models are formulated, i.e. the dimensionless parameter D in Eqs. (8.1) and (8.3) is assumed to be dependent upon mechanical indicators. For instance, the evolution of D may depend on the history of deformations and history of WSS measured on the internal surface of the vessel wall Li and Robertson [2009a]. From the modeling point of view, it is worth reminding that a constitutive model for damaged arterial tissue, i.e. $\widehat{\mathcal{W}}^{iso,D}$ or similarly $\widehat{\mathcal{W}}^{aniso,D}$, must satisfy the second law of thermodynamics, as discussed in Sec. 3.2.3. This implies that, for instance in the case of $\widehat{\mathcal{W}}^{iso,D}$ in Eq. (8.1), the following inequality must be satisfied:

$$\frac{1}{2} \mathbf{S} : \dot{\mathbf{C}} + \widehat{\mathcal{W}}^{iso,D} = \left(\frac{1}{2} \mathbf{S} - \partial_{\mathbf{C}} \widehat{\mathcal{W}}^{iso,D} \right) : \dot{\mathbf{C}} + \widehat{\mathcal{W}}^{iso} \dot{D} \geq 0, \quad (8.4)$$

where $\widehat{\mathcal{W}}^{iso}$ is the effective strain energy function describing the healthy tissue. From the mechanical point of view, the term $\widehat{\mathcal{W}}^{iso} \dot{D}$ represents the dissipation of energy due to the mechanical damage of the tissue Balzani [2006]. Different damage models have been proposed in literature, for instance in Li [2009] an anisotropic damage model of the form of Eq. (8.3) is considered; more precisely, it is assumed that, at a given time t corresponding to a level of deformation, the damage affecting the elastin depends on either the maximum equivalent strain at time t or on the accumulated strain of the material during the deformation process. In the first case, if an isotropic strain energy function describes the tissue, the maximum equivalent strain at the current time t is defined as

$$\eta_M = \max_{s \in [0,t]} \sqrt{2 \widehat{\mathcal{W}}^{iso}(I_1(s), I_2(s), I_3(s))}, \quad (8.5)$$

while in the second case, the mechanical indicator that affects the degradation parameter D is defined as

$$\eta_A = \int_0^t \left| \frac{d}{ds} \sqrt{2 \widehat{\mathcal{W}}^{iso}(I_1(s), I_2(s), I_3(s))} \right| ds, \quad (8.6)$$

where, if anisotropic models are considered for the tissue, the strain energy function in Eqs. (8.5) and (8.6) corresponds to $\widehat{\mathcal{W}}^{aniso,D}$ of Eq. (8.3) for $D = 0$. Afterwards, the form of the dimensionless parameter D in terms of the quantity η_M , or similarly η_A , will read

$$D = \begin{cases} 0 & 0 \leq \eta_M < \eta^{start} \\ g(\eta_M) & \eta^{start} \leq \eta_M < \eta^{fail} \\ 1 & \eta^{fail} \leq \eta_M, \end{cases} \quad (8.7)$$

where η^{start} and η^{fail} represent the value of maximum equivalent strains for which the properties of the elastin starts degrading and the value corresponding to the mechanical failure, respectively. In Eq. (8.7), in order to represent the progressive degradation of the mechanical properties of the elastin, the function $g(\eta_M)$ is of the form

$$g(\eta_M) = 1 - \frac{1 - e^{c_1 \left(1 - \frac{\eta_M}{\eta^{fail}}\right)}}{1 - e^{c_2 \left(1 - \frac{\eta^{start}}{\eta^{fail}}\right)}}, \quad (8.8)$$

where c_1 and c_2 are two constants characterizing the progression of the damage for increasing de-

8.3. Numerical simulations of unhealthy arterial tissue mechanics: static inflation tests

formation. It is worth pointing out that the quantities c_1 , c_2 , η^{start} , and η^{fail} should be determined from experimental measurements of the mechanical behavior of unhealthy, i.e. aneurysmal, tissue. In addition, due to the key role that hemodynamics plays for the onset of cerebral aneurysms, a damage model considering the averaged WSS on the vessel wall during the heart beat is proposed in Li [2009]. Still in Li [2009], a damage model as the one in Eqs. (8.5)-(8.8) is employed to describe the damage of the single family of collagen fibers as well. Exponential functions like the one in Eq. (8.8) are also considered in Calvo et al. [2007]; Dalong et al. [2012]; Balzani et al. [2012]; in this work, it is not shown that the aforementioned damage models satisfy the inequality (8.4) since the properties of such models have been investigated in Balzani [2006]; Li [2009] and references therein.

The mathematical modeling of the progressive degradation of the mechanical properties of the arterial tissue by means of damage models taking into account the history of deformations represents an extremely valuable tool to better understand the progression of cardiovascular diseases and support the design of medical interventions. However, there is a pressing need of experimental data for the calibration of the damage functions such as Eq. (8.7) Weisbecker et al. [2011]. This work focuses on the mechanical degradation of the cerebral arterial tissue that occurs during early phases of the formation of a cerebral aneurysm. In particular, the final aim is to consider the modeling of the unhealthy arterial tissue within the context of FSI numerical simulations in either idealized and anatomically realistic geometries of cerebral vessels. For this reason, as already mentioned, due to the fact that the characteristic time scales of the onset of an aneurysm and of the heart beat are extremely different, in this work we have not considered a damage model as the ones proposed in Calvo et al. [2007]; Dalong et al. [2012]; Balzani et al. [2012]. Alternatively, in this work different pre-set values of the dimensionless parameter D are considered to estimate the influence of the level of mechanical degradation on the numerical results of simulations of arterial wall mechanics and FSI. For this reason, the model for the unhealthy tissue will be referred to as a *weakening* model rather than a damage model. Isotropic and anisotropic laws have been considered in the numerical simulations. In particular, in the case of anisotropic laws, the mechanical weakening is assumed to affect only the isotropic part of the strain energy function (see Eq. (8.3)) in order to describe the degradation of the mechanical properties of the elastin inside the media and internal elastic lamina.

8.3 Numerical simulations of unhealthy arterial tissue mechanics: static inflation tests

Firstly, we focus on numerical simulations of inflation tests on weakened arterial tissue. Indeed, this step is important in order to analyze the influence on the numerical results, i.e. deformations and stresses, of the modeling choice for the arterial wall before considering FSI simulations where, as already presented in Ch. 7, the arterial wall dynamics during the heart beat is strongly influenced by a variety of factors, as the shape of the computational domains or boundary conditions. As mentioned before, the properties of the arterial tissue are degraded according to known levels of mechanical weakening. In order to have consistent comparisons among the different numerical simulations, it is necessary to calibrate the weakening parameter D for the different cases under consideration according to the constitutive model. For this reason, this section firstly presents the calibration technique used to set the parameter D and, afterwards, it presents the numerical results obtained from the simulation of inflation tests on unhealthy arterial tissue.

8.3.1 Calibration of the weakening parameter D for unhealthy cerebral arterial tissue

Based on the results obtained from the least-squares approximation of the experimental data, the arterial tissue is described by means of three of the constitutive models discussed in Sec. 5.4.1: the isotropic EXP2 model, and the anisotropic laws (EXP1, EXP2-RC) and (EXP1, EXP2-sMM). Indeed, among the isotropic laws, the best fitting of the experimental measurements and agreement between the numerical results and the fitting curve $\mathcal{F}(\lambda_{\hat{\theta}\hat{\theta}})$ (see Fig. 5.23) is obtained with the second order exponential model; on the other hand, the use of the two anisotropic laws is motivated by the will of comparing the numerical results obtained with a constitutive model commonly employed in literature for different types of arteries and the specific law proposed for cerebral arteries, see Sec. 4.2.2. According to Eqs. (8.1) and (8.3), the weakening parameter $(1 - D)$ multiplies the strain energy function describing the response of the healthy tissue; however, since in this work the volumetric-isochoric split is employed (see Sec. 4.3) it is worth pointing out that the factor $(1 - D)$ affects only the isochoric part of the strain energy function, i.e. the part characterizing the response to the material according to the deformation, and not the volumetric one. Thus, the isochoric isotropic U-EXP2 model for the unhealthy tissue, where the prefix U indicates the unhealthy material, reads:

$$\overline{\mathcal{W}}^{iso}(\bar{I}_1, \bar{I}_2; D) = \overline{\mathcal{W}}_{U-EXP2}^{iso}(\bar{I}_1, \bar{I}_2; D_{EXP2}) = \frac{(1 - D_{EXP2})\alpha_2}{2\gamma_2} \left(e^{\gamma_2(\bar{I}_1 - 3)^2} - 1 \right). \quad (8.9)$$

Similarly, when anisotropic models are considered, the weakened background material, i.e. elastin, in the isochoric anisotropic law (see Eq. (4.62)) is described by the following modified form of the EXP1 model (indicated as U-EXP1):

$$\widehat{\mathcal{W}}_{iso}^{aniso}(\bar{I}_1, \bar{I}_2; D) = \overline{\mathcal{W}}_{U-EXP1}^{iso}(\bar{I}_1, \bar{I}_2; D_{EXP1}) = \frac{(1 - D_{EXP1})\alpha_{iso}^{aniso}}{2\gamma_{iso}^{aniso}} \left(e^{\gamma_{iso}^{aniso}(\bar{I}_1 - 3)} - 1 \right). \quad (8.10)$$

From Eq. (8.10) it follows that the full anisotropic strain energy function for the unhealthy arterial tissue is:

$$\overline{\mathcal{W}}^{aniso}(\bar{I}_1, \bar{I}_2, \bar{I}_4; D_{EXP1}) = \overline{\mathcal{W}}_{U-EXP1}^{iso}(\bar{I}_1, \bar{I}_2; D_{EXP1}) + \sum_{i=1}^N \overline{\mathcal{W}}_{fibers}^{(i)}(I_4^{(i)}), \quad (8.11)$$

where the strain energy function $\widehat{\mathcal{W}}_{fibers}^{(i)}(I_4^{(i)})$ for the single collagen fiber family can be either the EXP2-RC or the EXP2-sMM law. In the following, the anisotropic models for unhealthy cerebral arterial tissue will be indicated as (U-EXP1, EXP2-RC) and (U-EXP1, EXP2-sMM), respectively, and $D_{EXP1}^{EXP2-RC}$ and $D_{EXP1}^{EXP2-sMM}$ will represent the weakening parameter affecting the material properties of the background material in the (U-EXP1, EXP2-RC) and (U-EXP1, EXP2-sMM), respectively.

As pointed out in Sec. 8.2, the mechanical weakening of the tissue affects only the mechanical properties of the background material (Eq. (8.3)). Although different constitutive models can be adjusted to a set of experimental measurements to represent the healthy cerebral arterial tissue (Sec. 5.4.1), the choice of the weakening parameter D in Eqs. (8.9) and (8.10) has an important effect on the characterization of unhealthy cerebral arterial tissues. In order to analyze the variation in the mechanical response of the tissue according to the weakening parameter D , let us consider the strain energy functions in Eqs. (8.1) and (8.3) in the stress-strain relations used to fit the experimental measurements, Eqs. (5.35) and (5.37). Fig. 8.3 shows the strain-stress functions $\mathcal{F}(\lambda_{\hat{\theta}\hat{\theta}})$ of Figs. 5.17 and 5.20 for the U-EXP2, (U-EXP1, EXP2-RC) and (U-EXP1, EXP2-sMM) models for different values of the weakening parameter D . It is worth pointing out that, as expected, the higher is the weakening parameter D the softer is the

8.3. Numerical simulations of unhealthy arterial tissue mechanics: static inflation tests

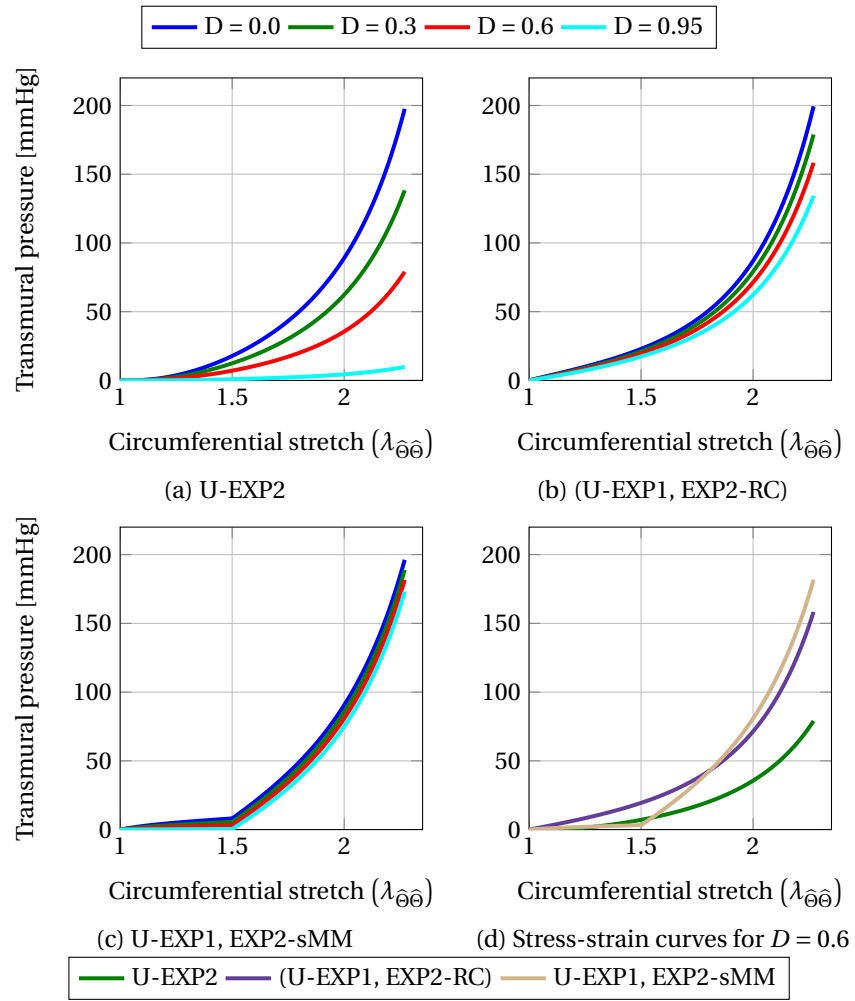
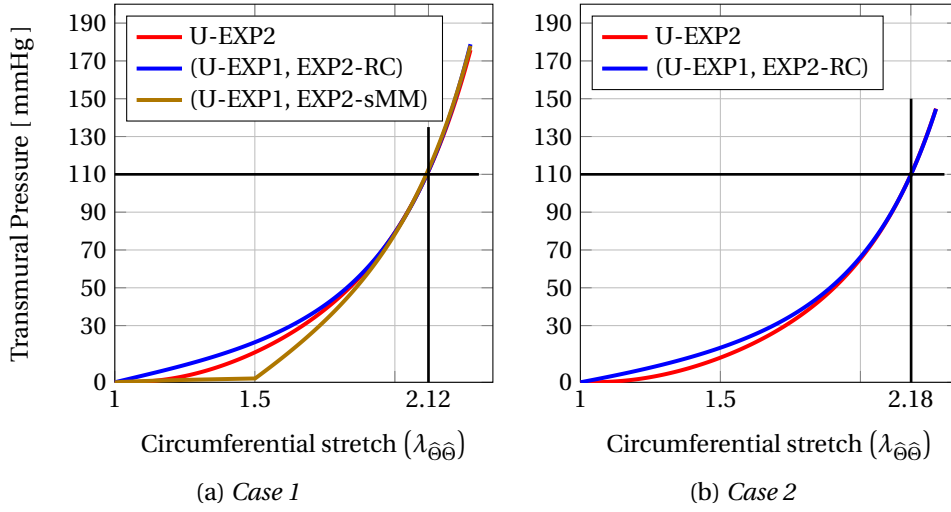


Figure 8.3: Functions $\mathcal{T}(\lambda_{\theta\theta})$ for different values of the weakening parameter D .


 Figure 8.4: Functions $\mathcal{T}(\lambda_{\hat{\theta}\hat{\theta}})$ with the weakening parameters of Tab. 8.1

tissue described by the isotropic model U-EXP2. On the other hand, with the two anisotropic models, only partial unhealthy states of the tissue can be described, due to the contribution to the mechanical response of the healthy collagen fibers. This highlights the fact that the approach considered in this work can be employed to describe the unhealthy arterial tissue during early phases of formation of an aneurysm, i.e. when the elastin starts degrading. In Fig. 8.3-(d), we observe that, for $D = 0.6$ the three curves do not intersect in the physiological range of transmural pressures ($\Delta P \in [70, 150]$); similarly for $D > 0.6$. For this reason, the proper calibration of the weakening parameter D according to the model describing the vessel wall is necessary. We have calibrated the values of the parameter D for the three constitutive models with respect to a reference value of D_{ref} for one of constitutive laws and the reference transmural pressure $\Delta P_{ref} = 110$ mmHg. More specifically, we have considered two cases. Firstly, we have fixed $D_{ref} = D_{EXP1}^{EXP2-sMM} = 0.75$ for the (U-EXP1, EXP2-sMM) model and determined the values of D_{EXP2} and $D_{EXP1}^{EXP2-RC}$ for the remaining two models such that the three functions $\mathcal{T} = \mathcal{T}(\lambda_{\hat{\theta}\hat{\theta}})$ intersect at the reference transmural pressure ΔP_{ref} . Then, we followed the same approach considering $D_{ref} = D_{EXP1}^{EXP2-RC} = 0.6$ for the (U-EXP1, EXP2-RC). We remark that in this case, it is not possible to find a value of $D \in [0, 1)$ for which the (U-EXP1, EXP2-sMM) model yields the reference deformation $\lambda_{\hat{\theta}\hat{\theta}} = 2.18$ at the reference pressure $\Delta P_{ref} = 110$ mmHg. Fig. 8.4 shows the functions $\mathcal{T} = \mathcal{T}(\lambda_{\hat{\theta}\hat{\theta}})$ for the three constitutive models under consideration with the material parameters of Tabs. 5.3 and 5.5 and the values of the weakening parameter D summarized in Tab. 8.1.

Case	Weakening parameter D
Case 1	$D_{ref} = D_{EXP1}^{EXP2-sMM} = 0.7500$, $D_{EXP1}^{EXP2-RC} = 0.3010$, $D_{EXP2} = 0.1103$
Case 2	$D_{ref} = D_{EXP1}^{EXP2-RC} = 0.6000$, $D_{EXP2} = 0.2641$

 Table 8.1: Values for the weakening parameter D used in the numerical simulations.

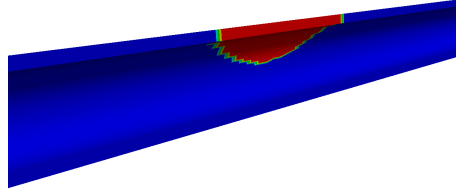


Figure 8.5: Representation of the weakened portion of the computational domain.

8.3.2 Numerical simulations of inflation tests on unhealthy cerebral arterial tissue

We now address the numerical simulation of static inflation tests on a cylindrical specimen of anterior cerebral artery of unhealthy arterial tissue by using the three models introduced in the previous section. The set of boundary conditions defining the structural mechanics problem is the same already described in Sec. 5.4.2.

In the current analysis it has been assumed that the weakening of the material properties occurs in a limited portion of the domain, also referred as weakened region, that has been obtained from the intersection of the computational domain considered in Sec. 5.4.2, with a sphere of radius $r_s = 0.095$ cm and center $C = (0, 0.09, 1.0)$, as indicated in Fig. 8.5.

Figs. 8.6 and 8.7 show the displacement field on the deformed mesh for $\Delta P_{ref} = 110$ mmHg for *Case 1* and *Case 2*, respectively. In Figs. 8.6 and 8.7 the mesh has been deformed according to the displacement field at the reference transmural pressure. We first notice that, for each of the two cases under consideration, the maximum value of the displacement magnitude is similar for all the constitutive models. This highlights the correct calibration of the weakening parameter D both for *Case 1* and *Case 2*. We also observe that, in both cases the pattern of the displacement fields is affected by the choice of the arterial wall model. The extension and shape of the area where the displacement field is influenced by the weakened region varies with the constitutive model and the weakening parameter D . We observe that in *Case 2*, where the weakening parameter D for the U-EXP2 and (U-EXP1, EXP2-RC) models is higher than in *Case 1*, the extension of the area where the displacement field is influenced by the weakened region becomes significantly larger than in *Case 1*. The displacement field reported in Figs. 8.6 and 8.7 indicate the formation of a bulge corresponding to the weakened region of the domain.

Figs. 8.8 and 8.9 present the volume ratio J at $z = 1$ at the reference transmural pressure for *Case 1* and *Case 2*. As already reported in Fig. 5.28, the approach used in this work to describe the nearly-incompressible behavior of arteries leads to an acceptable approximation of the incompressibility constraint.

Figs. 8.10, 8.11, 8.12, and 8.13 show the spatial distribution of the Von Mises stress σ_{VM} Holzapfel [2000] in a central portion of the computational domain for *Case 1* and *Case 2*. It is worth pointing out that in literature (see e.g. Balzani [2006]; Sommer [2008]) it has been observed that when considering damaged arterial tissue, it is important to take into account the opening angle of the vessel in order to properly compute the mechanical stresses inside the vessel wall. Indeed, when it is considered, and so are the consequent residual stresses, it has been shown that a more uniform spatial distribution of the mechanical stresses throughout the thickness of the vessel wall is achieved. Experimental observations

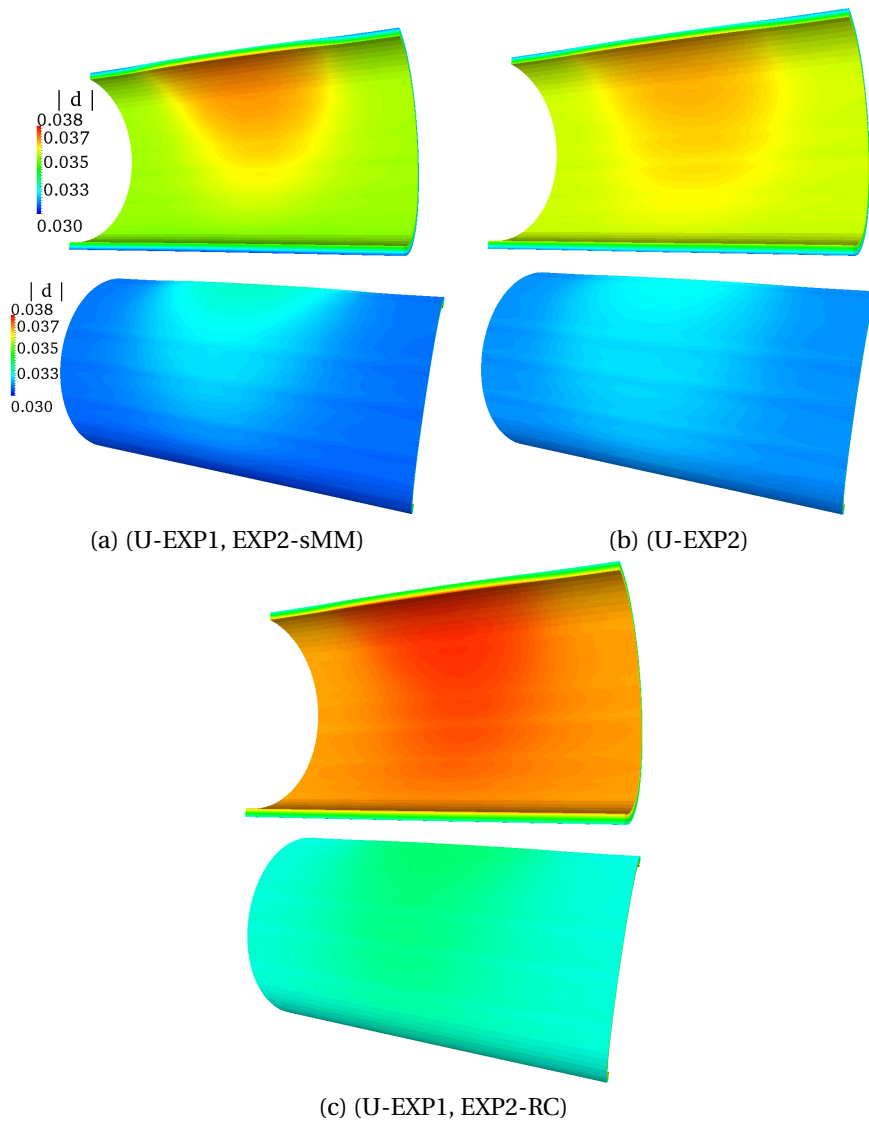


Figure 8.6: *Case 1*: displacement field [cm] at the internal and external surfaces of the computational domain at $\Delta P_{ref} = 110$ mmHg.

of the opening angle for cerebral arteries are only available in Monson [2001]; however information was not provided regarding the exact location of the vessels for the the opening angle and the experimental data present a strong variability among the samples. For this reason, residual stresses due to the opening angle are not considered in the current analysis, as similarly done e.g. in Li and Robertson [2009a]; Dalong et al. [2012]. In Figs. 8.10-8.13, for both cases the Von Mises stress σ_{VM} varies between $2.5 \cdot 10^5$ and $1.3 \cdot 10^6$ dyn/cm² and, as expected, the largest value occurs at the internal surface of the cylinder, where the radial displacement is higher. We observe that for *Case 1* the Von Mises stress on the internal and external surfaces of the cylinder does not present a strong variability with respect to the constitutive model. This is related to the fact that the displacement field on the internal and external surfaces in *Case 1* does not present a significant sensitivity to the constitutive model (as presented in Fig. 8.6), due to the calibration procedure. However, we report the dependency of the distribution of the Von Mises stress through the thickness of the vessel wall on the constitutive model, as presented in

8.3. Numerical simulations of unhealthy arterial tissue mechanics: static inflation tests

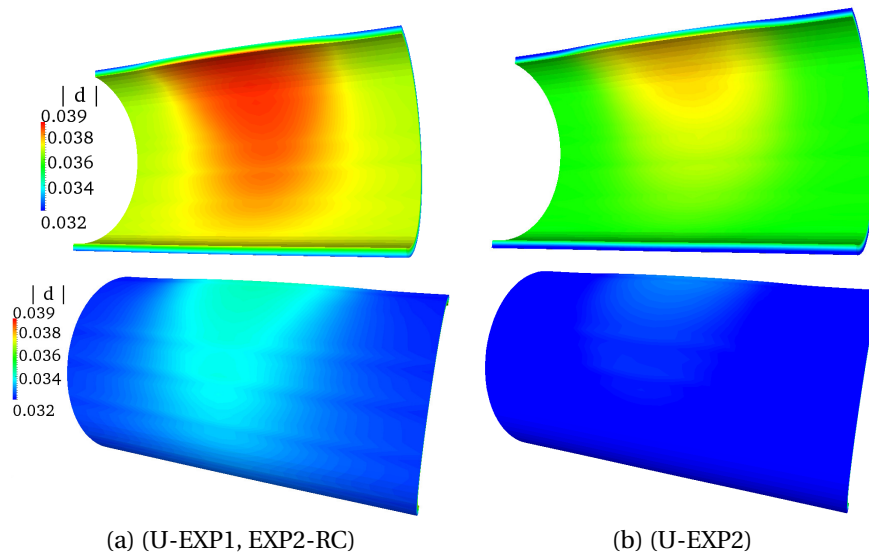


Figure 8.7: *Case 2*: displacement field [cm] at the internal and external surfaces of the computational domain at $\Delta P_{ref} = 110$ mmHg.

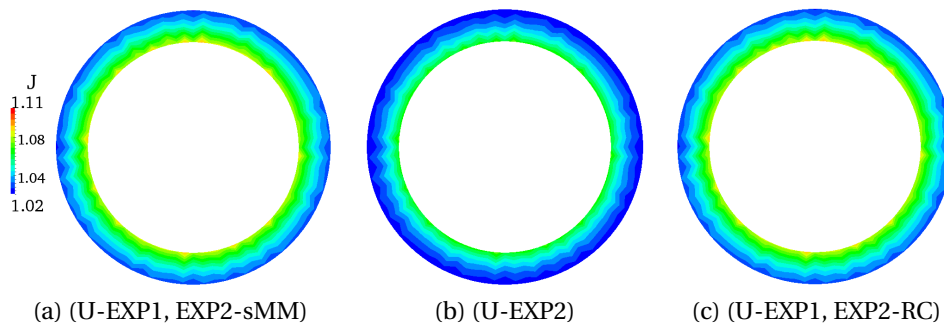


Figure 8.8: *Case 1*: Volume ratio J at $\Delta P = 110$ mmHg.

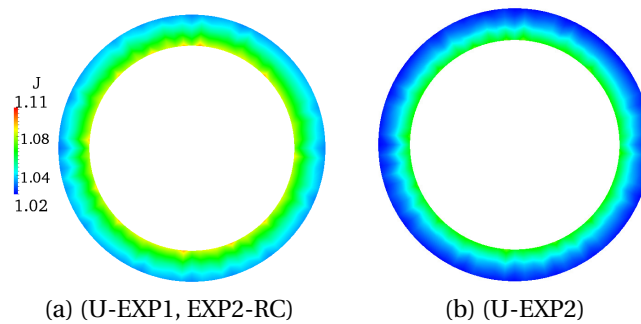


Figure 8.9: *Case 2*: Volume ratio J at $\Delta P = 110$ mmHg.

Fig. 8.11. However, for *Case 2*, represented in Figs. 8.12 and 8.13, the Von Mises stress strongly depends on the constitutive model. More specifically, the different displacement fields in Figs. 8.7 result in the different pattern of the Von Mises stress, shown in Fig. 8.12. Fig. 8.13 indicates that for high levels of mechanical weakening, the variations of the Von Mises stress through the thickness of the vessel wall are strongly affected by the choice of the constitutive model. To conclude, Figs. 8.11 and 8.13 highlight

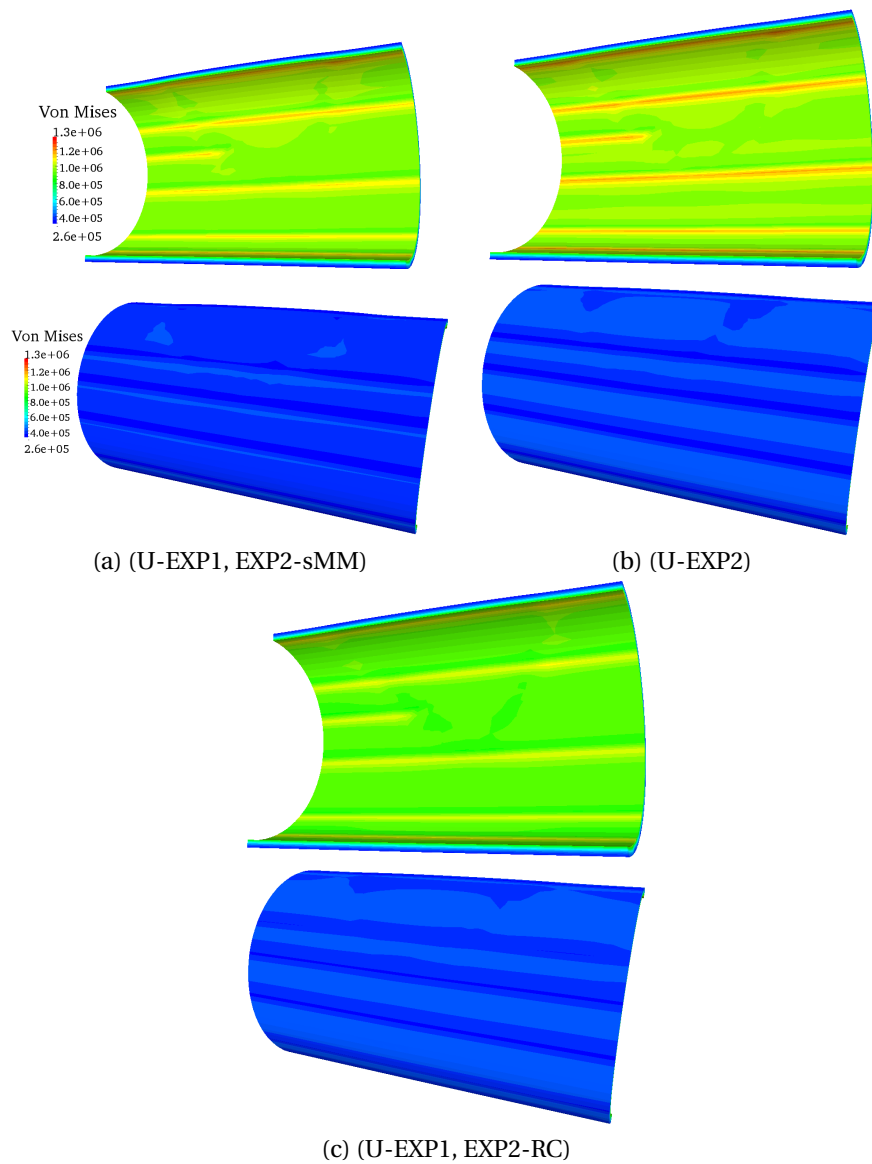


Figure 8.10: *Case 1*: Von Mises stress field σ_{VM} [dyn/cm²] at the internal and external surfaces of the computational domain at $\Delta P_{ref} = 110$ mmHg.

the relevance of carefully choosing the constitutive model to represent the unhealthy arterial tissue. Indeed, from the modeling point of view, the spatial distributions of the mechanical stresses in the physiological range of pressures, obtained with the constitutive models, may indicate locations of high stresses where a different long-term progression of the mechanical weakening of the arterial tissue can occur.

8.3. Numerical simulations of unhealthy arterial tissue mechanics: static inflation tests

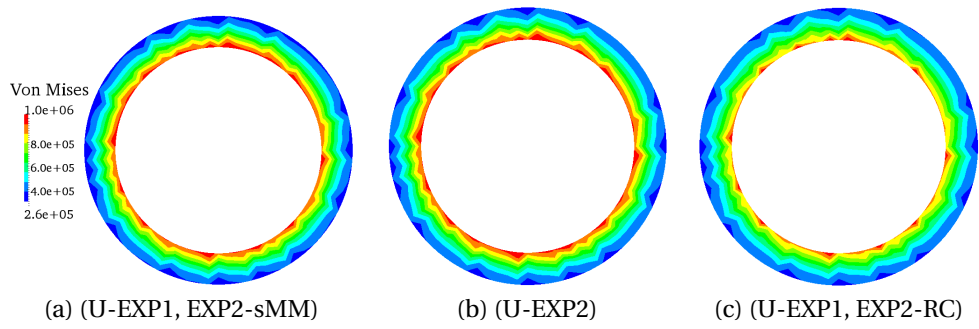


Figure 8.11: *Case 1*: Von Mises stress [dyn/cm^2] at $z = 1 \text{ cm}$ and $\Delta P = 110 \text{ mmHg}$.

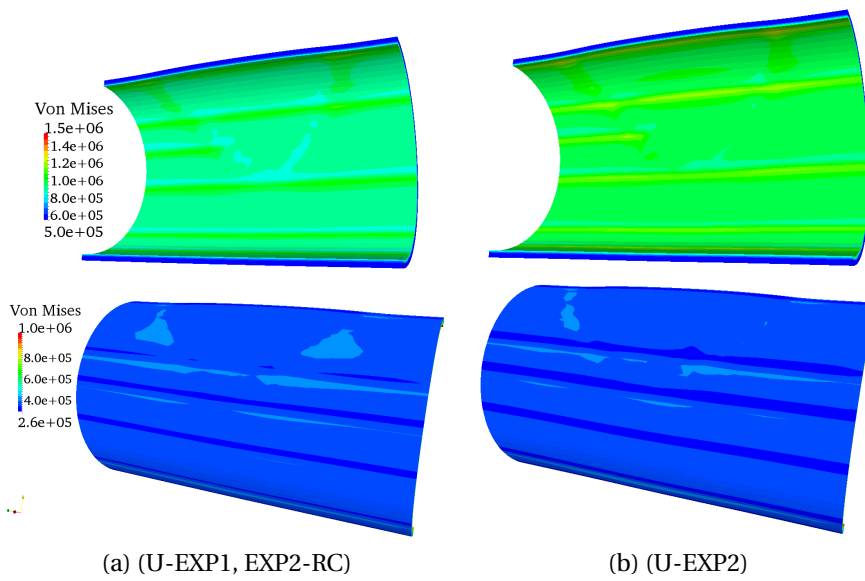


Figure 8.12: *Case 2*: Von Mises stress field σ_{VM} [dyn/cm^2] at the internal and external surfaces of the computational domain at $\Delta P_{ref} = 110 \text{ mmHg}$.

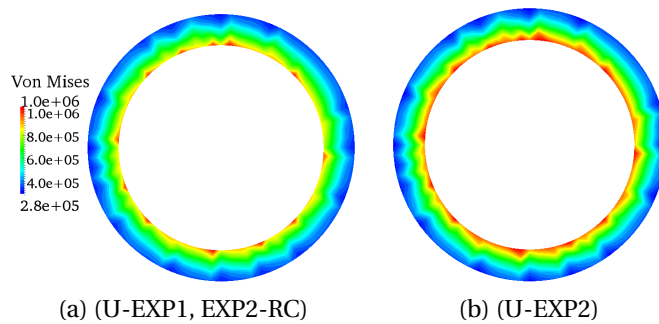


Figure 8.13: *Case 2*: Von Mises stress [dyn/cm^2] at $z = 1 \text{ cm}$ and $\Delta P = 110 \text{ mmHg}$.

9 Fluid-Structure Interaction numerical simulations of unhealthy cerebral arteries

This chapter deals with FSI numerical simulations of cerebral arteries with inhomogeneous mechanical properties to represent either unhealthy conditions of the vessel wall, such as the ones described in Ch. 8, or formed cerebral aneurysms (CA). The study of CA by means of FSI numerical simulations has been so far mainly devoted to the analysis of the sensitivity of the numerical results to variations of different aspects in the simulation setting, see e.g. Valencia et al. [2013]; Chen et al. [2009]; Bazilevs et al. [2010]; Torii et al. [2008, 2007, 2009]; Valencia and Solis [2006]; for instance, the constitutive model for the arterial tissue Chen et al. [2009]; Torii et al. [2008]; Valencia and Solis [2006], the vessel wall thickness Valencia et al. [2013]; Torii et al. [2010], or the blood pressure in normotensive and hypertensive conditions Torii et al. [2007, 2009].

In Valencia et al. [2013]; Chen et al. [2009]; Bazilevs et al. [2010]; Torii et al. [2008, 2007, 2009]; Valencia and Solis [2006] the numerical simulations are carried out on computational domains representing anatomically realistic geometries of cerebral aneurysms obtained from reconstructing the vessel lumen surface from MRI images Crosetto [2011]; Faggiano and Antiga [2014]. The set of boundary conditions is similar for all the numerical studies in Valencia et al. [2013]; Chen et al. [2009]; Bazilevs et al. [2010]; Torii et al. [2008, 2007, 2009]; Valencia and Solis [2006]; more precisely, it involves Dirichlet boundary conditions, usually computed from physiological flow rates Valencia et al. [2013]; Valencia and Solis [2006]; Bazilevs et al. [2010]; Torii et al. [2009], and resistance boundary conditions for the inflow and outflow sections of the fluid domain, respectively, and homogeneous Neumann (i.e. traction free) boundary conditions on the external surface of the solid domain. The sensitivity of the numerical results to changes in the simulation setting is estimated by analyzing different quantities: the flow structures inside the aneurysm dome, the fluid pressure, the vessel wall displacement, and hemodynamical indicators or mechanical stresses such as the Oscillatory Shear Index (OSI), Wall Shear Stress (WSS), or Von Mises equivalent stresses. In Torii et al. [2008]; Chen et al. [2009]; Valencia and Solis [2006] linear elastic and hyperelastic models are considered. It is shown that the choice of the arterial constitutive model strongly affects the vessel wall displacement, specially inside the aneurysm dome. This, in turn, leads to different predictions of the WSS and related OSI index; more precisely, the larger is the displacement of the dome, the lower are the values of WSS observed. Simultaneously, the strong influence on the numerical results of the aneurysmal wall thickness is presented in Valencia et al. [2013]; Torii et al. [2010]. These works report that the thinner is the aneurysmal wall the largest are its deformations during the cardiac cycle. Particularly, the numerical results presented in Torii et al.

[2010] show that when the thickness of the aneurysmal wall is one sixth of the thickness in the parent vessel, the displacement of the vessel wall in the dome is around 60% higher than the one observed in the parent artery. It is worth pointing out that, although the use of a reduced wall thickness for the aneurysmal tissue reproduces an histological feature of cerebral aneurysms Valencia et al. [2013]; Sherif et al. [2014], the numerical results are strongly affected by the combined effect of three aspects of the simulation setting: the reduced dome thickness, the use of constant material parameters for the constitutive law in the solid domain, and the traction free boundary conditions imposed on the external surface of the solid domain. However, the significant influence of the wall thickness on the numerical results suggests that the features of the aneurysmal tissue should be taken into account in FSI numerical simulations. Although the numerical results in Valencia et al. [2013]; Chen et al. [2009]; Bazilevs et al. [2010]; Torii et al. [2008, 2007, 2009]; Valencia and Solis [2006] show that the aneurysmal wall moves during the heart beat, we remark that, as discussed in Oubel et al. [2010], there is controversy both in the biomedical and medical communities about the effective aneurysmal tissue movement during the heart beat. In addition, as pointed out in Oubel et al. [2010], the movement of a cerebral aneurysm depends on different factors such as, for instance, its location, size, and possible contact constraints. On the other hand, in Torii et al. [2007, 2009] it is reported the negligible influence on the blood flow dynamics of the blood pressure regime, e.g. normotensive or hypertensive. Indeed, it is shown that the numerical results are more affected by the geometry of the computational domain rather than by the blood pressure regime.

As already mentioned in Ch. 7, FSI numerical simulations are computationally expensive. For this reason, in order to reduce the computational load of the numerical simulations needed to study a portion of the cardiovascular system, the spatial distributions of WSS and Von Mises stresses obtained from FSI studies have been compared with the ones obtained from less demanding numerical simulations, such as CFD or Computational Structural Dynamics (CSD); see e.g. Valencia et al. [2013]; Papaharilaou et al. [2007]; Scotti et al. [2005]. More precisely, CFD and FSI simulations are compared in terms of fluid velocity, pressures, and WSS, while CSD and FSI simulations are compared in terms of vessel wall displacement and mechanical stresses obtained for a mean blood pressure configuration. We remark that, in CSD studies, in order to take into account the spatial variability of the blood pressure, the mean blood pressure configuration might be deduced from numerical results of CFD simulations in the same portion of the cardiovascular system; on the other hand, the boundary conditions for the inlet/outlet surfaces of the fluid domain employed for the FSI problem can be readily employed in CFD simulations as well. In Valencia et al. [2013]; Papaharilaou et al. [2007]; Scotti et al. [2005] it is reported that the main features of the spatial distribution of the quantities of interest can be captured by CFD or CSD simulations, the values of important indicators such as the WSS or the tissue stresses might be significantly over or underestimated with respect to the ones observed in FSI studies. In addition to CFD, FSI, and CSD comparisons, in Valencia et al. [2013]; Papaharilaou et al. [2007]; Scotti et al. [2005] an explicit partitioned coupling (Formaggia et al. [2009]; Pozzoli [2011]) between blood flow and vessel wall is considered. This in order to reduce the computational burden of the numerical studies with respect to a fully coupled FSI simulation, i.e. implicit coupling or monolithic approach, see Ch. 6; as shown in Valencia et al. [2013], the numerical results obtained in the two cases differ significantly.

In this chapter we address the influence of the constitutive model for the unhealthy arterial tissue on the numerical results. As in Sec. 8.3, the unhealthy arterial tissue is modeled by means of the approach described in Sec. 8.2 and the numerical simulations are carried out for different levels of mechanical weakening. Since we specifically focus on the mechanical weakening characterizing the early stages development of cerebral aneurysms, we take into account the experimental observation for which aneurysms start developing in regions with low contact constraints with the surrounding tissue San

Millán Ruiz et al. [2006]; Sforza et al. [2012]; San Millán Ruiz et al. [2002] by considering different boundary conditions on the external surface of the solid domain. The analysis aims at evaluating the influence of the constitutive model on hemodynamical and mechanical indicators of interest during the heart beat; for this reason, FSI simulations have been preferred to stand alone CFD and CSD simulations. In the following, we point out that the unhealthy arterial tissue and idealized aneurysms will be modeled by means of isotropic and anisotropic models. More precisely, based on the study carried out in Sec. 8.3, the arterial tissue is described by means of the second order exponential EXP2 model and the anisotropic (EXP1, EXP2-RC) (see Sec. 4.2.2) law. Indeed, when possible, we want to study the impact on the numerical results of two different classes of constitutive models rather than focusing on different classes of the same type. The multi-mechanism model (EXP1, EXP2-sMM) has not been employed in our simulations; indeed, although the numerical issues discussed in Sec. 7.2.2 have been addressed when considering healthy arteries, its use has turned out to be extremely critical in the numerical simulations of unhealthy cerebral tissue and aneurysms and, similarly to what has been reported in Sec. 7.2.2, stagnation of the variational residual of the Newton method has been observed. However, due to the capability of such model to describe the active and passive states of collagen fibers during the heart beat, see Sec. 7.2.1, further investigations are needed in order to address the numerical issues observed in the numerical simulations.

This chapter is organized as follows. Sec. 9.1 details the set of boundary conditions applied on the computational domains in all the numerical simulations. Sec. 9.2 presents the numerical simulations on the idealized geometries of vessels of Ch. 7 with weakened arterial tissue. To conclude, in Sec. 9.3 the case of idealized and anatomically realistic geometries of cerebral aneurysms are discussed.

The numerical simulations presented in the next sections were carried out on the Supercomputer Monte Rosa at the Swiss Supercomputing Center and on the IBM AMD Opteron cluster Bellatrix at the EPFL.

9.1 Setup of the fluid-structure interaction simulations

The set of boundary conditions described in Sec. 6.1 has been considered also for the numerical simulations presented hereafter. The velocity profile of Fig. 7.1 has been applied as inlet boundary condition for the fluid domain after being rescaled with respect to the inlet cross-section area of the geometry under consideration. Resistance boundary conditions have been used to guarantee a physiological variation of the blood pressure between the systolic and the diastolic phases of the heart beat. Regarding the solid domain, elastic Robin boundary conditions with variable elastic coefficients on the external surface of the vessel wall model the tethering tissues. This choice is motivated by the experimental observations that saccular aneurysms develop initially within the free subarachnoid space San Millán Ruiz et al. [2002] and that unruptured aneurysms are found in regions with low contact constraints with the surrounding tissue San Millán Ruiz et al. [2006]; Sforza et al. [2012]; San Millán Ruiz et al. [2002]. Consequently, given a reference elastic coefficient K in Eq. (6.15) for the healthy arterial tissue, as e.g. the one considered in Sec. 7.2, a lower value of K , indicated as K_D , has been considered in correspondance of the weakened portion of the solid domain; in particular, we reduce K of a factor 0.8. It must be pointed out that the choice of K_D may strongly influence the numerical results, namely inducing higher displacements of the vessel wall in the weakened region compared to the ones obtained in the healthy portion of the solid domain. However, this choice seems to be a reasonable assumption in order to take into account either the tethering tissue around the healthy part of the vessel and the absence of strong contact constraints, e.g. bones, in the weakened region. In this work, the effects of

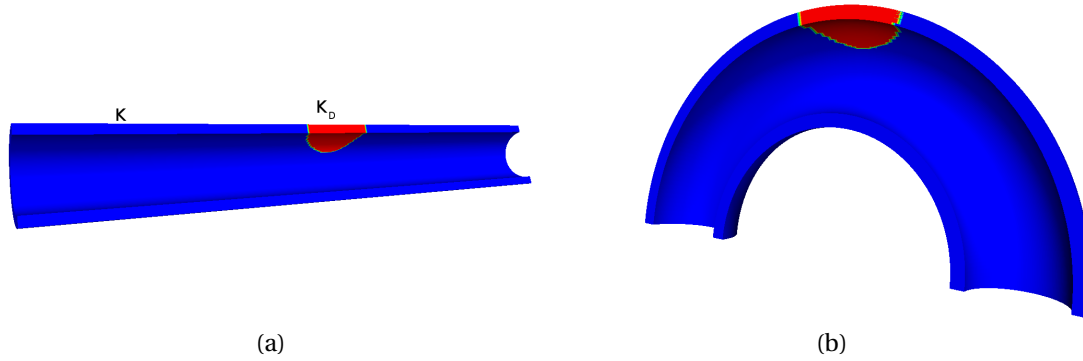


Figure 9.1: Representation of the sub-domains in which the mechanical weakening of the mechanical properties occurs for the two idealized blood vessels

residual stresses on the numerical simulations are not considered since in Williamson et al. [2003] it was reported that the tissues stresses at a certain deformation are more sensitive to the choice of the constitutive model for the wall rather than to the introduction of residual stresses; this choice has also been made in e.g. in Valencia et al. [2013]; Torii et al. [2009, 2010]. In the next sections, details regarding the mesh generation process, the choice of the material parameters for the constitutive laws, the finite element spaces, and the consequent size of the monolithic system in Eq. (6.26) are provided case by case.

9.2 Numerical simulations on idealized geometries of vessels

In order to evaluate the influence on the numerical results of the modeling choice for the arterial wall within the context of physiological FSI simulations with weakened arterial tissue, we firstly consider the two idealized geometries of blood vessels presented in Sec. 7.2; the characteristic dimensions of the computational domains are summarized in Fig. 7.2. As done in Sec. 7.2, the fluid equations are discretized by means of the *Inf-Sup* stable $\mathbb{P}1$ Bubble - $\mathbb{P}1$ pair of finite elements for velocity and pressure, respectively; in addition, linear elements are used for the solid and geometric problems as well. Consequently, the total number of DOFs of the monolithic problem is again around 600,000 and 800,000 for the cylindrical and toroidal geometry, respectively. We recall that we have focused on the use of one isotropic and one anisotropic law for the arterial wall among the ones considered in Sec. 5.4.2; more precisely, the U-EXP2 and (U-EXP1, EXP2-RC) laws are employed (see Eqs. (8.9) and (8.11)). Similarly to Sec. 8.3, we suppose that the mechanical properties of the healthy arterial tissue are affected by the weakening parameter $(1 - D)$ only in a restricted portion of the solid domain. Fig. 9.1 shows the region of the solid computational domains where the mechanical weakening occurs for the idealized blood vessels under consideration. In addition, Fig. 9.1-(a) highlights the use of two different elastic coefficients in the Robin boundary conditions for the two different regions with different mechanical properties. The elastic coefficient K for the healthy part of the vessel is set to $K = 1.0 \cdot 10^7$ dyn / cm³, while $K_D = 0.8 \cdot 10^7$ dyn / cm³. The two cases discussed in Sec. 8.3.1 have been considered for the current analysis; for both of them, the material parameters measuring the degraded mechanical properties of the unhealthy tissue for the isotropic U-EXP2 and for the isotropic part of the (U-EXP1, EXP2-RC) in the weakened part of the solid domain are presented in Tab. 9.1. More precisely, they have been computed from the ones for the healthy tissue, see Tabs. 5.3 and 5.5, and the weakening parameters in Tab. 8.1.

9.2. Numerical simulations on idealized geometries of vessels

<i>Case 1</i> ($D_{ref} = D_{EXP1}^{EXP2-sMM} = 0.7500$)		<i>Case 2</i> ($D_{ref} = D_{EXP1}^{EXP2-RC} = 0.6000$)	
Constitutive law	Material parameters	Constitutive law	Material parameters
U-EXP2	$\alpha_2 = 6.069 \cdot 10^4$, $\gamma_2 = 0.061$	U-EXP2	$\alpha_2 = 5.020 \cdot 10^4$, $\gamma_2 = 0.061$
U-EXP1	$\alpha_{iso}^{aniso} = 1.221 \cdot 10^4$, $\gamma_{iso}^{aniso} = 0.862$	U-EXP1	$\alpha_{iso}^{aniso} = 6.988 \cdot 10^3$, $\gamma_{iso}^{aniso} = 0.862$

Table 9.1: Material parameters in *Case 1* and *Case 2* for both constitutive models under consideration. Refer to Tabs. 5.3 and 5.5 for the parameters describing the healthy tissue. D_{ref} denotes the reference value of weakening parameters with respect to which the others have been computed; see Sec. 8.3.1

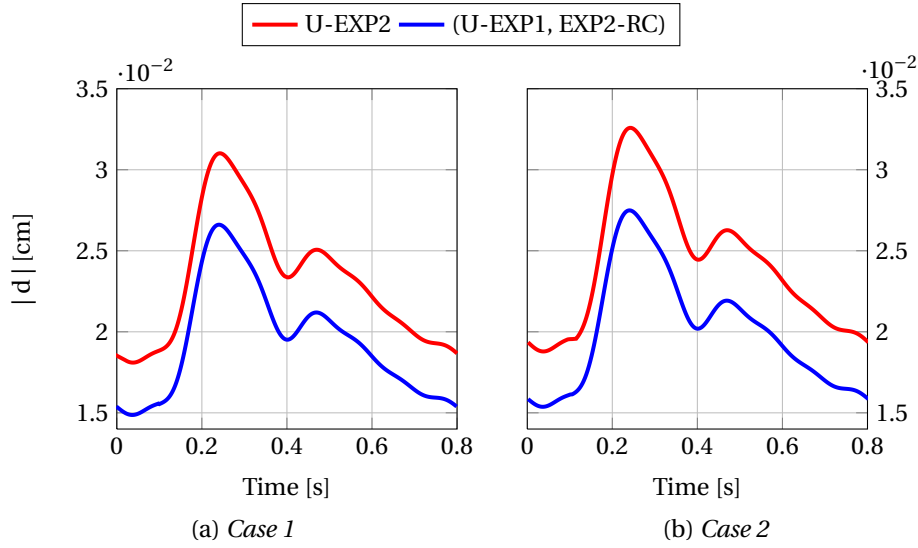


Figure 9.2: Magnitude of the vessel wall displacement [cm] at the center of the weakened region. The displacement magnitude in the healthy case is represented in Fig. 7.10

When local mechanical weakening of the arterial tissue is considered, the formation of a bulge in correspondance to the weakened region of the vessel wall is observed during the heart beat, especially in the systolic phase of the cardiac cycle, as reported in Figs. 9.3 and 9.4. Figs. 9.3 and 9.4, show the wall displacement in the healthy and unhealthy parts of a central cut of the computational domain; as reported, the numerical solution is symmetric with respect to the axis of the domain and the vessel wall deforms along the radial direction, similarly to Fig. 7.7, for all the cases under consideration. It is worth pointing out that, for both cases, the maximum vessel wall displacement in the weakened region obtained with the anisotropic (U-EXP1, EXP2-RC) model is smaller than the one measured with the isotropic U-EXP2 law and the maximum difference is reached at the center of the unhealthy part, as detailed in Fig. 9.2. Indeed, by measuring the relative difference among the two numerical solutions with respect to the highest displacement obtained in the two cases (as in Torii et al. [2008]), we report that the displacement obtained with the anisotropic (U-EXP1, EXP2-RC) law is 16% smaller than the one observed with the U-EXP2 model. In addition, as shown in Fig. 9.3, in the proximity of the weakened region, for the case of the U-EXP2 law, the vessel wall displacement along the direction of the flow is affected by the formation of the bulge. On the other hand, such influence is not observed when the anisotropic model is employed. This is due to the choice of the constitutive model and the consequent vessel wall displacement achieved, see Figs. (9.5) and (9.6). We recall that the effects

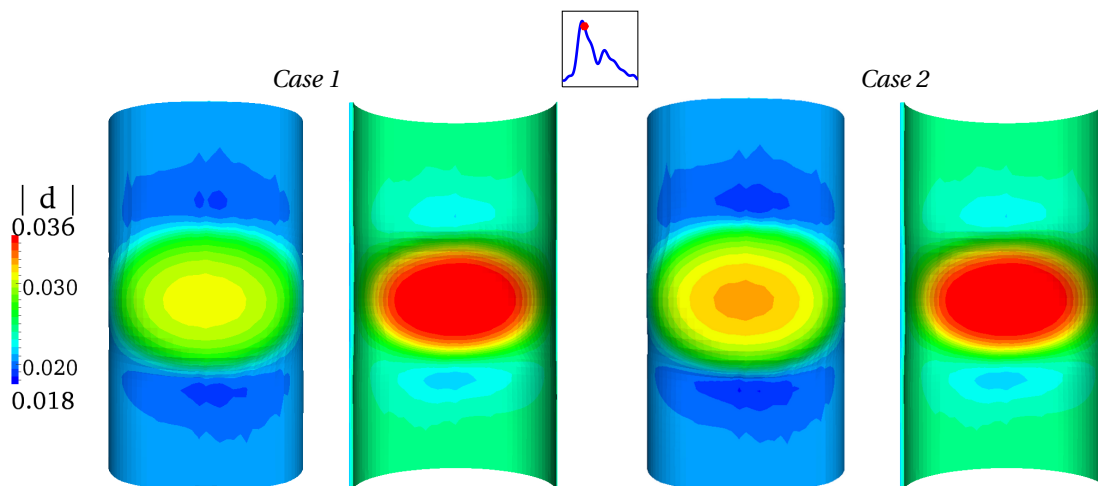


Figure 9.3: Deformed central cut of the solid domain according to the displacement field for the U-EXP2 model at the time $t = 0.239$. The deformation is amplified by a factor 1.5 in order to highlight the vessel wall deformations. Direction of the flow: from the bottom to the top

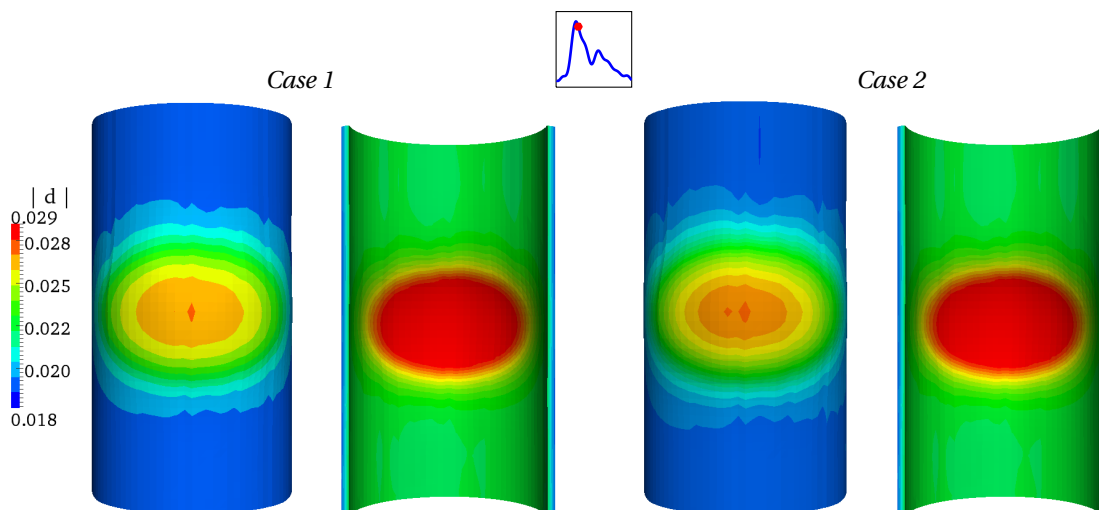


Figure 9.4: Deformed central cut of the solid domain according to the displacement field for the (U-EXP1, EXP2-RC) model at the time $t = 0.239$ s. The deformation is amplified by a factor 1.5 in order to highlight the vessel wall deformations. Direction of the flow: from the bottom to the top

of the bulge formation on the deformations of the surroundings of the weakened region have not been observed in the case of the numerical simulations of static inflation tests presented in Sec. 8.3.2. Therefore, this points out the relevance of carrying out FSI numerical studies together with numerical simulations of arterial wall mechanics to characterize the mechanical behavior of the unhealthy arterial tissue in different applications of interest.

Figs. 9.5-(a)-(b) and 9.6-(a)-(b) show the vessel wall displacement along a straight line parallel to the main axis of the cylindrical domain, between the two cross sections at $z = 0.2$ cm and $z = 0.45$ cm, and located at the middle point between the internal and external radii of the solid domain. In addition, the

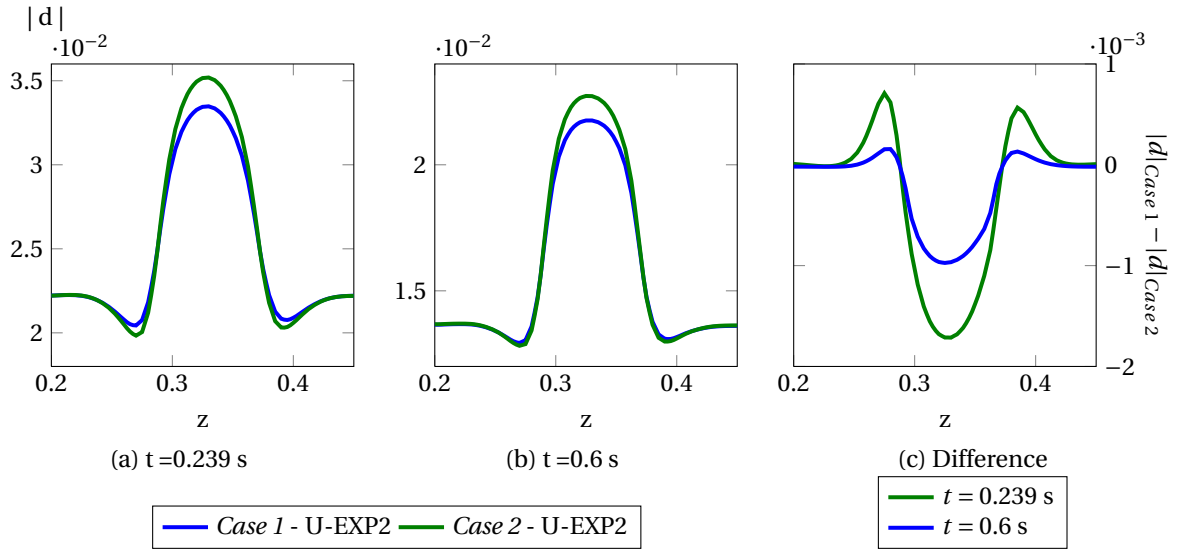


Figure 9.5: Vessel wall displacement magnitude for the U-EXP2 model at times $t = 0.239$ s and $t = 0.6$ s and their difference

difference between the displacement obtained in *Case 1* and *Case 2* at two different times of the heart beat are presented. As mentioned before, the higher the vessel wall displacement, the more evident are the effects due to the bulge formation in the vicinity of the weakened part. As reported in Fig. 9.5-(a)-(b), at the time $t = 0.239$ s, the minimum displacement reached in the proximity of the unhealthy portion of the domain is 10% smaller than the one in the healthy portion of the domain while such difference reduces to 1% during the diastolic phase. On the other hand, see Fig. 9.4, for the anisotropic model, due to the assumption for which the mechanical weakening affects only the strain energy function modeling the elastin, the vessel wall displacement monotonically increases when moving from the healthy to the unhealthy regions of the domain. Figs. 9.5-(c) and 9.6-(c) highlight the effects on the vessel displacement of the increase in the mechanical weakening; we observe that, although the weakening parameter D is increased by 50% between *Case 1* and *Case 2* (see Tab. 8.1), the peak displacement at $t = 0.239$ s in *Case 2* is around 4% higher than the one observed in *Case 1* for both constitutive models. The results on the vessel wall displacement point out two important aspects that must be taken into account when studying cerebral aneurysms by means of numerical simulations. The first one concerns the significance of modeling the progressive mechanical degradation of the single constituents of the tissue. Indeed, the modeling choice for the vessel wall, and the consequent mathematical modeling of the initial weakening of the tissue as affecting the overall mechanical properties of the mechanical behavior or only one of its constituents, affects the deformation of the weakened region and in turn the spatial distribution of the WSS, as it will be presented hereafter. Secondly, from Figs. 9.5-(c) and 9.6-(c), we conclude that although the mechanical weakening is a key process in the formation of cerebral aneurysms, it cannot fully describe the formation of the aneurysmal bulge, as also discussed in Chatziprodromou et al. [2007], but growth and remodeling processes of the arterial tissue must be considered in the numerical simulations.

Figs. 9.7 and 9.8 present the numerical solutions of the fluid problem for both *Case 1* and *Case 2*. For the sake of brevity, due to the strong similarities between the numerical simulations for *Case 1* and *Case 2*, the blood pressure and velocity are presented only for one of the two cases under consideration. For this reason, Fig. 9.7 shows the blood pressure during the heart beat for both the constitutive models

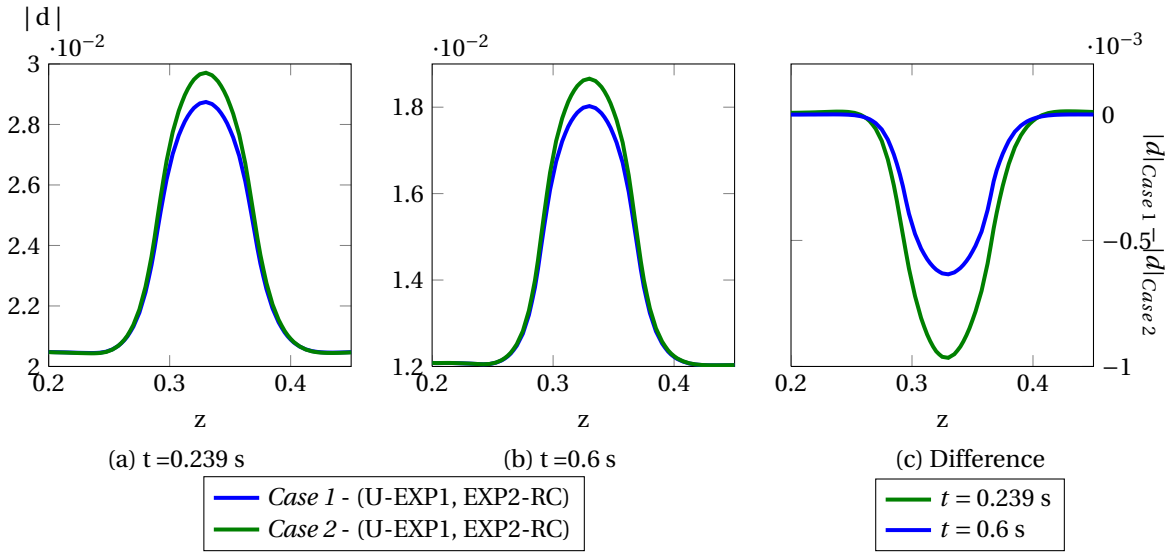


Figure 9.6: Vessel wall displacement magnitude for the (U-EXP1, EXP2-RC) model at times $t = 0.239$ s and $t = 0.6$ s and their difference

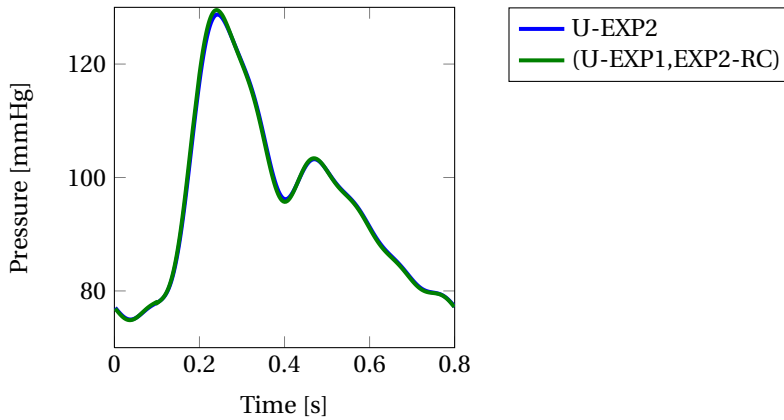


Figure 9.7: Blood flow pressure during the heart beat at the cross section $z = 0.33$ cm for *Case 1* for the U-EXP2 and (U-EXP1, EXP2-RC) models

obtained in *Case 1*, while Fig. 9.8 reports blood velocity streamlines at times $t = 0.212$ s and $t = 0.45$ s obtained with the U-EXP2 law in *Case 2*. In Fig. 9.7, we notice that the blood pressure varies between physiological values over time, as in Sec. 7.2.1, and that the influence of the constitutive model on the numerical result is negligible. Similarly, Fig. 9.8 reports that the laminar regime of the blood flow already observed in Fig. 7.6 is preserved and that the formation of the bulge does not induce the flow recirculation in the portion of the computational domain.

As reported in Figs. 9.9-9.10, the formation of a region of low WSS values, compared to the healthy case, is observed in correspondence of the bulge during all the cardiac cycle. In addition, as expected, the higher the mechanical weakening of the arterial tissue, the wider the region of low WSS and the lower the minimum WSS measured in the bulge formed in the fluid domain, as also reported in Chatziprodromou et al. [2007]. More precisely, when the maximum displacement in the weakened

9.2. Numerical simulations on idealized geometries of vessels

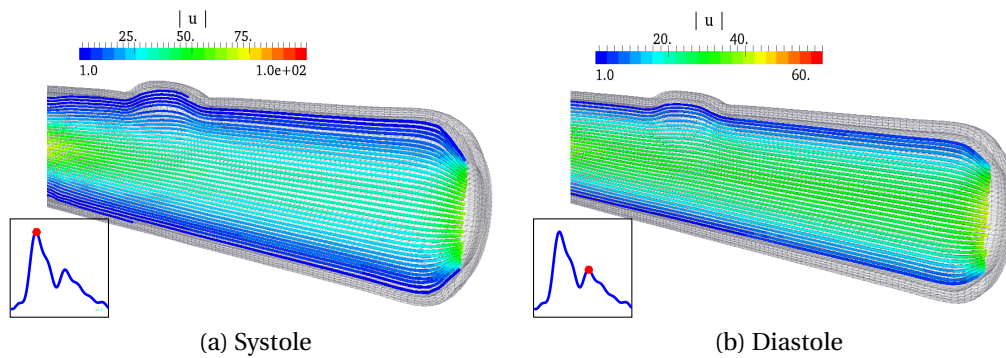


Figure 9.8: Blood flow streamlines [cm/s] in the deformed fluid domain at the times 0.212 s and $t = 0.45$ s. Constitutive model for the arterial wall: U-EXP2 and *Case 2* of mechanical weakening

portion is reached at time $t = 0.239$ s, the WSS magnitude in the bulge for the isotropic U-EXP2 law is 42% and 53% for *Case 1* and *Case 2*, respectively, than the WSS at the same point measured for the healthy case. Similarly, the WSS reduces of 16% and 21% for the two configurations of mechanical weakening, respectively, during the diastolic phase, as presented on the second row of Fig. 9.9. For the (U-EXP1, EXP2-RC) model, the reduction of the WSS in correspondence of the bulge is smaller than the one measured for the isotropic law, as a consequence of the smaller vessel wall deformation; indeed, with respect to the WSS obtained in the healthy case, at $t = 0.239$ s the WSS magnitude decreases of the 24% and 32% for *Case 1* and *Case 2*, respectively, while of the 10% for both cases at $t = 0.600$ s. Once again, from Figs. 9.9 and 9.10, we notice the effects of the constitutive model for the tissue on the spatial distribution of WSS. Indeed, in addition to the quantitative aspects already discussed, it is important to refer that when the isotropic U-EXP2 law is employed, an increase in the WSS values in the upstream proximity of the unhealthy region is observed, while such effect is not reported for the anisotropic model. Such variation in the WSS along the direction of the flow is related to the different deformations of the vessel wall reported in Figs. 9.3-9.6. In fact, the increase in the WSS magnitude for the U-EXP2 is due to the lower radial displacement in the proximity of the weakened region.

Fig. 9.11 shows the time evolution of the WSS magnitude at two different points of the fluid-structure interface. The qualitative behavior of the WSS magnitude function is the same for both constitutive models in both cases under consideration. However, the choice of the constitutive model has a strong impact on the WSS magnitude observed inside the bulge. Indeed, for *Case 1* and for a point of the bulge, as in the first row of Fig. 9.11-(a), the minimum value of WSS magnitude obtained with the U-EXP2 law is 35% smaller than the corresponding minimum value of WSS measured with the (U-EXP1, EXP2-RC) law, while for *Case 2* such difference increases up to the 44%. On the other hand, downstream of the weakened region the relative difference between the two minimum values of WSS magnitude reduces to 3% for both reference levels of mechanical weakening. Once again, the similarities in the numerical results in the downstream portion of the fluid and solid domain can be ascribed to the similar vessel wall deformations obtained. Fig. 9.12 presents the Von Mises stress (σ_V) at the time $t = 0.239$ s on the internal surface of the vessel wall. In the weakened portion of the domain, the choice of the constitutive model influences both the maximum value and the spatial distribution of the Von Mises stress. More precisely, given the level of mechanical weakening, when the isotropic U-EXP2 model is employed, the highest values of Von Mises stress are attained on almost the entire internal surface of the bulge, while for the anisotropic (U-EXP1, EXP2-RC) model such region is much smaller. In addition, the higher is the level of mechanical weakening, the wider is the region inside the bulge where the maximum value of

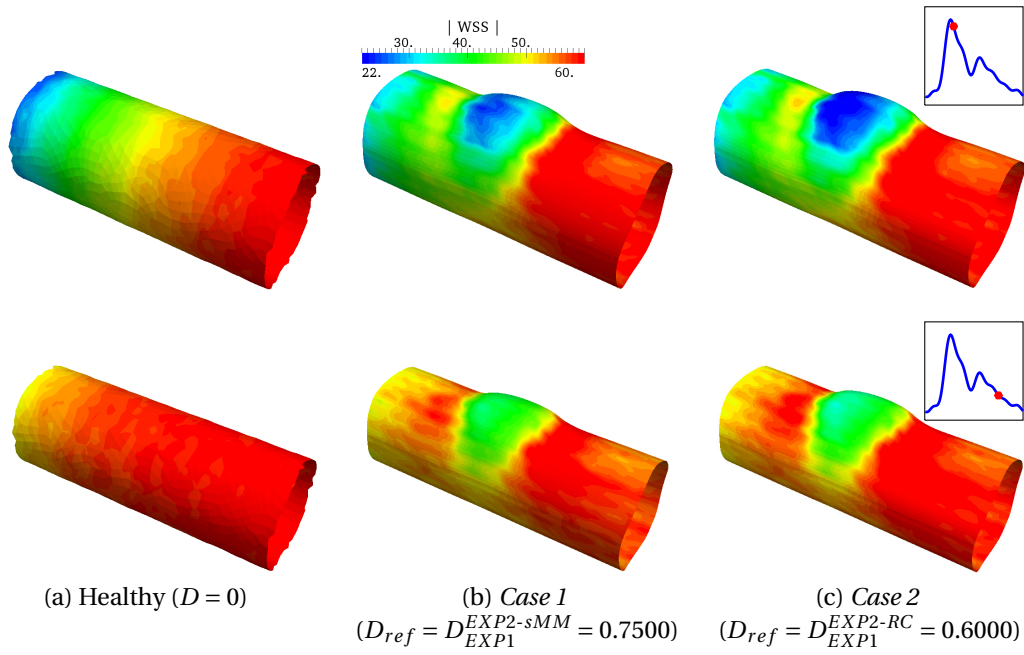


Figure 9.9: WSS magnitude [dyn/cm²] on the deformed vessel lumen surface in a central cut of the fluid domain at times $t = 0.239$ s and $t = 0.600$ s. Direction of flow: from left to right. Constitutive model: U-EXP2

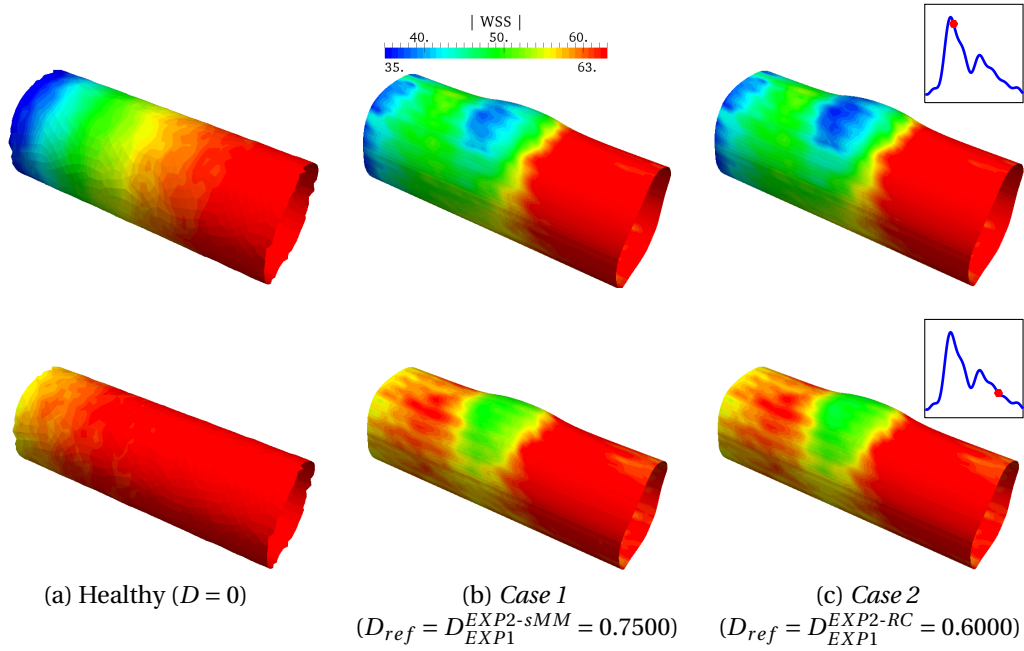


Figure 9.10: WSS magnitude [dyn/cm²] on the deformed vessel lumen surface in a central cut of the fluid domain at times $t = 0.239$ s and $t = 0.600$ s. Direction of flow: from left to right. Constitutive model: (U-EXP1, EXP2-RC)

stress is reached. We should refer that the highest value of Von Mises stress observed for the U-EXP2 law is 45% higher than the maximum value of σ_V obtained with the anisotropic model (U-EXP1, EXP2-RC).

9.2. Numerical simulations on idealized geometries of vessels

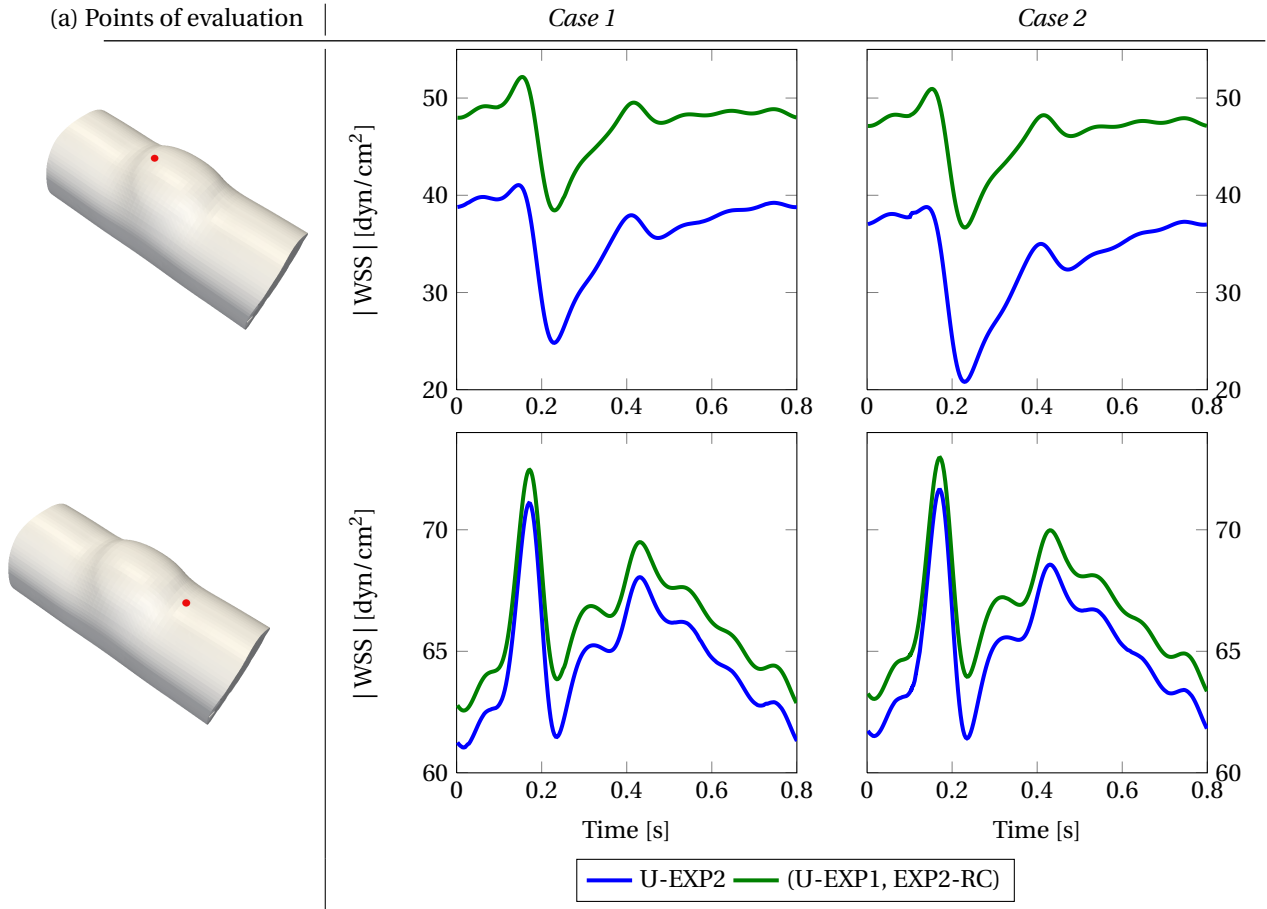


Figure 9.11: Pointwise WSS for the U-EXP2 and (U-EXP1, EXP2-RC) models during the heart beat for the unhealthy cases *Case 1* and *Case 2*

As discussed in Sec. 7.2.3, the numerical results on the toroidal geometry presented characteristics similar to the ones observed for the cylindrical geometry. Figs. 9.13-9.14 report the blood pressure and particle path lines measured during the heart beat. By comparing Figs. 9.13 and 7.27, we observe that the pressure field is not affected by the presence of the weakened region with respect to the healthy case. In addition, as presented in Fig. 9.14 the path lines followed by the blood particles confirm the laminar regime of the blood flow, as previously reported in Sec. 7.2.3. Figs. 9.15 and 9.16 present the arterial wall displacement in the weakened region for *Case 1* and *Case 2* at the time $t = 0.239$ s. We observe that the choice of the constitutive model induces the same side effect on the numerical solution also reported in Sec. 7.2.3. Indeed, in the case of the anisotropic (U-EXP1, EXP2-RC) law, the maximum displacement in the weakened region is attained on one side with respect to the direction of the flow, while for the isotropic case, the formation of the bulge is symmetric with respect to the flow direction.

The different displacement obtained with the two models under consideration affects the spatial distribution of the WSS. Here, for the sake of brevity, the time average of the WSS (TAWSS) over the heart beat is presented in Figs. (9.17)-(9.19). As discussed in Lee et al. [2009], the spatial distribution of the TAWSS is strongly linked to the one of the WSS and it is considered an effective indicator to study the hemodynamics inside blood vessels. As already mentioned for the cylindrical geometry, the WSS decreases in correspondence of the bulge. In particular, the WSS measured in the bulge for the isotropic

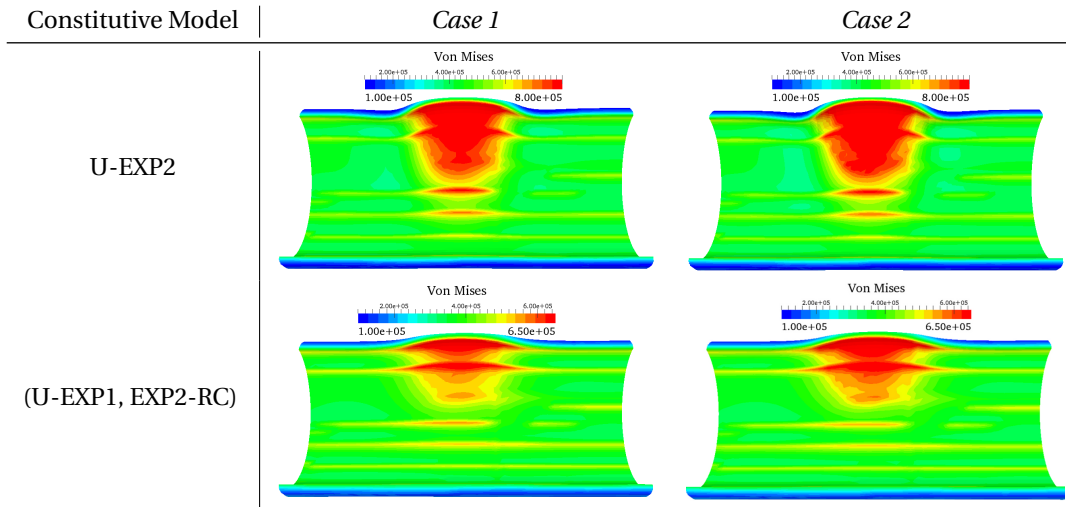


Figure 9.12: Von Mises stress at the time $t = 0.239$ s; the results are ordered by cases along the columns and the models along the rows

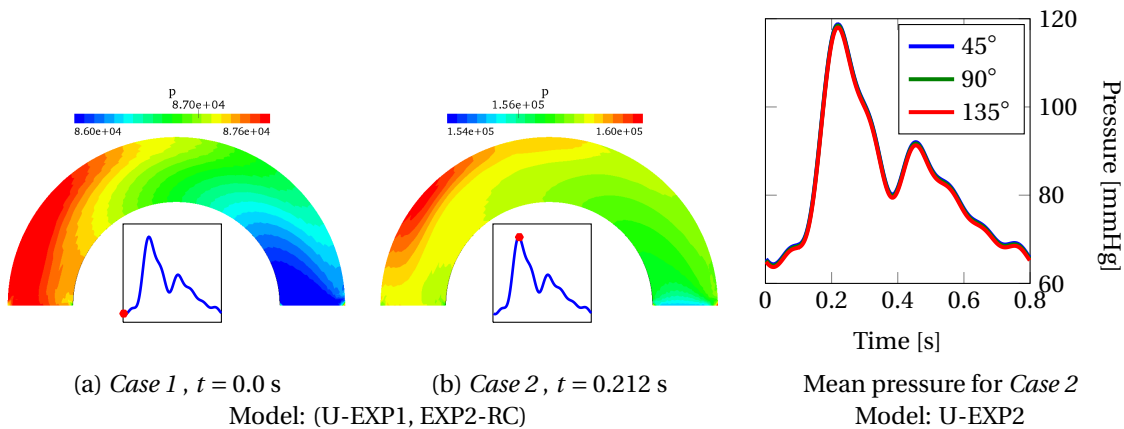


Figure 9.13: Blood pressure field in the toroidal geometry; (a) At two different times in *Case 1* for (U-EXP1, EXP2-RC) law; (b) time evolution of the blood pressure at three different sections of the fluid domain and for *Case 2* and U-EXP2 law

model is smaller than the one observed for the anisotropic one. In addition, when the anisotropic law is employed, for both cases under consideration, the spatial distribution of the time averaged WSS (TAWSS) is not symmetric with respect to the direction of the flow. In order to better present such distribution, Fig. 9.19 presents the WSS at the time $t = 0.239$ s for *Case 1* for both constitutive models.

The FSI simulations presented in this section highlighted the effects on the numerical results of the modeling choice for the arterial wall in the case of unhealthy cerebral arterial tissue. More precisely, the influence of the constitutive model for different levels of mechanical weakening has been analyzed. The simulations showed that the numerical results and the derived mechanical quantities, as WSS or Von Mises stress, are significantly influenced by the choice of the constitutive model being eventually more relevant than the level of mechanical weakening. Indeed, we have shown that the use of an isotropic model leads to an underestimation of the WSS in the weakened region with respect to the

9.2. Numerical simulations on idealized geometries of vessels

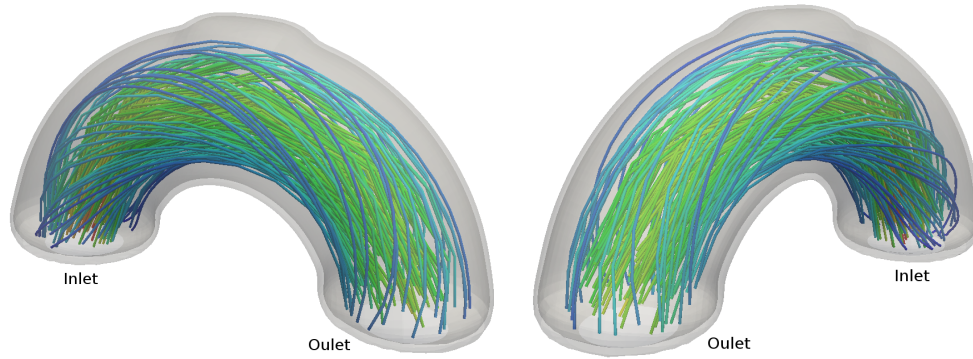


Figure 9.14: Path lines of blood flow particle during the time interval $t \in [0.35, 0.45]$ s. The blood flow particle enter in the computational domain at time $t = 0.3$ s

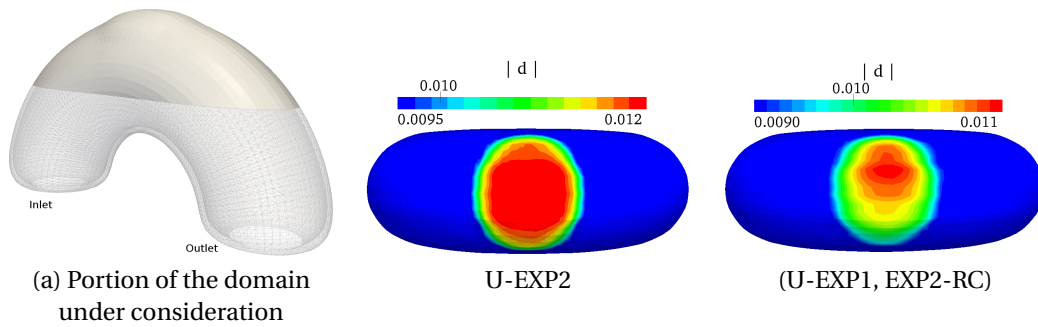


Figure 9.15: Vessel wall displacement in the weakened region for *Case 1* for the U-EXP2 and (U-EXP1, EXP2-RC) models at the time $t = 0.239$ s. Direction of the flow: from left to right

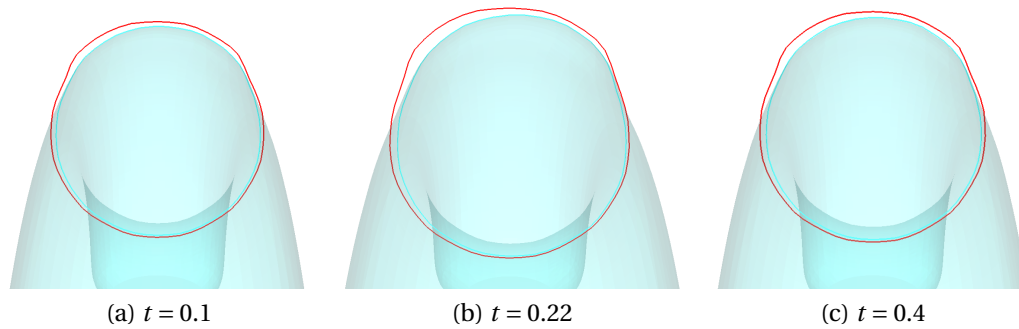


Figure 9.16: Displacement of the fluid-structure interface at three different times of the heart beat for *Case 2* with the isotropic U-EXP2 (red line) and (U-EXP1, EXP2-RC) (the light blue domain) laws at the cross section at $x = 0.138$

value obtained using the anisotropic law. This in turn, according to Bousset and McCulloch [2008], may induce a long-term mechanical degradation of the arterial tissue leading to the possible formation of a cerebral aneurysm. On the other hand, the Von Mises stress is overestimated, with respect to its counterpart obtained with the (U-EXP1, EXP2-RC) law, with the U-EXP2 model indicating different regions of the computational solid domain in which higher mechanical fatigue of the tissue may occur. This under and overestimation of important mechanical quantities can be explained by considering the larger deformations obtained with the isotropic law for both levels of mechanical weakening taken

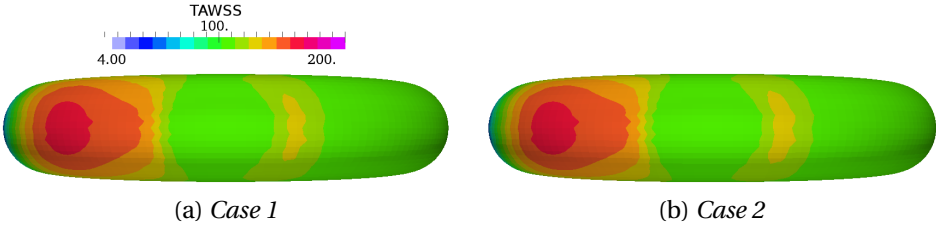


Figure 9.17: TAWSS over the heart beat for the U-EXP2 model: (a) Case 1 ; (b) Case 2

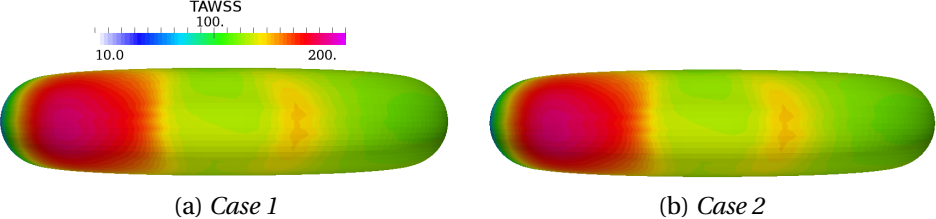


Figure 9.18: TAWSS over the heart beat for the (U-EXP1, EXP2-RC) model: (a) Case 1 ; (b) Case 2

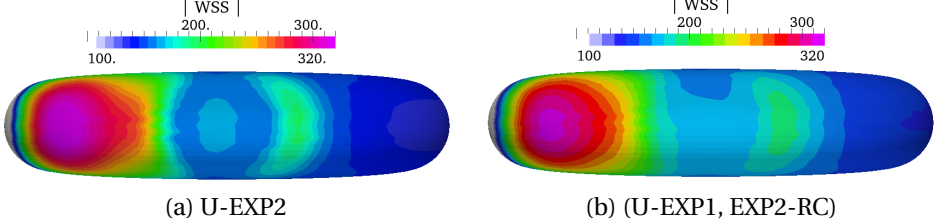


Figure 9.19: WSS at the systolic peak of the inflow profile Case 1 : (a) U-EXP2 law; (b) (U-EXP1, EXP2-RC) model

into account.

9.3 Numerical simulations on cerebral aneurysms

After having presented FSI numerical simulations on idealized blood vessels in which we considered the mechanical weakening of the arterial tissue characterizing the early stages developments of aneurysms, we now address FSI numerical simulations on idealized and anatomically realistic geometries of formed cerebral aneurysms. In order to describe the degraded mechanical properties of the aneurysmal tissue with respect to the ones of the parent vessel, the same weakening model described in Sec. 8.2 has been adopted in the analysis presented in the next sections. In particular, for the idealized geometry, the isotropic U-EXP2 and anisotropic (U-EXP1, EXP2-RC) laws are chosen to describe the weakened aneurysmal tissue; in the second case, due to the unavailability of experimental observations regarding the spatial orientation of the collagen fibers in the patient-specific domain under consideration, only the isotropic models U-EXP1 and U-EXP2 are the selected vessel wall laws. We point out that the isotropic U-EXP1 law is not employed in the numerical simulations of the idealized aneurysm since, due to the possibility of analytical description of the local alignment of the collagen fibers in the solid domain for the anisotropic law, we focus on the influence of the type of constitutive model on the numerical results rather than including different laws of the same type in the comparison. We remark that, although the strain energy function for the U-EXP1 model has not been explicitly formulated in Sec. 8.3.1, its definition can be readily obtained from the one of the U-EXP2 law by substituting in Eq. (8.9) the strain energy function of the EXP1 model $\widehat{\mathcal{W}}_{EXP1}^{iso}$ (see Sec. 4.2.1) at the place of $\widehat{\mathcal{W}}_{EXP2}^{iso}$. The computational domains that will be presented in the next sections have been created using different mesh generation softwares such as MeshLab of ISTI-CNR [2005–2014], Gmsh Geuzaine and Remacle [2009], and VMTK S. and L. [2013–2014]; Faggiano and Antiga [2014]. In particular, fluid boundary layers and flow extensions on the artificial inlet boundary of the fluid domain have been taken into account during the mesh generation process. The boundary layers have been considered in order to better capture the fluid dynamics near the arterial wall and accurately compute the WSS on the fluid-structure interface, while artificial extensions of the fluid inlet boundaries have been created in order to correctly define the parabolic profile presented in Fig. 7.1. Concerning the choice of the finite element spaces, linear $\mathbb{P}1$ elements have been used to represent all the unknowns of the FSI problem for both the idealized and realistic aneurysm. In particular, for the Navier-Stokes problem, the $\mathbb{P}1$ - $\mathbb{P}1$ pair of finite elements with IP stabilization Quarteroni and Valli [1999b] has been preferred to the pair $\mathbb{P}1$ Bubble- $\mathbb{P}1$ in order to avoid an excessive increase, with respect to the FSI simulations presented so far in this work, of the number of degrees of freedom of the fluid problem due to the presence of the boundary layer. In the following, firstly the numerical simulations on the idealized geometry of cerebral aneurysms are presented and, afterwards, the results obtained on the realistic geometry are discussed.

9.3.1 Idealized saccular aneurysm

The idealized geometry of the cerebral aneurysm considered in this section is presented in Fig. 9.20-(a). The characteristic dimensions of the parent vessels and vessel wall thickness are summarized in Tab. 9.2 together with the aspect ratio of the aneurysm and the number of elements of the fluid and solid meshes for which the corresponding number of degrees of freedom of the FSI monolithic problem is 922,781.

The dimensionless parameters for the two constitutive models under consideration have been set up by following the same approach discussed in Sec. 8.3.1. In particular, in this section, we consider the EXP2 law as the reference model for which a known value of the dimensionless parameter D is fixed; then, the weakening parameter D for the isotropic part of the (EXP1, EXP2-RC) law is computed with

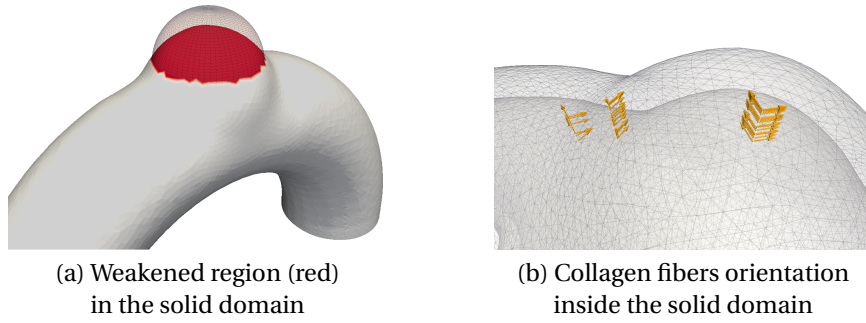


Figure 9.20: Weakened region and collagen fibers orientation in the solid domain for the idealized aneurysm

Characteristic dimensions		Computational domains	
Aspect ratio (AR) [-]	0.66	Fluid domain:	630,853 elements
Diameter inlet surface [cm]	0.066	Solid domain:	236,256 elements
Diameter outlet surface [cm]	0.066	Wall thickness [cm]:	0.01
(a)		(b)	

Table 9.2: Details of the characteristic dimensions and of fluid and solid triangulations of the idealized geometry of cerebral aneurysm under consideration

Constitutive model	Weakening parameter D	Material Parameters for weakened tissue
U-EXP2	0.25	$\alpha_2 = 5.116 \cdot 10^4, \gamma_2 = 0.061$
(U-EXP1, EXP2-RC)	0.75	$\alpha_1 = 4.367 \cdot 10^3, \gamma_1 = 0.862$

Table 9.3: Parameters for the U-EXP2 law and for the isotropic part of the (U-EXP1, EXP2-RC) model in the weakened region presented in Fig. 9.20-(a). The material parameters for the healthy portion of the solid domain are presented in Tabs. 5.3 and 5.5

respect to a fixed value of blood pressure. The choice of the EXP2 model as reference law is motivated by the better fitting of the experimental measurements presented in Sec. 5.4.1 obtained with such law with respect to the one reported for the anisotropic (EXP1, EXP2-RC) model. The fixed value of D for the U-EXP2 model in the weakened portion of the solid domain in Fig. 9.20-(a) is reported in Tab. 9.3. Its value has been set according to the study carried out in Wire et al. [2003]. More precisely, the cerebral aneurysms considered in Wire et al. [2003] have been grouped in four categories according to the measured aspect ratio (AR). For the sake of simplicity in fixing the reference level of mechanical weakening for the EXP2 law, we have associated to each group presented in Wire et al. [2003] a constant value of D . Since the aneurysm under consideration belongs to the first group of Wire et al. [2003] for which $AR \leq 1.4$, a known level of weakening $D_{ref}^{EXP2} = 0.25$ is assumed to affect the mechanical properties of the healthy tissue inside the aneurysm dome. Afterwards, the parameter $D_{EXP1}^{EXP2-RC}$ for the isotropic part of the (U-EXP1, EXP2-RC) law has been set with respect to the reference value of blood pressure of $p = 90$ mmHg. The stress-strain curves for the U-EXP2 and (U-EXP1, EXP2-RC) laws are presented in Fig. 9.21. The material parameters for the unhealthy arterial tissue are presented in Tab. 9.3. It is worth pointing out that, for the (U-EXP1, EXP2-RC) model, the local alignment of the

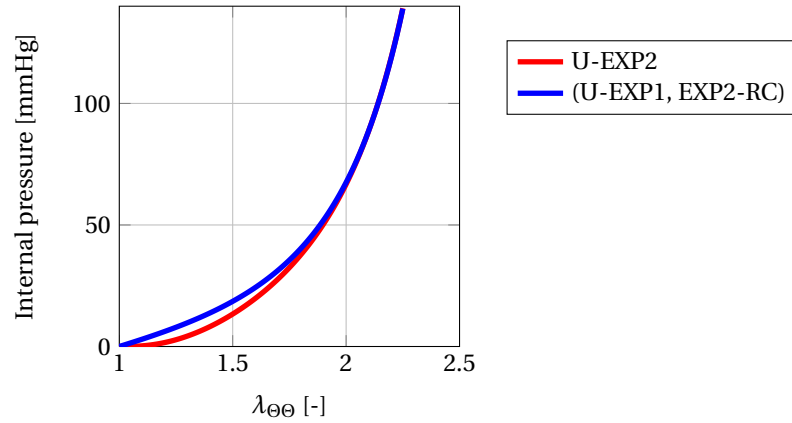


Figure 9.21: Stress-strain relations for the U-EXP2 and (U-EXP1, EXP2-RC) models for the weakened aneurysmal tissue in Fig. 9.20

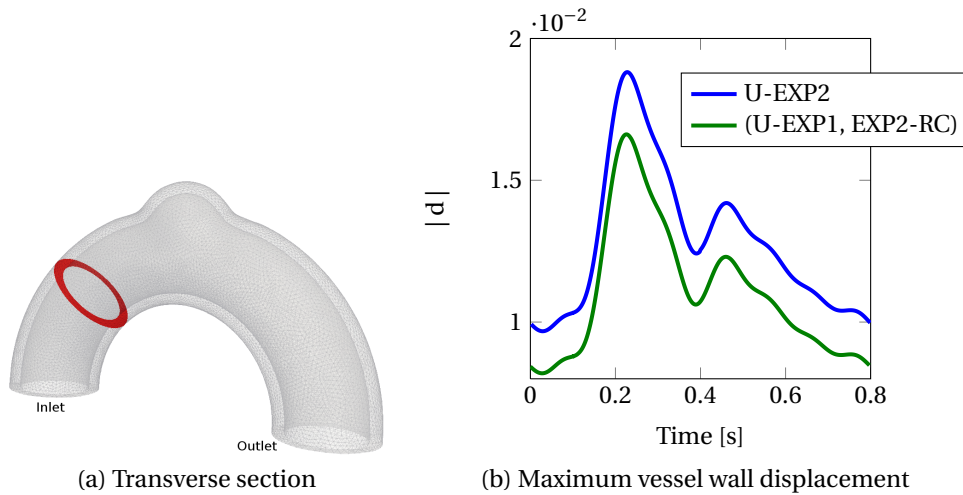


Figure 9.22: Maximum displacement magnitude [cm] on the internal surface of the solid domain on a transverse section of the parent vessel for the U-EXP2 and (U-EXP1, EXP2-RC) laws

collagen fibers determined in Sec. 5.4.1, and employed in Ch. 7.2.3 and Sec. 9.2, has been considered also for the current application. The collagen fibers are assumed to be aligned in the tangential plane of the vessel wall both in the parent vessel and the aneurysm dome, are reported in Schriefel [2012] and presented in Fig. 9.20-(b). As in the previous FSI simulations of Sec. 9.2, elastic Robin boundary conditions for which $K = 1.2 \cdot 10^7 \text{ dyn/cm}^3$, and $K_D = 0.8K$ in the weakened region in Fig. 9.20-(a), are applied on the external surface of the solid domain. Regarding the fluid domain, the parabolic velocity profile considered in Sec. 7.2 and a resistance boundary condition with coefficient $R = 9.0 \cdot 10^6 \text{ dyn} \cdot \text{s} / \text{cm}^5$ are applied on the inlet and outlet surfaces, respectively. As presented in Figs. (9.22)-(9.28), these boundary conditions for the fluid and solid domains ensure a physiological variation of the vessel wall diameter as well as physiological values of blood pressure during the heart beat with both constitutive models. We remark that the numerical simulation of two heart beats is needed in order to overcome the initial transitory phase due to the initialization of the simulation and reach the periodic regime during the cardiac cycle.

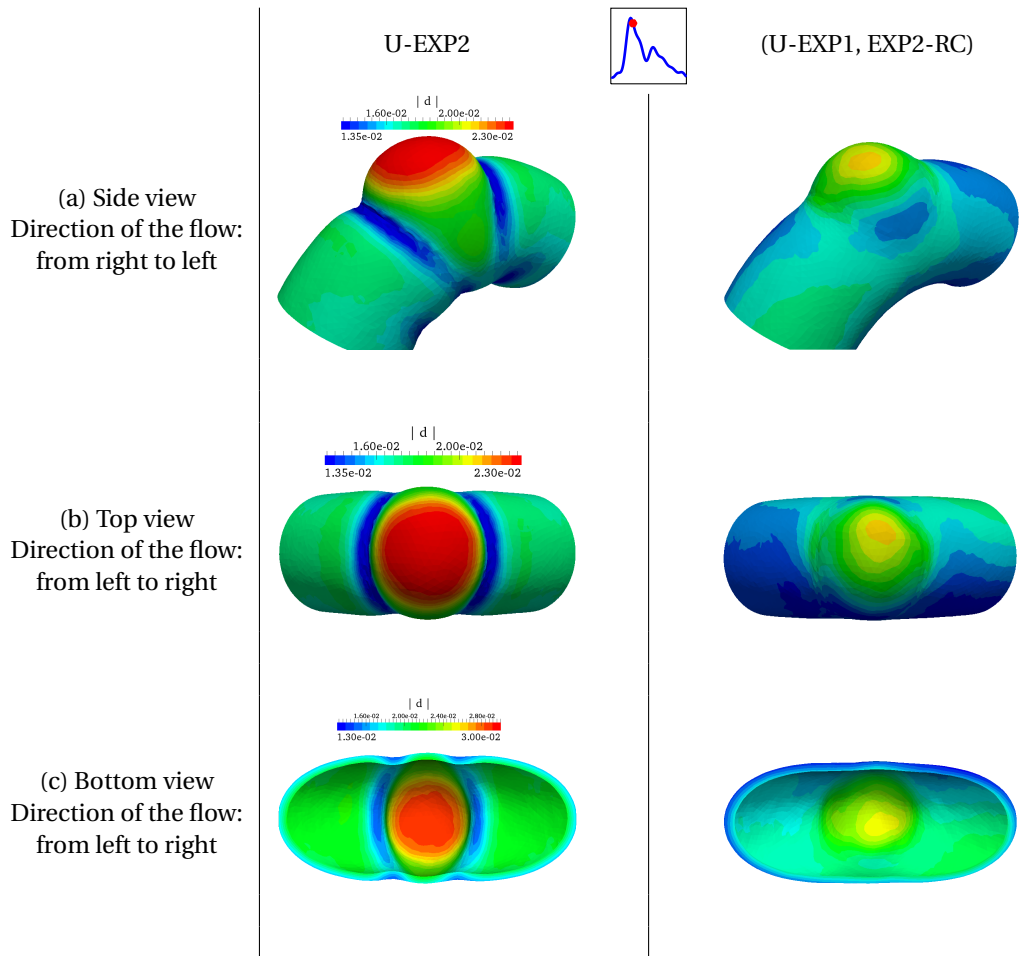


Figure 9.23: Different views of the vessel wall displacement magnitude [cm] at the time $t = 0.239$ s. First row: U-EXP2 law; Second row: (U-EXP1, EXP2-RC) model. The different color scale in (c) with respect to (a) and (b) is used to highlight the different levels of displacement on the internal surface of the vessel wall

We first present the deformations of the arterial wall during the heart beat and then we address the influence on the blood flow dynamics of the blood vessel constitutive model. Indeed, as it will be discussed in the following, the blood flow dynamics observed in this type of application is mainly driven by the vessel wall deformations. Fig. 9.22- (b) presents the maximum wall displacement magnitude measured on the internal surface of the solid domain at the cross section presented in Fig. 9.22-(a). Similarly to what has been reported in Sec. 7.2.3 on the toroidal geometry, a physiological displacement of the parent vessel during the heart beat is obtained in this case as well. In addition, we observe that the displacement of the parent vessel in the case of the U-EXP2 law is 10% higher than the one obtained with the the (U-EXP1, EXP2-RC) law; such difference is consistent with the results presented in Sec. 7.2 for geometries with the same characteristic dimensions. The vessel wall displacement at the time $t = 0.239$ s is shown in Fig. 9.23. Fig. 9.23 focuses on the vessel wall displacement of a central cut of the solid domain; as presented in Figs. 9.23-(b) and 9.23-(c), for both models the highest vessel wall displacements are obtained in correspondence of the weakened portion of the solid domain, see Fig. 9.20-(a); nevertheless, the two solutions present significant differences. The displacement around the aneurysm is strongly affected by the higher deformations occurring in the top part of the dome

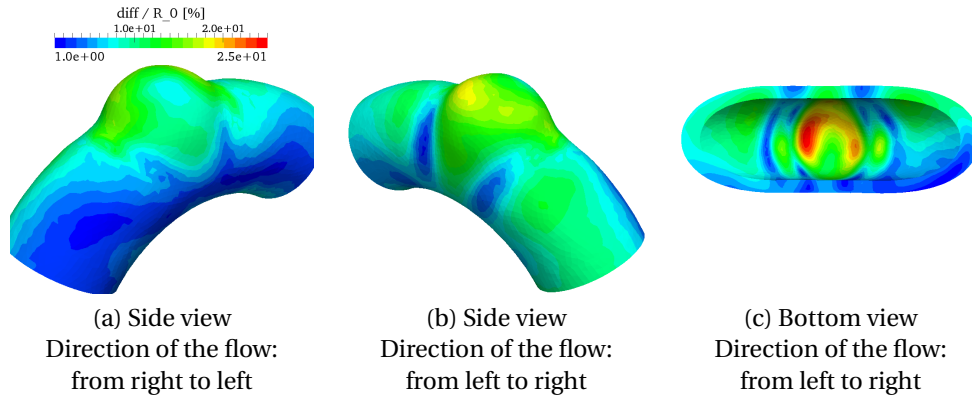


Figure 9.24: Relative difference of the two solutions presented in Fig. 9.23 with respect to the undeformed parent vessel internal radius R_0 at the time $t = 0.239$ s

due to the mechanical weakening, especially when the isotropic U-EXP2 model is employed. More precisely, for this law, two rings of lower displacement at the neck of the aneurysm are originated due to the deformation of the parent vessel along the radial direction, as previously reported in Sec. 7.2.3, and to the enlargement of the dome. On the other hand, in the case of the anisotropic model, the asymmetric displacement already observed in Secs. 7.2.3 and 9.2 is again obtained and it involves the aneurysm dome. Consequently, in Fig. 9.23-(a), a region of lower displacement is observed at the basis of the aneurysm when such law is employed. However, we remark that for the anisotropic law, the strong inhomogeneous deformation around the dome, especially along the direction of the flow presented for the isotropic one, is not reported. This difference can be entirely ascribed to the choice of the constitutive model; in particular, to the smaller displacements attained with the (U-EXP1, EXP2-RC) law with respect to the U-EXP2 model due to the fact that the collagen fibers, which are the stiffest constituents of the arterial tissue, are supposed to be mechanically intact.

In order to better evaluate the impact of the constitutive model on the vessel wall displacement, the relative difference of the two solutions measured with respect to the undeformed parent vessel internal radius has been computed and it is presented in Fig. 9.24. We remark that the choice of measuring the relative difference with respect to the undeformed parent vessel internal radius, rather than with respect to the maximum displacement observed with the two constitutive laws as in Torii et al. [2008], is motivated by the need of a fair comparison of the two different numerical results. The highest difference is around 25% and it occurs on the internal surface of the aneurysm dome. The differences reported in the vessel wall displacement persist during the whole cardiac cycle. Figs. 9.25 and 9.26 present the vessel wall displacement at the time $t = 0.7$ s, namely during the diastolic phase. The same qualitative behavior of the solution with respect to the one presented in Fig. 9.23 is obtained and, therefore, the relative difference of the two displacements fields, shown Fig. 9.26, is similar to the one of Fig. 9.24. In the following, it will be shown that the differences in the vessel wall displacements induce significant different blood flow patterns during the cardiac cycles.

Fig. 9.27 shows the minimum value of the blood pressure obtained in the fluid domain during the heart beat at the time $t = 0.026$ s. Although the similar spatial distribution of p inside the parent vessel for the two constitutive laws, significant differences must be reported inside the aneurysm dome. Indeed, as presented in Figs. 9.27-(a) and 9.27-(c), for the isotropic U-EXP2 model, the blood pressure inside the dome is higher than its counterpart obtained with the anisotropic law, especially in the downstream portion of the dome. Such difference is strongly related to the deformations of the arterial

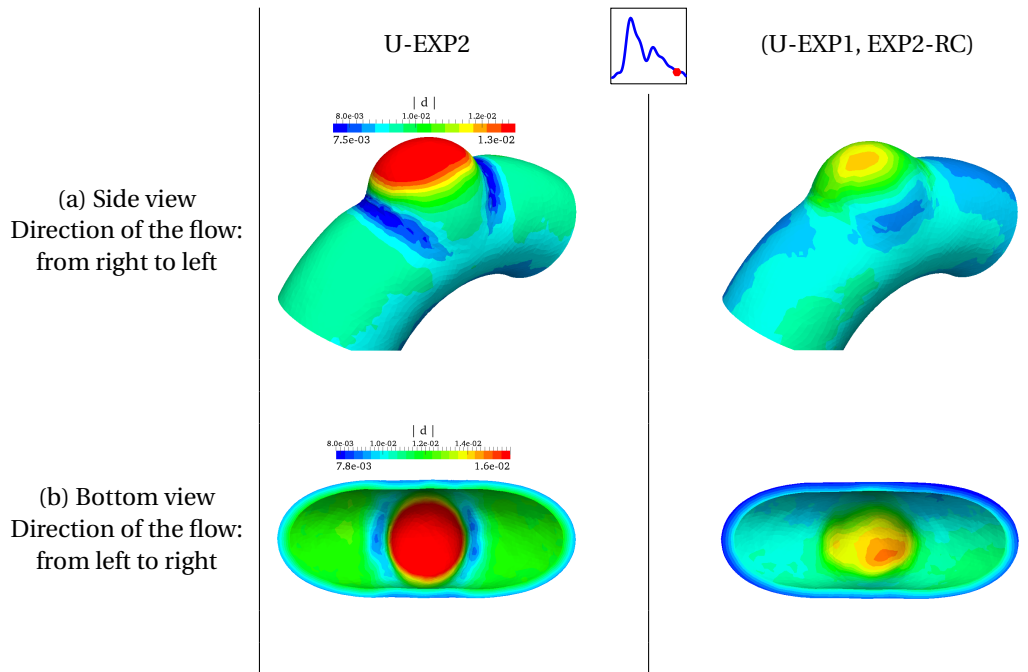


Figure 9.25: Different views of the vessel wall displacement magnitude [cm] at the time $t = 0.7$ s. First row: U-EXP2 law; Second row: (U-EXP1, EXP2-RC) model. The different color scale in (b) with respect to (a) is used to highlight the different levels of displacement on the internal surface of the vessel wall

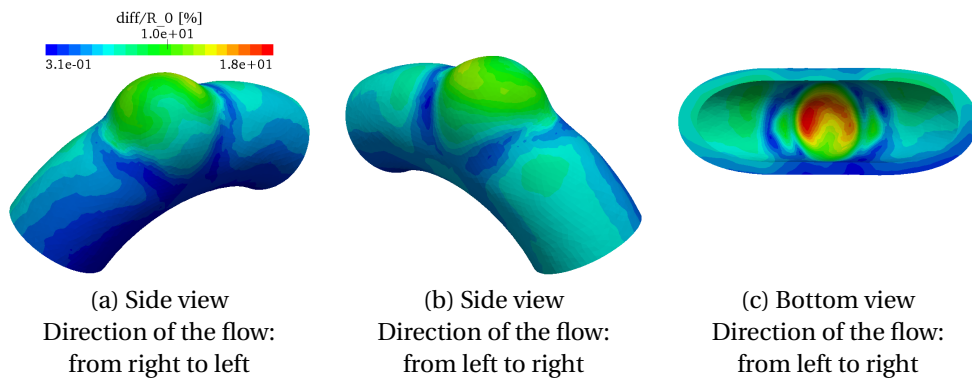


Figure 9.26: Relative difference of the numerical solutions presented in Fig. 9.25 with respect to the undeformed parent vessel internal radius R_0 at the time $t = 0.7$ s

wall in that portion of the domain and to the consequent blood flow recirculation inside the aneurysm dome during the heart beat. Indeed, the enlargement of the aneurysm dome induces flow impingement in that part of the dome. On the other hand, at the time $t = 0.212$ s, i.e. at the systolic peak of the inflow velocity profile, the blood pressure obtained with the two constitutive models presents important differences in its spatial distribution over the whole fluid domain. Indeed, as reported Fig. 9.28-(a) the blood pressure downstream the aneurysm obtained with the isotropic model is around 10% smaller than the one measured with the anisotropic law. Furthermore, when the U-EXP2 model describes the vessel wall, two regions of low pressure are generated by the deformations of the aneurysm around the dome in the direction of the blood flow, as in Figs. 9.28-(a) and 9.28-(c), while a uniform pressure field is obtained with the (U-EXP1, EXP2-RC) law. Regarding the part of the fluid domain located upstream

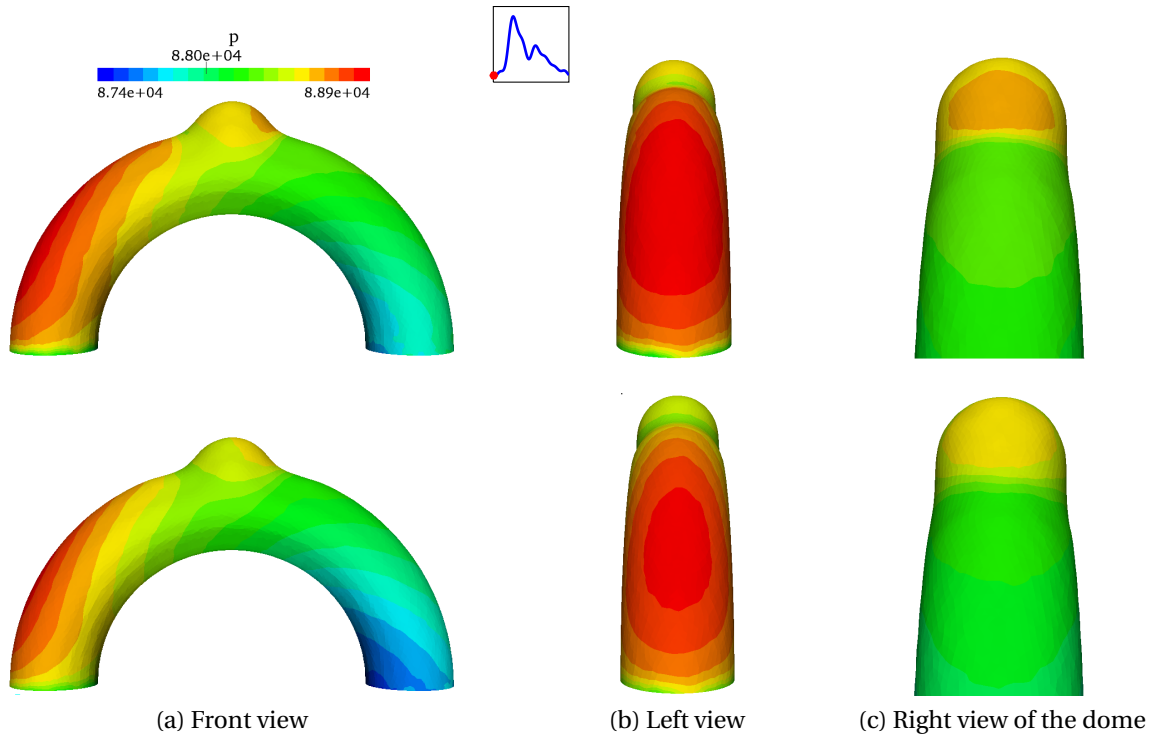


Figure 9.27: Blood pressure [dyn/cm²] inside the fluid domain at time $t = 0.026$ s for different views. First row: U-EXP2 model; second row: (U-EXP1, EXP2-RC) law

the aneurysm in Figs. 9.28-(a) and 9.28-(b), we remark that the deformations of the parent vessel at that location (see Fig. 9.22) explain the two different extensions of the high pressure regions: the higher is the parent vessel displacement, the smaller is the region of high pressure.

Strong flow recirculation inside the dome characterizes the blood flow inside the aneurysm dome for the isotropic law, as shown in Fig. 9.29-(a); on the other hand, we notice in Fig. 9.30 that the blood flow recirculation is observed only in the upstream part of the aneurysm in the case of the (U-EXP1, EXP2-RC) law. As reported in Fig. 9.29-(a), the systolic phase of the blood flow for the U-EXP2 model is characterized by the impingement of the blood particles against the internal surface of the vessel wall and the consequent recirculation inside the aneurysm. Afterwards, once the blood flow particles have reached the upstream part of the dome, they leave the aneurysm and exit the fluid domain. For the (U-EXP1, EXP2-RC) law such extended region of flow recirculation is not observed; indeed, as it can be noticed in Fig. 9.29, the blood flow in the downstream part of the aneurysm is driven by the mainstream flow in the parent vessel due to the lower and more uniform displacement of the dome. However, flow recirculation occurs also for the (U-EXP1, EXP2-RC) model; indeed Fig. 9.30 shows a small recirculation region in the upstream part of the aneurysm, as reported. As it will be discussed hereafter, the significant differences in the blood particles pathlines between the two numerical simulations will strongly affect the spatial distribution of hemodynamical indicators such as the WSS. This points out the relevance of adequately choosing the constitutive model for the arterial tissue when computational studies of cerebral aneurysms are addressed. It is worth noticing that, with both constitutive models, the particle path lines indicate that once the blood particles have left the dome, they reach the outlet surface of the fluid domain following path lines close to the fluid-structure interface; this is due to the fact that the blood flow velocity in the parent vessel is much higher than the one of the particles leaving the dome.

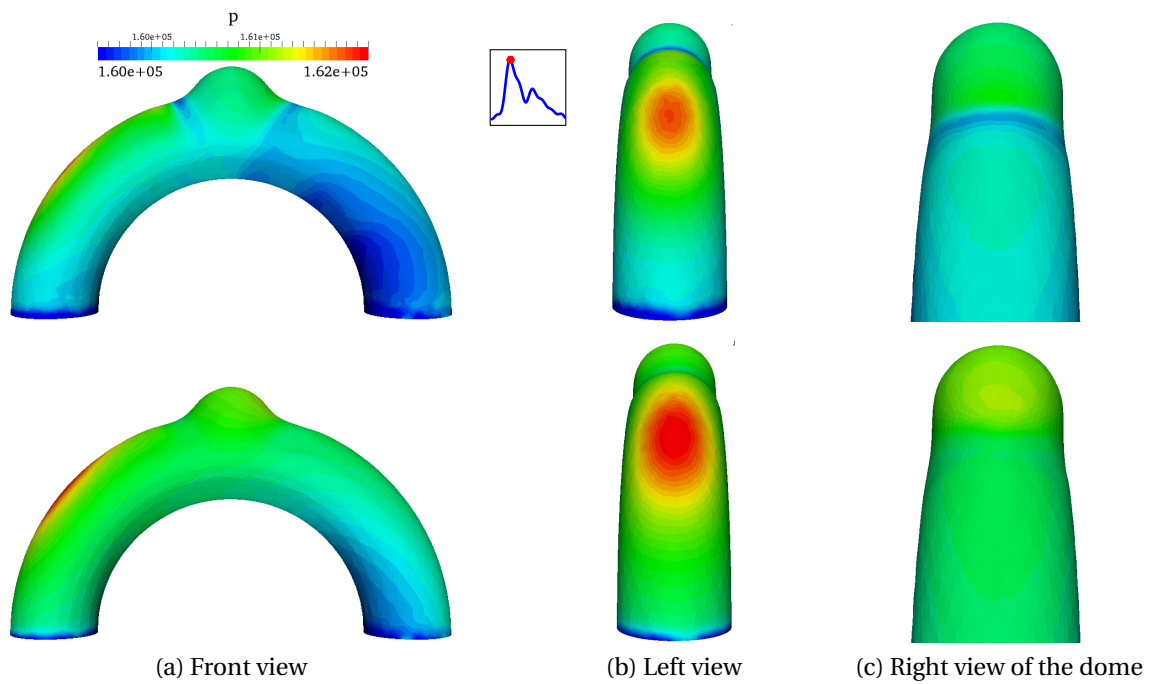


Figure 9.28: Blood pressure [dyn/cm²] inside the fluid domain at time $t = 0.212$ s for different views. First row: U-EXP2 model; Second row: (U-EXP1, EXP2-RC) law

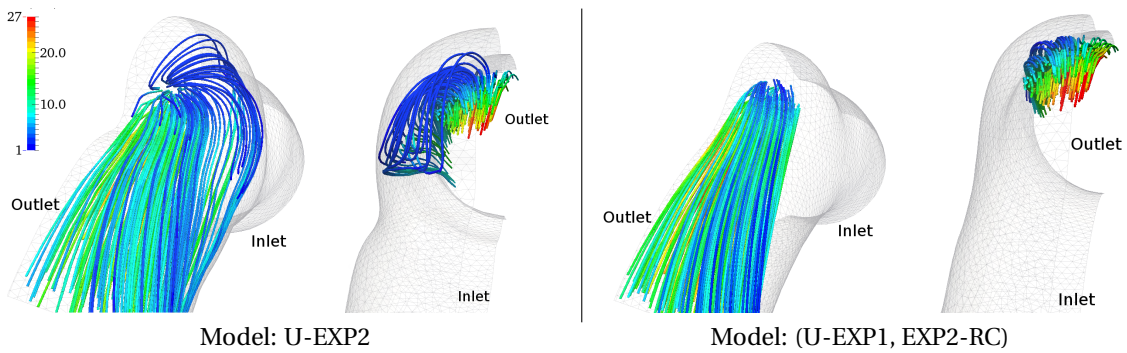


Figure 9.29: Blood flow particle path lines colored according to the blood velocity during the systolic phase of the heart beat for $t \in [0.15, 0.25]$ s for both constitutive models in the deformed fluid domain

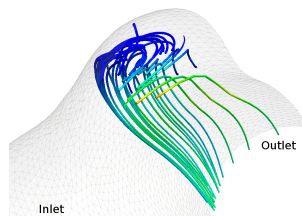


Figure 9.30: Flow recirculation inside the aneurysm dome during the systolic phase of the heart beat for $t \in [0.15, 0.25]$ s for the (U-EXP1, EXP2-RC) model.

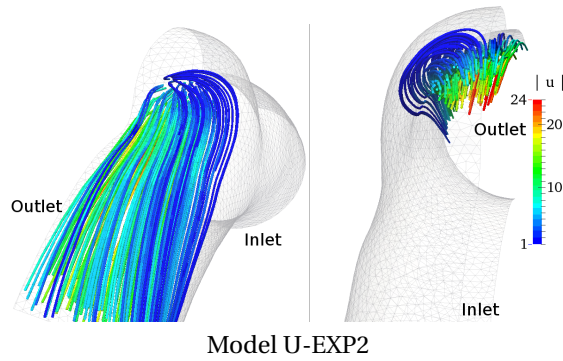


Figure 9.31: Blood flow particle path lines colored according to the blood velocity during the systolic phase of the heart beat for $t \in [0.6, 0.8]$ s for the U-EXP2 model in the deformed fluid domain

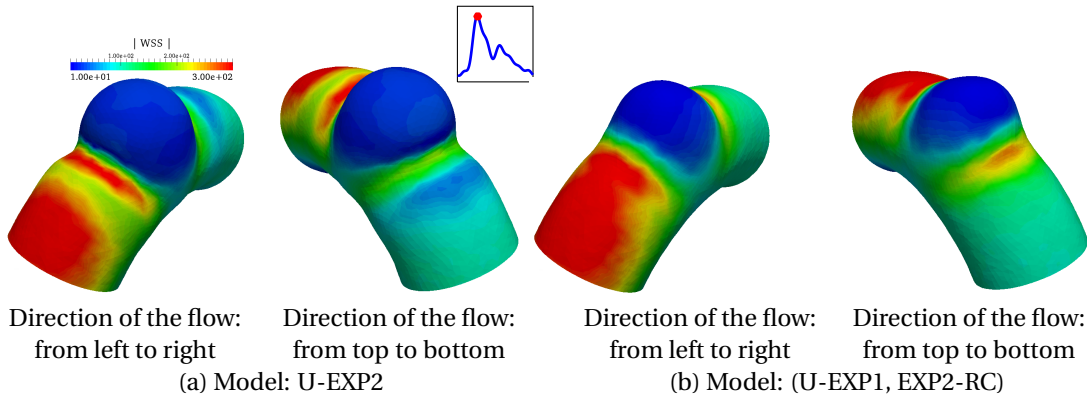


Figure 9.32: WSS magnitude [dyn/cm^2] at the systolic peak at time $t = 0.212$ s of the cardiac cycle

During the diastolic phase, i.e. for $t = [0.6, 0.8]$ s, the recirculation inside the dome decreases for both constitutive models; for this reason, Fig. 9.31 shows only the blood particle path lines obtained in the case of U-EXP2 model being those obtained with the (U-EXP1, EXP2-RC) law similar.

As a consequence of the different vessel wall deformations and blood flow dynamics inside the aneurysm, the WSS in the dome is strongly affected by the choice of the constitutive model. Figs. 9.32 and 9.33 show the WSS in the portion of fluid domain corresponding to the central cut of the solid domain presented for instance in Fig. 9.23. The values of WSS in the parent vessel are consistent with the ones presented in Fig. 9.19 obtained at the same instant of the heart beat for a similar test. For both constitutive models, the high WSS located upstream the dome is due to the fact that part of the fluid-structure interface is close to the impingement area of the blood inflow, as previously presented in Fig. 7.28. In Figs. 9.32-(a) and 9.33-(a) we observe significant local variations in the WSS magnitude around the dome related to the vessel wall displacement presented in Fig. 9.23. Similarly, the WSS distribution obtained in the case of the (U-EXP1, EXP2-RC) model can be explained mainly in terms of the vessel wall deformations. It should be mentioned that, as expected, a region of low WSS is measured in correspondence of the dome for both simulations due to the flow recirculation. However, by comparing the results shown in Figs. 9.32 and 9.33, we report that the WSS magnitude inside the aneurysm for the U-EXP2 law is significantly higher than the one obtained with the (U-EXP1, EXP2-RC) model, especially in the downstream part of the dome. In order to better present the two different time evolution of the WSS inside the dome, Fig. 9.34 shows the WSS magnitude during the cardiac cycle at two different points in the dome. At the first point, the maximum WSS measured with the isotropic

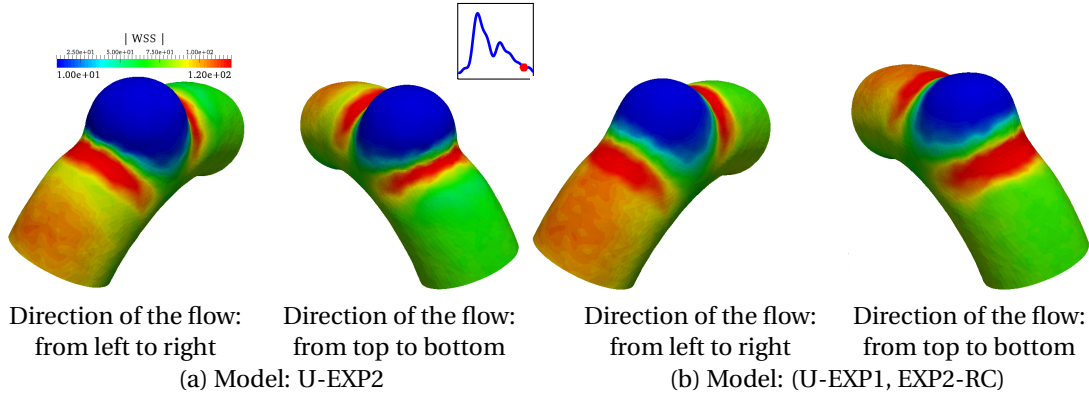


Figure 9.33: WSS magnitude [dyn/cm²] at the time $t = 0.7$ s of the cardiac cycle

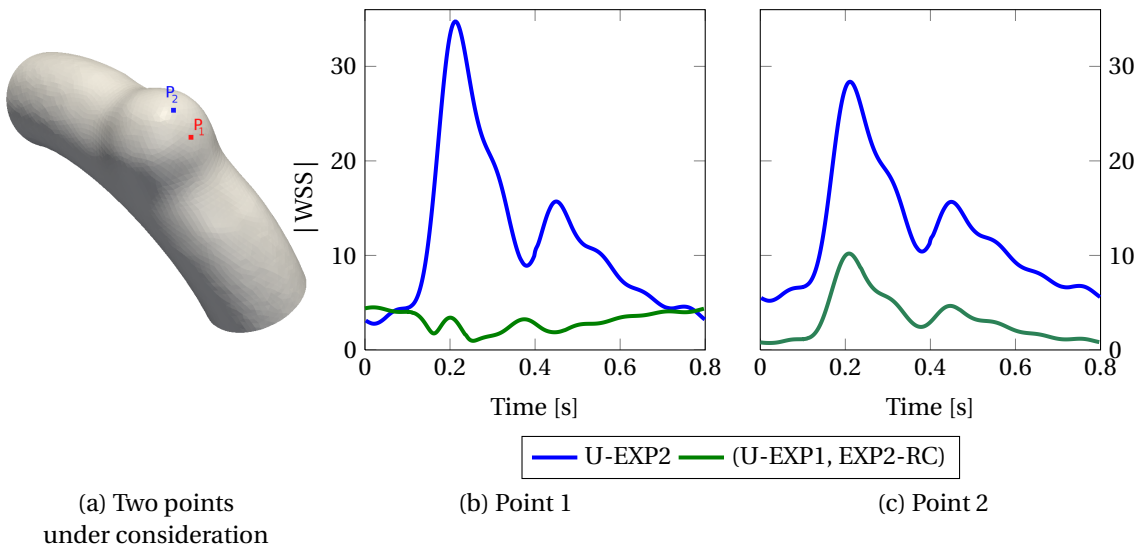


Figure 9.34: WSS magnitude [dyn/cm²] at two different points of the dome during the heart beat

U-EXP2 law is 10 times higher than its counterpart obtained with the anisotropic law. Such difference is reached during the systolic phase of the cardiac cycle during which, for the U-EXP2 model, the blood flow impinges the dome surface at the point under consideration, while, as already discussed for Fig. 9.29, the blood flow presents completely different features for the (U-EXP1, EXP2-RC) law. On the other hand, the differences between the two WSS fields are reduced close to the beginning and the end of the cardiac cycle; this is due to the reduced wall deformations and flow recirculation for both laws, see Figs. 9.25 and 9.29. Concerning the second point P_2 in the dome under consideration, we remark that the highest WSS obtained with the U-EXP2 model is 3 times higher than the one measured with the (U-EXP1, EXP2-RC) law. The smaller difference in Fig. 9.34-(c) compared to the ones in Fig. 9.34-(b) of the two WSS fields can be ascribed to the fact that the point P_2 is outside of the impingement area for the U-EXP2 and that a regime of flow recirculation is present in both cases; however, the constitutive model strongly affects the prediction of such important hemodynamical indicator. The differences in the WSS prediction computed from the two simulations are highlighted in Fig. 9.35. Indeed, it shows the time averaged WSS in the aneurysm dome. Differently from what has been reported for the toroidal geometry in Fig. 9.19, for the (U-EXP1, EXP2-RC) law, in the case of a developed cerebral aneurysm, the asymmetric displacement of the vessel wall does not induce an asymmetric distribution of the WSS

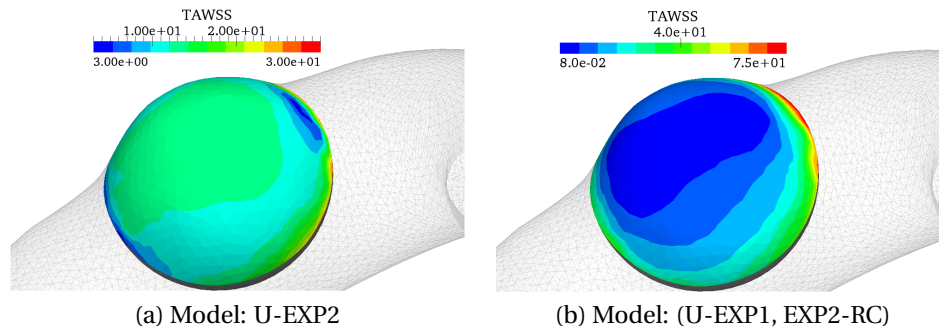


Figure 9.35: Time Averaged WSS on the aneurysm dome for the two constitutive models under consideration

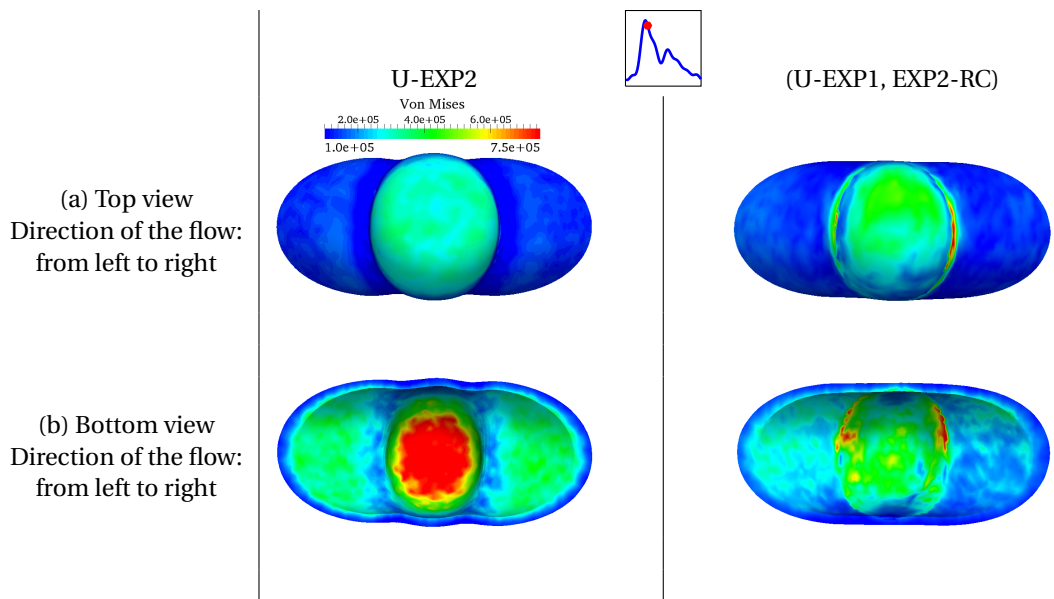


Figure 9.36: Von Mises stress at the systolic peak in the heart beat. Direction of the flow: from left to right

inside the aneurysm.

Fig. 9.36 displays the spatial distribution of the Von Mises stress at the systolic peak at the time $t = 0.212$ s. We remark that, with the U-EXP2 law, the highest Von Mises stresses are obtained in the dome, where the highest displacements are achieved as well. However, the spatial distribution of the Von Mises stress in the case of the isotropic model is symmetric with respect to the center line of the domain, while for the (U-EXP1, EXP2-RC) the asymmetry highlighted in the displacement field induces a similar asymmetry in the Von Mises. In particular, on the external surface the highest values of Von Mises are reached in correspondance to the highest displacements, see Fig. 9.23. It is worth pointing out that, the values of Von Mises stress obtained with the anisotropic model on the internal surface of the dome are 30% smaller than the ones measured with the U-EXP2 law; this is an important difference between the two models that must be taken into account when considering the progressive degradation, due to mechanical fatigue, of the arterial tissue over many cardiac cycles.

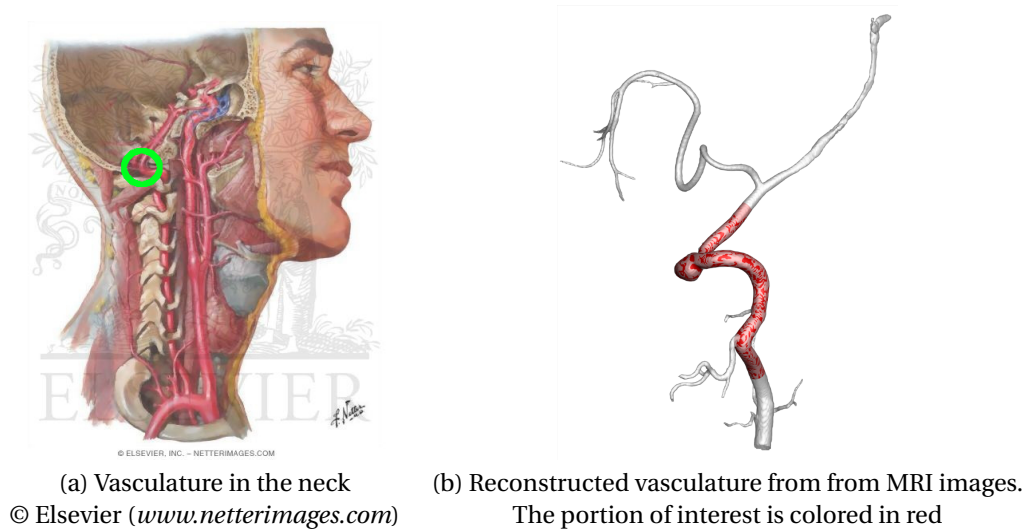


Figure 9.37: Representation of the vascular network in the neck and of the portion of interest

Characteristic dimensions		Computational domains	
Aspect ratio [-]	1.11	Fluid domain:	1,013,977 elements
Diameter inlet surface [cm]	0.48	Solid domain:	452,196 elements
Diameter outlet surface [cm]	0.3	Wall thickness [cm]:	0.033
(a)		(b)	

Table 9.4: Details of the characteristic dimensions and of the spatial discretization of the reconstructed anatomically realistic geometry of aneurysm presented in Fig. 9.37

9.3.2 Anatomically realistic geometry of saccular aneurysm

The anatomically realistic cerebral aneurysm under consideration is presented in Fig. 9.37-(b). The vascular network reconstructed from the acquired MRI images and the diameter of the parent vessel suggest that the aneurysm in Fig. 9.37-(b) has occurred on the vertebral artery and specifically in the curved region highlighted in Fig. 9.37-(a). Tabs. 9.4-(a) and (b) summarize the main information regarding the characteristic dimensions of reconstructed vessel lumen surface as well as the dimensions of the fluid and solid computational domains. We remark that with the choice of linear finite elements for the unknowns of the FSI problem (particularly $\mathbb{P}1$ - $\mathbb{P}1$ elements with IP stabilization for the Navier-Stokes equations) the number of degrees of freedom of the FSI monolithic problem is 1,550,399. Figs. 9.38-(a) and 9.38-(b) show the high quality triangulation of the fluid domain and fluid boundary layer resulting from the mesh generation process Crosetto [2011]; Faggiano and Antiga [2014]. Fig. 9.38-(c) details the portion of the solid domain that is considered as mechanically weakened with respect to the parent vessel, which is considered mechanically intact. It can be observed that the weakened region in the solid domain consists only of the aneurysm dome in order to take into account the lower mechanical strength of the aneurysmal tissue located at the fundus with respect to the tissue composing the neck of the aneurysm Humphrey and Canham [2000].

As already discussed in the previous sections, among the boundary conditions for the FSI problem, we recall that the resistance and the elastic Robin boundary conditions on the outlet and external surfaces of the fluid and solid domains, respectively, have been set in order to have physiological

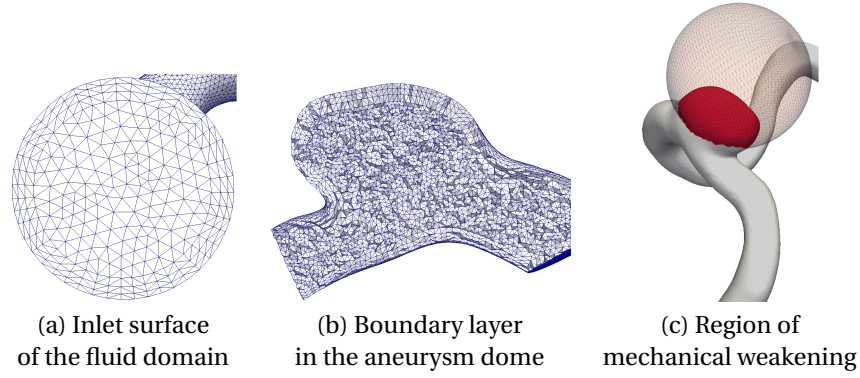


Figure 9.38: Details of the boundary layer in the fluid domain and of the region of mechanical weakening in the arterial wall

Constitutive model	Material Parameters for healthy tissue	Weakening parameter D	Material Parameters for weakened tissue
U-EXP2	$\alpha_2 = 5.811 \cdot 10^6, \gamma_2 = 4.080$	0.25	$\alpha_2 = 4.410 \cdot 10^6, \gamma_2 = 4.080$
U-EXP1	$\alpha_1 = 4.470 \cdot 10^5, \gamma_1 = 8.35$	0.15	$\alpha_1 = 3.799 \cdot 10^5, \gamma_1 = 8.350$

Table 9.5: Parameters for the EXP1 and EXP2 models for the healthy arterial tissue, weakening parameter and corresponding parameters of the U-EXP1 and U-EXP2 laws

variations of important quantities of interest; for instance the peak-to-peak amplitude of the blood pressure and the variations in the vessel wall diameter during the heart beat. More precisely, a resistance coefficient $R = 1.455 \cdot 10^4 \text{ dyn} \cdot \text{s} / \text{cm}^5$, corresponding to a peak-to-peak amplitude of the blood pressure of 40 mmHg, and an elastic coefficient $K = 1.2 \cdot 10^7 \text{ dyn/cm}^3$ for the Robin boundary conditions have been chosen. In addition, in the weakened region, we fix $K_D = 0.8K$. The material parameters for the EXP1 and EXP2 isotropic models for the healthy parent vessel and aneurysmal wall are provided in Tab. 9.5. We remark that, the material parameters for the EXP1 law describing healthy arterial tissue have been taken from Delfino et al. [1997] for the carotid artery, whose diameter is similar to the one of vertebral arteries. We have assumed that the constitutive stress-strain relation characterizing the mechanical response of the healthy tissue is of the form $\mathcal{T} = \mathcal{T}(\lambda_{\Theta\Theta})$ as in Eq. (5.35) for a vessel of undeformed internal radius of $r_0 = 0.2 \text{ cm}$. Such assumption is justified by the fact that, as presented in Ch. 7 and Sec. 9.1, the main deformations of the parent vessel lay along the radial direction. Prior to setting the weakening parameters for the two isotropic models under consideration, the second order exponential EXP2 law for the healthy tissue must be adequately calibrated. In this work, the material parameters for the healthy tissue described by the EXP2 law have been determined such that the stress-strain relations $\mathcal{T}_{EXP1}(\lambda_{\Theta\Theta})$ and $\mathcal{T}_{EXP2}(\lambda_{\Theta\Theta})$ intersect at the values of internal pressures of 40 and 100 mmHg. Afterwards, we determine the weakening parameters D_{EXP1} and D_{EXP2} following the same approach described in Sec. 9.3.1. Similarly to Sec. 9.3.1, the reference value of D with respect to which the other one is computed is $D_{ref} = D_{EXP2} = 0.25$, due to the small aspect ratio of the aneurysm under consideration. Afterwards, the dimensionless parameter $D_{EXP1} = 0.15$ has been computed with respect to the reference value of blood pressure of $p = 90 \text{ mmHg}$. Fig. 9.39 presents the stress-strain relations for the U-EXP1 and U-EXP2 models; we observe that the two curves predict a very similar mechanical response on the range of internal pressures of interest, i.e. $p \in [60, 110] \text{ mmHg}$, that is the physiological one.

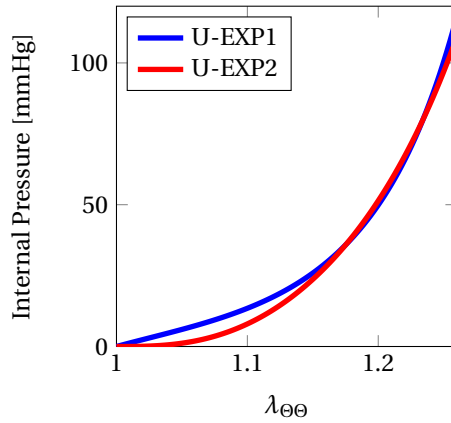


Figure 9.39: Stress-strain relations for the U-EXP1 and U-EXP2 models

We remark that, for the test under consideration, the numerical simulation of at least two heart beats is required to reach the periodic evolution of the blood flow. Figs. 9.40 and 9.41 present the blood pressure when the maximum displacement of the parent vessel is attained, namely at the time $t = 0.239$ s. We observe that the highest differences in the two pressure fields predicted with the two models occur inside the dome, especially along the transverse direction to the blood flow, as presented in Fig. 9.40-(c); on the other hand, similar qualitative behavior of the blood pressure distribution in the parent vessel is reported for the two cases under consideration. However, the highest difference is around the 0.45% of the blood pressure reported inside the aneurysm dome. As it will be discussed hereafter, this result suggests that, when considering constitutive models of the same type (i.e. nonlinear isotropic), the blood flow dynamics is not significantly affected by the choice of the constitutive model for the tissue. Fig. 9.41 details the blood pressure inside the aneurysm dome. As it can be observed, for both cases, the highest value is reached in correspondence of the impingement area of the blood flow; nevertheless, differences in the spatial distribution of the pressure field obtained with the two constitutive laws must be reported. Fig. 9.42 shows the blood pressure at the time $t = 0.026$ s, when the blood pressure reaches its minimum value; similarly to Fig. 9.40 the results obtained with the two constitutive models are similar. In addition, we observe that the values of blood pressure in Figs. 9.40 and 9.42 indicate that the peak-to-peak pressure amplitude during the heart beat is of 40 mmHg. For the sake of completeness, Fig. 9.43 presents the minimum and the maximum of the difference in the blood flow pressures over the whole heart beat. The values of both the minimum and the maximum difference, reached at the times $t = 0.95$ s and $t = 0.67$ s, respectively, are around 3% of the corresponding pressure obtained with the U-EXP2 law. Figs. 9.44 and 9.45 report the fluid particle path lines during the systolic and diastolic phases of the heart beat. We observe that the flow pattern presents common characteristic features in both cases. Indeed, fluid recirculation inside the aneurysm dome, small flow impingement area where the peak values of pressure are obtained, are shown in Figs. 9.40 and 9.41, and stable flow, i.e. blood flow with persistent flow pattern, is observed. In Figs. 9.44 and 9.45 the color scales are set according to the maximum blood flow velocity attained in the interval under consideration; in addition, it is worth pointing out that the values reached during the heart beat are consistent with the experimental measurements of blood velocity in the vessels of similar diameter to the one considered in this work Hart and Haluszkiewicz [2000].

The vessel wall displacement on the entire solid domain at the time $t = 0.2$ s is shown in Fig. 9.46. The arterial wall displacement is presented only for the U-EXP2 law since the same qualitative behavior for both constitutive laws was observed. We report that the vessel wall displacement in the aneurysm

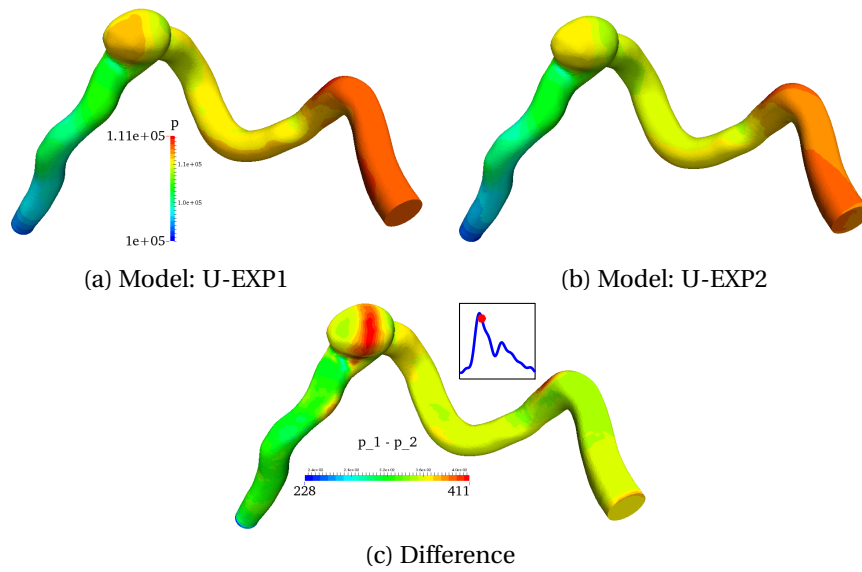


Figure 9.40: Blood flow pressure at the time $t = 0.239$ s and their difference

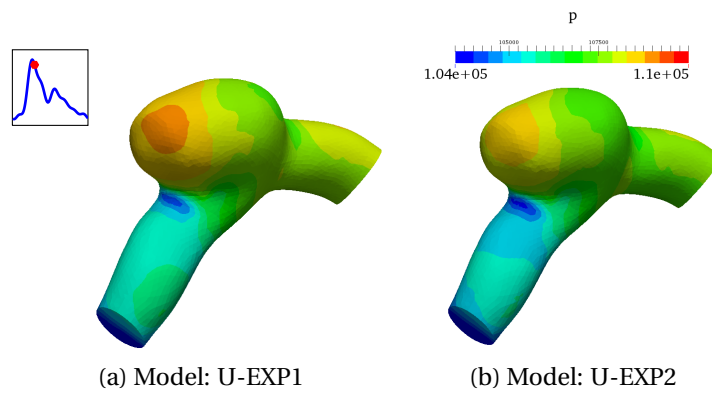


Figure 9.41: Blood flow pressure in the aneurysm dome at the time $t = 0.239$ s for the two constitutive models

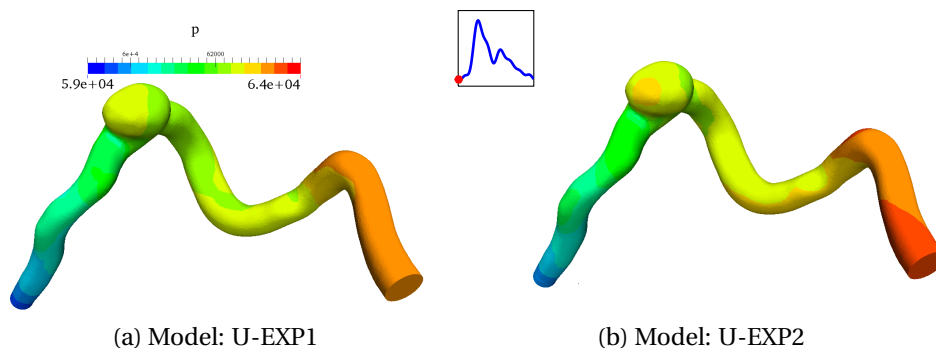


Figure 9.42: Blood flow pressure at the time $t = 0.026$ s for the two constitutive models

dome is higher with respect to the one measured for the parent vessel due to the combined effect of the mechanical weakening and the reduced elastic coefficient in the Robin boundary conditions. Moreover,

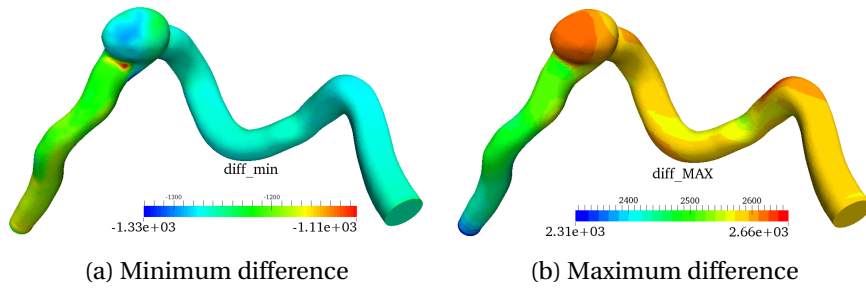


Figure 9.43: Maximum and minimum values of the difference of the blood pressure between the two cases under consideration over the heart beat

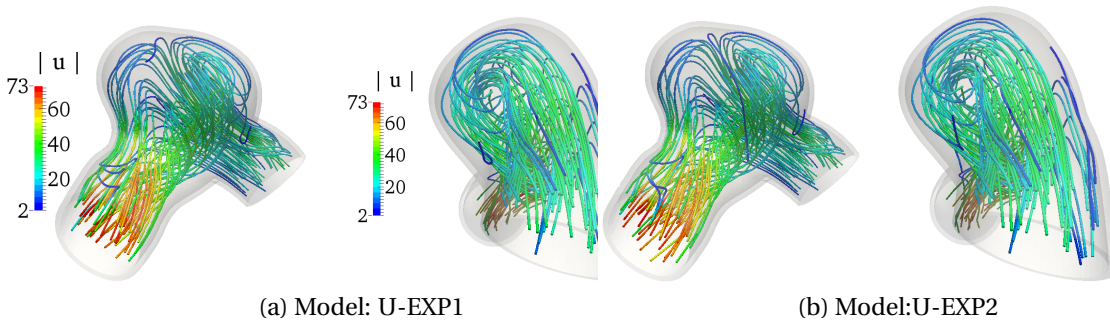


Figure 9.44: Blood particle path lines inside the aneurysm dome during the systolic phase, i.e. for $t \in [0.3, 0.45]$

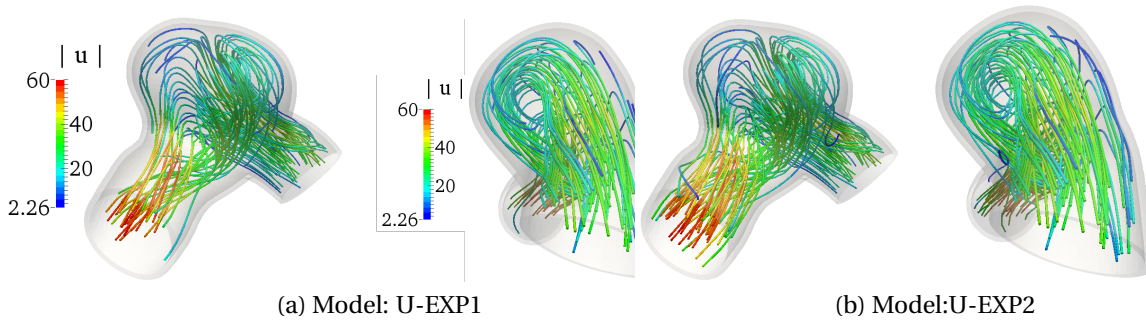


Figure 9.45: Blood particle path lines inside the aneurysm dome during the diastolic phase, i.e. for $t \in [0.5, 0.6]$

the wall displacement in the parent vessel is directed mainly along the local radial direction, namely the direction perpendicular to the center line of the vessel Faggiano and Antiga [2014]. In order to evaluate the correct setting of the elastic coefficient K for the healthy portion of the solid domain, the radial displacement of the internal surface of the parent vessel at the cross section shown in Fig. 9.46-(b) has been analyzed for both the numerical simulations. Fig. 9.46-(c) shows the vessel wall displacement at one point of the internal surface of the considered cross section with respect to the undeformed radius. We observe that a variation of 2.5% of the undeformed radius is reported during the heart beat; this result is consistent with the experimental measurements of the variation of the diameter for cerebral arteries presented in Giller et al. [1993]; Golemati et al. [2003] for the vertebral artery and internal carotid artery. Indeed, in Giller et al. [1993] a variation of less 4% of the arterial radius is reported for the vertebral artery while a minimum variation of 6% is measured in Golemati et al. [2003] for the carotid

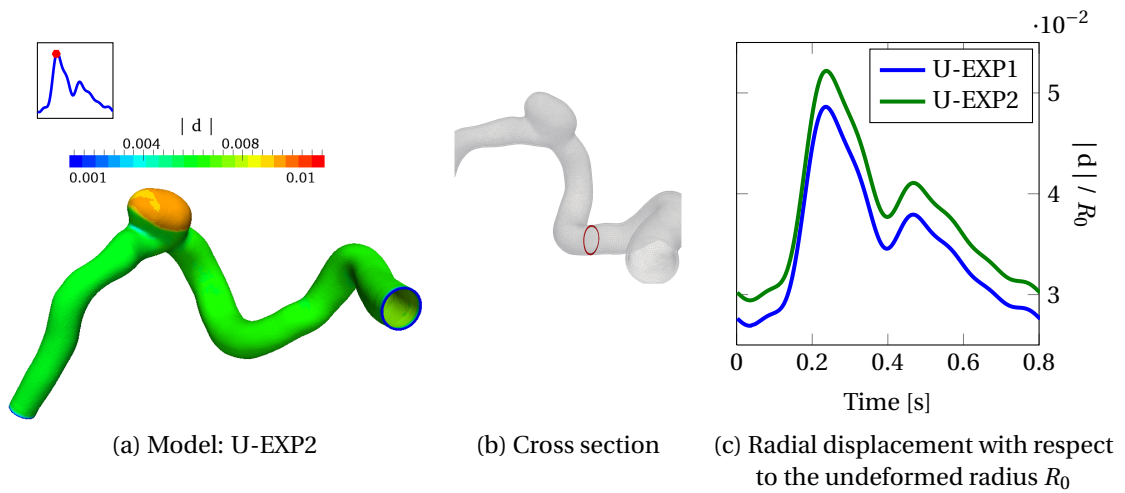


Figure 9.46: Vessel wall displacement: (a) snapshot at time $t = 0.2$ s; (b) Parent vessel displacement on the internal surface measured with respect to the internal radius R_0

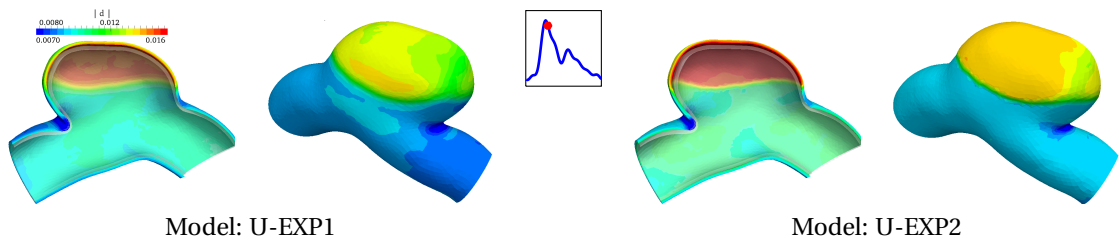


Figure 9.47: Vessel wall displacement in the aneurysm dome at the time $t = 0.239$ s. The grey overlay represents the undeformed geometry. The deformations are magnified of a factor 3

artery, whose internal radius is similar to the one of the vessel under consideration. By comparing the results presented in Fig. 9.46- (c), we notice that the deformations predicted by the two constitutive models are similar during the heart beat; indeed, the maximum displacement at the time $t = 0.239$ s predicted by the U-EXP2 law is the 6% higher than the one measured for the U-EXP1 model at the same time. Figs. 9.47 and 9.48 show the displacement of the aneurysm dome during the systole and the diastole. As previously mentioned, it can be observed that the displacement in the parent vessel is mainly directed along the radial direction and that the maximum values are attained in the aneurysm dome where the mechanical weakening occurs. Despite the small quantitative differences among the numerical results, we remark the different qualitative behavior of the two numerical solutions. Indeed, for the U-EXP1 law, the maximum displacement on the internal and external surfaces of the dome does not occur in correspondance of the flow impingement area but on one side of the dome. On the other hand, for the U-EXP2 law, the highest displacements are reached in correspondance of the flow impingement area and on a big portion of the aneurysm dome. The fact that, for the models, high displacements are measured in the aneurysm dome during both the systolic and diastolic phases of the heart beat is due to the high recirculation zone presented in Figs. 9.44 and 9.45 that persists all over the cardiac cycle. When studying cerebral aneurysms and the factors that may lead to rupture, an important indicator that is evaluated is the dome pulsatility in order to measure the variations of the aneurysm size during the heart beat Oubel et al. [2010]. The pulsatility index is a dimensionless

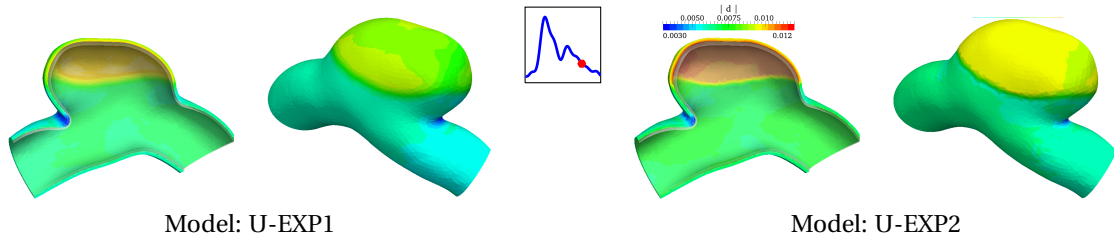


Figure 9.48: Vessel wall displacement in the aneurysm dome at the time $t = 0.6$ s. The grey overlay represents the undeformed geometry. The deformations are magnified of a factor 3

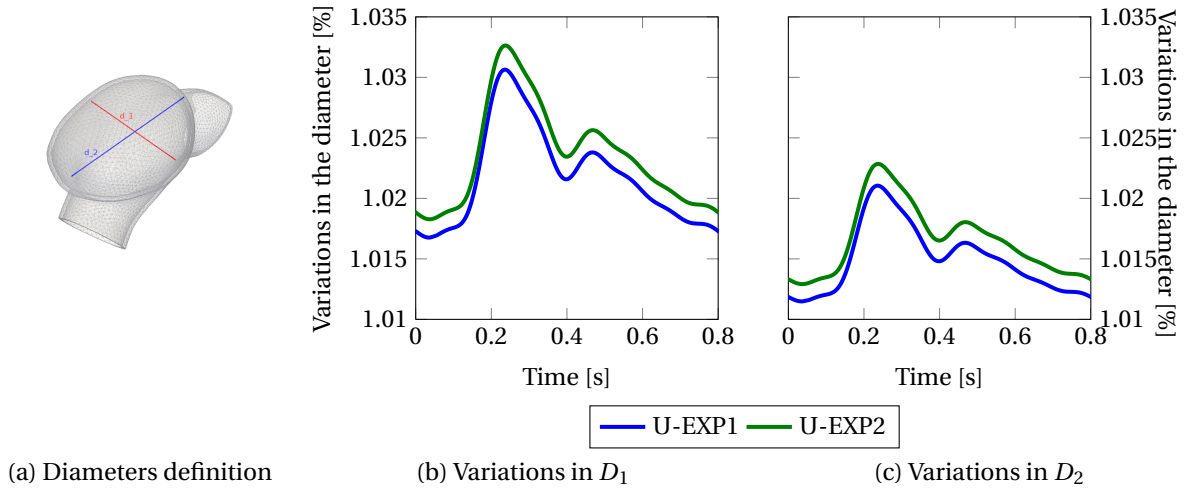


Figure 9.49: Changes in aneurysmal dome diameters; (a) Diameter definition; (b) Relative variations of D_1 with respect to the undeformed D_1 ; (c) Relative variations of D_2 with respect to the undeformed D_2

quantity defined in Oubel et al. [2010] as

$$\mu = \frac{|\max\{\hat{D}_1, \hat{D}_2\} - \hat{A}|}{D_0}, \quad (9.1)$$

where \hat{D}_1 and \hat{D}_2 are the peak-to-peak amplitude of the variations of two characteristic diameters of the aneurysm, \hat{A} is the amplitude of variation of the parent vessel diameter during the heart beat, and D_0 is the artery diameter. In this work, D_1 and D_2 , that are shown in Fig. 9.49-(a), have been chosen in order to capture the highest dome displacements along the transverse and parallel directions to the blood flow, while $D_0 = 0.41$ cm close to the dome. The index μ measures the difference in pulsation between aneurysm and artery, and expresses it as a fraction of the artery diameter. As pointed out in Oubel et al. [2010], the normalization with respect to the artery diameter was added to compare aneurysms at different locations, since the same absolute difference in pulsation has a different relevance for arteries of different size. Figs. 9.49-(b) and 9.49-(c) show the variations of the two diameters depicted in Fig. 9.49-(a) during the heart beat. We remark that, as previously commented for Figs. 9.47 and 9.48, the highest dilatation occurs for the diameter that is oriented transversally with respect to the direction of the blood flow in the parent vessel. We remark that, for the two cases under consideration, the pulsatility index μ is around 3.3%, which is consistent with the measurements reported in Oubel et al. [2010] for unruptured aneurysms.

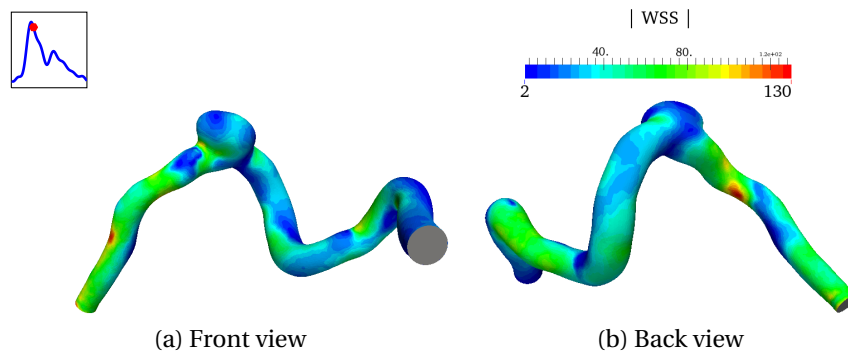


Figure 9.50: WSS magnitude at the time $t = 0.239$ s for the U-EXP2 model

Fig. 9.50 shows the WSS magnitude on the whole fluid domain at the time $t = 0.239$ s; due to the similarities in the blood flow dynamics already reported in Figs. 9.40 and 9.45, the magnitude of the WSS is presented only for the U-EXP2 model. We observe that the peak value is reached close to the outlet surface; indeed, in that part of the fluid domain, the blood flow is mainly driven by the resistance boundary conditions. However, high values of WSS are measured also upstream and downstream the aneurysm due to the tortuous nature of the blood vessel under consideration. On the other hand, the low values of WSS reached in most part of the aneurysm dome are due to the recirculation zone observed in Figs. 9.44 and 9.45. More precisely, the spatial distribution of the WSS inside the aneurysm dome is depicted in Figs. 9.51 and 9.52 at two different times of the heart beat. The similar spatial distribution of the WSS on the dome surface in Figs. 9.51 and 9.52 (a) and (b) obtained with the two models is due to the persistent features of the blood flow during the heart beat previously discussed. However, a non-negligible 10% peak difference in the WSS magnitude in the dome between the two cases is reported in Figs. 9.51 and 9.52; more precisely, the WSS obtained with the U-EXP1 law is 10% higher than the one obtained with the U-EXP2 at the same point. Concerning the OSI index Lee et al. [2009], due to the persistent spatial distribution of the WSS during the heart beat, it does not reach high values in the whole fluid domain, as presented in Fig. 9.53 for the U-EXP2 law.

Fig. 9.54 presents the Von Mises stress inside the aneurysm dome at the time corresponding to the largest displacement. We observe that, although the maximum value of Von Mises stress is very similar in both cases, for the U-EXP1 the region of high stresses is larger than the one obtained with the U-EXP2 law. In particular, the two color scales highlight the different values obtained. As reported in Fig. 9.54, the flow impingement area is characterized by high values of Von Mises stresses, while it decreases inside the dome. The analysis of the WSS magnitude and Von Mises stress inside the aneurysm dome in Figs. 9.51 and 9.54, respectively, indicates the relevance of considering both indicators when describing the progression of the mechanical degradation of the properties of the arterial tissue that occurs in cerebral aneurysms. Indeed, the high and low Von Mises stress regions in the dome can be explained by considering the deformations of the dome during the cardiac cycle, represented in Fig. 9.47; the larger are the deformations, the higher is the Von Mises stress. On the other hand, the inhomogeneous deformations of the dome affect the WSS magnitude induce high values in those parts of the aneurysm when the deformations are low and viceversa.

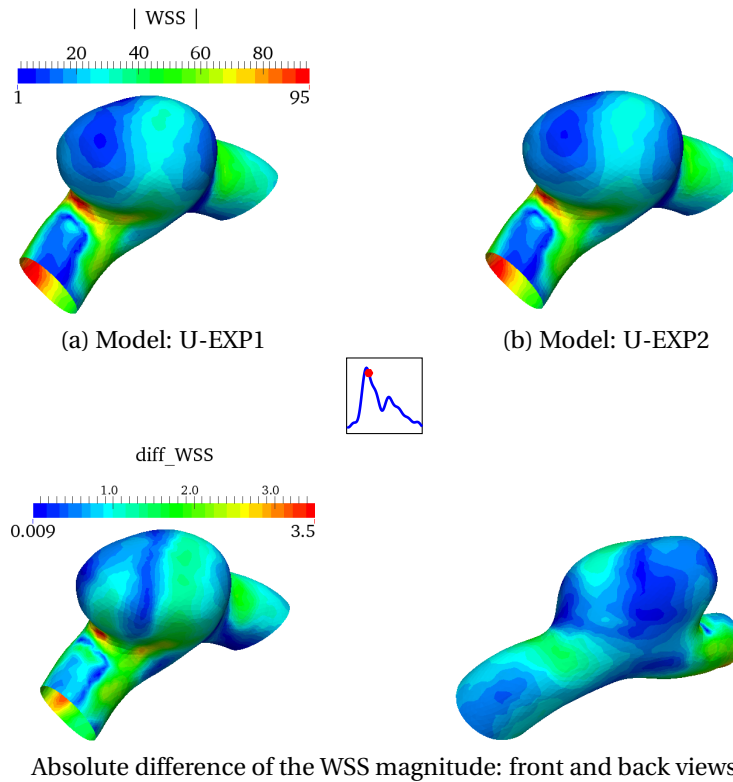


Figure 9.51: WSS magnitude in the aneurysm dome at the time $t = 0.212$ s for the two constitutive models and their difference

9.3.3 Conclusions

The numerical simulations on the idealized cerebral aneurysm pointed out the importance of suitably selecting the constitutive model for the arterial wall. Indeed, the choice of either an isotropic or anisotropic law strongly influences the numerical results and the derived quantities that are important in order to predict the the evolution of the cerebral aneurysm. On the other hand, the simulations on the realistic aneurysm pointed out another important aspect: when the anisotropic models cannot be used on anatomical geometries of aneurysms, the choice of the isotropic models does not significantly affect the numerical results. However, we recall that the use of an anisotropic law with weakened material properties represents a crucial aspect when studying the onset of cerebral aneurysms. This suggests that the nonlinearity of the mechanical behavior of arteries is the most important feature that must be considered when choosing isotropic models for the vessel. It is worth pointing out that, the approach employed in this work to represent the mechanical weakening of the arterial tissue is important to study the spatial distribution of hemodynamical and mechanical indicators during the heart beat. Indeed, by considering the numerical simulations of few cardiac cycles with unhealthy arterial tissue, useful information about the average distribution of important mechanical indicators could be deduced in order to improve the weakening model employed in this work; for instance considering a variable weakening parameter D inside the dome according to the regions of high (low) stresses.

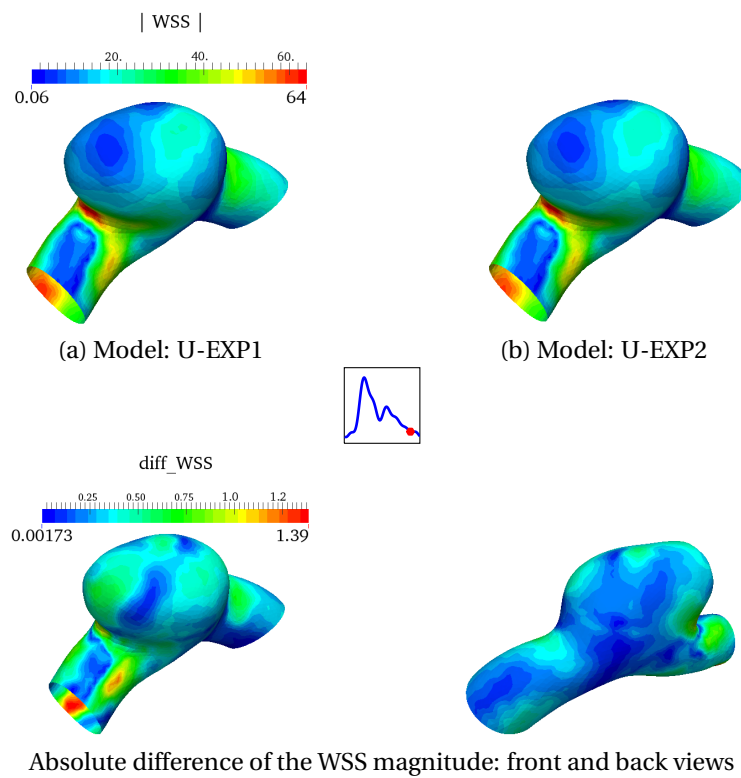


Figure 9.52: WSS magnitude in the aneurysm dome at the time $t = 0.7$ s for the two constitutive models and their difference

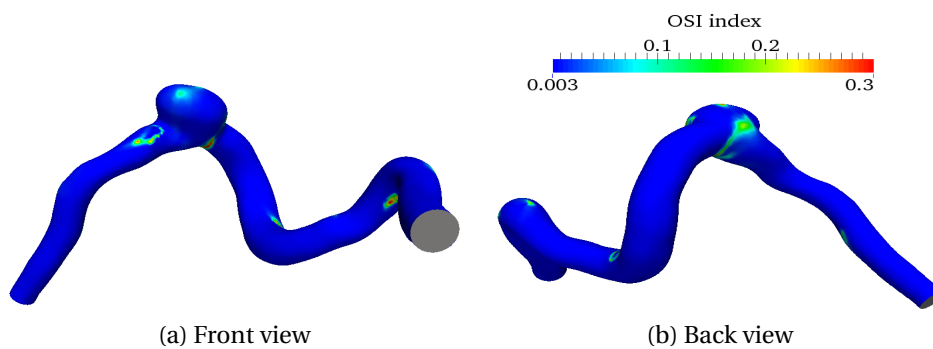


Figure 9.53: OSI index for one heart beat: (a) front view; (b) back view. Constitutive model: U-EXP2

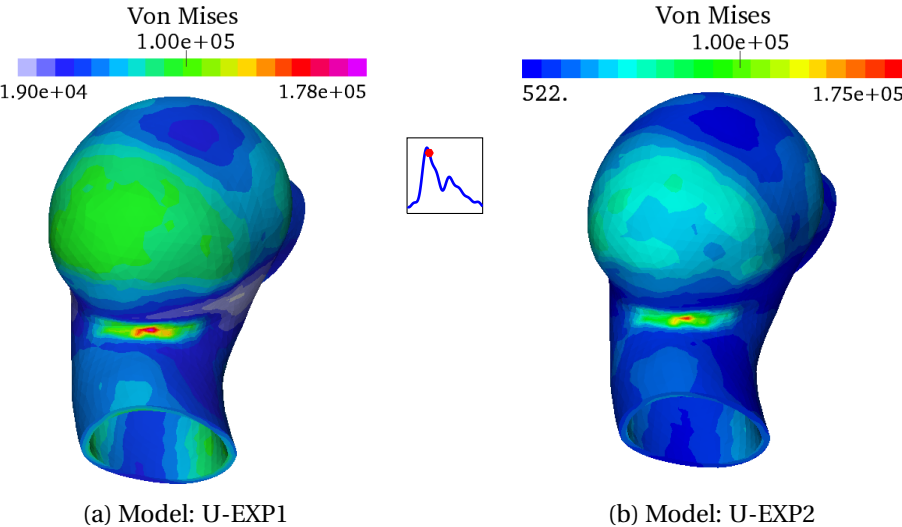


Figure 9.54: Von Mises stress in the aneurysm dome at the time $t = 0.239$ s

10 Conclusions and future perspectives

This work dealt with the mathematical and numerical modeling of healthy and unhealthy cerebral arterial tissues and provided a contribution to the current research on the computational hemodynamics, especially for cerebral aneurysms. In particular, it critically analyzed the influence of the modeling choice for the cerebral arteries on the numerical results of finite element simulations. With this aim, nonlinear hyperelastic isotropic and anisotropic constitutive laws, which represent the state of the art of arterial tissue modeling, were employed to describe the passive mechanical response of the vessel wall to applied loads. Indeed, isotropic models are still largely used in the biomechanics community due to their capability of describing the nonlinear mechanical response of the tissue without requiring information on the spatial distribution of collagen fibers. On the other hand, anisotropic models are receiving increasing attention in numerical simulations of vessel wall mechanics due to the advancements in microscopy techniques which provide information regarding the orientation and distribution of the collagen fibers. For biomechanical applications of interest, such as inflation tests, the numerical simulations showed the significance of isotropic constitutive models with respect to more complex anisotropic laws, once they are adequately calibrated to fit experimental data. On the other hand, the numerical simulations of blood flow in compliant healthy and unhealthy arteries revealed that the choice of the constitutive model, i.e. isotropic vs. anisotropic, strongly affects the vessel wall dynamics and, consequently, the hemodynamical indicators that play a role in the evolution of cerebral aneurysms. The main contributions provided in this Thesis by the different numerical studies are summarized hereafter.

Firstly, we presented the numerical validation of isotropic and anisotropic laws for the healthy arterial tissue by considering numerical simulations of static inflation tests on a cylindrical geometry representing a specimen of anterior cerebral artery (ACA). The St. Venant-Kirchhoff and two exponential type laws were used to describe the tissue as isotropic Holzapfel [2000]; Delfino et al. [1997]; Balzani [2006], while two anisotropic laws modeled the fibrous nature of the arterial wall considering both the mechanical behavior of elastin and collagen fibers. More precisely, for both anisotropic models we considered exponential type strain energy functions for both the elastin and collagen fibers. However, the two anisotropic models differ in the description of the collagen fibers activation; one considers the collagen fibers as active once their stretched length is higher than the one in the undeformed configuration of the artery (i.e. for zero strains), while the other, namely the multi-mechanical model, takes into account the recruitment of the collagen fibers at finite strains, as proposed for the cerebral arterial tissue in Holzapfel and Gasser [2000]; Li and Robertson [2009b]. All the constitutive laws were suitably fitted with respect to a set of experimental data describing the mechanical behavior of healthy ACA. Among the isotropic constitutive laws, the St. Venant-Kirchhoff model, which is still largely

employed in numerical simulations of the cardiovascular system, did not show a satisfactory fit of the experimental measurements, while the isotropic exponential type laws and the anisotropic models adequately match the experimental data. Particularly, the multi-mechanism law turned out to be the best model in capturing the stiffening effect in the mechanical response of the tissue that occurs at finite strains due to the collagen fibers activation. The constitutive stress-strain relations obtained from the data fitting were compared to the numerical results. A good agreement between the fitted and numerical stress-strain relations was achieved for all the constitutive laws under consideration, including the multi-mechanism model in the range of physiological transmural pressure. The numerical simulations highlighted the fact that isotropic exponential models can be considered as a valuable option to model the arterial tissue when experimental observations of the directions of the collagen fibers in the tissue are not available. Finally, we also analyzed different aspects related to the numerical simulation of realistic biomechanical applications, e.g. the approximation of the kinematic constraint of incompressibility. We observed the effectiveness of the adopted choices for the finite element spaces and of the penalization parameter for the volumetric deformations when numerically simulating the nearly-incompressible behavior of arteries in the range of physiological transmural pressures. These results lead to the choice of the finite element spaces for the fluid-structure interaction (FSI) simulations carried out in the rest of the work.

Next, we focused on FSI simulations of blood flow compliant arteries. Idealized geometries of ACA were considered and the arterial tissue was assumed to be mechanically intact; therefore, the same material parameters and constitutive models employed in the numerical simulations of inflation tests were employed for this numerical study as well. Physiological values of blood pressure, velocity, and vessel wall displacement over the heart beat were obtained by imposing a set of boundary conditions for the fluid and solid domain commonly employed in literature (see e.g. Torii et al. [2008, 2009]; Valencia et al. [2013]; Bazilevs et al. [2010]). The numerical results showed that, in the case of a cylindrical blood vessel, the blood flow dynamics and vessel wall displacement are not significantly affected by the choice of the constitutive model for the tissue, especially for the isotropic exponential and anisotropic laws. This, as previously mentioned, shows that a properly fitted isotropic constitutive law can be employed in place of a more complex anisotropic model when the main features of the fluid-structure system have to be studied. However, anisotropic models can provide important insights about the deformation of the collagen fibers during the cardiac cycle and on their contribution to the overall response of the vessel wall. Indeed, the multi-mechanism model turned out to be able of describing the progressive activation and deactivation of the collagen fibers throughout the wall thickness during the heart beat. In virtue of this model, it has been shown that the collagen fibers located on the vessel lumen are mechanically active for most of the heart beat, while the most external ones reach their active state only during the systole, i.e. when the largest deformations of the vessel occur. This computational result highlights the significance of the multi-mechanism model for the arterial tissue in FSI simulations. However, it is worth pointing out that the use of the multi-mechanism model is particularly critical from the numerical point of view within the context of FSI simulations. Indeed, numerical issues related to the inhomogeneous activation of the collagen fibers throughout the solid domain and the corresponding inhomogeneous transmission of the dynamic coupling condition between fluid and solid domains were faced. FSI numerical simulations were also presented on a toroidal geometry of blood vessel. In this case, the influence of the constitutive model for the tissue on the numerical results has been shown by reporting the different vessel wall displacements that are obtained when considering either isotropic or anisotropic laws. This result points out that the choice of the constitutive model for the arterial tissue is crucial for the correct simulation of the blood flow in compliant arteries and it highlights the need of the numerical validation of the results with respect to *in vitro* experiments.

Finally, we dealt with numerical simulations of static arterial wall mechanics and solution of FSI problems for unhealthy cerebral arterial tissues. More precisely, the unhealthy state of the tissue was represented by a weakening model in which a dimensionless parameter D Simo [1987]; Kachanov [1958] describes the level of mechanical weakening of the tissue. Different levels of the mechanical degradation were taken into account. The numerical simulations of static inflation tests showed that the choice of the type of constitutive model (i.e. isotropic vs. anisotropic) plays a key role in the spatial distribution of the mechanical stresses through the thickness of the vessel wall and on the internal surface of the vessel lumen. This highlights the relevance of properly selecting the constitutive model when addressing the study of the onset and development of cerebral aneurysms. Afterward, we addressed FSI numerical simulations on idealized blood vessels and geometries of cerebral aneurysms. For this study, we chose to model the arterial tissue by means of one of the exponential laws considered in the simulations of static inflation tests and of the anisotropic model for which the collagen fibers activation occurs at zero strains. From the numerical results, we can conclude that the use of isotropic models may lead to an underestimation of the Wall Shear Stress (WSS) with respect to one measured with the anisotropic laws, while, on the contrary, the Von Mises stress may be overestimated with the isotropic law. In addition, the simulations on the idealized geometry of cerebral aneurysm highlighted the large influence of the constitutive model on the numerical results. More precisely, strong differences in the vessel wall displacement induces significant differences in the WSS and Von Mises predictions. Conversely, for the anatomically realistic geometry of aneurysm, the numerical results obtained with the two isotropic exponential constitutive laws were both quantitatively and qualitatively very similar. We therefore conclude that the anisotropic model should be used whenever possible for unhealthy tissues since it represents the most adequate model to study and characterize the aneurysms development and onset. It is worth reminding that the FSI numerical results on unhealthy arterial tissues focused on the analysis of the influence of the type of constitutive model since the numerical simulations with the multi-mechanism model turned out to be impractical. This stresses the fact that further investigations are necessary to use this constitutive law in physiological FSI numerical simulations of the cardiovascular system in order to have an accurate description of the arterial wall mechanics and of the collagen fibers contribution.

Future perspectives

Several developments are foreseeable for this work; possible extensions involve different aspects related to either the numerical simulation of the cardiovascular system and the validation of the numerical results with respect to experimental measurements. We have already mentioned the necessary improvements that must be done with respect to numerical simulations of FSI problems with the multi-mechanism model; furthermore, the reduction of the computational times associated to complex material models is another important aspect for the future development of computational hemodynamics. For instance the study of inexact Newton techniques for the solution of the FSI monolithic problem may reduce the computational times. Indeed, the extension of the Convective-Geometric explicit approach proposed in Crosetto [2011] to a Geometric-Convective-Structural Explicit approach, stemming from linearizing also the nonlinear term associated to the solid problem, would certainly lead to a reduction of the computational times since it would avoid, for example, the repeated evaluation of the Jacobian matrix associated to the structural problem. Another important development of this work is the validation of the numerical results with respect to experimental measurements. In particular, other mechanical tests, such as biaxial tests, should be considered in addition to the inflation tests Scott et al. [1972]; Monson [2001]; Monson et al.; Kenneth et al. [2008] in order to further validate the constitutive models considered in this work. Concluding, the validation of the FSI numerical results with respect to in vitro FSI experiments represents an important step toward the creation of a reliable

Chapter 10. Conclusions and future perspectives

and flexible tool for the simulations of the blood flow in compliant arteries.

Bibliography

- T. Abruzzo, G.G. Shengelaia, III R.C. Dawson, D.S. Owens, C.W. Cawley, and M.B. Gravanis. Histologic and morphologic comparison of experimental aneurysms with human intracranial aneurysm. *American Journal of Neuroradiology*, 19:1309–1314, 1998.
- D. Ambrosi, G.A. Athesian, E.M. Arruda, S.C. Cowin, J. Dumais, A. Goriely, G.A. Holzapfel, J.D. Humphrey, R. Kimmener, E. Kuhl, J.E. Olberding, L.A. Taber, and K. Garikipati. Perspectives on biological growth and remodeling. *Journal of the Mechanics and Physics and Solids*, 59:863–883, 2011.
- G.A. Ateshian and J.D. Humphrey. Continuum mixture models of biological growth and remodeling: past successes and future opportunities. *Annual Reviews of Biomedical Engineering*, 14:97–111, 2012.
- D. Augsburger. *Fluid Mechanics of Cerebral Aneurysms and Effects of Intracranial Stents on Cerebral Aneurysmal Flow*. PhD thesis, École Polytechnique Fédérale de Lausanne, Switzerland, 2008.
- F. Auricchio, F. Brezzi, and C. Lovadina. Mixed Finite Elements Methods. In *Encyclopedia of Computational Mechanics*. Wiley Online Library, 2004.
- H. Baek, M.V. Jayaraman, P.D. Richardson, and G.E. Karniadakis. Flow instability and wall shear stress variation in intracranial aneurysms. *Journal of the Royal Society Interface*, 7:967–988, 2010.
- S. Baek, K.R. Rajagopal, and J.D. Humphrey. A theoretical model of enlarging intracranial fusiform aneurysms. *Journal of Biomechanical Engineering*, 128:142–149, 2006.
- J.M. Ball. Convexity conditions and existence theorems in non-linear elasticity. *Archive of Rational Mechanics and Analysis*, 63:337–403, 1977a.
- J.M. Ball. Convexity conditions and existence theorems in nonlinear elasticity. *Archive for Rational Mechanics and Analysis*, 63:337–403, 1977b.
- J.M. Ball. Constitutive inequalities and existence theorems in nonlinear elastostatics. In R.J. Knowps, editor, *Nonlinear Analysis and Mechanics*, volume 1 of *Heriot-Watt Symposium*. Pitman, 1997.
- D. Balzani. *Polyconvex Anisotropic Energies and Modeling of Damage Applied to Arterial Walls*. PhD thesis, University of Duisburg-Essen, Germany, 2006.
- D. Balzani, P. Neff, J. Schröder, and G.A. Holzapfel. A polyconvex framework for soft biological tissues. adjustment to experimental data. *International Journal of Solids and Structures*, 43:6052–6070, 2006a.
- D. Balzani, J. Schröder, and D. Gross. Simulation of discontinuous damage incorporating residual stresses in circumferentially overstretched atherosclerosis arteries. *Acta Biomaterialia* 2, 1:609–618, 2006b.

Bibliography

- D. Balzani, S. Brinkhues, and G.A. Holzapfel. Constitutive framework for the modeling of damage in collagenous soft tissues with application to arterial walls. *Computer Methods in Applied Mechanics and Engineering*, 1:139–151, 2012.
- D. Balzani, T. Schmidt, T. Schriefl, and G.A. Holzapfel. Constitutive modeling of damage mechanisms in arterial walls and related experimental studies. In *XLI APM Proceedings (Advanced Problems in Mechanics)*, pages 17–25, St. Petersburg, Russia, 2013.
- Y. Bazilev, M.C. Hsu, Y. Zhang, W. Wang, T. Kvamsdal, S. Hentschel, and J.G. Isaksen. Computational vascular fluid-structure interaction: methodology and application to cerebral aneurysms. *Biomechanics and Modeling in Mechanobiology*, 9:481–498, 2010.
- Y. Bazilevs, J.R. Gohean, T.J.R. Hughes, R.D. Moser, and Y. Zhang. Patient-specific isogeometric fluid-structure interaction analysis of thoracic aortic blood flow due to implantation of the Jarvik 2000 left ventricular assist device. *Computer Methods in Applied Mechanics and Engineering*, 198:3534–3550, 2009.
- Y. Bazilevs, M.C. Hsu, Y. Zhang, W. Wang, X. Liang, T. Kvamsdal, R. Brekken, and J.G. Isaksen. A fully-coupled fluid-structure interaction simulation of cerebral aneurysms. *Computational Mechanics*, 46: 3–16, 2010.
- E.D. Bell, R.S. Kunjir, and K.L. Monson. Biaxial and failure properties of passive rat middle cerebral arteries. *Journal of Biomechanics*, 46:91–96, 2013.
- J. Bonet and R.D. Wood. *Nonlinear Continuum Mechanics for Finite Element Analysis*. Cambridge University Press, Cambridge, 1997.
- V. Bousset, L. Rayz and C. McCulloch. Aneurysm growth occurs at regions of low wall shear stress: patient-specific correlation of hemodynamics and growth in a longitudinal study. *Stroke*, 39:2997–3002, 2008.
- D. Brands, A. Klawonn, O. Rheinbach, and J. Schröder. Modelling and convergence in arterial wall simulations using a FETI solution strategy. *Computer Methods in Biomechanics and Biomedical Engineering*, 11:569–583, 2008.
- S. Brinkhues, A. Klawonn, O. Rheinbach, and J. Schröder. Augmented Lagrange methods for quasi-incompressible material-Applications to soft biological tissue. *International Journal for Numerical Methods in Biomedical Engineering*, 29:332–350, 2013.
- J.L. Brisman, J.K. Song, and D.W. Newell. Cerebral aneurysms. *The New England Journal of Medicine*, 355:928–939, 2006.
- A.M. Brown. A step-by-step guide to nonlinear regression analysis of experimental data using microsoft Excel spreadsheet. *Computer Methods and Programs in Biomedicine*, 65:191–200, 2001.
- A.C. Burton. Relation of structure to function of the tissue of the wall of blood vessels. *Physiological Reviews*, 34:619–642, 1954.
- H.B. Callen. *Thermodynamics and an Introduction to Thermostatistics*. John Wiley & Sons, New York, 1985.
- B. Calvo, E. Pêna, M.A. Martinez, and M. Doblaré. An uncoupled directional damage model for fibred biological soft tissues. formulation and computational aspects. *International Journal for Numerical Methods in Engineering*, 69:2036–2057, 2007.

- G.J. Campbell and M.R. Roach. Fenestrations in the internal elastic lamina at bifurcations of the human cerebral arteries. *Stroke*, 12:489–495, 1981.
- F. Caranci, F. Briganti, L. Cirillo, M. Leonardi, and M. Muto. Epidemiology and genetics of intracranial aneurysms. *European Journal of Radiology*, 82:1598–1605, 2013.
- T.E. Carew, R.N. Vaishnav, and D.J. Patel. Compressibility of the arterial wall. *Circulation Research*, 23:61–68, 1968.
- M.A. Castro, C.M. Putman, and J.R. Cebal. Computational fluid dynamics modeling of intracranial aneurysms: effects of parent artery segmentation on intra-aneurysmal hemodynamics. *American Journal of Neuroradiology*, 27:1703–1709, 2006.
- P. Causin, J.-F. Gerbeau, and F. Nobile. Added-mass effect in the design of partitioned algorithms for fluid-structure problems. *Computers Method in Applied Mechanical Engineering*, 194:4506–2527, 2005.
- J.R. Cebal, M.A. Castro, O. Soto, R. Löhner, and N. Alperin. Blood flow models of the Circle of Willis from Magnetic Resonance data. *Journal of Engineering Mathematics*, 47:369–386, 2003.
- J.R. Cebal, M.A. Castro, S. Appanaboyina, C.M. Putman, D. Millan, and A. Frangi. Efficient pipeline for image-based patient-specific analysis of cerebral aneurysm hemodynamics: techniques and sensitivity. *IEEE Transactions on Medical Imaging*, 24:457–467, 2005.
- J.R. Cebal, F. Mut, F. Weir, and C.M. Putman. Association of hemodynamics characteristics and cerebral aneurysms rupture. *American Journal of Neuroradiology*, 32:264–270, 2011.
- I. Chatziprodomou, A. Tricoli, D. Poulikakos, and Y. Ventikos. Haemodynamics and wall remodelling of a growing cerebral aneurysm: a computational model. *Journal of Biomechanics*, 40:412–426, 2007.
- J. Chen, S. Wang, G. Ding, X. Yang, and H. Li. The effect of aneurysmal-wall mechanical properties on patient-specific hemodynamic simulations: two clinical reports. *Acta Mechanica Sinica*, 25:677–688, 2009.
- S. Chien, S. Usami, R.J. Dellenbakk, and M.I. Gregersen. Shear-dependent deformation of erythrocytes. *American Journal of Physiology*, 219:136–142, 1970.
- C.J. Chuong and Y.C. Fung. Three-dimensional stress distribution in arteries. *Journal of Biomechanical Engineering*, 105:268–274, 1983.
- P.G. Ciarlet. *Mathematical Elasticity, Volume 1: Three Dimensional Elasticity*. Elsevier Science Publishers, North-Holland, 1988.
- B.D. Coleman and W. Noll. On the thermostatics of continuous media. *Archive for Rational Mechanics and Analysis*, 4:97–128, 1959.
- R.H. Cox. Three-dimensional mechanics of arterial segments in vitro: methods. *Journal of Applied Physics*, 36:381–384, 1974.
- M.R. Crompton. Mechanism of growth and rupture in cerebral berry aneurysms. *British Medical Journal*, 1:1138–1142, 1966.
- P. Crosetto. *Fluid-Structure Interaction Problems in Hemodynamics: Parallel Solvers, Preconditioners, and Applications*. PhD thesis, École Polytechnique Fédérale de Lausanne, Switzerland, 2011.

Bibliography

- P. Crosetto, S. Deparis, G. Fourestey, and A. Quarteroni. Parallel algorithms for fluid-structure interaction problems in haemodynamics. *SIAM Journal of Scientific Computing*, 33:1598–1622, 2011.
- P. Crosetto, S. Deparis, L. Formaggia, G. Mengaldo, F. Nobile, and P. Triccerri. A comparative study of different nonlinear hyperelastic isotropic arterial wall models in patient-specific vascular flow simulations in the aortic arch. Technical report, MOX - Laboratory of Modeling and Scientific Computing - Milano, Italy, 2012.
- P. Crosetto, P. Reymond, S. Deparis, D. Kontaxakis, N. Stergiopoulos, and A. Quarteroni. Fluid structure interaction simulations of physiological blood flow in the aorta. *Medical Engineering & Physics*, 35:784–791, 2013.
- B. Dacorogna. *Direct Methods in the Calculus of Variations*, volume 78 of *Applied Mathematical Science*. Springer, New York, 2000.
- L. Dalong, A.M. Robertson, G. Lin, and M. Lovell. Finite element modeling of cerebral angioplasty using a structural multi-mechanism anisotropic damage model. *International Journal for Numerical Methods in Engineering*, 92:457–474, 2012.
- E.A. De Souza Neto, D. Perić, and D.R.J. Owen. Continuum modelling and numerical simulation of material damage at finite strains. *Archives of Computational Methods in Engineering*, 5:311–384, 1998.
- A. Delfino, N. Stergiopoulos, J.E. Moore, and J.J. Meister. Residual strain effects on the stress field in a thick wall finite element model of the human carotid bifurcation. *Journal of Biomechanics*, 30:777–786, 1997.
- T. den Heijer, I. Skoog, M. Oudkerk, F.-E. de Leeuw, J.C. de Groot, A. Hofman, and M.M.B. Bretle. Association between blood pressure levels over time and brain atrophy in the elderly. *Neurobiology of Aging*, 24:307–313, 2003.
- S.X. Deng, J. Tomioka, J.C. Debes, and Y.C. Gunf. New experiments on shear modulus of elasticity of arteries. *American Journal of Physiology*, 226:H1–H10, 1994.
- D.A. Di Pietro and A. Veneziani. Expression templates implementation of continuous and discontinuous galerkin methods. *Computer & Visual Science*, 12:421–436, 2009.
- P.B. Dobrin and A.A. Rovick. Influence of vascular smooth muscle on contractile mechanics and elasticity of arteries. *American Journal of Physiology*, 217:1644–1651, 1969.
- M.T. Draney, R.J. Herfkens, T.J.R. Hughes, N.J. Pelc, K.L. Wedding, C.K. Zarins, and C.A. Taylor. Quantification of vessel wall cyclic strain using cine phase contrast magnetic resonance imaging. *Annals of Biomedical Engineering*, 30:1033–1045, 2002.
- LifeV. École Polytechnique Fédérale de Lausanne (CMCS), CH; Politecnico di Milano (MOX), ITA; INRIA (REO, ESTIME), FR, and Emory University (Math&CS), GA US., 2010. LifeV user manual, <http://lifev.org>.
- T. Elguedj, Y. Bazilevs, V.M. Calo, and T.J.R. Hughes. \bar{B} and \bar{F} projection methods for nearly incompressible linear and nonlinear elasticity and plasticity using higher-order NURBS elements. *Computer Methods in Applied Mechanics and Engineering*, 197:2732–2762, 2008.
- E.B. Elliot. *Algebra of Quantics*. Oxford University Press, Oxford, 1913.

- E. Faggiano and L. Antiga. An open-source tool for patient-specific fluid-structure vessel mesh generation. *International journal for numerical methods in biomedical engineering*, 2014. submitted.
- N. Famaey, G. Sommer, J.V. Stolen, and G.A. Holzapfel. Arterial clamping: finite element simulation and in vivo validation. *Journal of the Mechanical Behavior of Biomedical Materials*, 12:107–118, 2012.
- G.G. Ferguson. Direct measurements of mean and pulsatile blood pressure at operation in human intracranial saccular aneurysms. *Journal of Neurosurgery*, 36:560–563, 1972a.
- G.G. Ferguson. Physical factors in the initiation, growth, and rupture of human intracranial aneurysms. *Journal of Neurosurgery*, 37:666–677, 1972b.
- M.Á. Fernández and M. Moubachir. A Newton method using exact jacobians for solving fluid-structure coupling. *Computers and Structures*, 83:127–142, 2005.
- A. Fischle. *A parallel Newton-Krylov-FETI-DP solver*. PhD thesis, University of Duisburg-Essen, Germany, In Preparation.
- P.J. Flory. Theory of elastic mechanism in fibrous proteins. *Journal of American Chemical Society*, 78: 5222–5235, 1956.
- P.J. Flory. Thermodynamical relations for high elastic materials. *Transactions of the Faraday Society*, 78: 5222–5235, 1961.
- M.D. Ford, N.H. Nikolov, J.S. Milner, S.P. Lownie, E.M. Demont, W. Kalata, F. Loth, D.W. Holdsworth, and D.A. Steinman. PIV-measured versus CFD-predicted flow dynamics in anatomically realistic cerebral aneurysm models. *Journal of Biomechanical Engineering*, 130:1–15, 2008.
- L. Formaggia, J.-F. Gerbeau, F. Nobile, and A. Quarteroni. On the coupling of 3D and 1D Navier-Stokes equations for flow problems in compliant vessels. *Computer Methods in Applied Mechanical Engineering*, 191:561–582, 2001.
- L. Formaggia, J.F. Gerbeau, F. Nobile, and A. Quarteroni. Numerical treatment of defective boundary conditions for the Navier-Stokes equations. *SIAM Journal of Numerical Analysis*, 40:376–401, 2006a.
- L. Formaggia, A. Moura, and F. Nobile. On the stability of the coupling of 3D and 1D fluid-structure interaction models for blood flow simulations. Technical report, MOX - Laboratory of Modeling and Scientific Computing - Milano, Italy, 2006b.
- L. Formaggia, A. Quarteroni, and A. (Eds) Veneziani. *Cardiovascular Mathematics. Modeling and Simulation of the circulatory System*. MS & A. Springer-Verlag, Berlin Heidelberg, 2009.
- A. Fumagalli. *Numerical Modelling of Flows in Fractured Porous Media by the XFEM Method*. PhD thesis, Politecnico di Milano, Italy, 2012.
- Y.C. Fung. *Biomechanics. Mechanical Properties of Living Tissues*. Springer, New York, 1993.
- Y.C. Fung, K. Fronek, and P. Patitucci. Pseudo elasticity of arteries and the choice of its mechanical expression. *American Journal of physiology*, 237:1340–1349, 1979.
- A.M. Gambaruto and A.J. João. Flow structures in cerebral aneurysms. *Computer & Fluids*, 65:56–65, 2012.
- E. Gamma, R. Helm, R. Johnson, and J. Vlissides. *Design Patterns. Elements of Reusable Object-Oriented Software*. Addison-Wesley, New York, 1995.

Bibliography

- T.C. Gasser and G.A. Holzapfel. Hyperelastic modelling of arterial layers with distributed collagen fiber orientations. *Journal of the Royal Society*, 3:15–35, 2006.
- T.C. Gasser, C.A.J. Schulze-Bauer, and G.A. Holzapfel. A three-dimensional finite element model for arterial clamping. *Journal of Biomechanical Engineering*, 124:355–363, 2002.
- J.-F. Gerbeau and M. Vidrascu. A quasi-Newton algorithm based on a reduced model for fluid-structure interaction problems in blood flows. Technical report, INRIA - Institut National de Recherche en Informatique et en automatique, 2003.
- C. Geuzaine and J.-F. Remacle. Gmsh: a three-dimensional finite element mesh generator with built-in pre- and post-processing facilities. *International Journal for Numerical Methods in Engineering*, 79:1309–1331, 2009.
- C.A. Giller, G. Bowman, H. Dyer, L. Mootz, and W. Krippner. Cerebral arterial diameters during changes in blood pressure and carbon dioxide during craniotomy. *Neurosurgery*, 32:737–741, 1993.
- R. Glowinski and P. Le Tallec. Numerical solution of problems in incompressible finite elasticity by augmented Lagrangian methods i: Two-dimensional and axisymmetric problems. *SIAM Journal on Applied Mathematics*, 42:400–429, 1982.
- R. Glowinski and P. Le Tallec. Numerical solution of problems in incompressible finite elasticity by augmented Lagrangian methods ii: Three-dimensional problems. *SIAM Journal on Applied Mathematics*, 44:710–733, 1984.
- S. Golemati, A. Sassano, M.J. Lever, A. Bharath, S. Dhanjil, and A.N. Nicolaides. Carotid artery wall motion estimated from B-mode ultrasound using region tracking and block matching. *Ultrasound in Medicine and Biology*, 29:387–399, 2003.
- J.H. Grace and A. Young. *The Algebra of Invariants*. Cambridge University Press, 1903.
- A.E. Green and P.M. Nagdi. A note on invariance under superimposed rigid body motions. *Journal of Elasticity*, 9:1–8, 1979.
- S.E. Greenwald, J.E.J. Moore, A. Rachev, T.P.C. Kane, and J.J. Meister. Experimental investigation of the distribution of residual strains in the artery wall. *Journal of Biomechanical Engineering*, 119:438–444, 1997.
- P.R. Gummert. General constitutive equations for simple and non-simple materials. In J.J. Altenbach, H. and Skrzypek, editor, *Creep and Damage in Materials and Structures, Courses and Lectures of CISM*, pages 1–42. Springer, Italia, 1999.
- N. Gundiah, M.B. Ratcliffe, and L.A. Pruitt. Determination of strain energy function for arterial elastin: experiments using histology and mechanical tests. *Journal of Biomechanics*, 40:586–594, 2007.
- N. Gundiah, M.B. Ratcliffe, and L.A. Pruitt. The biomechanics of arterial elastin. *Journal of the Mechanical Behavior of Biomedical Materials*, 2:288–296, 2008.
- G.B. Gurevich. *Foundations of the Theory of Algebraic Invariants*. Noordhoff, Groningen, 1964.
- R. Hart and E. Haluszkiewicz. Blood flow velocity using transcranial doppler velocimetry in the middle and anterior cerebral arteries: correlation with sample volume depth. *Ultrasound in Medicine and Biology*, 26:1267–1274, 2000.

- S. Hartmann and P. Neff. Polyconvexity of generalised polynomial-type hyperelastic strain energy functions for nearly-incompressibility. *International Journal of Solids and Structures*, 40:2767–2791, 2003.
- J. Helfenstein, M. Jabareen, E. Mazza, and S. Govindjee. On non-physical response in models for fiber-reinforced hyperelastic materials. *International Journal of Solids and Structures*, 47:2056–2061, 2010.
- J.G. Heywood, R. Rannacher, and S. Turek. Artificial boundaries and flux and pressure conditions for the incompressible Navier-Stokes equations. *Numerical Methods in Fluids*, 22:325–352, 1996.
- M.R. Hill, X. Duan, G.A. Gibson, S. Watkins, and A.M. Robertson. A theoretical and non-destructive experimental approach for direct inclusion of measured collagen orientation and recruitment into mechanical models of the arterial wall. *Journal of Biomechanics*, 45:762–771, 2012.
- R. Hill. On uniqueness and stability in the theory of finite elastic strain. *Journal of the Mechanics and Physics of Solids*, 5:229–241, 1957.
- Y. Hoi, S.H. Woodward, M. Kim, D.B. Taulbee, and H. Meng. Validation of CFD simulations of cerebral aneurysms with implication of geometric variations. *Journal of Biomechanical Engineering*, 128:844–851, 2006.
- G.A. Holzapfel and T.C. Gasser. A viscoelastic model for fiber-reinforced composites at finite strains: continuum basis, computational aspects, and applications. *Computer Methods in Applied Mechanics and Engineering*, 190:4379–4403, 2001.
- G.A. Holzapfel. *Nonlinear Solid Mechanics: a Continuum Approach for Engineering*. John Wiley & Sons Ltd, England, 2000.
- G.A. Holzapfel. *Biomechanical Modelling at the Molecular, Cellular and Tissue Levels, CISM Courses and Lectures*, chapter Arterial tissue in healthy and disease: Experimental data, collagen-based modeling and simulation, including aortic dissection. Springer, Wien, New York, 2009.
- G.A. Holzapfel and T.C. Gasser. A new constitutive framework for arterial wall mechanics and a comparative study of material models. *Journal of Elasticity*, 61:1–48, 2000.
- G.A. Holzapfel and T.C. Gasser. A three-dimensional finite element model for arterial clamping. *Journal of Biomechanical Engineering*, 14:355–363, 2002.
- G.A. Holzapfel and T.C. Gasser. Computational stress-deformations analysis of arterial walls including high-pressure response. *International Journal of Cardiology*, 116:78–85, 2007.
- G.A. Holzapfel and R.W. Ogden. *Mechanics of Biological Tissue*. Springer-Verlag, Heidelberg, 2006.
- G.A. Holzapfel and R.W. Ogden. Constitutive modelling of passive myocardium: a structurally based framework for material characterization. *Philosophical Transactions of The Royal Society A: Mathematical, Physical & Engineering Sciences*, 367:3445–3475, 2009.
- G.A. Holzapfel and R.W. Ogden. On planar biaxial tests for anisotropic nonlinearly elastic solids. A continuum mechanical framework. *Mathematics and Mechanics of Solids*, 14:474–489, 2008.
- G.A. Holzapfel and R.W. Ogden. Constitutive modeling of arteries. *Proceedings of the Royal Society A*, 466:1551–1597, 2010.

Bibliography

- T.J.R. Hughes. *The Finite Element Method: Linear Static and Dynamic Finite Element Analysis*. Dover Publications, New York, 2000.
- J.D. Humphrey. Mechanics of arterial wall: Review and directions. *Critical Reviews in Biomedical Engineering*, 23:1–162, 1995a.
- J.D. Humphrey. Mechanics of arterial wall: Review and directions. *Critical Reviews in Biomedical Engineering*, 23:1–162, 1995b.
- J.D. Humphrey. *Cardiovascular Solid Mechanics. Cells, Tissues, and Organs*. Springer-Verlag, New York, 2002.
- J.D. Humphrey. Continuum mechanics of soft biological tissues. *The Royal Society*, 459:3–46, 2003.
- J.D. Humphrey and P.B. Canham. Structure, mechanical properties, and mechanics of intracranial saccular aneurysms. *Journal of Elasticity*, 61:49–81, 2000.
- J.D. Humphrey and K.R. Rajagopal. A constrained mixture model for growth and remodeling of soft tissues. *Mathematical Models and Methods in Applied Sciences*, 12:407–430, 2002a.
- J.D. Humphrey and K.R. Rajagopal. A constrained mixture model for growth and remodeling of soft tissue. *Mathematical Models and Methods in Applied Sciences*, 12:407–430, 2002b.
- J.D. Humphrey and C.A. Taylor. Intracranial and abdominal aortic aneurysms: similarities, differences, and need for a new class of computational models. *Annual Reviews of Biomedical Engineering*, 10: 221–246, 2008.
- J.G. Isaksen, Y. Bazilevs, T. Kvamsdal, Y. Zhang, J.H. Kaspersen, K. Waterloo, B. Romner, and T. Ingebrigtsen. Determination of wall tension in cerebral artery aneurysms by numerical simulation. *Stroke*, 39: 3172–3178, 2008.
- J. Janela, A. Moura, and A. Sequeira. Absorbing boundary conditions for a 3D non-Newtonian fluid structure interaction model for blood flow in arteries. *International Journal of Engineering Science*, 48:1332–1349, 2010a.
- J. Janela, A. Moura, and A. Sequeira. A 3D non-Newtonian fluid-structure interaction model for blood flow in arteries. *Journal of Computational and Applied Mathematics*, 234:2783–2791, 2010b.
- J. Janela, A. Moura, and A. Sequeira. Absorbing boundary conditions for a 3d non-Newtonian fluid-structure interaction model for blood flow in arteries. *International Journal of Engineering Science*, 48:1332–1349, 2010c.
- W. Jeong and K. Rhee. Hemodynamics of cerebral aneurysms: computational analyses of aneurysm progress and treatment. *Computational and Mathematics Methods in Medicine*, 2012:1–11, 2012.
- Y.G. Jeong, Y.T. Jung, M.S. Kim, C.K. Eun, and S.H. Jang. Size and location of ruptured intracranial aneurysms. *Journal of Korean Neurosurgical Society*, 45:11–15, 2009.
- L.M. Kachanov. Time of rupture process under creep conditions. *Izvestija Akademii Nauk Sojuza Sovetskich Socialisticeskich Respubliki (SSSR) Otdelenie Techniceskich Nauk (Moskra)*, 8:26–31, 1958.
- N.F. Kassel and J.C. Torner. Size of intracranial aneurysms. *Neurosurgery*, 12:291–297, 1983.
- L.M. Kenneth, N.M. Barbaro, and G.T. Manley. Biaxial response of passive human cerebral arteries. *Annals of Biomedical Engineering*, 36:2028–2041, 2008.

- J. Kim and S. Baek. Circumferential variations of mechanical behavior of the porcine thoracic aorta during the inflation test. *Journal of Biomechanics*, 44:1941–1947, 2011.
- O. Klass, A. Maniatty, and M.S. Shephard. A stabilized mixed finite element method for finite elasticity. Formulation for linear displacement and pressure interpolation. *Computer Methods in Applied Mechanics and Engineering*, 180:65–79, 1999.
- M. Kroon. A numerical framework for material characterisation of inhomogeneous hyperelastic membranes by inverse analysis. *Journal of Computational and Applied Mathematics*, 234:563–578, 2010.
- M. Kroon and G.A. Holzapfel. A model for saccular cerebral aneurysm growth by collagen fibre remodelling. *Journal of Theoretical Biology*, 247:775–787, 2007.
- M. Kroon and G.A. Holzapfel. Estimation of the distributions of anisotropic, elastic properties and wall stresses of saccular cerebral aneurysms by inverse analysis. *Proceeding of the Royal Society A*, 464: 807–825, 2008.
- U. Küttler, M. Gee, Ch. Förster, A. Comerford, and W.A. Wall. Coupling strategies for biomedical fluid-structure interaction problems. *International Journal for Numerical Methods in Biomedical Engineering*, 26:305–321, 2010.
- W.M. Lai, V.C. Mow, and W. Zhu. Constitutive modelling of articular cartilage and biomacromolecular solutions. *ASME Journal of Biomechanical Engineering*, 115:474–480, 1993.
- S. Lang. *Linear Algebra*. Addison-Wesley, Massachusetts, 1968.
- R.W. Lawton. The thermoelastic behavior of isolated aortic strips of the dog. *Circulation Research*, 2: 344–353, 1954.
- S.W. Lee, L. Antiga, and D.A. Steinman. Correlations among indicators of disturbed flow at the normal carotid bifurcation. *Journal of Biomechanical Engineering*, 131:1–7, 2009.
- D. Li. *Structural Multi-Mechanism Model with Anisotropic Damage for Cerebral Arterial Tissues and its Finite Element Modeling*. PhD thesis, University of Pittsburgh, USA, 2009.
- D. Li and A.M. Robertson. A structural multi-mechanism damage model for cerebral arterial tissue. *Journal of Biomechanical Engineering*, 131, 2009a.
- D. Li and A.M. Robertson. A structural multi-mechanism constitutive equation for cerebral arterial tissue. *International Journal of Solids & Structures*, 46:2920–2928, 2009b.
- J.D. Lou, D.H. Lee, H. Morsi, and M.E. Mawad. Wall shear stress on ruptured and unruptured intracranial aneurysms at the internal carotid artery. *American Journal of Neuroradiology*, 29:1761–1767, 2008.
- A.M. Malek, S.L. Alper, and S. Izumo. Hemodynamic shear stress and its role in atherosclerosis. *The Journal of the American Medical Association*, 282:2035–2042, 1999.
- A.C.I. Malossi. *Partitioned Solution of Geometrical Multiscale Problems for the Cardiovascular System: Models, Algorithms, and Applications*. PhD thesis, École Polytechnique Fédérale de Lausanne, Switzerland, 2012.
- A.C.I. Malossi and J. Bonemann. Numerical comparison and calibration of geometrical multiscale models for the simulation of arterial flows. *Cardiovascular Engineering and Technology*, 2013. accepted.

Bibliography

- A. Mantha, C. Karmonik, G. Bendorf, C. Strother, and R. Metcalfe. Hemodynamics in a cerebral artery before and after the formation of an aneurysm. *American Journal of Neuroradiology*, 27:1113–1118, 2006.
- D. Marquardt. An algorithm for Least-Squares estimation of nonlinear parameters. *SIAM - Journal on Applied Mathematics*, 2:431–441, 1963.
- J.E. Marsden and J.R. Hughes. *Mathematical Foundations of Elasticity*. Prentice-Hall, Englewood Cliffs, 1983.
- A. Marzo, P. Singh, P. Reymond, N. Stergiopoulos, U. Patel, and R. Hose. Influence of inlet boundary conditions on the local haemodynamics of intracranial aneurysms. *Computer Methods in Biomechanics and Biomedical Engineering*, 12:431–444, 2009.
- A. Marzo, P. Singh, I. Larrabide, A. Radaelli, S. Coley, M. Gwilliam, I.D. Wilkinson, P. Lawford, P. Reymond, U. Patel, A. Frangi, and D.R. Hose. Computational hemodynamics in cerebral aneurysms: the effects of modeled versus measured boundary conditions. *Annals of Biomedical Engineering*, 39:848–896, 2010.
- I. Masson, C. Fassinot, and M. Zidi. Finite dynamic deformations of a hyperelastic, anisotropic, incompressible, and prestressed tube. applications to in vivo arteries. *European Journal of Mechanics A/Solids*, 29:523–529, 2010.
- A. Masud and T. Truster. A framework for residual-based stabilization of incompressible finite elasticity: stabilized formulations and \bar{F} methods for linear triangles and tetrahedra. *Computer Methods in Applied Mechanical Engineering*, 267:359–399, 2013.
- T. Matsuo, S.I. Watanabe, M. Sorimachi, M. Kanda, Y. Ohta, and T. Takahashi. Blood flow velocity waveforms in the middle cerebral artery at rest and during exercise. *Artificial Life and Robotics*, 16:398–402, 2011.
- T. (Ed) McGloughlin. *Biomechanics and Mechanobiology of Aneurysms*, volume 7 of *Studies in Mechanobiology, Tissue Engineering and Biomaterials*. Springer-Verlag, Heidelberg, 2011.
- P. Moireau, N. Xiao, M. Astorino, C.A. Figueroa, D. Chapelle, C.A. Taylor, and J.-F. Gerbeau. External tissue support and fluid-structure simulation in blood flows. *Biomechanics and Modeling in Mechanobiology*, 11:1–18, 2012.
- K.L. Monson. *Mechanical and Failure Properties of Human Cerebral Blood Vessels*. PhD thesis, University of California, USA, 2001.
- K.L. Monson, W. Goldsmith, N.M. Barbaro, and G. Manley. Multiaxial response of human cerebral arteries. *Journal of Biomechanics*, 13:175–179.
- C.B. Morrey. Quasi-convexity and the lower semicontinuity of multiple integrals. *Pacific Journal of Mathematics*, 2:25–53, 1952.
- V.C. Mow, S.C. Kuei, W.M. Lai, and C.G. Armstrong. Biphasic creep and stress relaxation of articular cartilage in compression: theory and experiments. *ASME Journal of Biomechanical Engineering*, 102:73–84, 1980.
- J.L. Murray and A.D. Lopez. *The Global Burden of Disease*. The Global Burden of Disease and Injury Series. Harvard University Press, Cambridge, 1996.

- P.M. Naghdi. The Theory of Shells and Plates. In *Handbuch der Physik. Mechanics of Solids.*, volume 2. Springer, Berlin Heidelberg New York, 1984.
- P.M. Naghdi and P.Y. Tang. Large deformation possible in every isotropic elastic membrane. *Philosophical Transactions of the Royal Society A*, 287:145–187, 1977.
- W.W. Nichols and M.F. O'Rourke. *McDonald's Blood Flow in Arteries: Theoretical, Experimental, and Clinical Principles*. Arnold, London, 1998.
- A.M. Nixon, M. Gunel, and B.E. Sumpio. The critical role of hemodynamics in the development of cerebral vascular disease: a review. *Journal of Neurosurgery*, 112:1240–1253, 2010.
- F. Nobile. *Numerical Approximation of Fluid-Structure Interaction Problems with Application to Haemodynamics*. PhD thesis, École Polytechnique Fédérale de Lausanne, Switzerland, 2001.
- F. Nobile, M. Pozzoli, and C. Vergara. Time accurate partitioned algorithms for the solution of fluid-structure interaction problems in haemodynamics. *Computer & Fluids*, 86:470–482, 2013a.
- F. Nobile, M. Pozzoli, and C. Vergara. Time accurate partitioned algorithms for the solution of fluid-structure interaction problems in haemodynamics. *Computer & Fluids*, 86:470–492, 2013b.
- R.W. Odgen. *Nonlinear Elastic Deformations*. Courier Dover Publications, New York, 1997.
- Visual Computing Lab of ISTI-CNR. Meshlab. <http://meshlab.sourceforge.net/>, 2005–2014.
- S. Ogoh, P.J. Fadel, R. Zhag, C. Selmer, I. Jans, N.H. Secher, and P.B. Raven. Middle cerebral artery flow velocity and pulse pressure during dynamic exercise in humans. *Heart and Circulation Physiology - American Journal of Physiology*, 288:1526–1531, 2005.
- M. Oshima, R. Torii, T. Kobayashi, N. Taniguchi, and K. Takagi. Finite element simulation of blood flow in the cerebral artery. *Computer Methods in Applied Mechanics and Engineering*, 191:661–671, 2001.
- M. Oshima, H. Skai, and R. Torii. Modelling of inflow boundary conditions for image-based simulation of cerebrovascular flow. *International Journal for Numerical Methods in Fluids*, 47:603–617, 2005.
- J.T. Ottesen, M.S. Olufsen, and J.K. Larsen. *Applied Mathematical Models in Human Physiology*. Society for Industrial and Applied Mathematics, New York, 2004.
- E. Oubel, J.R. Cebral, M. De Craene, R. Blanc, J. Blasco, J. Macho, C.M. Putman, and A.F. Frangi. Wall motion estimation in intracranial aneurysms. *Physiological Measurements*, 31:1119–1135, 2010.
- Y. Papaharilaou, J.A. Ekaterinaris, E. Manousaki, and A.N. Katsamouris. A decoupled fluid structure approach for estimating wall stress in abdominal aortic aneurysms. *Journal of Biomechanics*, 40:367–377, 2007.
- M. Pozzoli. *Efficient Partitioned Algorithms for the Solution of Fluid-Structure Interaction Problems in Haemodynamics*. PhD thesis, Politecnico di Milano, Italy, 2011.
- A. Quarteroni and A. Valli. *Domain Decomposition Methods for Partial Differential Equations*. Oxford University Press, Oxford, 1999a.
- A. Quarteroni and A. Valli. *Numerical Approximation of Partial Differential Equations*. Springer-Verlag, Berlin Heidelberg, 1999b.
- A. Quarteroni, R. Sacco, and F. Saleri. *Numerical Mathematics*. Springer, Berlin Heidelberg, 2007.

Bibliography

- S. Quinodoz. *Numerical Simulations of Orbitally Shaken Reactors*. PhD thesis, École Polytechnique Fédérale de Lausanne, Switzerland, 2012.
- A. Rachev and K. Hayashi. Theoretical study of the effects of vascular smooth muscle contraction on strain and stress distributions in arteries. *Annals of Biomedical Engineering*, 27:459–468, 1999.
- A. Rachev, N. Stergiopoulos, and J.J. Meister. A model for geometric and mechanical adaptation of arteries to sustained hypertension. *ASME Journal of Biomechanical Engineering*, 120:9–17, 1998.
- K.R. Rajagopal and L. Tao. *Mechanics of Mixture*, volume 35 of *Series on Advances in Mathematics for Applied Sciences*. World Scientific, 1995.
- A. Raoult. Non-polyconvexity of the stored energy function of a Saint Venant-Kirchhoff material. *Applications of Mathematics*, 31:417–419, 1986.
- A. Raoult. Symmetry groups in nonlinear elasticity: an exercise in vintage mathematics. *Communications on Pure and Applied Analysis*, 8:435–456, 2009.
- P. Reymond. *Pressure and Flow Wave Propagation in Patient-Specific Models of the Arterial Tree*. PhD thesis, École Polytechnique Fédérale de Lausanne, Switzerland, 2011.
- P. Reymond, Y. Bohraus, F. Perren, F. Lazeyras, and N. Stergiopoulos. Validation of a patient-specific one-dimensional model of the systemic arterial tree. *Heart and Circulation Physiology - American Journal of Physiology*, 301:1173–1182, 2010.
- J.A.G. Rhodin. Architecture of the vessel wall. In H.V. Sparks, D.F. Bohr, A.D. Somlyo, and S.R. Geiger, editors, *Handbook of Physiology, The Cardiovascular System*, volume 2. American Physiological Society, Bethesda, 1980.
- M.C. Roach and A.C. Burton. The reason for the shape of the distensibility curves of arteries. *Canadian Journal of Biochemistry*, 35:681–690, 1957.
- A.M. Robertson, A. Sequeira, and M.V. Kameneva. Hemorheology. In G.P. Galdi, R. Rannacher, A.M. Robertson, and S. Turek, editors, *Hemodynamical Flows*, volume 37 of *Oberwolfach Seminars*, pages 63–120. Springer-Verlag, Basel, 2008.
- A.M. Robertson, M.R. Hill, and L. Dalong. Structurally motivated damage models for arterial walls. Theory and application. In L. Formaggia, A. Quarteroni, and A. (Eds) Veneziani, editors, *Cardiovascular Mathematics. Modeling and Simulation of the Circulatory System*, volume 1 of *MS&A*, pages 143–187. Springer-Verlag, Milano, 2009.
- S. Rossi. *Anisotropic Modeling of Cardiac Mechanical Activation*. PhD thesis, École Polytechnique Fédérale de Lausanne, Switzerland, 2014.
- S. Rossi, T. Lassila, R. Ruiz-Baier, A. Sequeira, and A. Quarteroni. Thermodynamically consistent orthotropic activation model capturing ventricular systolic wall thickening in cardiac electromechanics. *European Journal of Mechanics - A/Solids*, 2013. in press.
- Manini S. and Antiga L. Vmtk, The Vascular Modeling Toolkit. <http://www.vmtk.org/>, 2013–2014.
- Y. Saad. *Iterative Methods for Sparse Linear Systems*. Siam, Philadelphia, 2003.
- D. San Millán Ruiz, K. Tokunaga, A.R. Dehdahsti, K. Sugia, J. Delavelle, and D.A. Rüfenacht. Is the rupture of cerebral berry aneurysms influenced by the perianeurysmal environment? *Acta Neurochirurgica*, 82:31–34, 2002.

- D. San Millán Ruiz, H. Yilmaz, A.R. Dehdahsti, A. Alimenti, N. de Tribolet, and D.A. Rüfenacht. The perianeurysmal environment: influence on saccular aneurysm shape and rupture. *American Journal of Neuroradiology*, 27:504–512, 2006.
- Sansour. On the physical assumptions underlying the volumetric-isochoric split and the case of anisotropy. *European Journal of Mechanics A/Solids*, 27:28–39, 2008.
- A.J. Schriefl. *Quantification of Collagen Fiber Morphologies in Human Arterial Walls: Novel Experimental Methodologies yielding 2D and 3D Structural Data*. PhD thesis, Graz University of Technology, Austria, 2012.
- J. Schröder and P. Neff. Invariant formulation of hyperelastic transverse isotropy based on polyconvex free energy functions. *International Journal of Solids and Structures*, 40:401–445, 2003.
- J. Schröder, P. Neff, and D. Balzani. A variational approach for materially stable anisotropic hyperelasticity. *International Journal of Solids and Structures*, 42:4352–4371, 2004.
- S. Scott, G.G. Ferguson, and M.R. Roach. Comparison of the elastic properties of human intracranial arteries and aneurysms. *Canadian Journal of Physiology and Pharmacology*, 50:328–332, 1972.
- C.M. Scotti, A.D. Shkolnik, S.C. Muluk, and E.A. Finol. Fluid-structure interaction in abdominal aortic aneurysms: effects of asymmetry and wall thickness. *Biomedical Engineering Online*, 4:1–22, 2005.
- L.N. Sekhar and R.C. Heros. Origin, growth and rupture of saccular aneurysms: a review. *Neurosurgery*, 8:248–260, 1981.
- D.M. Sforza, C.M. Putman, and J.R. Cebal. Hemodynamics of cerebral aneurysms. *Annual Review of Fluid Mechanics*, 41:91–107, 2009.
- D.M. Sforza, C.M. Putman, S. Tateshima, F. Viñuela, and J.R. Cebal. The effects of perianeurysmal environment during the growth of cerebral aneurysms: a case study. *American Journal of Neuroradiology*, 33:1115–1120, 2012.
- C. Sherif, G. Kleinpeter, G. Mach, M. Loyoddin, T. Haider, R. Plasenzotti, H. Bergmeister, A. Di Ieva, D. Gibson, and M. Krssak. Evaluation of cerebral aneurysm wall thickness in experimental aneurysms: comparison of 3t-mr imaging with direct microscopic measurements. *Acta Neurochirurgica*, 156:27–34, 2014.
- M Shojima, Y. Oshima, and K. Takagi. Magnitude and role of wall shear stress on cerebral aneurysm: computational fluid dynamic study on 20 middle cerebral artery aneurysms. *Stroke*, 35:2500–2505, 2004.
- J.C. Simo. On a fully three-dimensional finite-strain viscoelastic damage model: formulation and computational aspects. *Computer Methods in Applied Mechanics and Engineering*, 60:153–173, 1987.
- J.C. Simo and J.W. Ju. Strain- and stress-based continuum damage models, I. Formulation, II. Computational aspects. *International Journal of Solids and Structures*, 23:821–869, 1987.
- J.C. Simo and R.L. Taylor. Penalty function formulations for incompressible nonlinear elastostatics. *Computer Methods in Applied Mechanics and Engineering*, 35:107–118, 1982.
- J.C. Simo and R.L. Taylor. Quasi-incompressible finite elasticity in principal stretches. Continuum basis and numerical algorithms. *Computer Methods in Applied Mechanics and Engineering*, 85:273–310, 1991.

Bibliography

- J.C Simo, R.L. Taylor, and K. Pister. Variational and projection methods for the volume constraint in finite deformations elasto-plasticity. *Computer Methods in Applied Mechanics and Engineering*, 51: 177–208, 1985.
- G. Sommer. *Mechanical Properties of Healthy and Diseased Human Arteries and Related Material Modeling*. PhD thesis, Graz University of Technology, Austria, 2008.
- G. Sommer, P. Regitnig, L. Költringer, and G.A. Holzapfel. Biaxial mechanical properties of intact and layer-dissected human carotid arteries at physiological and suprphysiological loadings. *American Journal of Physiology. Heart and Circulatory Physiology*, 298:898–912, 2010.
- A.J.M. Spencer. *Theory of Invariants*. Academic Press, 1971.
- W.E. Stehbens. Etiology of intracranial berry aneurysms. *Journal of Neurosurgery*, 70:823–831, 1989.
- H.J. Steiger, R. Aaslid, S. Keller, and H.J. Reulen. Strength, elasticity and viscoelastic properties of cerebral aneurysms. *Heart Vessels*, 5:41–46, 1986.
- B. Stroustrup. *The C++ Programming Language (4th Edition)*. Addison-Wesley, New-York, 2013.
- T. Szasz, G.F. Bomfim, and R.C. Webb. The influence of perivascular adipose tissue on vascular homeostasis. *Vascular Health and Risk Management*, 9:105–116, 2013.
- L.A. Taber. Biomechanics of growth, remodeling, and morphogenesis. *Applied Mechanics Reviews*, 48: 487–546, 1995.
- L.A. Taber. A model for aortic growth based on fluid shear and fiber stresses. *ASME Journal of Biomechanical Engineering*, 120:348–354, 1998.
- L.A. Taber. *Nonlinear Theory of Elasticity - Applications in Biomechanics*. World Scientific Publishing Co. Pte. Ltd., River Edge, New Jersey, 2004.
- K. Takamizawa and K. Hayashi. Strain energy functions and uniform strain hypothesis for arterial mechanics. *Journal of Biomechanics*, 20:7–17, 1987.
- M.J. Thubrikar, J. Al-Soudi, and F. Robicsek. Wall studies of abdominal aortic aneurysm in a clinical model. *Annals of Vascular Surgery*, 15:355–366, 2001.
- R. Torii, M. Oshima, T. Kobayashi, K. Takagi, and T.E. Tezduyar. Fluid-structure interaction modeling of aneurysmal conditions with high and normal blood pressures. *Computational Mechanics*, 43: 151–159, 2006.
- R. Torii, M. Oshima, T. Kobayashi, K. Takagi, and T.E. Tezduyar. Numerical investigation of the effect of hypertensive blood pressure on cerebral aneurysm - dependence of the effect on the aneurysm shape. *International Journal for Numerical Methods in Fluids*, 54:995–1009, 2007.
- R. Torii, M. Oshima, T. Kobayashi, K. Takagi, and T.E. Tezduyar. Fluid-structure interaction modeling of a patient-specific cerebral aneurysm: influence of structural modeling. *Computational Mechanics*, 38:482–490, 2008.
- R. Torii, M. Oshima, T. Kobayashi, K. Takagi, and T.E. Tezduyar. Fluid-structure interaction modeling of blood flow and cerebral aneurysm: significance of artery and aneurysm shapes. *Computer Method in Applied Mechanics in Engineering*, 198:3613–3621, 2009.

- R. Torii, M Oshima, T. Kobayashi, K. Takagi, and T.E. Tezduyar. Influence of wall thickness on fluid-structure interaction computations of cerebral aneurysms. *International Journal for Numerical Methods in Biomedical Engineering*, 26:336–347, 2010.
- L.R.G. Treloar. *The Physics of Rubber Elasticity*. Oxford University Press, Oxford, 1975.
- P. Tricceri, L. Dedé, A. Quarteroni, and A. Sequeira. Numerical validation of isotropic and transversely isotropic constitutive models for healthy and unhealthy cerebral arterial tissue. *Biomechanics and Modeling in Mechanobiology*, 2014. submitted.
- C. Truesdell. *Rational Thermodynamics*. McGraw-Hill, New York, 1969.
- C. Truesdell and W. Noll. *The Nonlinear Field Theories of Mechanics*. Springer-Verlag, Berlin Heidelberg New York, 1965.
- C. Truesdell and R. Toupin. *The Classical Field Theories*. Springer, Berlin Heidelberg, 1960.
- A. Valencia and F. Solis. Blood flow dynamics and arterial wall interaction in a saccular aneurysm model of the basilar artery. *Computers & Structures*, 84:1326–1337, 2006.
- A. Valencia, P. Burdiles, M. Ignat, J. Mura, E. Bravo, R. Rivera, and J. Sordo. Fluid structural analysis of human cerebral aneurysm using their own wall mechanical properties. *Computational and Mathematical Methods in Medicine*, 2013:1–18, 2013.
- R.N. Vanishav and J. Vossoughi. Estimation of residual strains in aortic segments. In C.W. Hall, editor, *Biomedical Engineering II: Recent Developments*, pages 330–333. Pergamon Press, New York, 1983.
- I.E. Vignon-Clementel. *A Coupled Multidomain Method for Computational Modeling of Blood Flow*. PhD thesis, Stanford University, USA, 2006.
- I.E. Vignon-Clementel, C.A. Figueroa, K.E. Jansen, and C.A. Taylor. Outflow boundary conditions for 3D simulations of non-periodic blood flow and pressure fields in deformable arteries. *Computer Methods in Biomechanics and Biomedical Engineering*, 1:1–16, 2010.
- P. Watton, Y. Ventikos, and G.A. Holzapfel. Modelling the mechanical response of elastin for arterial tissue. *Journal of Biomechanics*, 42:1320–1325, 2009a.
- P.N. Watton, Y. Ventikos, and G.A. Holzapfel. Modelling the growth and stabilization of cerebral aneurysms. *Mathematical Medicine and Biology*, 26:133–164, 2009b.
- H. Weisbecker, D.M. Pierce, and G.A. Holzapfel. Modeling of damage-induced softening for arterial tissue. In *Proceedings of the 2011 SCATh Joint Workshop on New Technologies for Computer/Robot Assisted Surgery*, pages 1–4, Graz, Austria, 2011.
- J. Weiss, B. Maker, and S. Govindjee. Finite element implementation of incompressible, transversely isotropic hyperelasticity. *Computer Methods in Applied Mechanics and Engineering*, 135:107–128, 1996.
- H. Weyl. *The Classical Groups*. Princeton University Press, Princeton, 1939.
- T. Wick. Fluid-Structure Interactions using different mesh motion techniques. *Computers & Structures*, 89:1456–1467, 2011.
- S.D. Williamson, Y Lam, H.F. Younis, H. Huang, S. Patel, M.R. Kaazempur-Mofrad, and R.D Kamm. On the sensitivity of wall stresses in diseased arteries to variable material properties. *Journal of Biomechanical Engineering*, 125:147–155, 2003.

Bibliography

- B. Wire, C. Amidei, G. Kongable, J.M. Findlay, N.F. Kassell, J. Kelly, L. Dai, and T.G. Karrison. The aspect ratio (dome/neck) of ruptured and unruptured aneurysms. *Journal of Neurosurgery*, 99:447–451, 2003.
- R. Wulandana. *A Nonlinear and Inelastic Constitutive Equation for Human Cerebral Arterial and Aneurysm Walls*. PhD thesis, University of Pittsburgh, USA, 2003.
- R. Wulandana and A.M. Robertson. An inelastic multi-mechanism constitutive equation for cerebral arterial tissue. *Biomechanics and Modeling in Mechanobiology*, 4:235–248, 2005.
- J. Xiang, J. Tremmel, M.m Kolega, E.I. Levy, S.K. Natarajan, and H. Meng. Newtonian viscosity model could overestimate wall shear stress in intracranial aneurysm domes and underestimate rupture risk. *Journal of Neurointerventional Surgery*, 4:351–357, 2012.
- H. Zakaria, A.M. Robertson, and C.Q. Kerber. A parametric model for studies of flow in arterial bifurcations. *Annals of Biomedical Engineering*, 36:1515–1530, 2008.
- S. Zeinali-Davarani, J. Choi, and S. Baek. On parameter estimation for biaxial mechanical behavior of arteries. *Journal of Biomechanics*, 42:524–530, 2009.
- O.C. Zienkiewicz, R.L. Taylor, and D.D. Fox. *The Finite Element Method for Solid and Structural Mechanics 7th Edition*. Butter-Heinmann, Oxford, 2000.

Paolo Tricerri, PhD

c/o Veronica Anguita,
Avenue Jomini 2,
1004 Lausanne
Tel: +41(0)76 707 09 84 / +39 333 46 76 363
Email: i.paolo.tricerri@gmail.com

22 – September - 1984
Italian



Available from: September 2014

PROFILE

I have **four experience in C++ software development** that I have acquired working on the open source finite element library LifeV. My **strong and extensive background in mathematics** provides me of the ability of tackling heterogeneous problems with a certain level of abstraction in order to solve them. I have been involved in different projects within which **I have realized important contributions**.

EDUCATION

2010 – 2014: **Doctoral Studies in Mathematics**, Joint Doctoral Programme between Instituto Superior Técnico (IST, Portugal) and École Polytechnique Fédérale de Lausanne (EPFL, Switzerland).
2003 – 2009: **Bachelor & Master of Science in Applied Mathematics**, Politecnico di Torino (Italy).

SKILLS

TECHNICAL SKILLS

OS & Office Packages	Windows, Linux, MS & Libre Office
Programming Languages	C++, Matlab
3D Mesh generation software	Gmsh, MeshLab, VMTK
Project management software	Git, CVS
Parallel computing library	OpenMPI
Debugging library	GDB
Numerical simulations software	Comsol Multiphysics, LifeV, FreeFEM, Fluent, Paraview

MATHEMATICAL BACKGROUND

Continuum and computational mechanics, mathematical modeling of continuous bodies, fluid dynamics, solid mechanics, fluid-structure interaction problems, crowd-structure interaction problems, numerical analysis, finite element method, linear algebra, differential geometry, probability and statistics, optimization

LANGUAGES PROFICIENCY

Italian	English	French	Portuguese
Native language	Fluent	Intermediate	Basic
-	(Level: C1)	(Level: B1)	(Level: A1)

PERSONAL SKILLS

Ambitious, persistent and determined to meet my objectives; open-minded personality, commitment to the assigned projects and multitasking approach; ability to work both independently or in a team; supportive and approachable.

WORKING EXPERIENCES AND INTERNSHIPS

2010 – 2014: C++ developer for the parallel finite element library LifeV for the simulation of the cardiovascular system
2010 – 2014: Doctoral student and teaching assistant in the Department of Mathematics of IST and EPFL
2009 – 2010: Accounting assistant at MIDA s.a.s in Turin, Italy
2006: Internship at Studio Laser s.r.l in Turin, Italy

PROJECTS DESCRIPTION

2010-2014: **PhD project**. It has focused on the study, by means of finite element simulations, of the mechanics of the cerebral arterial tissue considering both isotropic and anisotropic constitutive models. In addition, I have addressed the study of

the onset of cerebral aneurysms by means of numerical simulations of fluid-structure interaction problems in human arteries. I am the creator and main developer of the “structure module” for parallel numerical simulations of arterial tissue mechanics problems of the C++ finite element library LifeV. The implementation is based on template meta-programming techniques for the fast computation of the necessary matrices and vectors defining the problem. In particular, thanks to the approach I have adopted, **the computational time** needed for the assembly of the matrices and vectors defining the problems **has been reduced of the 50%** with respect to the one measured with classical finite element assembly techniques. Moreover, I have implemented a set of post-processing tools for the analysis of the numerical results. These tools let the user of LifeV compute important quantities, such as mechanical stresses, during run time without affecting the overall computational time of a numerical simulation. During my Doctoral Studies **I have been in charge of the maintenance and support of the structure and fluid-structure interaction modules of LifeV.**

2009: **Master Thesis project.** The project concerned the **modelization of crowd dynamics.** Particularly, I focused on the crowd-structure interaction phenomena that may occur in the case of footbridges, such as for instance for the Millenium Bridge in London. I have attempted to model different human behaviors that may affect the crowd dynamics in different conditions, such as rush hours or leisure. In addition, I have analyzed the influence of the movement of a footbridge on the crowd reaction and organization along its length. **Nowadays, the mathematical modeling of crowd dynamics is of particular interest when designing public spaces such as metro stations of stadiums in order to optimize the placement of security exits.**

2006: **Internship at Studio Laser s.r.l.** The work focused on the study of the spherical aberration, an optical effect that decreases the vision quality in aged people, and to build an early mathematical model to optimize the construction of corrective lenses. I implemented a Matlab code in order to represent, in a two dimensional space, the refraction of the light rays inside the human eye given the mathematical representation of the corneal surface. Furthermore, I have addressed the solution of optimization problems in order to compute the “optimal” form of a corrective lens to restore the correct vision. **The work that I carried out was then expanded by the Company and the computational model sold to one of the major actors in the market of corrective lenses.**

INTERESTS & ACTIVITIES

Graphics, Economics, Politics, Squash and Tennis, Jogging, Languages, and listening to different types of music.